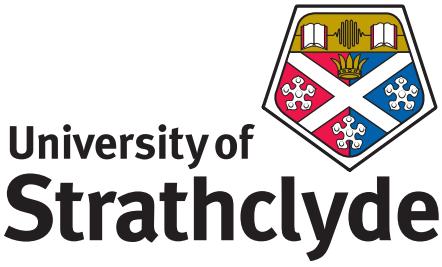

Mathematical Model Based Methods for Characterising Defects Within Ultrasonic Non Destructive Evaluation

Laura Jay Cunningham

February 20, 2015

This thesis is submitted to the University of Strathclyde for the degree of Doctor of Philosophy in the Faculty of Science.

Acknowledgements

I would firstly like to thank my supervisor Dr. Tony Mulholland for his time, support, direction and patience throughout my PhD. I am grateful for all the advice he has provided throughout the time we have worked together. I would also like to thank my industrial supervisor Colin Bird who provided us with the motivation for this research, essential higher level guidance and half of the funding. I would like to thank ESPRC for providing the other half of the funding supporting this work. I am pleased to thank my office mate Katy Tant who has made the PhD process feel like team work and ensured that we always have a good time in and out of the office. Last but not least, I would like to thank my friends and family for all of their support throughout the last 4 years. I especially want to thank my Dad, Mum, Nan, Brother and his soon to be wife Sara for being there no matter how busy or stressed they were in their own lives.

Abstract

This thesis considers the inverse problem of detecting and characterising flaws within heterogeneous materials using ultrasonic phased array transducers. Many imaging techniques include subjective measurements and the aim of this thesis is to develop objective mathematical model based methods which alleviate such subjectivity. Within the first method, the Kirchhoff model is used to derive an explicit expression which relates the maximum eigenvalue from a scattering matrix to the length of a crack in a homogeneous medium. It is shown that there exists a one to one relationship between this maximum eigenvalue and the crack length. The advantage of deriving this analytical approximation is that it can then be analysed to assess the crack sizing capabilities of the method given some scattering matrices from experimental data (the inverse problem). The procedure for using this method is then demonstrated by applying it to finite element simulated data from a homogeneous medium with a 5 mm long crack inclusion, the crack length recovered using this method is 4.4 mm. A second method is then presented which exploits another feature of the scattering matrix. An analytical expression which is an approximation to the first minimum in the pulse echo response of a scattering matrix is derived from the Kirchhoff model. This approach is also illustrated by sizing a 5 mm long crack within a homogeneous medium from finite element simulated data, the crack length recovered using this method is 5.8 mm. The

method is then extended to form a multi-frequency technique which enables it to be applied to finite element simulated data from a 5mm long crack inclusion in a heterogeneous medium. The method is enhanced by using a convolution method to reduce the noise prior to the multi-frequency method being used. The recovered crack length using this method once the noise has been reduced is 4 mm. Finally, a detection technique based on the first stage of a time reversal is presented, within which a detection threshold specific to steel welds is proposed. This method is applied to both finite element simulated data and experimental data. Having detected a flaw the time reversal algorithm (DORT) is then used to create images which are then compared to those obtained using the Total Focusing Method.

Contents

Chapter 1

Introduction

1.1 Background and Motivation

Non destructive evaluation (NDE) is the name given to the group of techniques which can be employed to inspect safety critical structures without causing any damage to them. Such structures include oil rigs, nuclear power stations and aircrafts [1]. The development of NDE is invaluable as the detection and characterisation of flaws in such structures can prevent failure and can be cost effective as components need only be replaced when a defect occurs within them. Some common NDE technologies include industrial radiography [2], electromagnetic testing [3], laser inspection [4], liquid penetrant testing and ultrasonic testing [5]. Ultrasonic testing is the most widely applicable of these techniques as it is comparatively inexpensive, portable and it can be used for sizing defects of various shapes and sizes within a structure [6]. Ultrasound is an elastic wave (or acoustic if in a fluid) which has a frequency higher than that within the hearing range of a human, which is 20 kilohertz (kHz). There exists a collection of animals which communicate using ultrasound including bats, dolphins, porpoises, insects [7], mice

and it is now believed that frogs communicate using high frequency sounds (communicating at up to 34 kHz) [8]. An ultrasound device emits and receives high frequency ultrasonic waves and has applications across various sectors, for example medical ultrasonography, NDE and seismology. Within medical and veterinary applications ultrasonic devices are deployed as a diagnostic imaging tool and are used to generate real time images of internal body structures. A commonly known application is the use of ultrasound for examining pregnant women, this is referred to as obstetric sonography [9]. Ultrasound devices are used within seismology to collect data which is used to image the interior of the earth's structure. These images are used to locate gas and oil reserves and to investigate the potential occurence of earthquakes [10]. Within the field of NDE they are used to inspect components which are subject to stress and may develop cracks or other defects within them. Examples of such structures include high pressure steam boilers used within nuclear electricity generation plants [11], the wings of aeroplanes [12] and railway tracks [13]. Within these structures the weld between two pieces of parent material is one of the most important to inspect, as this is a particularly weak point of a structure. A steel weld is comprised of a single material but during the casting process the material structure changes due to remelting and solidifying of the steel. This process causes grains of different sizes and orientations to form within the material. Ultrasonic inspection of steel welds is very challenging as these grains scatter the wave emitted from the transducer and a very noisy signal is received by the device which makes it difficult to extract any information within the signal which could be associated with a defect in the weld. Steel welds are just one example of heterogeneous materials which are difficult to inspect, other examples include concrete [14] and the layers within the interior of the earth. Ultrasonic arrays can be used to inspect heterogeneous materials and in recent years there

has been an increase in the use of arrays for NDE inspections [15, 16]. Piezoelectric transducers [17] are the most widely used and contain an active piezoelectric element which converts the electrical pulse generated into mechanical energy (and vice versa). The elastic wave is emitted from the transducer and travels through the composite under inspection. The wave is then reflected and scattered from any obstacles within the composite and received by the transducer. An ultrasonic array is a single transducer that is comprised of a number of piezoelectric elements (typically between 64 and 256), and each acts as both a transmitter and a receiver. There are several advantages of arrays to conventional ultrasonic probes (a device which contains only a single element); they cover a larger inspection area thus reducing the time taken to conduct an inspection and they can be used to produce a range of ultrasonic fields such as plane, focused and steered beams. The full set of time domain transmitted and received signals recorded by an ultrasonic array is referred to as the Full Matrix Capture (FMC) data. This is a three dimensional (transmitting element, receiving element and time) data block and is generated by firing an ultrasonic wave through one element and then receiving the reflected signal on all of the elements in the array. This process is repeated for each element until the entire set of signals is recorded to form the FMC data set. Once the FMC data has been collected from the inspection it is necessary to apply post processing algorithms in order to extract any information from the data which is associated with a flaw; this is the inverse problem.

The forward problem (or the modelling problem) predicts the outcome of a physical system given the complete set of physical parameters which describe it. An inverse problem is the reverse of this process. That is, using the outcome of the system (from experimental measurements) unknown parameters which characterise the system are derived [18, 19]. In the case of inspecting a steel weld

the forward problem would involve modelling the material to be inspected, the ultrasonic transducer and the elastic wave travelling from the transducer through the medium and back [16, 20, 21]. The outcome of the forward problem would be the time domain FMC data set. The inverse problem would then comprise of recovering the parameters associated with any defect within the material using the experimental FMC data set. The *a priori* knowledge of this system would be the properties of the ultrasonic transducer and any known properties of the material. Another example of an inverse problem from the medical field is computerised tomography (CT) [22]. While inside the CT scanner, the human body is subjected to X-rays which are received by a detector on the opposite side of the body. The inverse problem consists of applying imaging techniques to this data to reconstruct the internal structure of the human body. A final example is from geophysics in seismology where the aim is to generate an image of the earth's interior [10]. The ultrasonic data is recovered from receivers placed on the earth's surface and the inverse problem is to use this data to recover the image of the geometry below the surface of the earth. Techniques which tackle the inverse problem of recovering the geometry of an object within an elastic medium using data from ultrasonic devices have been developed and investigated extensively over the last few decades [23]. For ultrasonic inspection many of the existing techniques involve the production of an image from the ultrasonic data which can be used to both detect and characterise objects within the material. Within the field of NDE, considerable effort has been made to fully exploit the FMC data in order to characterise flaws within a structure [15,20,24–37]. The method which is often referred to as the 'gold standard' technique is the Total Focusing method (TFM) [27]. This method uses the time domain signals from the FMC data set to focus at every point in a domain to create an image of the inspection area. The same method is

used within seismology to produce a map of the earth's interior although here the approach is referred to as Kirchhoff migration [38]. Within the medical field the same approach is referred to as delay and sum beamforming [39]. This method has been applied to various experimental set-ups [40] with some success, however the method does have its limitations. It relies heavily on accurate time of flight (the travel time between the transmitting array element to the pixel location and back to the receiving array element) calculations which will not be correct when the material is highly heterogeneous. The TFM has been developed to produce more sophisticated versions such as the vector TFM [24]. This method produces a vector field output which can be used to determine the orientation and size of a scatterer embedded in a medium and produces a second scalar function which gives the specularity of any reflectors. The multi-mode TFM was also derived [25] which is an extension of the TFM that considers multiple wave modes and uses reflected pressure and shear waves to generate an image. It is possible to compare various imaging algorithms using the signal to noise ratio from the image. The methods compared in [28] are the wavenumber algorithm [26], the TFM and a back propagation method [31]. It was concluded in this work that the back propagation and wavenumber algorithms produced images with a higher signal to noise ratio. However, the TFM is more suited to parallel processing and as a result can be implemented in real time. The TFM is a subjective detection and characterisation technique. In order to determine the size of a defect highlighted using the method it is necessary to set a subjective threshold at which to measure the extent of the point spread function. A more objective method was developed by this group to characterize crack-like defects [30, 32] which uses the scattering information in the frequency domain that is extracted from the time domain FMC data. This method was applied to experimental samples and defect sizes were extracted which were

commensurate with the known defect sizes. However, the methods were applied to test blocks made of a homogeneous medium and these methods rely on a low signal to noise ratio within the time domain FMC data which will not be the case for a heterogeneous medium. Efforts have been made to develop imaging methods which overcome the shortcomings of Kirchhoff migration (TFM) and are capable of imaging defects within moderately heterogeneous media [41–45]. The coherent interferometry (CINT) method back propagates array data after the signals have been cross correlated in the time-frequency domain to create an image. The cross correlation of the singals reduces the noise although it does contain a free parameter which needs to be chosen appropriately (subjectively) in order to ensure that too much smoothing does not occur. It was shown that CINT produced images from which the parameters of scatterers within a random medium could be extracted more accurately than those when Kirchhoff migration was used.

Another branch of imaging techniques are those which use time reversal principles [46–54]. This work demonstrated that time reversed signals could be used to focus through an inhomogeneous medium on an object whose position was not known. It also showed that this process could be used for selective focusing and can be used iteratively to focus one by one on several scatterers within a medium. The decomposition of the time reversal operator (DORT) method [51, 52, 55, 56] uses the singular value decomposition (SVD) of time-frequency domain data, which is determined from the FMC data. An image of a scatterer in an inhomogeneous medium is generated using the eigenvectors of the resulting scattering amplitude matrices which are identified as containing the phase laws that need to be applied in order to focus on the scatterer. The DORT method consists of a detection stage and an imaging stage and has recently been applied successfully to image a target in a strongly scattering medium [57]. The SVD of the scattering matrices can also

be used for analysing the contributions to the ultrasonic data from single scattering and multiple scattering. This has been investigated in [58] and a method for separating single and multiple scattered waves in a heterogeneous medium was derived. This approach is used to separate the signals from a defect from the noise within a scattering medium [58]. A more general approach based on the SVD of array data was proposed by Borcea et al. [42] which can be used to detect defects in a highly cluttered medium. They propose a more adaptive version of the DORT method where the distribution of the first singular values is not known.

1.2 Outline of thesis

The aim of this thesis is to develop methods which are model based and can be used to objectively detect and characterise defects within an elastic medium. The model used throughout the thesis is the Kirchhoff model [23] and this is presented in Chapter 2. That chapter goes on to introduce a new method which derives an objective one to one correspondence between the size of a crack within an elastic medium and the maximum eigenvalue from a scattering matrix. This method uses the SVD of the time-frequency domain response matrix calculated from the FMC data and was inspired by the work of Aubry and Derode [57–59]. The expression derived in Chapter 2 is analysed in Chapter 3 where the effects of varying the system parameters are discussed. In addition, the model is interrogated to review the sensitivity of the technique to the size of the crack inclusion and the other parameters. The method in these chapters was applied then to finite element simulated data of a crack in a homogeneous medium.

In Chapter 4 a crack sizing method which uses the pulse echo response from the scattering matrices is presented and the analysis explains the empirical approach

in [30]. An analytical expression is derived which relates the first minimum of the pulse echo response to the crack size. This expression provides analytical insight into the limitations of the method. In addition, a multi-frequency extension of this technique is presented for sizing cracks in steel welds. This method was applied to finite element simulated data from a steel weld (heterogeneous medium) with a crack inclusion.

Finally, in Chapter 5 an objective method for the detection of defects within a steel weld which requires no a priori knowledge of the material properties is presented. This method is based on the first stage of the DORT method. In addition, the DORT imaging algorithm is applied to finite element simulated data (heterogeneous medium) and experimental data from a steel weld with firstly a side drilled hole flaws and then a crack inclusion. The results are compared to those produced using the TFM. The original work in the thesis is stated below.

1. In Chapter 2, Section 2.4 the Kirchhoff approximation is adapted for a linear array and the error associated with this is examined. An analytical approximation which relates the largest eigenvalue from a scattering matrix to the size of a crack inclusion in an elastic medium is then derived and presented in Section 2.3. This has been derived by making a Toeplitz approximation to the scattering matrices approximating the scattering matrices and using a known upper bound to the maximum eigenvalue from such matrices.

2. In Chapter 3, the approximation derived in Chapter 2 is interrogated to investigate the effects of the system parameters on the approximation. In addition, the approximation is differentiated in order to assess the sensitivity of the maximum eigenvalue to the crack radius (the inverse problem).

3. In Chapter 4, Section 4.2.1 an analytical approximation to the first minimum

in the pulse echo response of the scattering matrix at a single frequency is derived, analysed, and then applied to finite element simulated data.

4. The DORT and TFM methods are utilised to detect and then image flaws in Sections 5.3 and 5.4. The detection method is applied to simulated and experimental ultrasonic data from a steel weld in Sections 5.3.3 and 5.3.2, and the DORT imaging method is applied to this data in Section 5.4.

Chapter 2

Kirchhoff model and analysis of scattering matrices

2.1 Introduction

In this chapter a model based method is presented for tackling the inverse problem of sizing cracks within an elastic solid. This method is derived from the Kirchhoff model which is a high frequency approximation to the scattering of a linear elastic wave from an ellipsoid within a homogeneous medium. This multi-frequency method provides a formula which relates the crack size to the maximum eigenvalue of the associated scattering matrix as extracted from the model.

2.2 Kirchoff model and scattering matrices

The Kirchhoff model is used to provide a high frequency approximation to the scattering of a linear elastic wave from a crack in a homogeneous medium. The signals scattered from a crack in the host material are then represented in the frequency domain by scattering matrices, which are a function of the transmitted

and received waves. Figure 2.1 shows a schematic of the model geometry, where the ellipsoidal crack is lying in the plane $x_1 = 0$ and the ultrasonic waves emanating from the array lie in the plane $x_3 = 0$. An analytical form for the scattering amplitude can be derived by assuming that the flaw is ellipsoid (with axes lengths a_1, a_2 and a_3 as in Figure 2.1). To simulate a zero volume flaw (a crack) in the $x_3 = 0$ plane then the ellipsoidal axis a_1 is set equal to zero. The flaw is positioned so that its centre lies at the origin. The Kirchhoff approximation provides an expression for the scattering amplitude of an ellipsoidal crack by a transmitted pressure wave in a homogeneous elastic medium and is given by (equation (10.168), [23])

$$A_n^{P;\beta}(\mathbf{e}_i^\beta, \mathbf{e}_s^P) = -\frac{ia_2a_3e_{sl}^P e_{sn}^P e_{sj}^P C_{kplj} D_p^\beta n_k}{2\rho c_1^2 |(c_1/c_\beta)\mathbf{e}_i^\beta - \mathbf{e}_s^P| r_e^{P;\beta}} J_1\Big(\frac{2\pi}{\lambda}|(c_1/c_\beta)\mathbf{e}_i^\beta - \mathbf{e}_s^P| r_e^{P;\beta}\Big), \qquad (2.1)$$

where $\mathbf{e}_i^\beta$ ($\beta = S, P$ where S is a shear wave and P is a pressure wave), $\mathbf{e}_s^P$ are the unit vectors in the transmitting and receiving direction of the ultrasonic wave and c_1 is the wavespeed of the pressure wave. The unit vector $\mathbf{e}_r^P$ is in the direction of the specular reflection from the crack; the specular reflection is in the direction of the maximum amplitude reflected wave. The angle between the specular reflection direction and the normal to the crack is equal to that between the direction of the transmitted wave and the normal, as demonstrated in Figure 2.2. In addition, a_2, a_3 are the other radii of the ellipsoid, $c_\beta, (\beta = P, S)$ are the wave speeds for pressure (P) and shear waves (S), ρ is the material density, λ is the wavelength of the transmitted pressure wave, C_{kplj} is the elastic modulus tensor. Also, J_1 is the Bessel function of the first kind of order 1, $r_e^{P;\beta}$ is the effective radius of the crack and

$$D_p^\beta = d_{ip}^\beta + \sum_{m=P,SV,SH} R^{m;\beta} d_{rp}^m \qquad (2.2)$$

where $R^{m;\beta}$ are plane wave reflection co-efficients at the interface between the host material and the crack and d^m_{ip} (d^m_{rp} respectively) is the pth component unit vector in the direction of a transmitted wave of type m travelling in the $\mathbf{e}_i$ direction (specular reflected wave from the interface in the $\mathbf{e}_r$ direction respectively). In equation (2.2) SV and SH are acronyms for shear vertical and shear horizontal waves, these waves are not considered in this work.

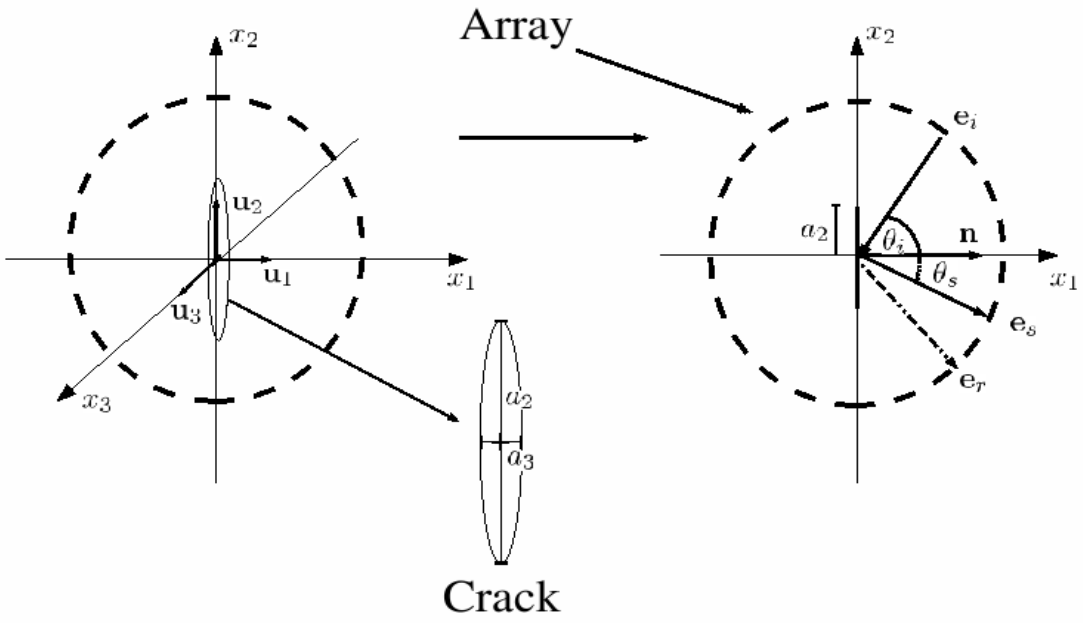

Figure 2.1: A schematic of the geometry used to derive the scattering matrices that arise in the Kirchhoff model (equation (2.7)) for a crack inclusion in an elastic solid. Here $2a_2$ is the crack length, $\mathbf{n}$ is the normal to the crack, $\mathbf{e}_i$ ($\mathbf{e}_r, \mathbf{e}_s$) is the transmitted (receiving, specular) wave direction, $\theta_i(\theta_s)$ is the angle measured in an anticlockwise direction from the positive x_1 axis of the transmitted (received) wave and $\mathbf{u}_1, \mathbf{u}_2$ and $\mathbf{u}_3$ are unit vectors in the x_1, x_2 and x_3 directions.

In an isotropic, homogeneous medium the elastic modulus tensor in equation (2.1) reduces to

$$C_{kplj} = L\delta_{kp}\delta_{lj} + \mu(\delta_{kl}\delta_{pj} + \delta_{kj}\delta_{pl}) \tag{2.3}$$

where L and μ are the Lamé co-efficients. Let

$$\mathbf{e}_q = \frac{\mathbf{e}_i - \mathbf{e}_s}{|\mathbf{e}_i - \mathbf{e}_s|} \tag{2.4}$$

and $\mathbf{u}_2, \mathbf{u}_3$ be unit vectors along the x_2, x_3 axes respectively. Then the effective radius of the crack is defined as

$$r_e^{P;\beta} = \sqrt{a_2^2(\mathbf{e}_q \cdot \mathbf{u}_2)^2 + a_3^2(\mathbf{e}_q \cdot \mathbf{u}_3)^2} = a_2|\mathbf{e}_q \cdot \mathbf{u}_2| \tag{2.5}$$

since $\mathbf{e}_i$ and $\mathbf{e}_s$ are perpendicular to $\mathbf{u}_3$.

Here only pressure waves are considered, that is $\beta = P$ in equation (2.1) and therefore the direction of the displacement of the wave is in the same direction as the transmitting/receiving direction, that is $e_{ip} = d_{ip}$ and $e_{rp} = d_{rp}$. Substituting this into equation (2.2) gives

$$D_p^p = e_{ip}^P - e_{rp}^P, \tag{2.6}$$

where $R^{P;P} = -1$. When equations (2.3) and (2.6) are substituted into equation (2.1) then it can be written as

$$A_n(\mathbf{e}_i; \mathbf{e}_s) = -\frac{ia_2a_3e_{sn}(L((\mathbf{e}_i - \mathbf{e}_r) \cdot \mathbf{n}) + 2\mu((\mathbf{e}_i - \mathbf{e}_r) \cdot \mathbf{e}_s)(\mathbf{e}_s \cdot \mathbf{n}))}{2\rho c^2|\mathbf{e}_i - \mathbf{e}_s|r_e} J_1\Big(\frac{2\pi}{\lambda}|\mathbf{e}_i - \mathbf{e}_s|r_e\Big). \tag{2.7}$$

Finally, substituting equation (2.5) into equation (2.7) gives

$$\begin{aligned} A_n(\mathbf{e}_i; \mathbf{e}_s) = &-\frac{ia_3e_{sn}(L((\mathbf{e}_i - \mathbf{e}_r) \cdot \mathbf{n}) + 2\mu((\mathbf{e}_i - \mathbf{e}_r) \cdot \mathbf{e}_s)(\mathbf{e}_s \cdot \mathbf{n}))}{2\rho c^2|(\mathbf{e}_i - \mathbf{e}_s) \cdot \mathbf{u}_2|} \\ &\times J_1\Big(\frac{2\pi a_2}{\lambda}|(\mathbf{e}_i - \mathbf{e}_s) \cdot \mathbf{u}_2|\Big). \end{aligned} \tag{2.8}$$

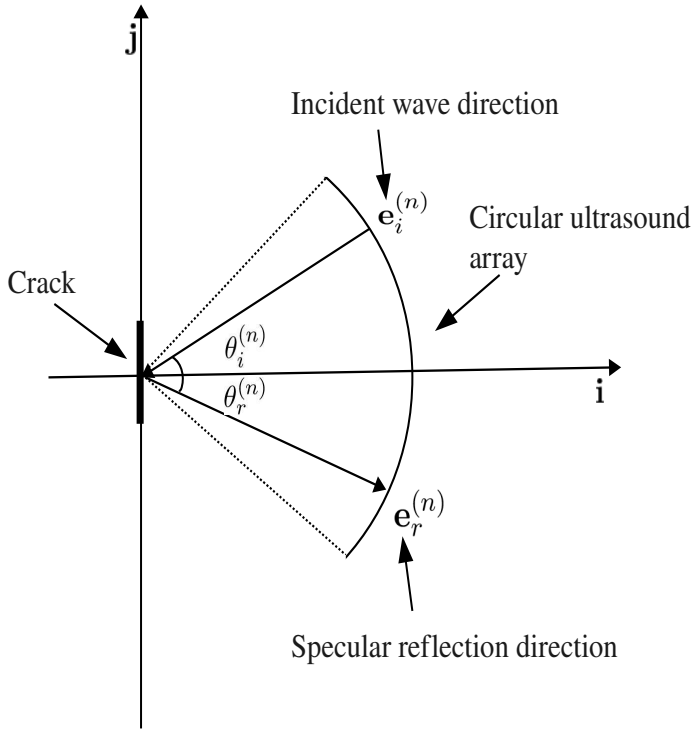

Figure 2.2: A schematic showing the location of the unit vector in the specular reflection direction, $\mathbf{e}_r^{(n)}$, with respect to the unit vector in the incident direction, $\mathbf{e}_i^{(n)}$, on a limited aperture, circular array.

The transmitted and received wave directions can be defined at a discrete set of values and if these completely surround the flaw it is called a *full aperture*. By calculating the absolute value of the scattering amplitude given in equation (2.8) for every possible pair of transmitting and receiving angles (at a fixed frequency) a scattering matrix can be constructed. An example of a scattering matrix for a full aperture, circular array is shown in Figure 2.3. The highest amplitudes in the scattering matrix occur close to the specular reflection and are shown in Figure 2.3 in black.

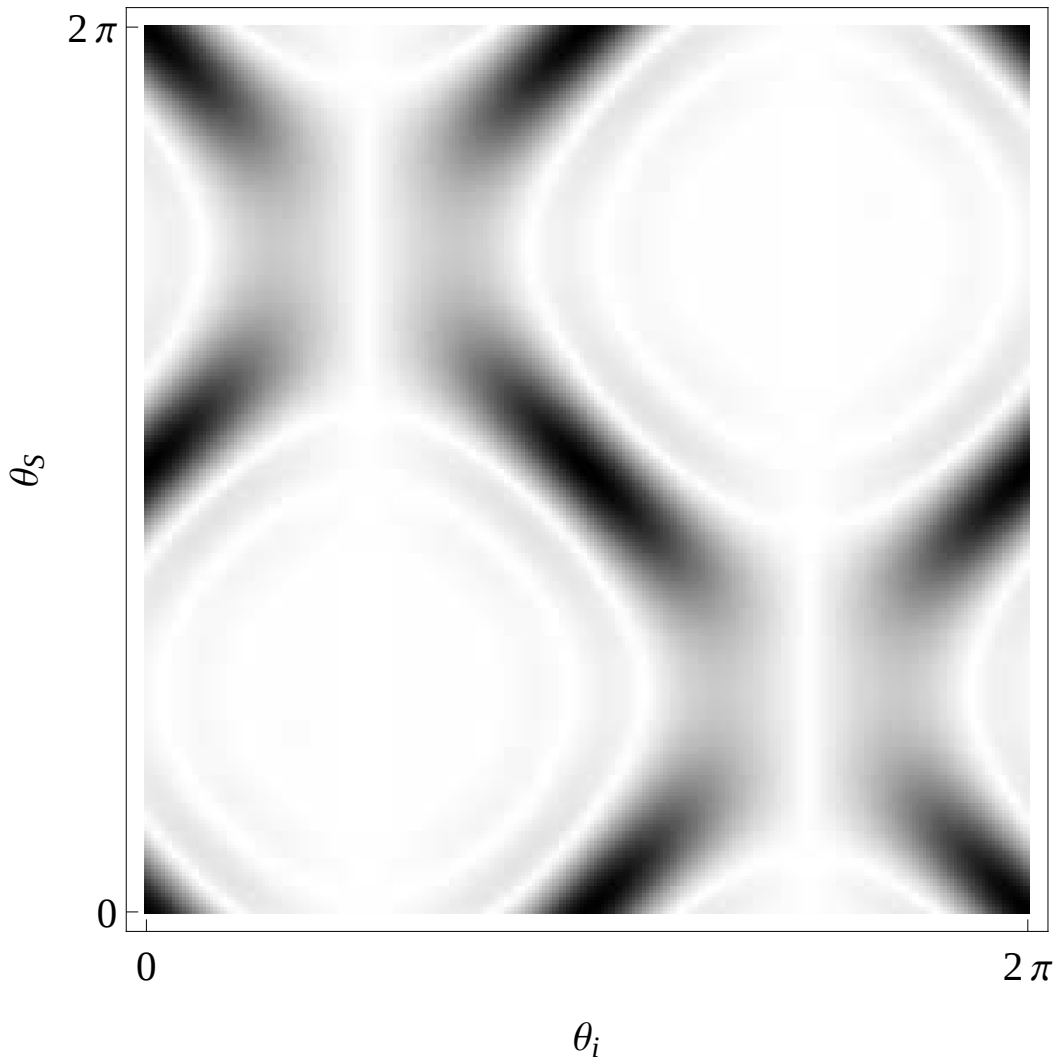

Figure 2.3: An example of a scattering matrix for a full aperture, circular array where θ_s is the receiving angle and θ_i is the transmitting angle. Here the number of elements N is 256, the depth of the flaw d is 50 mm and the crack length to wavelength ratio, $\hat{a} = 1$.

2.3 Full Matrix Capture data

Obtaining data using experimental test pieces with embedded flaws is extremely costly, as the manufacture of such test pieces is very expensive and time consuming. In the absence of such data, finite element simulations have been used in order to develop and test methods for the non-destructive detection and characterisation

of weld defects using ultrasound transducer arrays [60]. In particular, the explicit time-domain code PZFlex (Weidlinger Associates, CA) has been used and the experimentally measured heterogeneity of the weld, and defects of varying size, position and orientation can be included, as can the effects of the transducer array [61].

2.3.1 Finite element simulated data

A simulation which includes the microstructure of a steel weld was generated in the work by G.Harvey et al. [60], the details of which are summarised here. In order to run such simulations it is imperative to have knowledge of the internal microstructure of these welds as the heterogeneous nature of the material has a marked effect on the passage of elastic energy through it. To begin with, it is important to have one experimental test piece that can be fully characterised in this way. This test piece can then be used to validate the computer simulation by comparing experimental and simulated data. This should always be done prior to these simulations being expanded to incorporate a range of different flaws. Fortunately, considerable effort has already been expended in this direction and a fully characterised austenitic steel weld has been achieved using Electron Backscatter Diffraction (EBSD) [62]. The resulting spatial resolution within the sample was of the order of 40 μm for a 67 mm thick weld (see Figure 2.4). It is important to note that, although the weld is comprised of a single anisotropic material, there are boundaries around crystals within the weld which are a consequence of the welding process. In fact, the internal microstructure consists of a partitioning of the weld area into a large set of sub-regions, each one of which has a different crystal orientation. Within the finite element simulation each element is associated with a crystal stiffness and orientation, and groups of contiguous elements associated

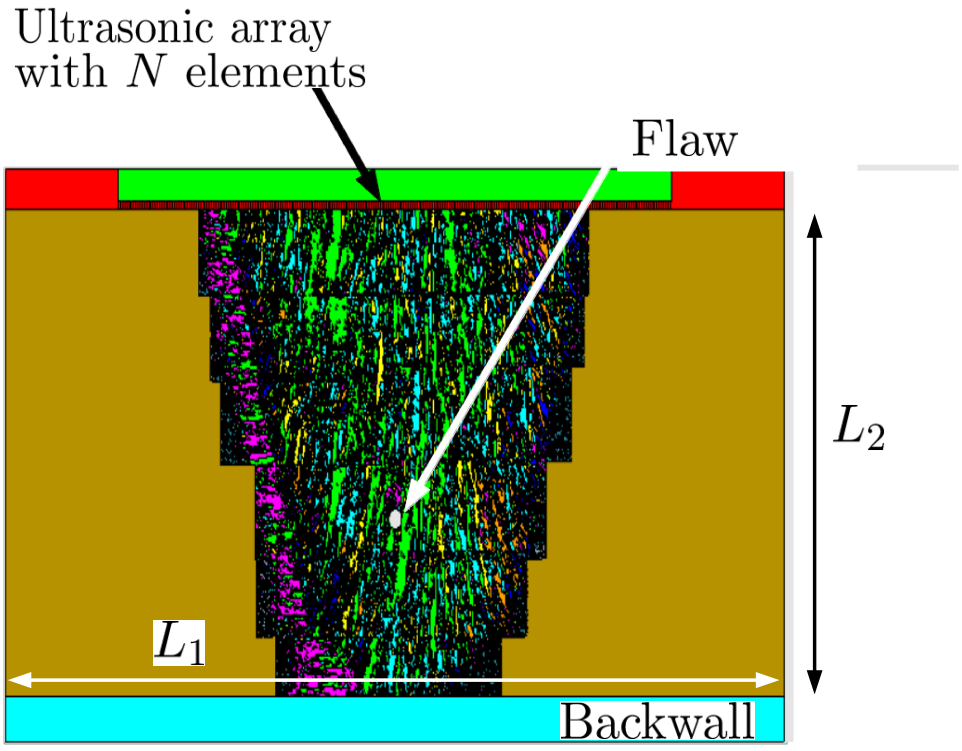

Figure 2.4: The microstructure of the heterogeneous weld, where each colour is associated with a different grain orientation and L_1=67 mm and L_2=128 mm.

with the same stiffness and orientation form a grain within the weld. In order to attribute elastic stiffnesses to these regions a second experiment is necessary. Here a thin slice of the material is taken to create a 2-D model and a series of through-transmission ultrasonic velocity calculations are performed on each of the different sub-regions. The simulation of the weld from [60] was used in this work, in addition a zero volume crack was inserted into the PZFlex simulation geometry [61] in order to test the crack sizing algorithms. A schematic demonstrating the set up is shown in Figure 2.4. A square grid was used within the simulation and so the crack is represented by a thin rectangular void (no stiffness) and will behave as a perfect reflector. In the forthcoming chapter, more finite element simulations are generated which include the weld microstructure and side drilled hole inclusions rather than cracks. The simulation also included a 64 element ultrasonic

array placed directly above the weld microstructure. The width of each element was 1.5 mm, the pitch of the array was 2 mm and with $N = 64$ elements the total array length (aperture) was 128 mm. A 1.5 MHz single cycle sinusoid was transmitted by one element and the time domain echo received by all 64 elements was recorded. Figure 2.5 shows typical signals recorded by the ultrasonic array transducer within the simulation for one transmit/receive pair of array elements when (a) the medium is homogeneous and (b) the medium is heterogeneous (a steel weld). These figures clearly show the effect of including the heterogeneous weld microstructure within the simulation. In Figure 2.5 (a), there is an echo from the crack at about 15 μs and an echo from the backwall at about 25 μs. However, neither the reflection from the flaw or the backwall can be visually identified in the analogous signal from the simulation containing the weld microstructure. These parameters are summarised in Appendix C Table C.1. The particular transmitting element was then systematically changed by moving along the array until the full matrix of time domain data was captured, for a total of 64 unique simulations per virtual inspection scenario. Full matrix capture (FMC) data is the name given to this complete set of time domain signals recorded by the phased array controller, Figure 2.6 shows a schematic of a typical FMC matrix. This simulated data will be used in all forthcoming chapters to test the proposed methods. It is important to note that this form of data collection using an ultrasonic array controller is not yet the standard method for gathering data within industry. There exist other types of data acquisition, for example focal law sequencing can be used to generate a desired beam shape [63]. In addition to the simulated data containing the microstructure of the weld, simulated data where the heterogeneity in the host material was removed leaving an isotropic material was generated. This ability to isolate the effects of the weld structure by switching it on or off is another

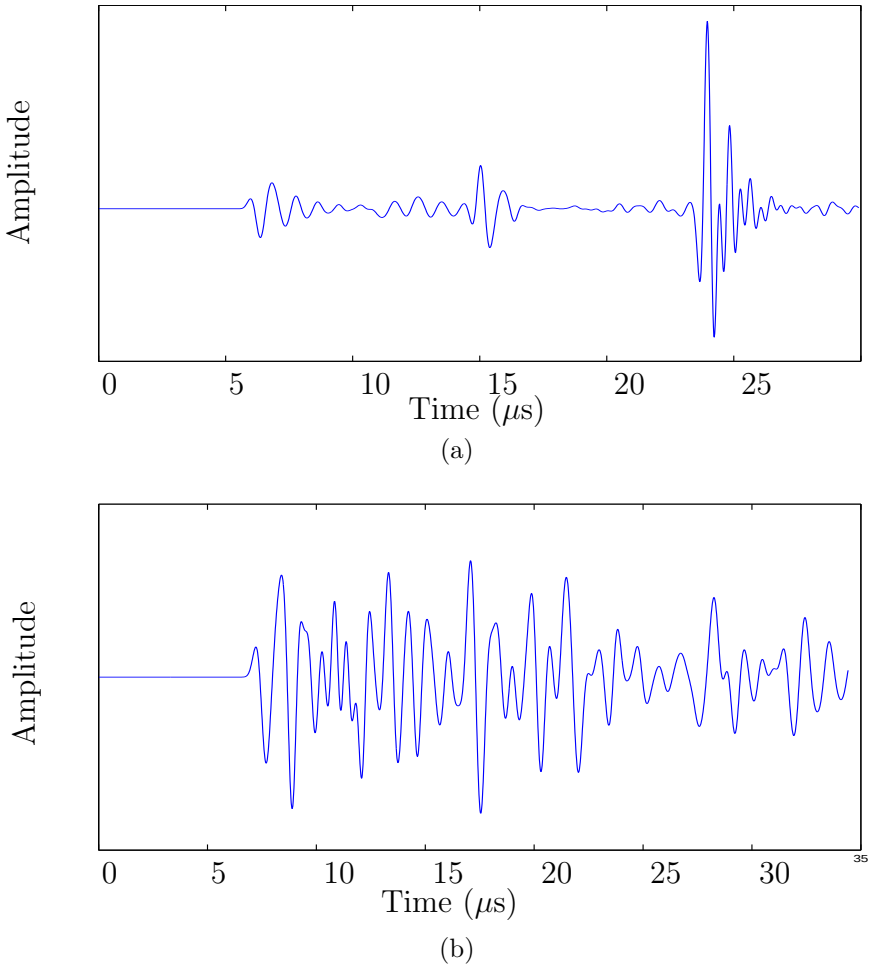

Figure 2.5: Typical signals, as recorded by the ultrasonic array transducer in the finite element simulations for (a) the homogeneous medium and (b) the heterogeneous medium (steel weld), where in each case a 2.5mm radius crack has been included 50mm from the back wall. The other system parameters are given in Appendix C, Table C.1.

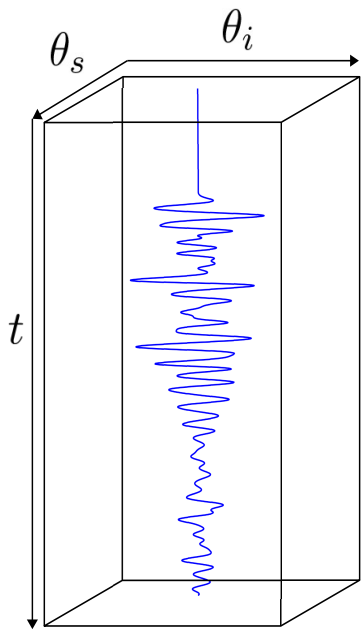

Figure 2.6: A schematic demonstrating Full Matrix Capture (FMC) data, where the dimensions of the matrix are the transmitting ultrasonic array aperture angle, θ_i, the receiving array aperture angle, θ_s and time t.

advantage of using simulations.

2.4 Approximation to a limited aperture ultrasonic array

The Kirchhoff model provides the response from a full aperture, circular array which is shown by the dashed line in Figure 2.1. However, in this work the circular array is approximated by a discretised linear limited aperture array, as this is what is used in practice. The approximation to a limited aperture array allows the expression for the scattering matrices given by equation (2.8) to be parameterised. The scattering amplitude is converted into a scalar value, as recorded by the ultrasonic transducer receiver, by taking the scalar product of the vector of

components equation (2.8) with the direction of reception, $\mathbf{e}_s$ to give

$$A(\mathbf{e}_i;\mathbf{e}_s) = -\frac{(L(\mathbf{e}_i-\mathbf{e}_r)\cdot\mathbf{n}+2\mu((\mathbf{e}_i-\mathbf{e}_r)\cdot\mathbf{e}_s)(\mathbf{e}_s\cdot\mathbf{n}))}{2\rho c^2|(\mathbf{e}_i-\mathbf{e}_s)\cdot\mathbf{u}_2|}J_1\Big(\frac{2\pi a_2}{\lambda}|(\mathbf{e}_i-\mathbf{e}_s)\cdot\mathbf{u}_2|\Big) \tag{2.9}$$

where the scale factor ia_3 has been dropped for simplicity. The unit vector in the receiving direction for the n^{th} element in the ultrasound array is given by

$$\mathbf{f}_s^{(n)} = d\mathbf{i} + q_n\mathbf{j} = \mathbf{e}_s^{(n)}|\mathbf{f}_s^{(n)}|, \tag{2.10}$$

where d is the minimum distance between the flaw and the ultrasound array (it is assumed here that the centre of the array is the closest point in the array to the flaw),

$$q_n = \frac{\triangle q}{2}(N+1-2n), \tag{2.11}$$

N is the total number of elements in the ultrasound array and the periodicity of the array elements (the pitch) is given by

$$\triangle q = \frac{l}{N-1}, \tag{2.12}$$

where l is the array length (aperture), as shown in Figure 2.7.

Hence,

$$\mathbf{e}_s^{(n)} = \frac{d}{\sqrt{d^2+q_n^2}}\mathbf{i} + \frac{q_n}{\sqrt{d^2+q_n^2}}\mathbf{j} = \sqrt{1-\hat{q}_n^2}\mathbf{i} + \hat{q}_n\mathbf{j}. \tag{2.13}$$

In the analysis below it is assumed that N is even and that the array elements are evenly spaced (that is, the array pitch $\triangle q$ is a constant). The forthcoming analysis is simplified if $\hat{q}_n$ is linear as a function of n. So, to approximate q_n as a linear function, equation (2.11) is manipulated as follows:

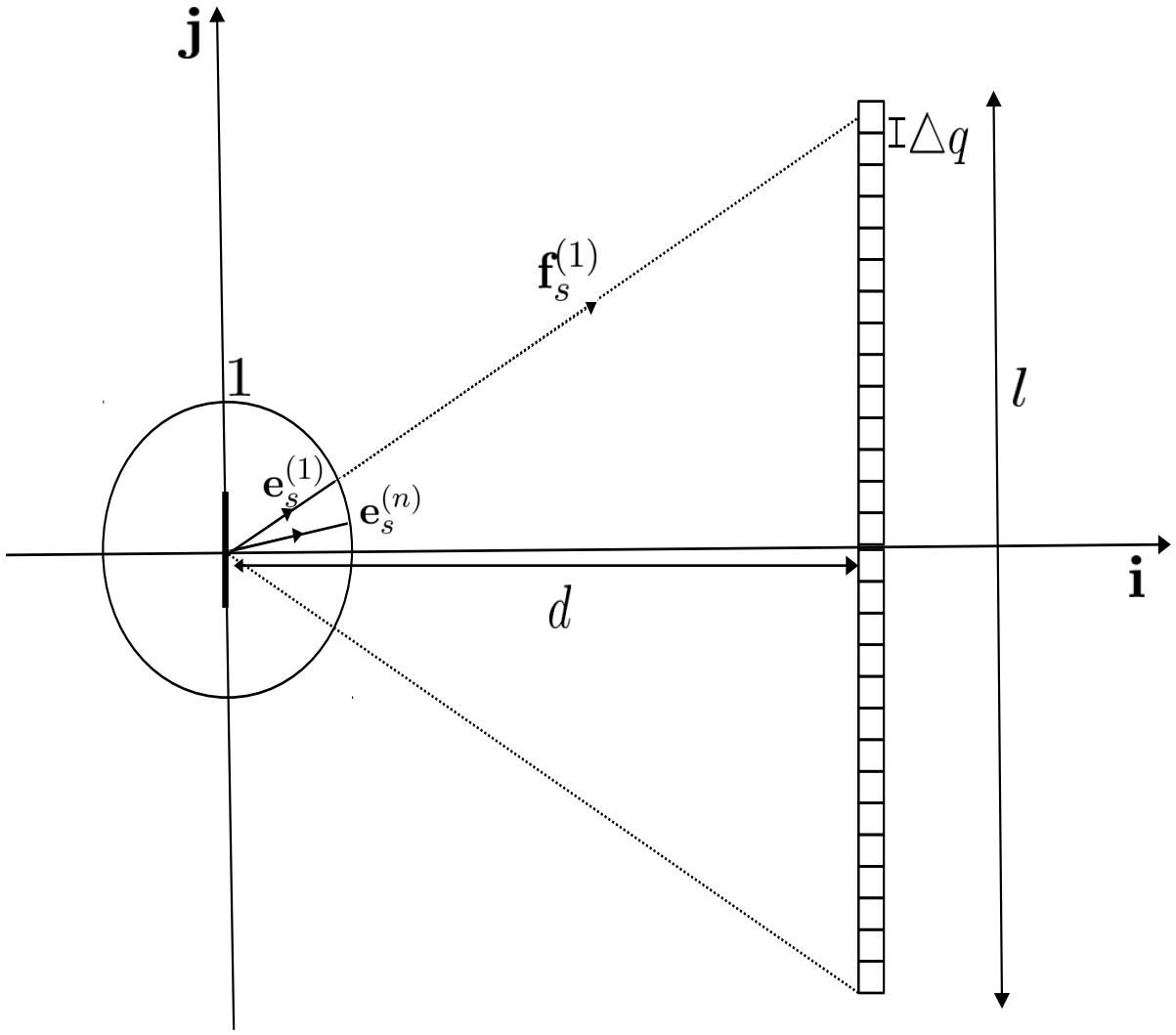

Figure 2.7: A schematic demonstrating the geometry of the linear ultrasound array. The unit vector $\mathbf{e}_s^{(n)}$ is in the receiving direction for array element n on the array. The array is of length l and the flaw is at a depth d from the array, $\triangle q$ gives the pitch between the array elements.

$$\begin{aligned}\hat{q}_n &= \frac{q_n}{\sqrt{d^2+q_n^2}} = \frac{(N+1-2n)\triangle q/2}{\sqrt{d^2+(\triangle q/2)^2\,(N+1-2n)^2}} \\ &= \frac{l}{\sqrt{4d^2+l^2(1-h(n))^2}}\frac{N+1-2n}{N-1},\end{aligned} \tag{2.14}$$

where

$$h(n) = \frac{2(n-1)}{N-1}. \tag{2.15}$$

The denominator in the expression for $\hat{q}_n$ in equation (2.14) is manipulated further to give

$$\begin{aligned} \hat{q}_n &= \frac{l}{\sqrt{4d^2 + l^2 + l^2(h^2 - 2h)}} \frac{N+1-2n}{N-1} \\ &= \frac{l}{\sqrt{4d^2 + l^2}} \frac{N+1-2n}{N-1} \frac{1}{\sqrt{1 - l^2(2h - h^2)/(4d^2 + l^2)}} \\ &= \frac{l}{\sqrt{4d^2 + l^2}} \frac{N+1-2n}{N-1} \frac{1}{\sqrt{1-\alpha}} \end{aligned} \tag{2.16}$$

where

$$\alpha = \frac{l^2}{4d^2 + l^2}(2h - h^2). \tag{2.17}$$

Since $0 \leq h \leq 2$ for $n = 1, ..., N$ then $0 \leq 2h - h^2 \leq 1$, and

$$0 < \frac{l^2}{4d^2 + l^2} < 1, \tag{2.18}$$

then α is small. The Taylor series approximation $(1-\alpha)^{-1/2} = 1 - \alpha/2$ is applied to equation (2.16) to approximate $\hat{q}_n$ as

$$\begin{aligned} \hat{q}_n &= \frac{l}{\sqrt{4d^2 + l^2}} \frac{N+1-2n}{N-1} \left(1 - \frac{\alpha}{2}\right) + \mathcal{O}(\alpha^2) \\ &= \frac{\triangle y}{2}(N+1-2n)\left(1 - \frac{\alpha}{2}\right) + \mathcal{O}(\alpha^2) \\ &= y_n \left(1 - \frac{\alpha}{2}\right) + \mathcal{O}(\alpha^2) = y_n + \mathcal{O}(\alpha), \end{aligned} \tag{2.19}$$

where

$$\triangle y = \frac{l}{(N-1)\sqrt{4d^2 + l^2}} \tag{2.20}$$

Sign	Element Index n	y_n
+	1	$\triangle y(N-1)/2$
⋮	2	$\triangle y(N-3)/2$
⋮	⋮	⋮
⋮	$N-1$	$-\triangle y(N-3)/2$
-	N	$-\triangle y(N-1)/2$

Table 2.1: This table shows the relationship between the array index n and the approximation to the coordinate y_n (equation (2.21)).

and

$$y_n = \frac{\triangle y}{2}(N+1-2n). \tag{2.21}$$

The relationship between $\hat{q}_n$ and y_n is illustrated in Figure 2.4. The exact value,

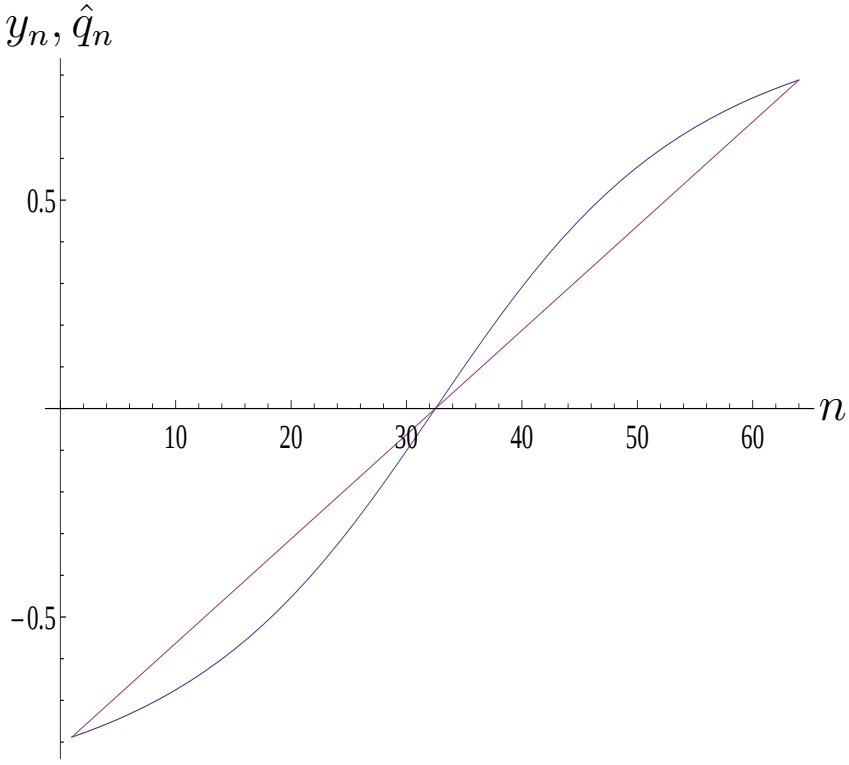

Figure 2.8: A plot comparing the exact **j**-component of the scattering direction unit vector, $\hat{q}_n$ (blue line) to the approximation, y_n (red line) for typical parameter values given in Table 2.1

n^*, where the error in the approximation is largest can be found by considering

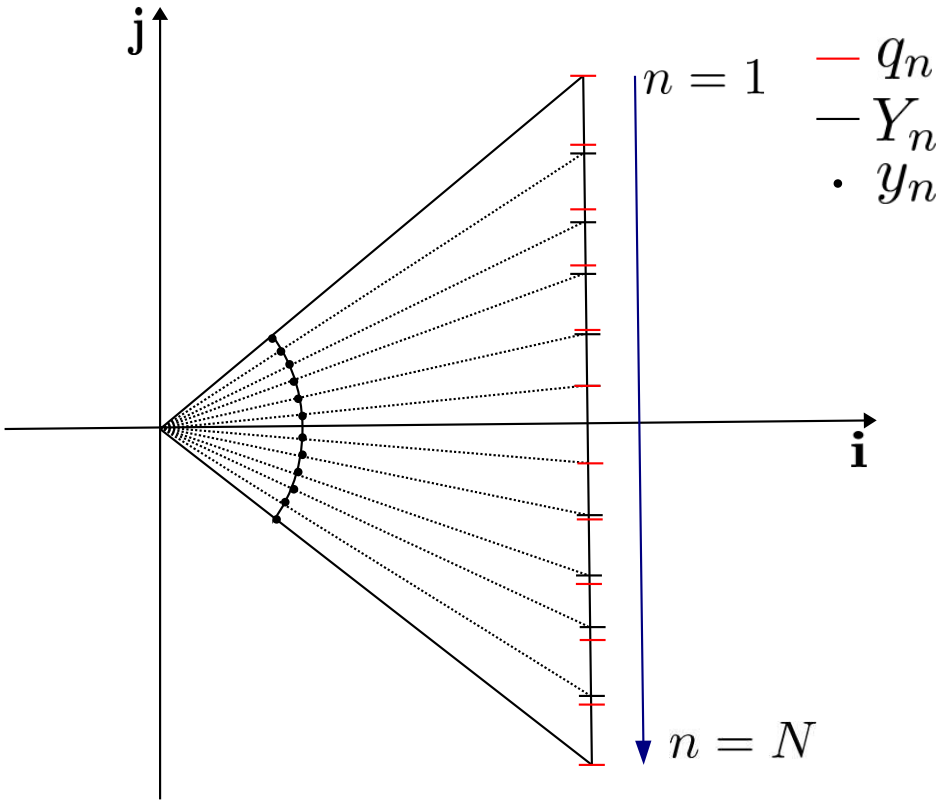

Figure 2.9: A schematic demonstrating the geometry of the exact array element positions, q_n (red dashes) from equation (2.11), the approximate array element positions, Y_n (black dashes) from equation (2.22) and the approximate array elements on the unit circle, y_n (black dots) from equation (2.21).

the difference between q_n and

$$Y_n = \frac{y_n}{\sqrt{1 - y_n^2}} d, \tag{2.22}$$

which is the projection of the approximate array element position, y_n, on the unit circle onto the linear array at depth d. The schematic in Figure 2.9 demonstrates the geometry of the exact array element positions, q_n (red dashes), the approximate array element positions, Y_n (black dashes), and the approximate array element positions, y_n (black dots), on the unit circle. The difference between q_n and Y_n

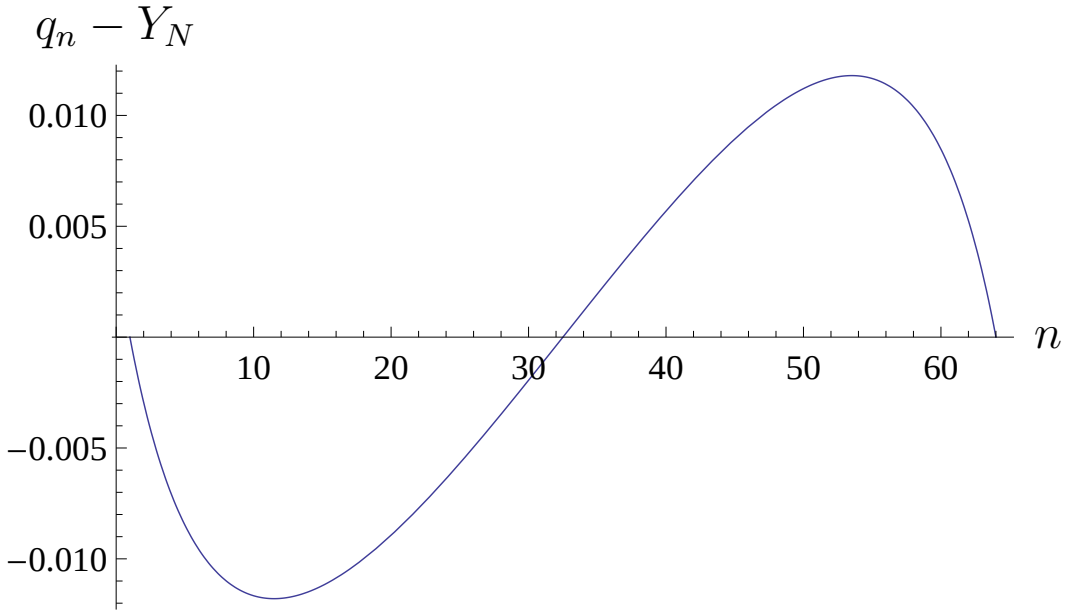

Figure 2.10: The difference between the exact array element positions, q_n, and the approximate array element positions, Y_n as given by equation (2.22), for typical parameters: N=64, l = 128mm and d = 50mm.

is plotted for typical values of N, l and d and is shown in Figure 2.10; this figure shows numerically that the difference between the true array element positions q_n and the approximate positions Y_n is of the order 10^{-2}.

From equation (2.13) the approximate transmitting and receiving unit vectors are therefore given by

$$\mathbf{e}_i^{(m)} = -\sqrt{1 - y_m^2}\mathbf{i} - y_m\mathbf{j} \tag{2.23}$$

and

$$\mathbf{e}_s^{(n)} = \sqrt{1 - y_n^2}\mathbf{i} + y_n\mathbf{j}. \tag{2.24}$$

The schematics shown in Figures 2.11(a) and 2.11(b) demonstrate the positions of $\mathbf{e}_i^{(m)}$ and $\mathbf{e}_s^{(n)}$, respectively. By restricting attention to the case where the flaw is orientated to lie along the x_2-axis then the specular reflection is given by

$$\mathbf{e}_r^{(m)} = \sqrt{1 - y_m^2}\mathbf{i} - y_m\mathbf{j}, \tag{2.25}$$

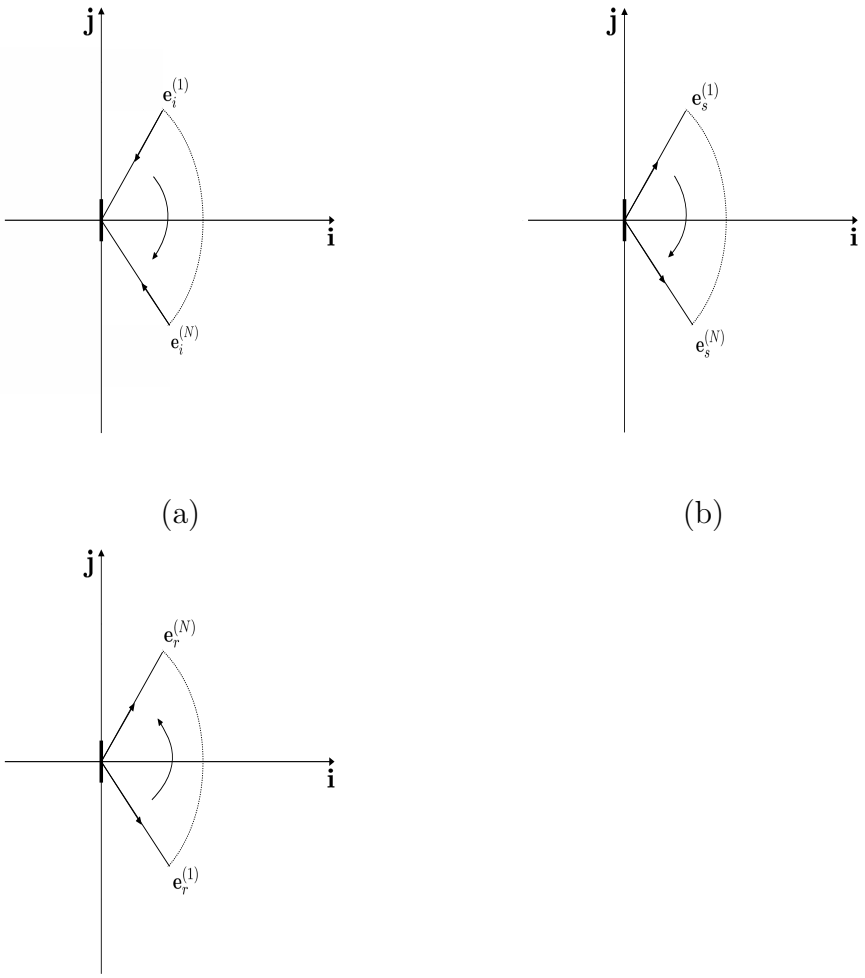

Figure 2.11: The position and direction of the transmitting ($\mathbf{e}_i^{(n)}$), receiving ($\mathbf{e}_s^{(n)}$) and reflecting vectors ($\mathbf{e}_r^{(n)}$), given by equations (2.23)-(2.25), for $n = 1, ..., N$.

where the absolute value of the angle, $|\theta_i^{(n)}|$, between $\mathbf{e}_i^{(n)}$ and the **i**-direction is equal to $|\theta_r^{(n)}|$, as demonstrated in Figure 2.2. The position of the specular reflection vector directions are shown in Figure 2.11(c). Since the flaw lies on the x_2-axis (that is $\mathbf{u}_2 = \mathbf{j}$ and $\mathbf{n}$=**i**) then

$$(\mathbf{e}_i^{(m)} - \mathbf{e}_r^{(m)}) \cdot \mathbf{n} = -2\sqrt{1 - y_m^2},$$

$$(\mathbf{e}_i^{(m)} - \mathbf{e}_r^{(m)}) \cdot \mathbf{e}_s^{(n)} = -2\sqrt{(1 - y_m^2)(1 - y_n^2)},$$

and

$$(\mathbf{e}_i^{(m)} - \mathbf{e}_s^{(n)}) \cdot \mathbf{u}_2 = -(y_m + y_n). \tag{2.26}$$

Substituting these into equation (2.9) yields

$$A(y_m, y_n) = \frac{\sqrt{1 - y_m^2}}{\rho c^2 |y_n + y_m|}(L + 2\mu(1 - y_n^2))J_1\Big(2\pi\hat{a}|y_n + y_m|\Big) \doteq \frac{1}{\rho c^2} A_{m,n} \tag{2.27}$$

where $\hat{a} = a_2/\lambda$ and $2a_2$ is the crack length. Figure 2.12 shows the scattering matrix given by equation (2.27) for a limited aperture array. In the next section, a crack sizing method is developed which relates the maximum eigenvalue to the length of the crack. The scattering matrix is used again in Chapter 4 to develop another crack sizing method which uses the first minimum of the pulse echo response to determine the length of the crack inclusion.

2.5 Crack sizing using the maximum eigenvalue

In this section the scattering matrix from the Kirchhoff model, discussed in Section 2.2, is used to develop a crack sizing algorithm. This algorithm uses the maximum eigenvalue from scattering matrices generated over a range of frequencies.

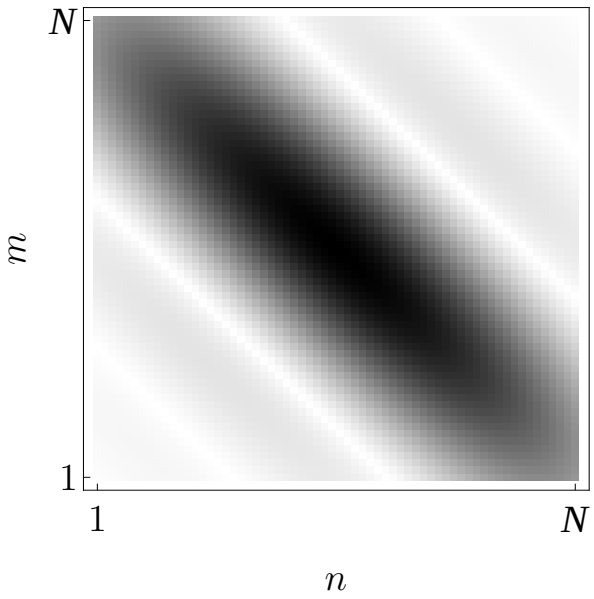

Figure 2.12: An example of a scattering matrix for a limited aperture array which is generated using equation (2.27). This shows a subsection of the scattering matrix for a full aperture array as shown in Figure 2.3, here the array angle is limited. Typical parameter values of $N = 64$, $l = 128$ mm and $d = 50$ mm were used to generate this image.

Note that the corresponding maximum singular value will be used in Chapter 5 to develop a time-frequency domain detection method. In the present chapter the maximum eigenvalue from the scattering matrices is approximated to allow analytical insight into the effects of the system parameters on the crack sizing capabilities of the method.

2.5.1 Toeplitz approximation to the scattering matrices

It is clear from empirical observations that there is a relationship between the size of the crack and the form of the scattering matrix. It would therefore be advantageous if an analytical approach could be developed to capture this correlation. From the images of the scattering matrix in Figure 2.12 it can be seen that the dominant values aggregate around the skew diagonal. There is a considerable body

of research concerning Toeplitz matrices and in an effort to benefit from this body of work the scattering matrix, A (given by equation (2.27)), will be approximated by a Toeplitz matrix. First, the matrix A is transformed to A_T via

$$A_T(y_{m'}, y_n) = A(y_m, y_n) \qquad \text{where} \qquad m' = N - m + 1 \tag{2.28}$$

so that the dominant values accumulate around the main diagonal. The transformed scattering matrix, A_T, is now in a suitable form and will be approximated by a Toeplitz matrix. A Toeplitz matrix is of the form

$$T_{n,n} = \begin{pmatrix} t_1 & t_2 & t_3 & \cdots & \cdots & t_n \\ t_2 & t_1 & t_2 & \ddots & & \vdots \\ t_3 & t_2 & \ddots & \ddots & \ddots & \vdots \\ \vdots & \ddots & \ddots & \ddots & t_2 & t_3 \\ \vdots & & \ddots & t_2 & t_1 & t_2 \\ t_n & \cdots & \cdots & t_3 & t_2 & t_1 \end{pmatrix} \tag{2.29}$$

and is fully determined using the entries from the first row, $T_1 = (t_1, ..., t_n)$. Here the row where the maximum of $A_T(y_m, y_n)$ occurs will be used to create a Toeplitz approximation, $\bar{A}_T$. This row is highlighted by the green squares in the original scattering matrix, A, in Figure 2.13(a) and in the transformed matrix, A_T, in Figure 2.13(b). The Toeplitz matrix resulting from this matrix is shown in Figure 2.13(c), where all remaining entries in the row are filled with zeroes. The original matrix, A, is used in the forthcoming analysis which proves firstly, which row the maximum occurs in and secondly, that the Toeplitz approximation is justified. This will be demonstrated by showing that all rows are approximately equal to that where the maximum occurs. This maximum amplitude occurs on the specular

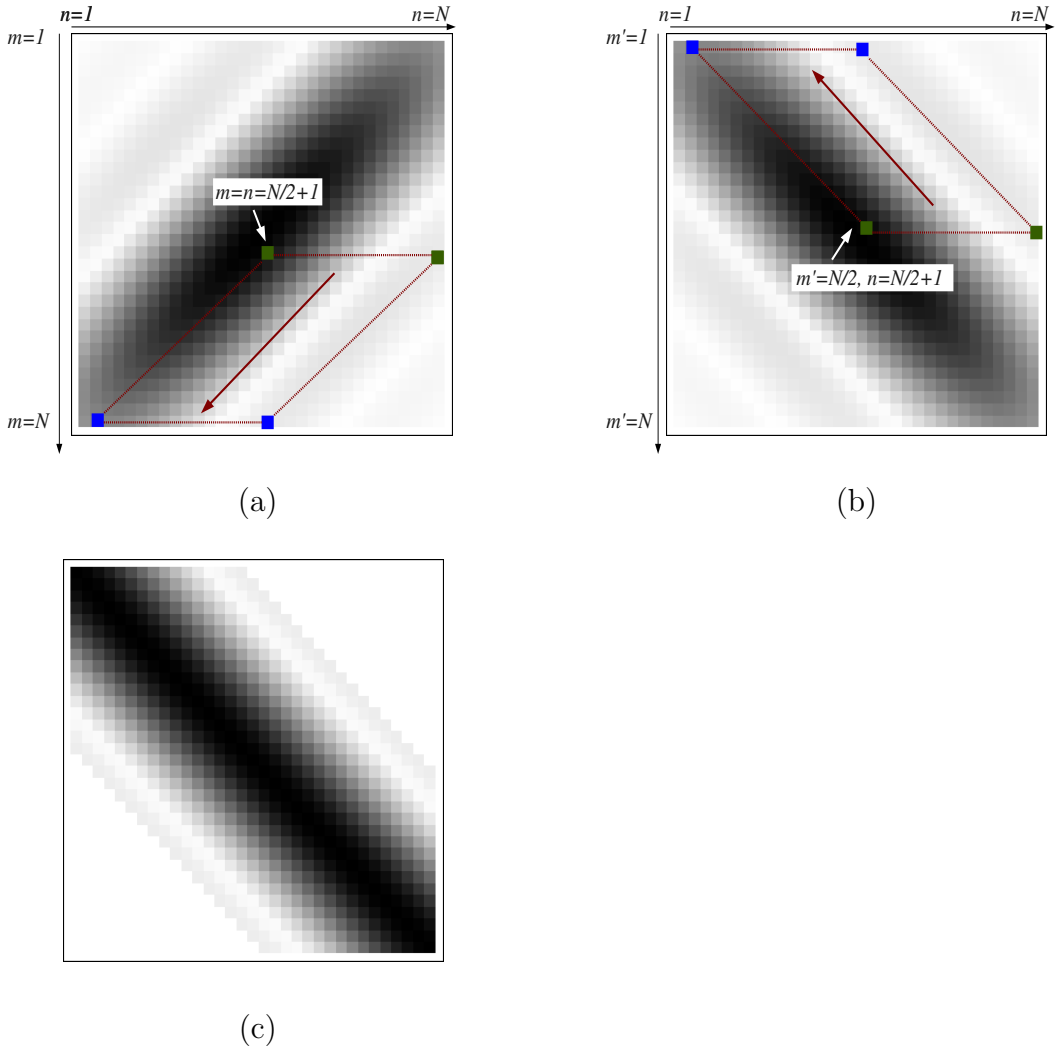

Figure 2.13: The original scattering matrix, A (equation (2.27)), is shown in (a) where the green squares highlight the section of the row which is used to construct the Toeplitz approximation. This is the row where the maximum occurs at $n = m = N/2 + 1$. The red dashed lines demonstrate the rows which are proved to be approximately equal to the portion of the row where the maximum occurs (shown by the green squares). The equivalent is highlighted in the transformed matrix, A_T (equation (2.28)), in (b), and (c) shows the Toeplitz matrix, $\bar{A}_T$ (equation (2.32)), constructed using the row where the maximum occurs.

reflection diagonal of the scattering matrix, as will be shown below. The specular response is obtained when $n = m$ (that is when $m' = N - m + 1$) within the matrix A and in equation (2.27) the term

$$\frac{J_1\left(2\pi\hat{a}(y_n + y_m)\right)}{y_n + y_m} \tag{2.30}$$

coincidentally obtains its maximum when $y_n + y_m = 0$. The prefactor to the Bessel function in equation (2.27) is given by

$$\sqrt{1 - y_m^2}(L + 2\mu(1 - y_{n'}^2)). \tag{2.31}$$

Since $0 < y_m^2, y_n^2 < 1$ this is maximised when $y_m = y_n = 0$ and, since the array is centred on the x_1-axis, this means that $y_m = y_n = 0$ corresponds to the centre of the array. If N is odd then the central element is given by $n = m = (N + 1)/2$ and if N is even then the smallest value is $y_m = y_n = -\triangle y/2$ which occurs at $n = m = N/2 + 1$. In what follows the focus will be on the case where N is even and the steps in the analysis that follows are virtually identical for the case where N is odd. Substituting $y_m = -\triangle y/2$ into equation (2.27) gives the first $N/2$ entries in the first row of the Toeplitz matrix $\bar{A}_T$ as

$$\bar{A}_T(y_p) = \frac{2\sqrt{1 - \triangle y^2/4}(L + 2\mu(1 - y_p^2))}{\rho c^2(2y_p - \triangle y)} J_1\Big(2\pi\hat{a}\left(y_p - \frac{\triangle y}{2}\right)\Big), \tag{2.32}$$

where $p = N/2 + 1, ..., N$ and the absolute value can be removed as $y_p - \triangle y/2 < 0$ and $J_1(2\pi\hat{a}(y_p - \triangle y/2)) < 0$. This row is highlighted in the scattering matrix shown in Figure 2.13. The remaining terms in the first row of $\bar{A}_T$ are set equal to zero, that is $(\bar{A}_T)_j = 0, j = N/2 + 1, ..., N$. The approximation of the scattering

matrix by a Toeplitz matrix is justified here by showing that

$$\left|\frac{A(y_{N/2+1}, y_n) - A(y_m, y_{n-m+N/2+1})}{A(y_{N/2+1}, y_n)}\right| = \mathcal{O}(\epsilon), \qquad \forall m, n = N/2+1, ..., N, \quad (2.33)$$

where $0 < \epsilon \ll 1$ is of the order of the array aperture size squared (typically $\epsilon \sim \mathcal{O}(10^{-2})$). The aim here is to show that each row of $N/2$ elements starting at the specular reflection diagonal is approximately equal to the row of $N/2$ elements where the maximum occurs, $A(y_{N/2+1}, y_n)$, and so justify the Toeplitz approximation. From equation (2.21)

$$y_{n-m+N/2+1} + y_m = \frac{\triangle y}{2}(N - 2n) \quad (2.34)$$

and

$$y_{N/2+1} + y_n = y_n - \frac{\triangle y}{2} = \frac{\triangle y}{2}(N - 2n). \quad (2.35)$$

Hence, from equation (2.27)

$$A_{N/2+1,n} = \frac{2\sqrt{1-(\triangle y)^2/4}}{\rho c^2 \triangle y(2n-N)}\left(L + 2\mu\left(1 - \frac{(\triangle y)^2}{4}(N-2n+1)^2\right)\right) J_1(\pi \hat{a} \triangle y(2n-N)), \quad (2.36)$$

and

$$A_{m,n-m+N/2+1} = \frac{2\sqrt{1-((\triangle y)^2/4)(N-2m+1)^2}}{\rho c^2 \triangle y(2n-N)} \times \left[L + 2\mu\left(1 - \frac{\triangle y^2}{4}\left(\frac{N}{2} - 2n + 2m - 1\right)^2\right)\right] J_1(\pi \hat{a} \triangle y(2n-N)) \quad (2.37)$$

which gives

$$A_{N/2+1,n} - A_{m,n-m+N/2+1} = \frac{J_1\left(\pi\hat{a}\triangle y(2n-N)\right)}{\rho c^2 \triangle y(2n-N)}\left[2\sqrt{1-\frac{(\triangle y)^2}{4}}\right.$$
$$\times\left(L+2\mu\left(1-\frac{(\triangle y)^2}{4}(N-2n+1)^2\right)\right) - 2\sqrt{1-\frac{(\triangle y)^2}{4}(N-2m+1)^2}$$
$$\left.\times\left(L+2\mu\left(1-\frac{(\triangle y)^2}{4}\left(\frac{N}{2}-2n+2m-1\right)^2\right)\right)\right]. \tag{2.38}$$

If we denote

$$\chi = L+2\mu\left(1-\frac{(\triangle y)^2}{4}(N-2n+1)^2\right) \tag{2.39}$$

then equation (2.38) becomes

$$A_{N/2+1,n} - A_{m,n-m+N/2+1} = \frac{J_1(\pi\hat{a}\triangle y(2n-N))}{\rho c^2\triangle y(2n-N)}\left(2\sqrt{1-\frac{(\triangle y)^2}{4}}\chi\right.$$
$$-2\sqrt{1-\frac{(\triangle y)^2}{4}(N-2m+1)^2}\left(\chi-\frac{\mu(\triangle y)^2}{2}\left(\left(\frac{N}{2}-2m+2\right)^2\right.\right.$$
$$\left.\left.\left.-2\left(\frac{N}{2}-2m+2\right)(N-2n+1)\right)\right)\right). \tag{2.40}$$

Now since $m \in [N/2+1, N]$ then the maximum that $|(\triangle y)/2(N-2m+1)|$ can achieve is when $m = N$ and so this is bounded by

$$\left(-\frac{\triangle y(N-1)}{2}\right)^2 = \frac{l^2}{4(4d^2+l^2)} = \epsilon, \tag{2.41}$$

where $0 < \epsilon \ll 1$ for small apertures, as demonstrated in Figure 2.14. This then allows the Taylor series expansion

$$\sqrt{1-\left(\frac{\triangle y}{2}(N-2m+1)\right)^2} = 1-\frac{\epsilon}{2}+\mathcal{O}(\epsilon^2). \tag{2.42}$$

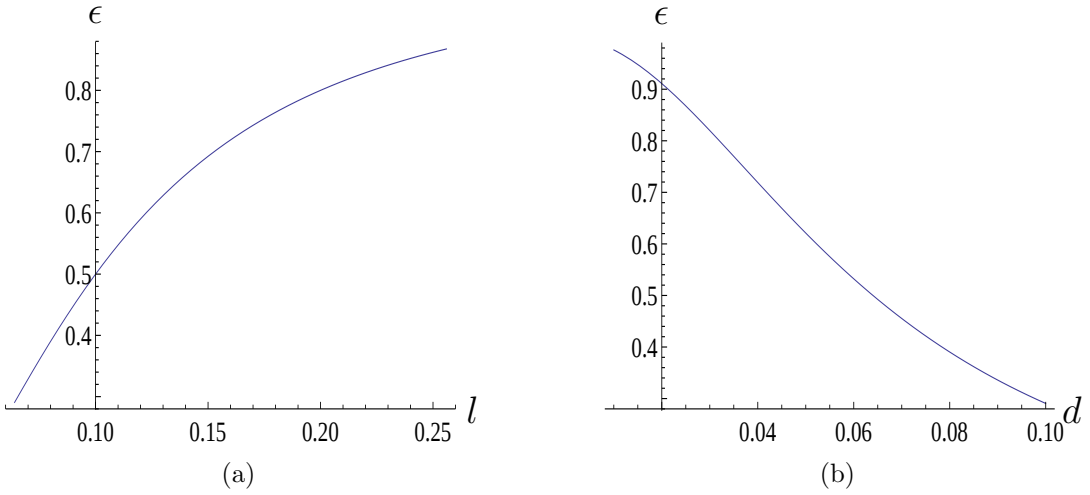

Figure 2.14: The small parameter ϵ given by equation (2.41) is used in the justification of the Toeplitz approximation, equation (2.32), to the scattering matrices. This plot shows that ϵ is small for a flaw at (a) a fixed depth, $d = 50$ mm, as the length of the array l(m) is varied and (b) a fixed array length, l =128 mm, as the depth of the flaw, d(m), is varied.

In addition, for $m = N$ and $n = N/2 + 1$ the following approximation is made within equation (2.40) to give

$$\begin{aligned}
&\frac{(\triangle y)^2}{2}\left(\left(\frac{N}{2}-2m+1\right)^2-2\left(\frac{N}{2}-2m+2\right)(N-2n+1)\right)\\
&=\frac{(\triangle y)^2}{2}\left(\left(\frac{3N}{2}-1\right)^2-2\left(\frac{3N}{2}-2\right)\right)\\
&=\frac{9}{2}\frac{(\triangle y)^2}{4}\left(N^2-\frac{8}{3}N+\frac{20}{9}\right)=\approx\frac{9}{2}\mathcal{O}(\epsilon),
\end{aligned}\tag{2.43}$$

for large N (as the N^2 term dominates) and from equation (2.41)

$$\frac{(\triangle y)^2}{4}N^2=\mathcal{O}(\epsilon).\tag{2.44}$$

Substituting the approximations given by equations (2.42) and (2.43) into equation (2.40) gives

$$\begin{aligned} A_{N/2+1,n} - A_{m,n-m+N/2+1} &= \frac{J_1(\pi\hat{a}\triangle y(2n-N))}{\rho c^2 \triangle y(2n-N)} \left(2\chi - 2\left(1-\frac{\epsilon}{2}\right)(\chi+\mu\epsilon)\right) \\ &= \frac{2J_1(2\pi\hat{a}\triangle y(N/2+1-n))}{\rho c^2 \triangle y(2n-N-2)}(\epsilon(\chi+\mu\epsilon-2\mu)) \end{aligned} \quad (2.45)$$

where $\sqrt{1-(\triangle y)^2/4} \approx 1$ since $0 < \triangle y << \epsilon$. In order to obtain the relative error, equation (2.45) is divided by

$$A_{N/2+1,n} = \frac{2J_1(\pi\hat{a}\triangle y(2n-N))}{\rho c^2 \triangle y(2n-N)}\chi \quad (2.46)$$

to give

$$\left|\frac{A_{N/2+1,n} - A_{m,n+m-N/2+1}}{A_{N/2+1,n}}\right| = \epsilon - \frac{2\mu}{\chi}\epsilon + \frac{\mu}{\chi}\epsilon^2 = \mathcal{O}(\epsilon) \quad (2.47)$$

since $\chi = \mathcal{O}(\mu)$ from equation (2.39) and therefore, $\mu/\chi \approx 1$. Hence, the approximation of the limited aperture scattering matrix by a Toeplitz matrix is vindicated here.

2.5.2 An approximation for the maximum eigenvalue of the Toeplitz form of the scattering matrix

In the forthcoming section an approximation which relates the length of a crack in terms of the wavelength, $\hat{a}$, to the maximum eigenvalue σ_{max} of the Toeplitz approximation to the scattering matrix will be derived. This maximum eigenvalue

is approximated using an upper bound, σ_B, which is given by [64]

$$\sigma_B = (\bar{A}_T)_1 \cdot \mathbf{w} \tag{2.48}$$

where $(\bar{A}_T)_1 = ((\bar{A}_T)_{1,1}, |(\bar{A}_T)_{1,2}|, ..., |(\bar{A}_T)_{1,N}|)$, $\mathbf{w} = (1, w_2, ...w_N)$ and

$$w_k(N) = 2\cos\left(\frac{\pi}{\left\lfloor\frac{N-1}{k-1}\right\rfloor + 2}\right). \tag{2.49}$$

where $\lfloor . \rfloor$ denotes the *floor* function. The first row of the Toeplitz matrix, $\bar{A}_T(y_p)$, is given by equation (2.32) and when substituted into equation (2.48) gives

$$\begin{aligned}\sigma_B &= \bar{A}_T(y_{N/2+1}) + \sum_{t=N/2+2}^{N} |A_T(y_t)| w_t \\ &= \bar{A}_T(y_{N/2+1}) + \sum_{t=N/2+2}^{N} F_t(\hat{a}) \frac{J_1\left(2\pi\hat{a}\left(y_t - \triangle y/2\right)\right)}{2\pi\hat{a}\left(y_t - \triangle y/2\right)} w_t,\end{aligned} \tag{2.50}$$

where

$$w_t(N) = 2\cos\left(\frac{\pi}{\left\lfloor\frac{2(N-1)}{2t-2-N}\right\rfloor + 2}\right), \tag{2.51}$$

with $k = t - N/2$ and the prefactor is given by

$$F_t(\hat{a}) = \frac{2\pi\hat{a}\sqrt{1-(\triangle y)^2/4}}{\rho c^2}(L + 2\mu(1-y_t^2)). \tag{2.52}$$

The approximation, σ_B (green line), given by equation (2.50) is compared to the numerically calculated eigenvalue, σ_{max} (blue line), in Figure 2.15 as $\hat{a}$ is varied and where the array length and the flaw depth are fixed at $l = 128$ mm and $d = 50$ mm. It can be seen that not only is the Toeplitz approximation valid but so also is the use of the upper bound as an approximation to the largest eigenvalue. In order

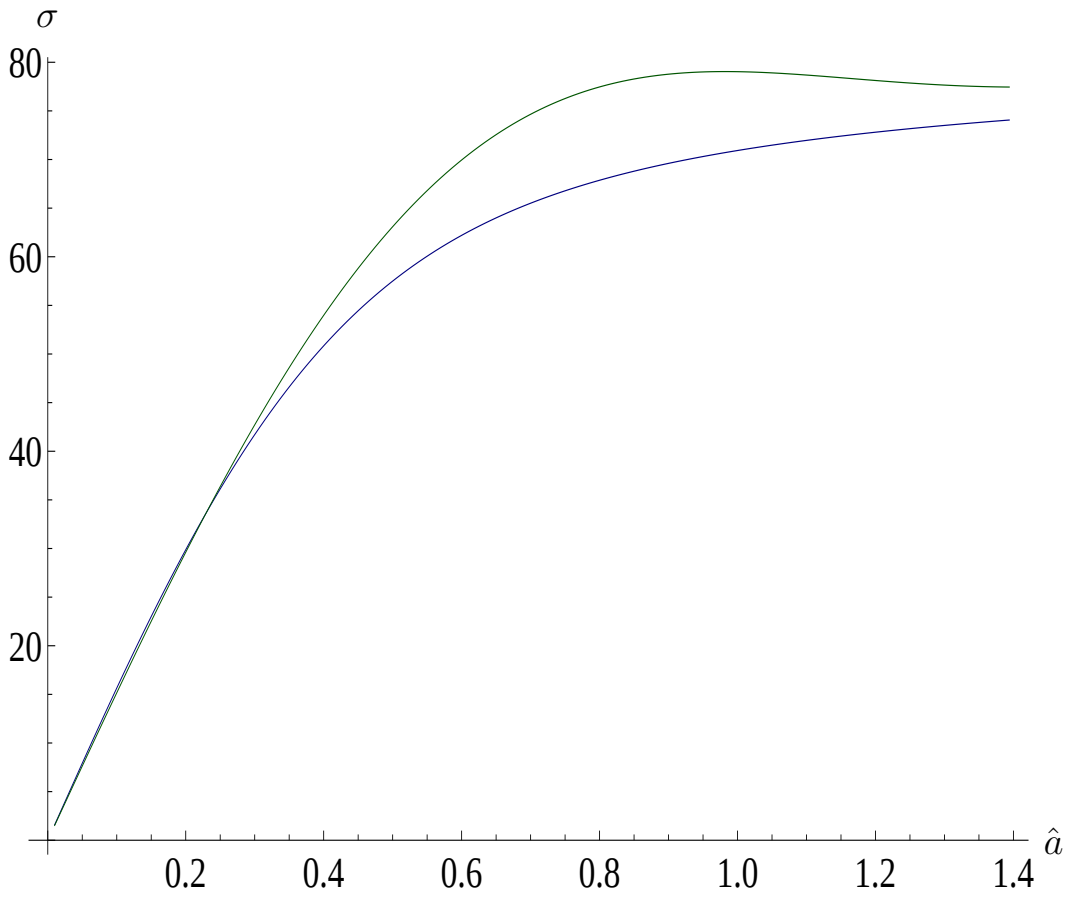

Figure 2.15: The maximum eigenvalue, σ_{max}, as a function of $\hat{a}$ from the scattering matrices, given by equation (2.27) (blue line) and the upper bound approximation to the maximum eigenvalue, σ_B given by equation (2.50) (green line) from the Toeplitz approximation to the scattering matrices. The array length and the flaw depth are fixed at $l = 128$ mm and $d = 50$ mm.

to view the explicit dependency of σ_B on $\hat{a}$ it is necessary to make approximations to the expression within the summation in equation (2.50). The Bessel function within equation (2.50) is approximated by

$$\frac{J_1\left(2\pi\hat{a}\left(y_t - \triangle y/2\right)\right)}{2\pi\hat{a}\left(y_t - \triangle y/2\right)} = \begin{cases} f_t^{(1)}(\hat{a}) & \text{if } N/2+2 \leq t \leq t^* \\ f_t^{(2)}(\hat{a}) & \text{if } t^*+1 \leq t \leq N \end{cases}$$

where the approximation for small arguments [65] is used to obtain

$$f_t^{(1)}(t,\hat{a}) = \overbrace{\frac{1}{2}\left(1-\frac{1}{4}\left(\pi\hat{a}\left(y_t-\frac{\triangle y}{2}\right)\right)^2\right)}^{\bar{f}_t^{(1)}} + \mathcal{O}\left(\frac{1}{384}\left(\pi\hat{a}\left(y_t-\frac{\triangle y}{2}\right)\right)^4\right) \tag{2.53}$$

and for large arguments [65]

$$\begin{aligned} f_t^{(2)}(t,\hat{a}) = & \overbrace{\frac{1}{2\pi^2}\left(\hat{a}\left(y_t-\frac{\triangle y}{2}\right)\right)^{-\frac{3}{2}}\cos\left(2\pi\hat{a}\left(y_t-\frac{\triangle y}{2}\right)-\frac{3\pi}{4}\right)}^{\bar{f}_t^{(2)}} \\ & + \mathcal{O}\left(\frac{3}{24\pi^3}\sin\left(\hat{a}\left(y_t-\frac{\triangle y}{2}\right)-\frac{3\pi}{4}\right)\left(\hat{a}\left(y_t-\frac{\triangle y}{2}\right)\right)^{-\frac{5}{2}}\right). \end{aligned} \tag{2.54}$$

The index t^* determines when the argument of the Bessel function converts from small values to large values. An expression for t^* is determined in section 2.5.2.1 and is given in terms of the system parameters and $\hat{a}$. This approximation to the Bessel function is shown in Figure 2.16, where it can be seen that the approximation is valid. Equation (2.53) is used to approximate

$$\bar{A}_T(y_{N/2+1}) = \bar{A}_T\left(-\frac{\triangle y}{2}\right) = F_{N/2+1}(\hat{a}) = \frac{2\hat{a}\pi\sqrt{1-(\triangle y)^2/4}\,(L+2\mu\,(1-(\triangle y)^2/4))}{\rho c^2} \tag{2.55}$$

in equation (2.50). The approximation to equation (2.50) is split into two summations and is therefore given by

$$\begin{aligned} \sigma_B = & F_{N/2+1}(\hat{a}) + \sum_{t=N/2+1}^{t^*} F_t(\hat{a})\bar{f}_t^{(1)}(\hat{a})w_t(N) + \sum_{t=t^*+1}^{N} F_t(\hat{a})\bar{f}_t^{(2)}(\hat{a})w_t(N) \\ & + \mathcal{O}\left(\max\{e_1,e_2\}\right) \end{aligned} \tag{2.56}$$

where

$$e_1 = \frac{\pi^4 \hat{a}^4}{384} \sum_{t=N/2+1}^{t^*} \left(y_t - \frac{\triangle y}{2} \right)^4 w_t(N) F_t(\hat{a}) \tag{2.57}$$

and

$$e_2 = \frac{3}{24\pi^3} \sum_{t=t^*+1}^{N} \left(\hat{a} \left(y_t - \frac{\triangle y}{2} \right) \right)^{-\frac{5}{2}} \sin\Big(2\pi \hat{a} \left(y_t - \frac{\triangle y}{2} \right) - \frac{3\pi}{4} \Big) F_t(\hat{a}) w_t(N). \tag{2.58}$$

As these error functions are monotonically increasing in t then, by taking $t = t^*$ for all t, the following upper bound to the error can be derived

$$e_1 = \frac{\hat{a}^4}{24} \left(y_{t^*} - \frac{\triangle y}{2} \right)^4 w_{t^*}(N) F_{t^*}(\hat{a})(t^* - N/2) \tag{2.59}$$

and similarly setting $t = N$ for all t gives the upper bound

$$e_2 = \frac{3}{24\pi^3} \left(\hat{a} \left(y_N - \frac{\triangle y}{2} \right) \right)^{-\frac{5}{2}} \sin\Big(2\pi \hat{a} \left(y_N - \frac{\triangle y}{2} \right) - \frac{3\pi}{4} \Big) F_N(\hat{a}) w_N(N)(N - t^*). \tag{2.60}$$

Further approximations are applied to equation (2.54) to allow σ_B to be expressed in terms of a polynomial in t. This will be useful later where the aim is to extract the parameter $\hat{a}$ in order to obtain an explicit expression which relates σ_B to $\hat{a}$. Let

$$\bar{f}_t^{(2)}(\hat{a}) = s_t^{(1)}(\hat{a}) s_t^{(2)}(\hat{a}), \tag{2.61}$$

where

$$s_t^{(1)}(t, \hat{a}) = \frac{1}{2\pi^2} \Big(\frac{1}{\hat{a}\,(y_t - \triangle y/2)} \Big)^{\frac{3}{2}} = \frac{1}{\pi^2} \Big(2 \frac{1}{\hat{a} \triangle y (N - 2t)} \Big)^{\frac{3}{2}}, \tag{2.62}$$

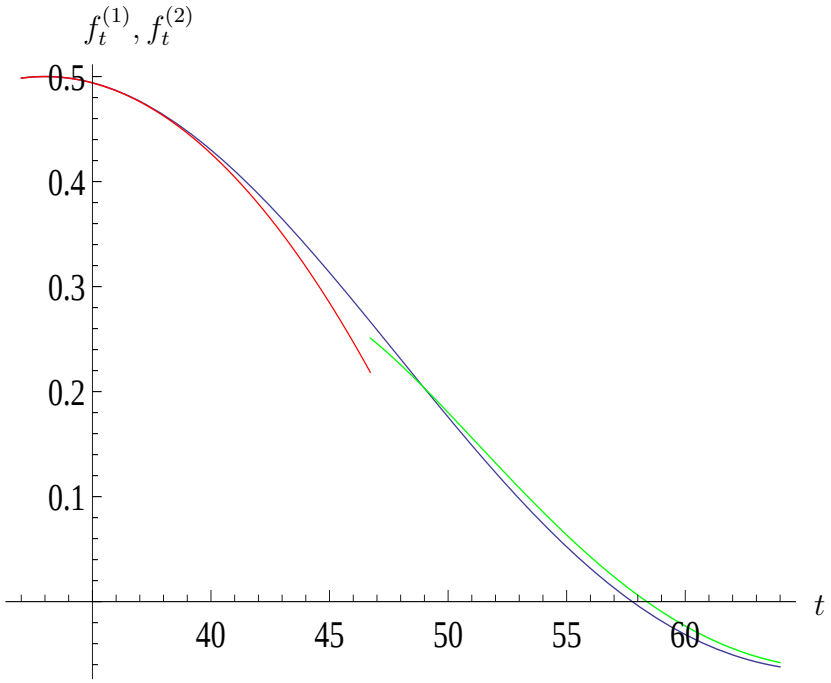

Figure 2.16: The approximation to the Bessel function $J_1\left(2\pi\hat{a}\left(y_t - \frac{\triangle y}{2}\right)\right)/(2\pi\hat{a}\left(y_t - \frac{\triangle y}{2}\right))$ (blue line) for small arguments, $\bar{f}_t^{(1)}$, (red line) given in equation (2.53) and for large arguments, $\bar{f}_t^{(2)}$, (green line) given in equation (2.54), for typical system parameter values: d=50 mm, N=64, l=128 mm and $\hat{a} = 1$.

and

$$s_t^{(2)}(\hat{a}) = \cos\left(2\pi\hat{a}\left(y_t - \frac{\triangle y}{2}\right) - \frac{3\pi}{4}\right) = \cos\left(\pi\hat{a}\triangle y(N-2t) - \frac{3\pi}{4}\right). \tag{2.63}$$

The Taylor series approximation of s_1 around the point $t = m = (t^* + N)/2$ (the midpoint between t^* and N) is given by

$$\begin{aligned} s_t^{(1)}(\hat{a}, m) = & \overbrace{\frac{1}{2\pi^2}\left(\frac{1}{\hat{a}\triangle y(N-2m)}\right)^{3/2}\left(1 + \frac{3}{N-2m}(t-m)\right)}^{\bar{s}_t^{(1)}} \\ & + \mathcal{O}\left(15\hat{a}^2(\triangle y)^2\left(\frac{1}{\hat{a}\triangle y(N-2m)}\right)^{7/2}(t-m)^2\right) \end{aligned} \tag{2.64}$$

and similarly

$$
\begin{aligned}
s_t^{(2)}(\hat{a},m) &= \cos\Big(\pi\hat{a}\triangle y(N-2t)-\frac{3\pi}{4}\Big)\left(1-2\Big(\hat{a}\pi\triangle y(t-m)\Big)^2\right)\\
&\quad+\sin\Big(\pi\hat{a}\triangle y(N-2t)-\frac{3\pi}{4}\Big)\left(-2\hat{a}\pi\triangle y(t-m)+\frac{4}{3}\Big(\hat{a}\pi\triangle y(t-m)\Big)^3\right)\\
&\quad+\mathcal{O}\left(\frac{2}{3}\left(\pi\hat{a}\triangle y\right)^4(t-m)^4\cos\Big(\pi\hat{a}\triangle y(N-2t)-\frac{3\pi}{4}\Big)\right)\\
&= \bar{s}_t^{(2)}+\mathcal{O}\left(\frac{2}{3}\left(\pi\hat{a}\triangle y\right)^4(t-m)^4\cos\Big(\pi\hat{a}\triangle y(N-2t)-\frac{3\pi}{4}\Big)\right). \qquad (2.65)
\end{aligned}
$$

This gives the approximation

$$
\bar{f}_t^{(2)}(\hat{a},m)=\bar{s}_t^{(1)}\bar{s}_t^{(2)}+\mathcal{O}(\max\{e_3,e_4\}), \qquad (2.66)
$$

where

$$
e_3=\mathcal{O}\left(\bar{s}_t^{(2)}(\hat{a},m)F_t(\hat{a})w_t(N)15\hat{a}^2(\triangle y)^2\left(\frac{1}{\hat{a}\triangle y(N-2m)}\right)^{7/2}(t-m)^2\right) \qquad (2.67)
$$

and

$$
e_4=\mathcal{O}\left(\bar{s}_t^{(1)}(\hat{a},m)F_t(\hat{a})w_t(N)\frac{2}{3}\left(\pi\hat{a}\triangle y\right)^4(t-m)^4\cos\Big(\pi\hat{a}\triangle y(N-2t)-\frac{3\pi}{4}\Big)\right). \qquad (2.68)
$$

Figure 2.17 compares the Taylor series approximation given by equation (2.66) (orange line) to $f_t^{(2)}$ in equation (2.54) (green line) for typical parameter values. Substituting equations (2.64) and (2.65) into equation (2.56) gives

$$
\begin{aligned}
\sigma_B &= F_{N/2+1}(\hat{a})+\sum_{t=p+1}^{t^*}\Big[F_t(\hat{a})\bar{f}_t^{(1)}w_t(N)\Big]\\
&\quad+\sum_{t=t^*}^{N}\Big[F_t(\hat{a})\bar{s}_t^{(1)}(t,\hat{a},m)\bar{s}_t^{(2)}(t,\hat{a},m)w_t(N)\Big]+\mathcal{O}\left(\max\{e_1,e_2,e_3,e_4\}\right). \qquad (2.69)
\end{aligned}
$$

Finally, w_t given by equation (2.51) is approximated by a linear function. First,

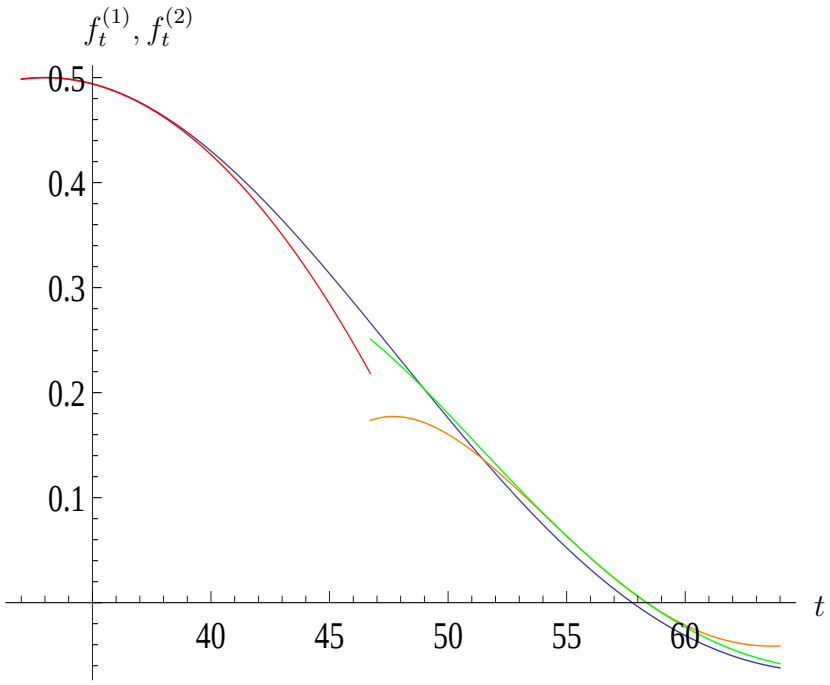

Figure 2.17: The approximation to the Bessel function $J_1\left(2\pi\hat{a}\left(y_t - \frac{\triangle y}{2}\right)\right)/(2\pi\hat{a}\left(y_t - \frac{\triangle y}{2}\right))$ (blue line) for small arguments, $f_t^{(1)}$, (red line) given in equation (2.53), for large arguments, $f_t^{(2)}$, (green line) given in equation (2.54), and the Taylor series approximation to $f_t^{(2)}$, (orange line) given in equation (2.66) for typical system parameter values: d=50mm, N=64, l=128mm and $\hat{a} = 1$.

the *floor* function within the cosine in equation (2.49) is dropped to give

$$w_t = 2\cos\left(\frac{\pi}{\frac{2(N-1)}{2t-N-2} + 2}\right) = 2\cos\left(\frac{\pi(2t-2-N)}{2(2t-3)}\right). \tag{2.70}$$

To justify the removal of the floor function it necessary to show that

$$\cos(\alpha_1) - \cos(\alpha_2) = \epsilon, \tag{2.71}$$

for $0 < \epsilon \ll 1$, where

$$\alpha_1 = \frac{\pi}{2(N-1)/(2t-2-N)+2} \qquad \text{and} \qquad \alpha_2 = \frac{\pi}{2(N-1)/(2t-2-N)+3}, \tag{2.72}$$

since the maximum error that occurs with the floor function is 1. The range of t is $t = N/2+2, ..., N$ which gives

$$\frac{2(N-1)}{2t-2-N} = N-1, \frac{N-1}{2}, ..., \frac{2(N-1)}{N-2} \approx N-1, \frac{N-1}{2}, ..., 2 \tag{2.73}$$

for large N and so, the ranges of α_1 and α_2 are

$$\alpha_1 = \frac{\pi}{N+1}, ..., \frac{\pi}{4} \tag{2.74}$$

and

$$\alpha_2 = \frac{\pi}{N+2}, ..., \frac{\pi}{5}, \tag{2.75}$$

and therefore, $0 < \alpha_1, \alpha_2 < \pi/2$. The derivative of $\cos(\alpha_i)$ is maximised at $\pi/2$ and minimised at 0 and therefore the maximum difference between $\cos(\alpha_1)$ and $\cos(\alpha_2)$ occurs when $t = N$ and is such that

$$\epsilon = \cos\left(\frac{\pi}{4}\right) - \cos\left(\frac{\pi}{5}\right) = \mathcal{O}(10^{-1}). \tag{2.76}$$

The function w_t in equation (2.70) is approximated by a Taylor series about $3N/4$

(the midpoint in the range $t = N/2 + 1$ to $t = N$) to give

$$w_t(N) = \overbrace{2\cos\left(\frac{\pi(N-4)}{6(N-2)}\right) - \frac{8\pi(N-1)\,(t-3N/4)}{9(N-2)^2}\sin\left(\frac{\pi(N-4)}{6(N-2)}\right)}^{\bar{w}_t(N)} + \mathcal{O}\Bigg(2\left(t-\frac{3N}{4}\right)^2\left(\frac{8\pi(N-1)}{27(N-2)^3}\right)\left(2\sin\left(\frac{\pi(N-4)}{6(N-2)}\right) - \frac{\pi^2(N-1)}{3(N-2)}\cos\left(\frac{\pi(N-4)}{6(N-2)}\right)\right)\Bigg). \tag{2.77}$$

This is substituted into equation (2.78) to give

$$\sigma_B = F_{N/2+1}(\hat{a}) + \sum_{t=N/2+2}^{t^*} F_t(\hat{a})\bar{f}_t^{(1)}\bar{w}_t(N) + \sum_{t=t^*}^{N} F_t(\hat{a})\bar{s}_t^{(1)}(\hat{a},m)\bar{s}_t^{(2)}(\hat{a},m)\bar{w}_t(N) + \mathcal{O}\left(\max\{e_1,e_2,e_3,e_4,e_5,e_6\}\right) \tag{2.78}$$

where

$$e_5 = \mathcal{O}\Bigg(2\left(t-\frac{3N}{4}\right)^2\left(\frac{8\pi(N-1)}{27(N-2)^3}\right)\left(2\sin\left(\frac{\pi(N-4)}{6(N-2)}\right) - \frac{\pi^2(N-1)}{3(N-2)}\cos\left(\frac{\pi(N-4)}{6(N-2)}\right)\right)\bar{s}_t^{(1)}(\hat{a},m)F_t(\hat{a})\bar{s}_t^{(2)}(\hat{a},m)(N-t)\Bigg) \tag{2.79}$$

and

$$e_6 = \mathcal{O}\Bigg(2\left(t-\frac{3N}{4}\right)^2\left(\frac{8\pi(N-1)}{27(N-2)^3}\right)\left(2\sin\left(\frac{\pi(N-4)}{6(N-2)}\right) - \frac{\pi^2(N-1)}{3(N-2)}\cos\left(\frac{\pi(N-4)}{6(N-2)}\right)\right)\bar{f}_t^{(1)}(\hat{a})F_t(\hat{a})(t-N/2)\Bigg). \tag{2.80}$$

The expressions within each summation in equation (2.78) are polynomials in t

which allows σ_B to be expressed in the following form

$$\sigma_B(\hat{a}) = \hat{A}\hat{a} + \sum_{l=1}^{6} S_l^{(1)}(\hat{a}) b_l(\hat{a}) + \sum_{l=1}^{8} S_l^{(2)}(\hat{a}) d_l(\hat{a}), \tag{2.81}$$

where

$$\hat{A} = \frac{\pi\sqrt{1-(\triangle y)^2/4})(L + 2\mu\,(1-(\triangle y)^2/4))}{\rho c^2}, \tag{2.82}$$

$$S_l^{(1)}(\hat{a}) = \sum_{t=N/2+2}^{t^*} t^{l-1}, \qquad S_l^{(2)}(\hat{a}) = \sum_{t=t^*+1}^{N} t^{l-1}. \tag{2.83}$$

The coefficients of the terms in the polynomial, t^{l-1}, given by b_l and d_l are functions of the crack radius over the wavelength, $\hat{a}$, and are defined later to show the dependency on $\hat{a}$ explicitly. The limits on the summation given in equation (2.83) involve t^* and it will be shown later that t^* is a function of $\hat{a}$. Therefore, to derive an equation where the dependency on $\hat{a}$ is explicit it is necessary to rewrite these summations so that t^* does not appear as a limit. A closed form expression for the sum to n terms of t^p is given by

$$\sum_{t=0}^{n} t^p = \frac{(n+1)^{p+1}}{p+1} + \sum_{k=1}^{p} \frac{B_k}{p-k+1} \binom{p}{k} (n+1)^{p-k+1} \tag{2.84}$$

where B_k is the k^{th} Bernoulli number. In equation (2.84) it can be seen that the limit, n, on the summation on the left hand side is no longer a limit on the summation on the right hand side. This means that n can be a real number, providing a smooth differentiable function. This is important here because t^* is a function of $\hat{a}$ and the system parameters (l, d, N). In order to analyse this expression in the forthcoming sections it is necessary to have an explicit function in terms of $\hat{a}, l, d$ and N, as the final form of σ_B, will be differentiated to assess the sensitivity of the method presented. Therefore, the function $S_l^{(1)}(\hat{a})$ is expressed

in the form

$$S_l^{(1)}(\hat{a}) = \frac{(t^*+1)^l}{l} + \sum_{k=1}^{l} \frac{B_k}{l-k}\binom{l-1}{k}(t^*+1)^{l-k} - \frac{(N/2+2)^l}{l} - \sum_{k=1}^{l} \frac{B_k}{l-k}\binom{l-1}{k}\left(\frac{N}{2}+2\right)^{l-k} \tag{2.85}$$

and

$$S_l^{(2)}(\hat{a}) = \frac{(N+1)^l}{l} + \sum_{k=1}^{l} \frac{B_k}{l-k}\binom{l-1}{k}(N+1)^{l-k} - \frac{(t^*+1)^l}{l} - \sum_{k=1}^{l} \frac{B_k}{l-k}\binom{l-1}{k}(t^*+1)^{l-k} \tag{2.86}$$

using equation (2.84). The coefficients b_l are expressed in terms of a polynomial function in $\hat{a}$, as follows:

$$b_l(\hat{a}) = b_l^{(1)}\hat{a} + b_l^{(2)}\hat{a}^3, \tag{2.87}$$

where $b_l^{(1)}$ and $b_l^{(2)}$ are functions of the number of elements in the array, N, $\triangle y$, Lamé coefficients L and μ, wave speed c and material density ρ and are given in Appendix A. The dependency on $\hat{a}$ is extracted from the first summation in equation (2.81) to give

$$\sum_{l=1}^{6} S_l^{(1)}(\hat{a})b_l(\hat{a}) = \sum_{l=1}^{6} S_l^{(1)}(\hat{a})(b_l^{(1)}\hat{a} + b_l^{(2)}\hat{a}^3)\hat{a}\hat{S}_1(\hat{a}) + \hat{a}^3\hat{S}_2(\hat{a}), \tag{2.88}$$

where

$$\hat{S}_1(\hat{a}) = \sum_{l=1}^{6} S_l^{(1)}(\hat{a})b_l^{(1)} \qquad \text{and} \qquad \hat{S}_2(\hat{a}) = \sum_{l=1}^{6} S_l^{(1)}(\hat{a})b_l^{(2)}. \tag{2.89}$$

The coefficients d_l are extracted from equation (2.78) and are of the form

$$\begin{aligned} d_l(\hat{a}) \quad &= B(\hat{a})\Big(((d_l^{(0)} + d_l^{(1)}\hat{a} + d_l^{(2)}\hat{a}^2 + d_l^{(3)}\hat{a}^3 + d_l^{(4)}\hat{a}^4)\cos(p(\hat{a})) \\ &\quad + (d_l^{(5)} + d_l^{(6)}\hat{a} + d_l^{(7)}\hat{a}^2 + d_l^{(8)}\hat{a}^3 + d_l^{(9)}\hat{a}^4)\sin(p(\hat{a}))\Big), \end{aligned} \tag{2.90}$$

where

$$B(\hat{a}) = \left(\frac{1}{\pi\hat{a}\triangle y(2N - 2t^* - 3)}\right)^{5/2}, \tag{2.91}$$

and

$$p(\hat{a}) = \frac{\pi}{4} + \hat{a}\pi\triangle y t^*. \tag{2.92}$$

The second summation in the expression for σ_B, equation (2.81), can now be expressed in the form

$$\begin{aligned} \sum_{l=1}^{8} S_l^{(2)}(\hat{a}) d_l(\hat{a}) &= B\sum_{l=1}^{8} S_l^{(2)}(\hat{a})\Big((d_l^{(0)} + \hat{a}d_l^{(1)} + \hat{a}^2 d_l^{(2)} + \hat{a}^3 d_l^{(3)} + \hat{a}^4 d_l^{(4)})\cos(p(\hat{a})) \\ &\quad + (d_l^{(5)} + \hat{a}d_l^{(6)} + \hat{a}^2 d_l^{(7)} + \hat{a}^3 d_l^{(8)} + \hat{a}^4 d_l^{(9)})\sin(p(\hat{a}))\Big) \\ &= \hat{S}_3(\hat{a})\cos(p(\hat{a})) + \hat{S}_4(\hat{a})\sin(p(\hat{a})) \end{aligned} \tag{2.93}$$

with

$$\hat{S}_3(\hat{a}) = B(\hat{a})(D_0 + D_1\hat{a} + D_2\hat{a}^2 + D_3\hat{a}^3 + D_4\hat{a}^4) = B(\hat{a})\sum_{k=0}^{4} D_k(\hat{a})\hat{a}^k \tag{2.94}$$

and

$$\hat{S}_4(\hat{a}) = B(\hat{a})(D_5 + D_6\hat{a} + D_7\hat{a}^2 + D_8\hat{a}^3 + D_9\hat{a}^4) = B(\hat{a})\sum_{k=5}^{9} D_k(\hat{a})\hat{a}^{k-5}, \tag{2.95}$$

where

$$D_j(\hat{a}) = \sum_{l=1}^{8} S_l^{(2)}(\hat{a}) d_l^{(j)}. \tag{2.96}$$

The terms $d_l^{(i)}$ where $i = 1, ..., 10$ and $l = 1, ..., 6$ are independent of $\hat{a}$ and again are functions of the system parameters and are given in Appendix A. The expression in equation (2.93) is finally written in the form

$$\sum_{l=1}^{8} S_l^{(2)}(\hat{a}) d_l(\hat{a}) = Q(\hat{a}) \cos(p(\hat{a}) - \phi(\hat{a})) \tag{2.97}$$

where

$$\phi(\hat{a}) = \tan^{-1}\left(\frac{\hat{S}_4(\hat{a})}{\hat{S}_3(\hat{a})}\right) = \tan^{-1}\left(\frac{D_6 + D_7\hat{a} + D_8\hat{a}^2 + D_9\hat{a}^3 + D_{10}\hat{a}^4}{D_1 + D_2\hat{a} + D_3\hat{a}^2 + D_4\hat{a}^3 + D_5\hat{a}^4}\right) \tag{2.98}$$

and

$$\begin{aligned}
Q(\hat{a}) &= \sqrt{\hat{S}_3(\hat{a})^2 + \hat{S}_4(\hat{a})^2} \\
&= B(\hat{a}) \left(\left(\sum_{k=0}^{4} D_k(\hat{a}) \hat{a}^k \right)^2 + \left(\sum_{k=5}^{9} D_k(\hat{a}) \hat{a}^{k-5} \right)^2 \right)^{1/2} \\
&= B(\hat{a})(D_1^2 + D_6^2 + (2D_1D_2 + 2D_6D_7)\hat{a} + (D_2^2 + 2D_1D_3 + D_7^2 + 2D_6D_8)\hat{a}^2 \\
&+ (2D_3D_2 + 2D_1D_4 + 2D_7D_8 + 2D_6D_9)\hat{a}^3 + (D_3^2 + 2D_2D_4 + 2D_1D_5 \\
&+ 2D_{10}D_6 + D_8^2 + 2D_7D_9)\hat{a}^4 + (2D_3D_4 + 2D_2D_5 + 2D_{10}D_7 + 2D_8D_9)\hat{a}^5 \\
&+ (D_4^2 + 2D_3D_5 + 2D_{10}D_8 + D_9^2)\hat{a}^6 + (2D_4D_5 + 2D_{10}D_9)\hat{a}^7 + (D_{10}^2 + D_5^2)\hat{a}^8)^{1/2}.
\end{aligned} \tag{2.99}$$

Finally, the approximation to the maximum eigenvalue, σ_B, from the scattering

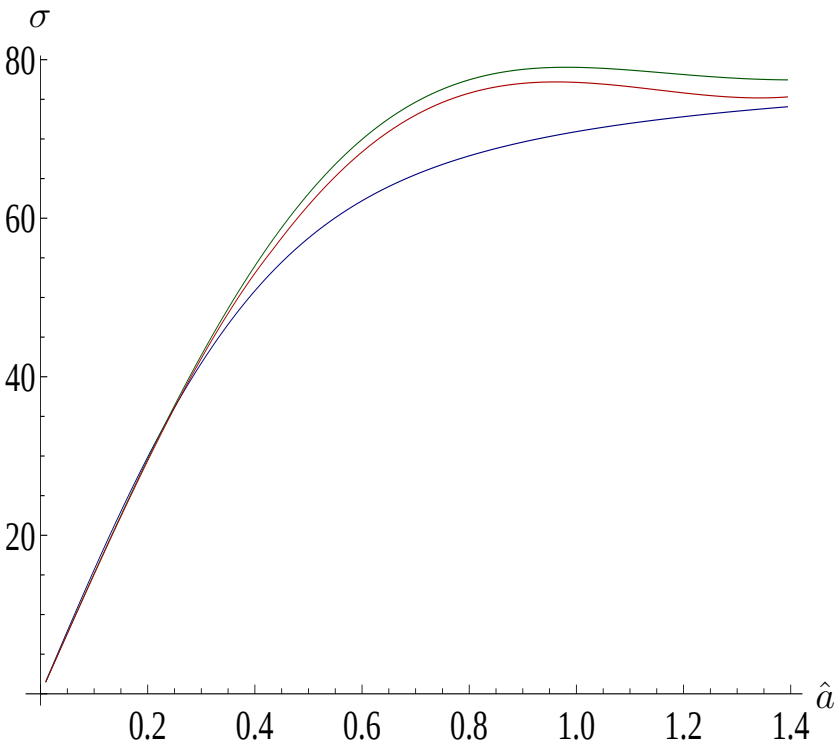

Figure 2.18: The maximum eigenvalue as a function of $\hat{a}$ from the scattering matrices given by equation (2.27) (Blue line), the upper bound to the maximum eigenvalue from the Toeplitz approximation to a scattering matrix given by equation (2.50) (Green line) and the final approximation, equation (2.100) (Red line).

matrix, A, defined by equation (2.27) is

$$\begin{aligned}\sigma_B(\hat{a}) &= (\hat{A} + \hat{S}_1(\hat{a}))\hat{a} + \hat{S}_2(\hat{a})\hat{a}^3 + Q(\hat{a})\cos(p(\hat{a}) - \phi(\hat{a})) \\ &\quad + \mathcal{O}\left(\max\{e_1, e_2, e_3, e_4, e_5, e_6\}\right) \end{aligned} \tag{2.100}$$

after equations (2.88) and (2.97) are substituted into equation (2.81). If $t^* > N$ then $\sigma_B(\hat{a})$ is reduced to to give

$$\sigma_B(\hat{a}) = (\hat{A}_1 + \hat{S}_1(\hat{a}))\hat{a} + \hat{S}_2(\hat{a})\hat{a}^3 + \mathcal{O}\left(\max\{e_1, e_6\}\right) \tag{2.101}$$

using only equation (2.88). The final approximation for σ_B given by equation

(2.100) is shown in Figure 2.18 (red line). This shows a good comparison between the approximation given by σ_B to the true eigenvalue from the Kirchhoff model.

2.5.2.1 Determining the transition parameter t^*

In section 2.5.2, the Bessel function in equation (2.50) is approximated by two expansions, one for small arguments and one for large arguments, as given by equations (2.53) and (2.54). The parameter t^* is the index which determines when the argument transitions from small to large. If we denote the argument in the Bessel function by T then at $t = t^*$

$$T = 2\pi\hat{a}\left(\frac{\triangle y}{2}\left(N - 2t^*\right)\right) \tag{2.102}$$

from equation (2.21). Rearranging gives

$$t^*(\hat{a}) = \frac{N}{2} - \frac{T}{2\pi\hat{a}\triangle y}. \tag{2.103}$$

The value of T needs to be determined in order to have an explicit expression for t^* in terms of $\hat{a}$ and the system parameters. The higher order terms from the approximations in equations (2.53) and (2.54) are used to find a suitable numerical value for T. These are given by

$$E_1(t,\hat{a}) = \left|\frac{1}{384}\left(\pi\hat{a}\left(y_t - \frac{\triangle y}{2}\right)\right)^4\right| \tag{2.104}$$

and

$$E_2(t,\hat{a}) = \left|\frac{3}{24\pi^2}\sin\left(2\pi\hat{a}\left(y_t - \frac{\triangle y}{2}\right) - \frac{3\pi}{4}\right)\left(2\pi\hat{a}\left(y_t - \frac{\triangle y}{2}\right)\right)^{-\frac{5}{2}}\right|. \tag{2.105}$$

A function $\hat{t^*}$ is introduced and is taken to be the array element index, n, closest

Ultrasonic Transducer Array Parameters	Value	Units
Number of elements	64	-
Pitch	2	mm
Depth of flaw	50	mm
Array Length	128	mm

Table 2.2: Typical system parameters.

to the point of intersection of the functions $E_1(t, \hat{a})$ and $E_2(t, \hat{a})$, that is

$$\hat{t^*}(\hat{a}) = \max_{E_1(t,\hat{a})>E_2(t,\hat{a})} t \qquad \text{if } t \in [N/2+2, N]. \tag{2.106}$$

The error functions given in equations (2.104) and (2.105) are plotted in Figure 2.19 for typical parameter values and $\hat{t^*}$ is shown to be the point of intersection at $\hat{t}^* = 46$. The value T in equation (2.102) is chosen to minimise the difference between $\hat{t}^*$ in equation (2.106) and t^* in equation (2.103) and is given by $T = 2.1$. Figure 2.20 shows an excellent agreement between the plot of $t^*(\hat{a})$ (red line) where $T = 2.1$ and $\hat{t^*}(\hat{a})$ (black line). This plot also shows that $\hat{t^*}(\hat{a}) = N$ for $\hat{a} < 0.45$ for these particular parameter values, and this means that for $\hat{a} < 0.45$ only the small argument approximation to the Bessel function is used.

2.6 Conclusions

In this chapter, equation (2.100) which relates the maximum eigenvalue from a scattering matrix to the length of a crack within an elastic solid was presented. This formula shows that there is a one to one relationship between the two and can be used to tackle the inverse problem of sizing a crack in an elastic solid given the ultrasonic array output data. The Kirchhoff model was used to approximate the scattering matrices which arise when a linear elastic wave encounters a crack within

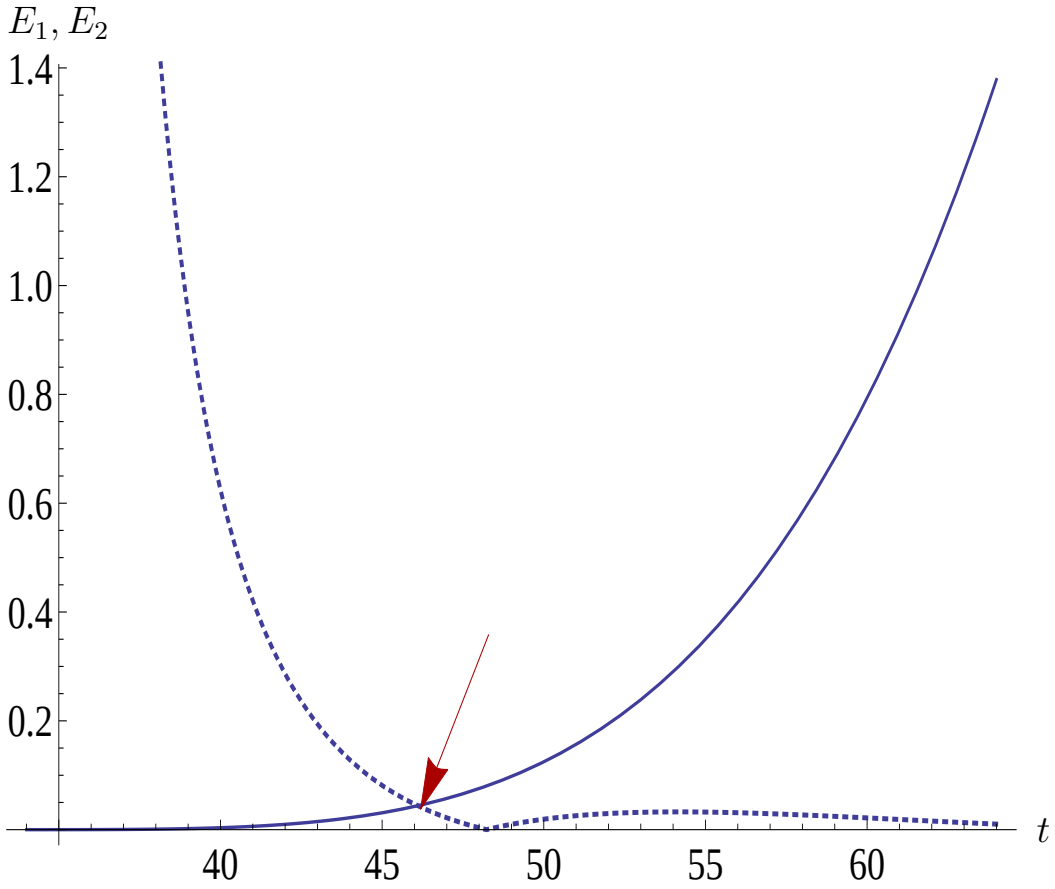

Figure 2.19: The error functions for small arguments $E_1(t, \hat{a})$ (dashed line), equation (2.104), and large arguments $E_2(t, \hat{a})$ (solid line), equation (2.105) where typical system parameters d=50 mm, l=128 mm, N=64 and $\hat{a}$=1. The red arrow shows the point of intersection and $\hat{t}^* = 46$.

a homogeneous medium. The scattering matrix from the model was approximated by a Toeplitz matrix in order to make analytical progress. The metric used to relate the size of the crack inclusion to a scattering matrix was the maximum eigenvalue. An upper bound to the maximum eigenvalue from a Toeplitz matrix was used to derive an explicit relationship between the maximum eigenvalue and the crack length over the wavelength. Having established this relationship, the next chapter considers the use of it to drive the inverse problem of objectively sizing a crack from FMC ultrasonic data.

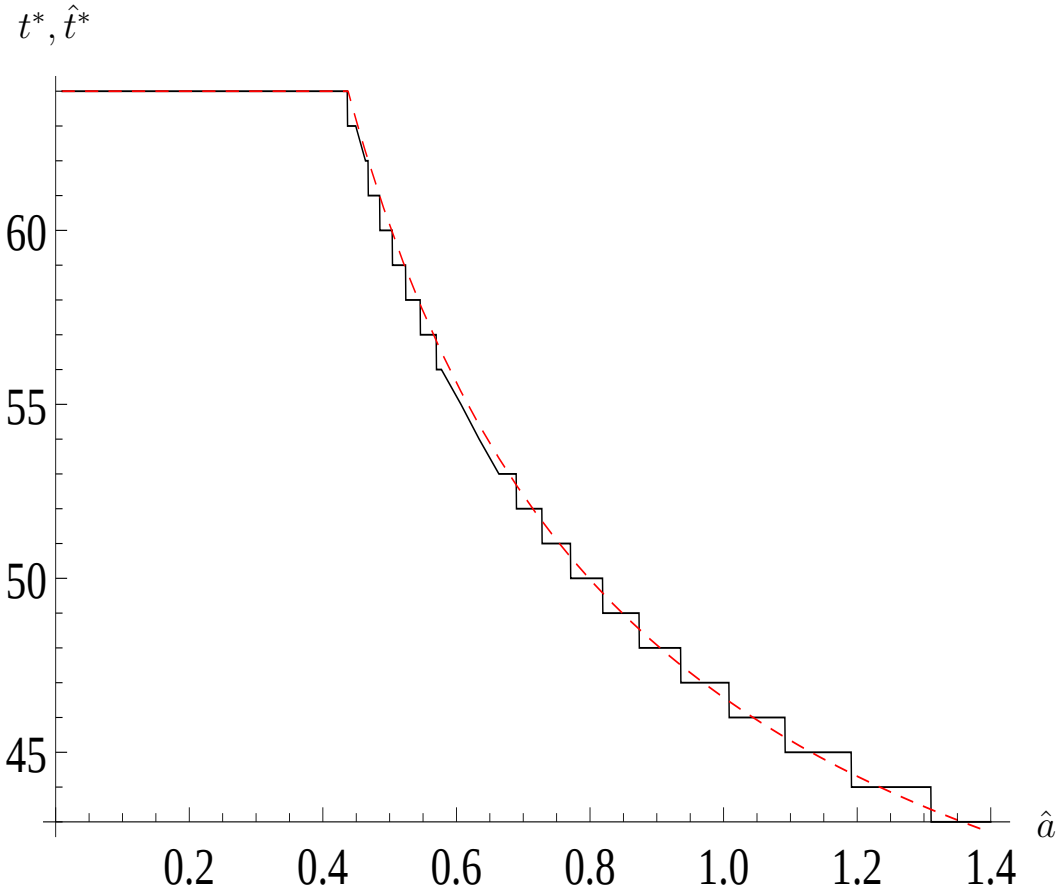

Figure 2.20: The functions $t^*(\hat{a})$ (red line) and $\hat{t}^*(\hat{a})$ (black line) given by equations (2.103) and (2.106) are plotted as a function of $\hat{a}$ for the typical parameter values given by Table 2.2.

Chapter 3

Sensitivity Analysis

3.1 Introduction

In this chapter, the multi-frequency method for sizing cracks in a homogeneous medium presented in Chapter 2 is analysed numerically and its sensitivity to the system parameters is assessed. The system parameters are varied within the expression that was derived to approximate the maximum eigenvalue of the scattering matrix. This can be used to determine the sensitivity of the associated crack sizing method to these parameters and to confirm that the approximation to the true maximum eigenvalue is still reasonable as the parameters are varied. Furthermore, the advantage of deriving an analytical approximation, σ_B, to the maximum eigenvalue is that the derivative can be explicitly determined and hence used to examine the sensitivity of the maximum eigenvalue to errors in the system parameters. Finally, the method for recovering the crack size is applied to simulated data from finite element calculations.

3.2 The effects of varying the system parameters on the maximum eigenvalue

In this section, each of the system parameters (N, the number of array elements, d, depth of the flaw, and l, length of the array) are varied in turn. The effects observed are explained by investigating the changes in the scattering matrices and how these affect the Toeplitz approximation.

3.2.1 Varying the depth of the flaw, d

The depth of the flaw, d, is varied in the expression for the approximation to the maximum eigenvalue, σ_B, given by equations (2.100) and (2.103), and in the original expression from the Kirchoff model in equation (2.27). The effects of varying, d, are shown in Figure 3.1(a), where the dashed lines show σ_B, the approximation to the maximum eigenvalue from a scattering matrix given in equation (2.100), and the solid lines show σ_K, the numerically calculated maximum eigenvalue from a scattering matrix which is via equation (2.27), as $\hat{a}$ is varied for $d = \{30, 50, 70, 90, 110\}$ (mm). This figure demonstrates an excellent correlation between the model and the approximation for each value of d. It also shows that, as the depth increases, the maximum eigenvalue (from both approximation, σ_B, and the original model, σ_K) associated with each $\hat{a}$ increases. Figure 3.2(a) shows the plot of the maximum eigenvalue, σ_B, as the depth, d is varied between 10mm and 110mm and where $l = 128$ mm and $N = 64$. This plot confirms that as d increases the maximum eigenvalue increases. This is counter-intuitive as it implies that the sensitivity of the method derived in Chapter 1 increases as the flaw moves further away from the ultrasonic array. As the depth of the flaw is increased the angle which the array makes with the flaw decreases, this is demonstrated in

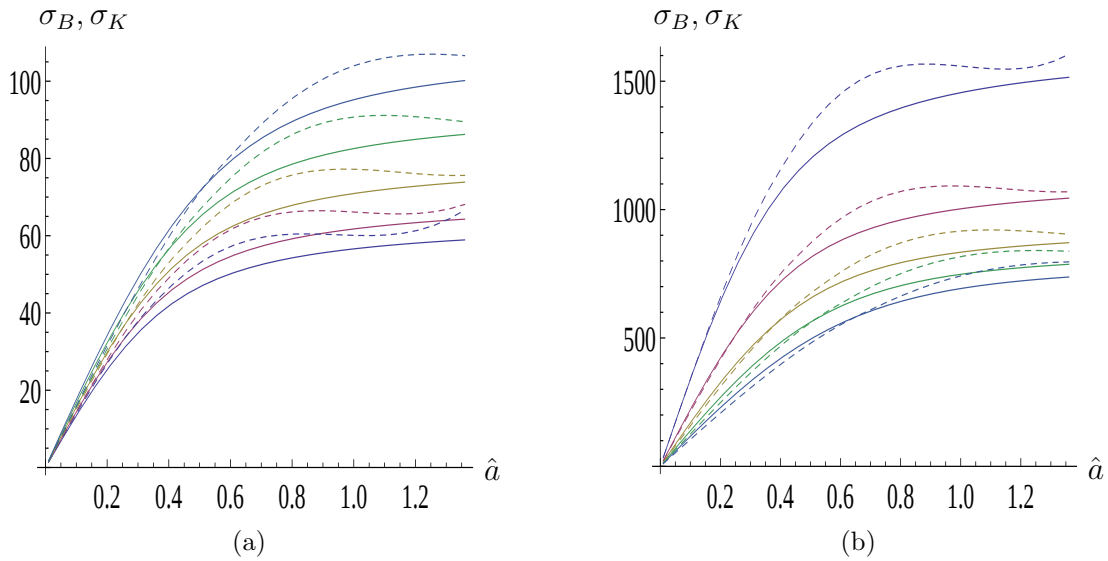

Figure 3.1: These plots show the approximation to the largest eigenvalue from a scattering matrix, σ_B (dashed lines), equation (2.100), and the numerically calculated eigenvalue from the scattering matrix, σ_K (solid lines), equation (2.27), as the crack radius over wavelength, $\hat{a}$, is varied where (a) no prefactor is included and (b) a prefactor to account for loss of amplitude with depth $\frac{1}{\sqrt{2d}}$ multiplies equation (2.100). Each different coloured pair of lines shows this plot for increasing depths of crack from the array; the flaw depth d is 30 mm (purple), 50 mm (red), 7 0mm (yellow), 90mm (green) and 110 mm (blue). The other system parameters are fixed with the number of array elements, $N = 64$ and the array aperture, $l = 128$ mm.

the schematic in Figure 3.3 where $\theta_1 > \theta_2 > \theta_3$. This decrease in the array angle causes a reduction in the size of the window around the main lobe in a scattering matrix, as shown in Figure 3.4. This results in a higher proportion of large values in the scattering matrix and consequently the associated maximum eigenvalue is higher. Note that there is no prefactor incorporated into the Kirchhoff model, equation (2.27), to account for the decrease in amplitude caused by an increase in the depth of the crack. Figure 3.5(a) shows the pulse echo response from the scattering matrices as the depth of the flaw is increased and where $N = 64$, $l = 128$ mm and $\hat{a} = 1$. It is clear that the amplitudes are not varying as a function of

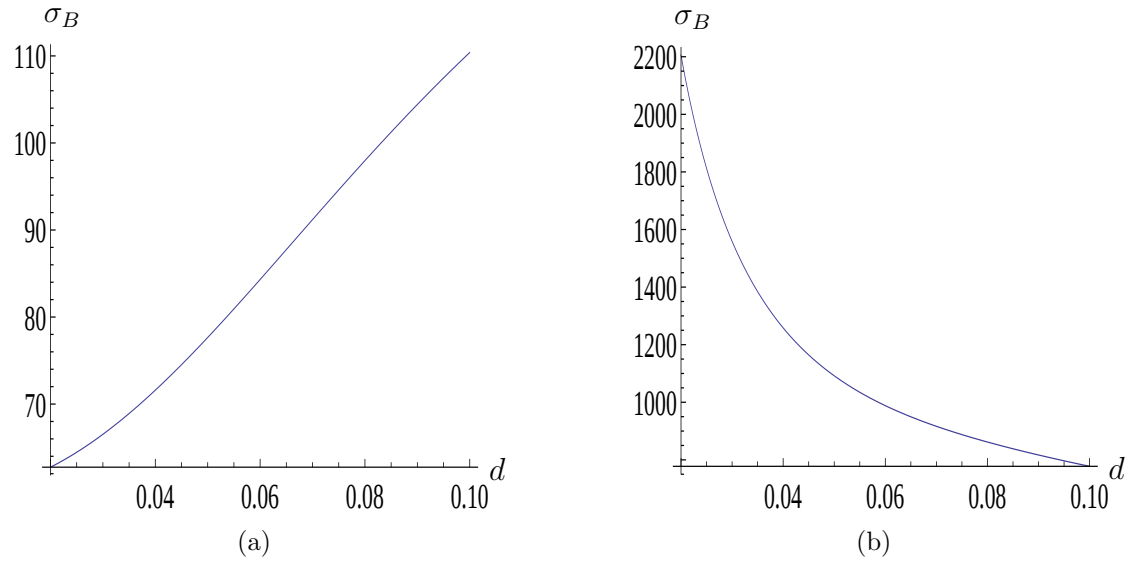

Figure 3.2: The maximum eigenvalue, σ_B, is plotted here as the depth d (mm) is varied where (a) no prefactor is included and equation (2.100) is used and (b) a prefactor is included to account for change in amplitude due to increase in depth and equation (3.6) is used. The other parameters are fixed here with $l = 128$mm, $N = 64$ and $\hat{a} = 1$.

depth.

The prefactor to account for the change in the depth of the flaw is given by

$$A(r_m) = \frac{e^{ikr_m}}{r_m}, \tag{3.1}$$

where

$$r_m = \sqrt{x_m^2 + d^2} \tag{3.2}$$

and Figure 3.6 shows the geometry of x_m, d and r_m. The absolute values of the entries in the scattering matrix are used and so the decrease in amplitude, as depth varies, is given by

$$|A(r_m)| = \frac{1}{r_m} = \frac{1}{x_m^2 + d^2}. \tag{3.3}$$

Since $d = \mathcal{O}(10^{-2})$ and $x_m = \mathcal{O}(10^{-2})$ then $d \approx x_m$ and so, $|A(r)|$ is approximated

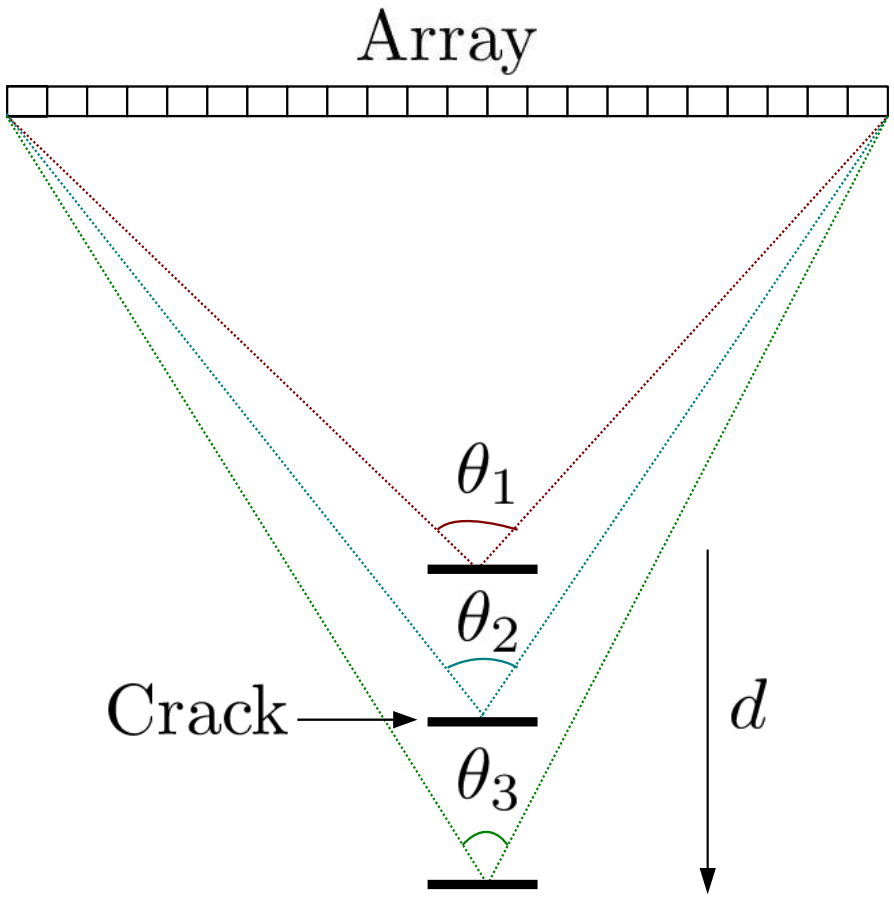

Figure 3.3: This schematic demonstrates that as the depth of the flaw is increased, where $\theta_1 < \theta_2 < \theta_3$, the angle made with the array decreases.

by

$$|A(d)| = \frac{1}{\sqrt{2}d}. \tag{3.4}$$

The expression for the scattering coefficients given in equation (2.27) is multiplied by $|A(d)|$ in equation (3.4) to give

$$A(y_m, y_n) = \frac{\sqrt{1-y_m^2}}{\sqrt{2}d\rho c^2|y_m+y_n|}(L+2\mu(1-y_n^2))J_1\Big(2\pi\hat{a}|y_m+y_n|\Big) \doteq \frac{1}{\rho c^2}A_{m,n}. \tag{3.5}$$

Figure 3.5(b) shows the pulse echo response from the scattering matrices given

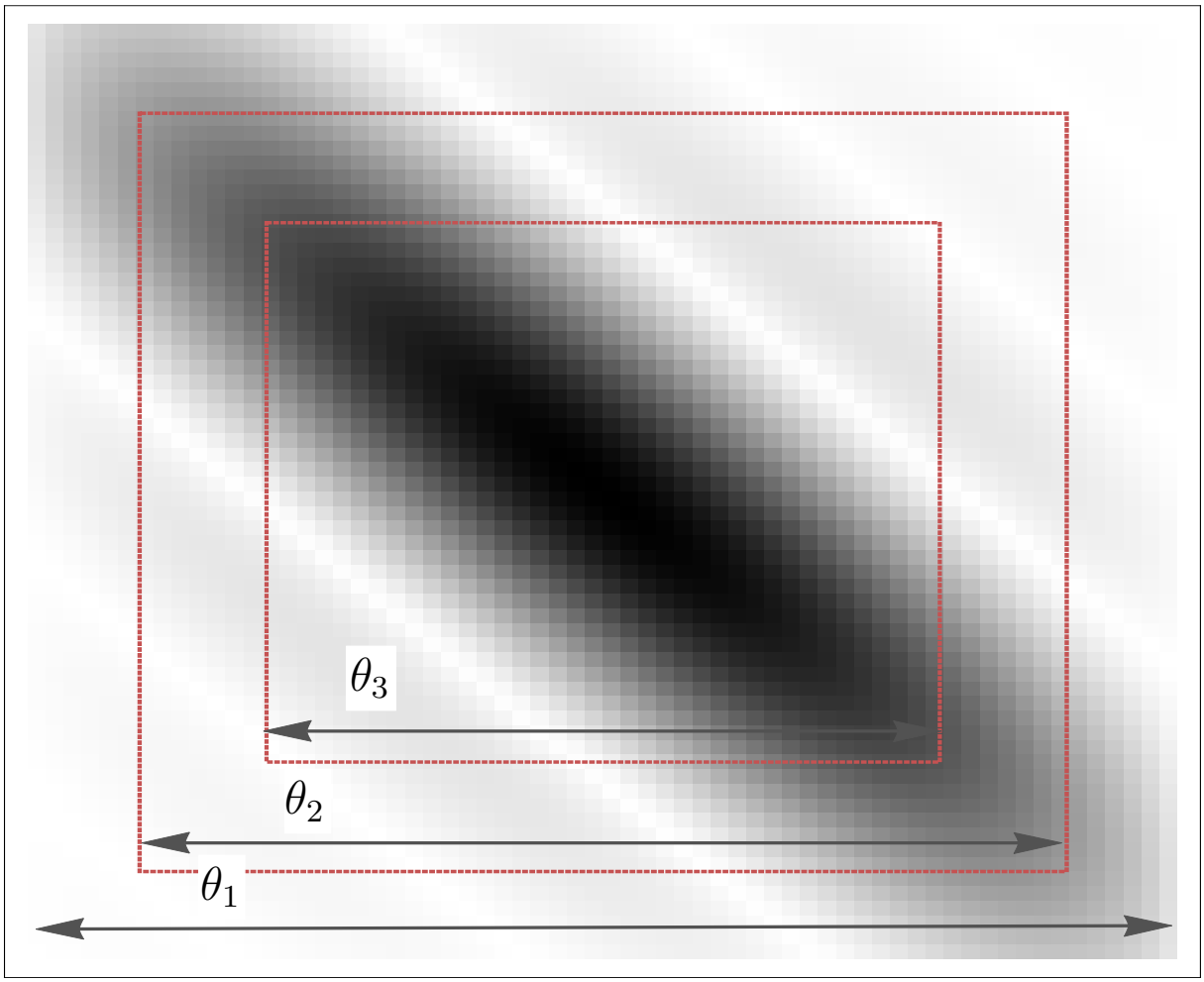

Figure 3.4: A schematic which demonstrates that as the depth of the crack is increased in the Kirchhoff model, and consequently the array aperture angle, (θ) decreases, the window around the main lobe in the scattering matrix decreases.

by equation (3.5) and it is clear that as the depth of the flaw, d, increases the scattering amplitudes along the pulse echo diagonal (and the remainder of the scattering matrix) decrease. The coefficient $|A(d)|$ is simply a scaling factor and so the expression for σ_B from equation (2.100) becomes

$$\sigma_B(\hat{a}) = \frac{1}{\sqrt{2}d}\left((\hat{A}_1 + \hat{S}_1(\hat{a}))\hat{a} + \hat{S}_2(\hat{a})\hat{a}^3 + \hat{Q}(\hat{a})\cos(p(\hat{a}) + \phi(\hat{a}))\right). \tag{3.6}$$

The maximum eigenvalues from the scattering matrices from the approxima-

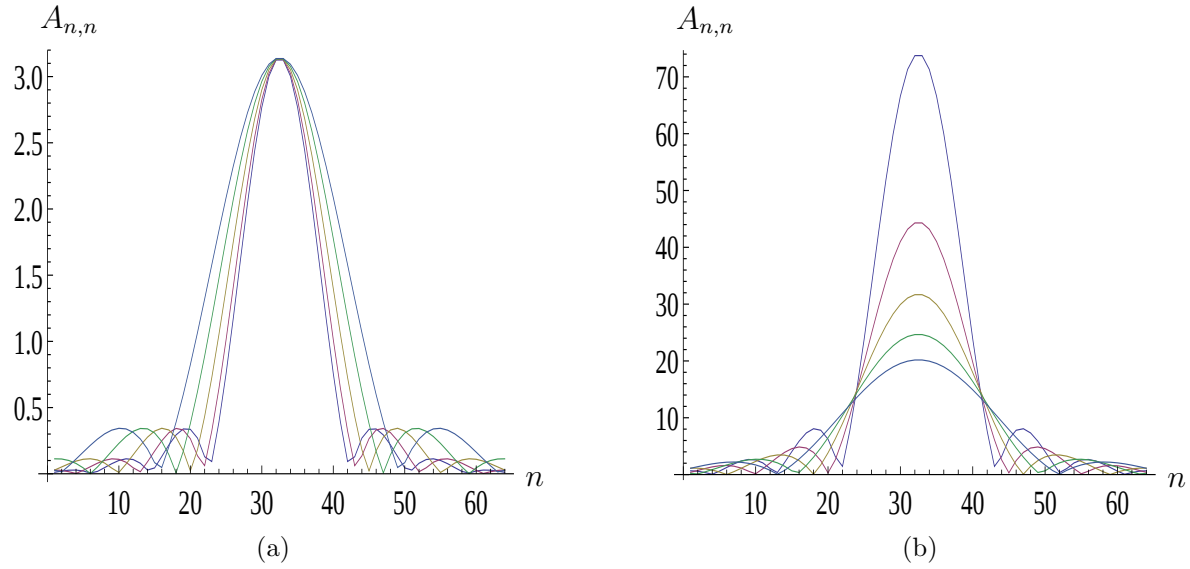

Figure 3.5: These figures show the plot of the pulse echo diagonal amplitudes from the scattering matrices as a function of receiving array element index, n, where (a) no prefactor is included, equation (2.27), and (b) a prefactor is included, equation (3.5) for varying depths; 30 mm (purple), 50 mm (red), 70 mm (yellow), 90 mm (green) and 110 mm (blue). The other system parameters are fixed here with N=64, l=128 mm and $\hat{a} = 1$.

tion, σ_B, (dashed lines) in equation (3.6) and those calculated numerically (solid lines), σ_K, from the model given by equation (3.5) are plotted in Figure 3.1(b) as $\hat{a}$ is varied for $d = \{30, 50, 70, 90, 110\}$ (mm). The values of σ_B and σ_K now decrease, as d increases, for each value of $\hat{a}$ which is more intuitive. This is validated in Figure 3.2(b) which shows the plot of σ_B plotted as d is varied between 20 mm and 100 mm, and all other system parameters are fixed at $\hat{a} = 1$, $l = 128$ mm and N=64.

3.2.2 Varying the number of elements, N

Now the effect of varying the number of elements in the ultrasonic, linear array on the maximum eigenvalue is examined. In this subsection the other system parameters are fixed at $d = 50$ mm and $l = 128$ mm. Figure 3.7(a) shows the plot

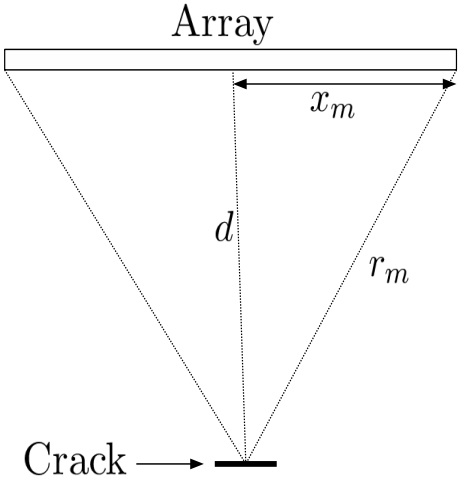

Figure 3.6: A schematic demonstrating the geometry of x_m (the distance along the x-axis to the array element with index m), d (depth of the crack) and r_m (the distance between the array element x_m and the crack) which are included in the prefactor given by equation (3.1).

of the maximum eigenvalue from the approximation σ_B, equation (2.100), (dashed line) and the exact maximum eigenvalue from the scattering matrices σ_K (solid line) as $\hat{a}$ is varied for N= 32 (blue), 64 (red), 128 (yellow) and 256 (green). This figure shows that the maximum eigenvalue from the scattering matrix increases, as the number of elements increases in an array of fixed length. In other words, σ_B is more sensitive to the size of the crack as the number of array elements increases. This trend is also evident in Figure 3.7(b), where σ_B is plotted as function of N, with $\hat{a} = 1$, $l = 128$ mm and $d = 50$ mm. This is to be expected as the increase in the number of array elements enables more information to be recorded by the ultrasonic transducer and therefore a higher volume of detail is contained within the scattering matrix; this is demonstrated in Figure 3.8, where the scattering matrix is pictured for (a) $N = 32$ and (b) $N = 256$ for $\hat{a}$=1.

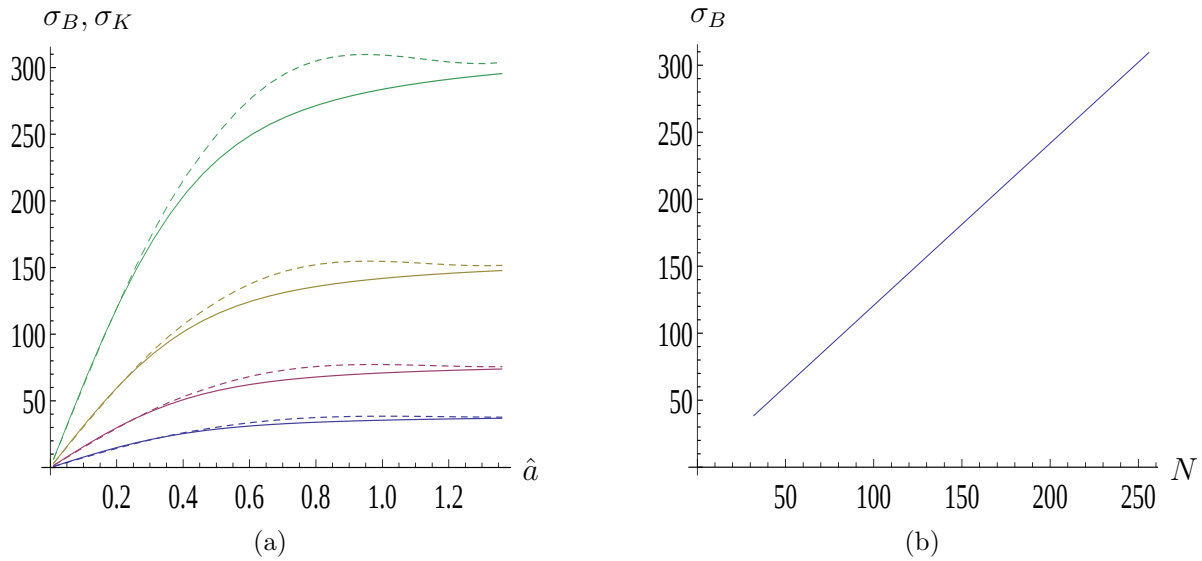

Figure 3.7: The effect of varying the number of elements, N, on the maximum eigenvalue, σ_B. The approximation to the largest eigenvalue (dashed lines), equation (2.100), and the numerically calculated eigenvalue from the scattering matrix (solid lines), equation (2.27), are plotted in (a) as a function of the crack radius over the wavelength $\hat{a}$ for various numbers of array elements (N= 32 (blue), 64 (red), 128 (yellow), 256 (green)), with $l = 128$ mm and $d = 50$ mm. The plot in (b) shows σ_B, as N is varied, where $\hat{a} = 1$, $l = 128$ mm and $d = 50$ mm.

3.2.3 Varying the array length, l

Increasing the array length has the same effect as decreasing the depth of the flaw. That is, the total angle the array makes with the crack (the array aperture angle) increases as the length of the array increases, as is demonstrated in Figure 3.9.

As the length of the array is increased the maximum eigenvalue, σ_B (dashed lines), from equation (2.100) and the actual maximum eigenvalue, σ_K (solid lines), decrease, as is shown in Figures 3.10(a), where σ_B and σ_K are plotted ,as a function of $\hat{a}$, for various lengths of array (l=32 mm (blue), 64 mm (red), 128 mm (yellow) and 256 mm (green)). This is also evident in Figure 3.10(b) which shows the plot of σ_B, as a function of l where N=64, d=5 mm and $\hat{a} = 1$. This seems counter-intuitive, however, Figure 3.4 demonstrates that, as the array length is increased

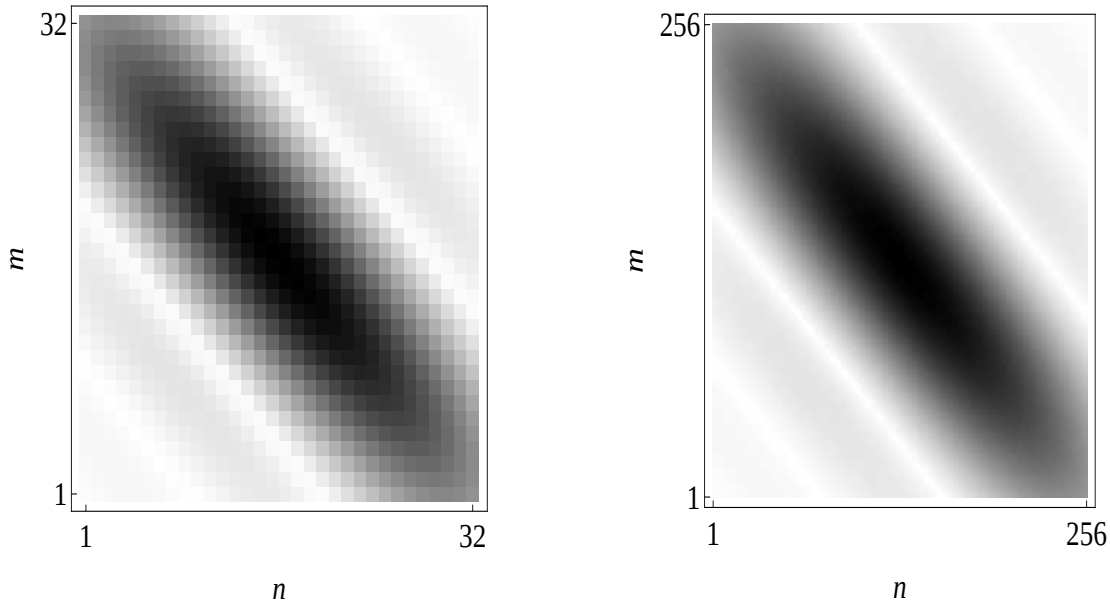

(a) (b)

Figure 3.8: This figure portrays the effect of increasing the number of elements in the scattering matrix, A (equation (2.27), from (a) 64 to (b) 256 elements. Here the other system parameters are fixed at $l = 128$ mm, $d = 50$ mm and $\hat{a} = 1$.

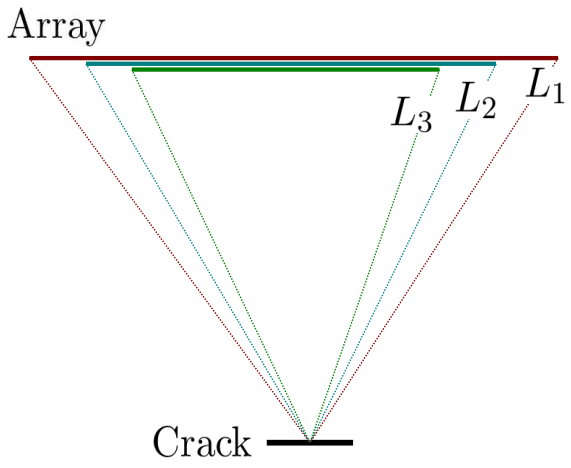

Figure 3.9: A schematic showing that, as the array length increases, $L_3 < L_2 < L_1$, then the array aperture angle θ increases.

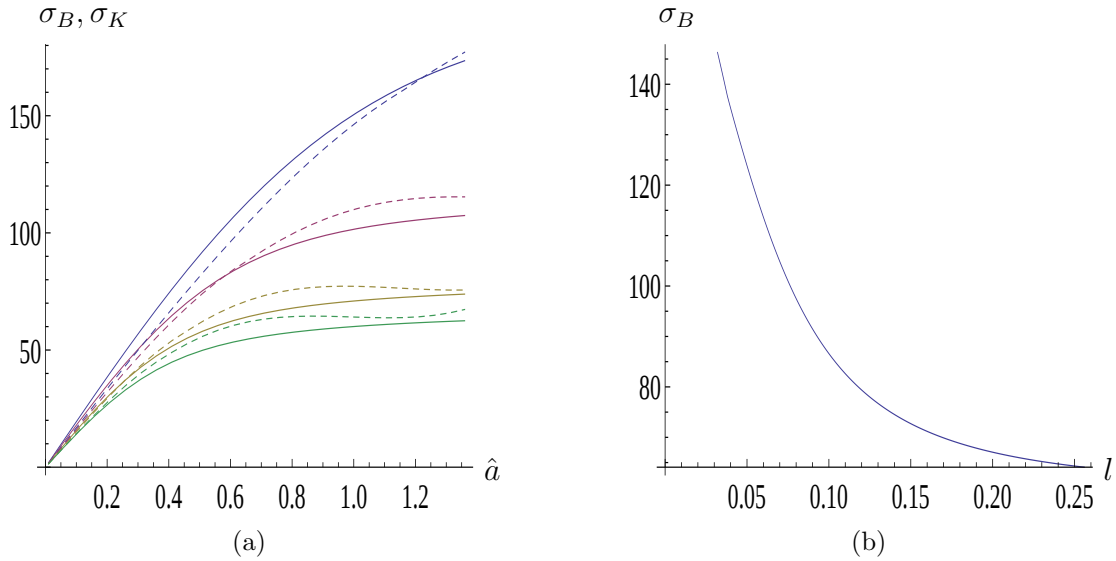

Figure 3.10: The effect of varying the length of the array, l, on the maximum eigenvalue, σ_B. The approximation to the largest eigenvalue (dashed lines), equation (2.100), and the numerically calculated eigenvalue from the scattering matrix (solid lines), equation (2.27), are plotted in (a) as a function of the crack radius over the wavelength $\hat{a}$ for various array lengths (l= 32 mm (blue), 64 mm (red), 128 mm (yellow), 256 mm (green)), with $N = 64$ and $d = 50$ mm. The plot in (b) shows σ_B, as l is varied, where $\hat{a} = 1$, $N = 64$ and $d = 50$ mm.

(and the array aperture angle is increased) then, there is a higher proportion of small to large amplitude values in the matrix. Another note is that here the number of array elements, N, is fixed and so the information recorded by the ultrasonic transducer is more sparse. In the next subsection, the array length is varied but with the pitch, $\triangle y$, fixed and so the number of array elements, N, and the array length, l, increase proportionally.

3.2.4 Varying the array length, l, and the number of elements, N

In this subsection, the length of the array is varied, however the pitch, $\triangle y$ is fixed; this means that the number of elements in the array is a function of the array

length and is given by

$$N = \frac{2l}{\triangle y\sqrt{4d^2 + l^2}} + 1 \tag{3.7}$$

which is obtained by rearranging the expression for $\triangle y$ in equation (2.20). In this section $\triangle y = 0.025$ and $d = 50$ mm. Figure 3.11 shows the approximation to the maximum eigenvalue σ_B (dashed line) and the actual maximum eigenvalue σ_K (solid line), as $\hat{a}$ is varied, and for $l = \{32, 64, 128, 256\}$ (mm) which gives corresponding values for $N = \{25, 44, 64, 76\}$ (to the nearest whole number). This figure shows that the maximum eigenvalue increases as the length of the array and the number of elements are increased simultaneously, which seems more intuitive than the results given in Section 3.2.3.

This investigation into the effects of the system parameters is practically useful for experimental design. For instance, Figure 3.11 shows that there is very little increase in sensitivity of σ_B to $\hat{a}$ when the array length is increased from 128 mm to 256 mm (and the number of elements is increased from 64 to 76 since the pitch is fixed at 2mm here). This suggests that if this method is going to be used to resolve the size of a subwavelength crack within this medium then it is unnecessary to use an array larger than 128 mm, for a fixed pitch of 2.5 mm.

3.3 The derivative of the approximation to the largest eigenvalue σ_B

In order to analytically assess the sensitivity of the maximum eigenvalue to changes in the system parameters, such as the number of elements in the array N, the length of the array l, the depth of the flaw d and $\hat{a}$, it is necessary to determine

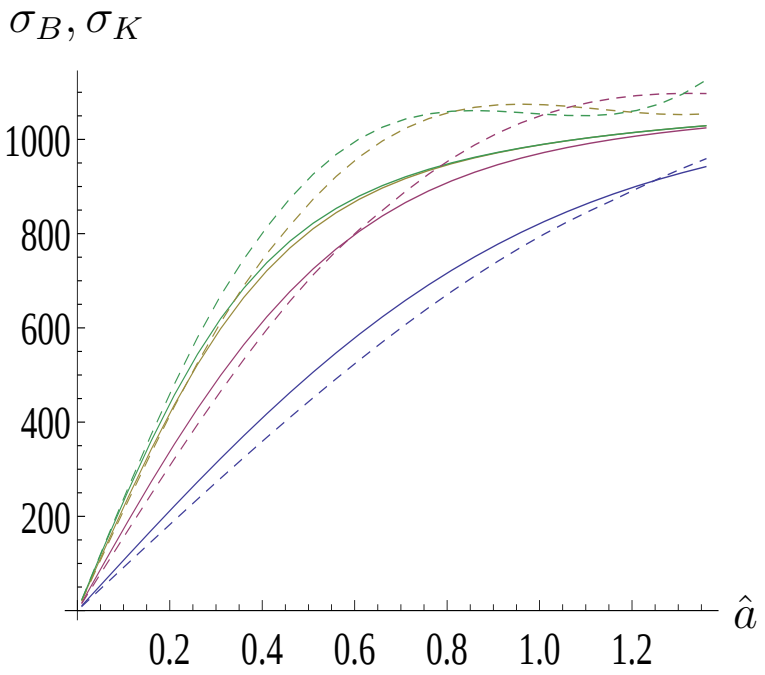

Figure 3.11: The effect of varying the number of elements, N, and the length of the array l simultaneously on the maximum eigenvalue, σ_B. The approximation to the largest eigenvalue (dashed lines), equation (2.100), and the numerically calculated eigenvalue from the scattering matrix (solid lines), equation (2.27), are plotted in (a) as a function of the crack radius over the wavelength $\hat{a}$ for various numbers of array lengths (l= 32 mm (blue), 64 mm (red), 128 mm (yellow), 256 mm (green)), with corresponding N ={25, 44, 64, 76} (to the nearest whole number) and the depth of the flaw fixed at $d = 50$ mm. The plot in (b) shows σ_B, as N is varied, where $\hat{a} = 1$ and $d = 50$mm.

the derivatives in the following expression for the relative change in σ_B,

$$\frac{\triangle\sigma_B}{\sigma_B} = \frac{\partial\sigma_B}{\partial\hat{a}}\frac{\hat{a}}{\sigma_B}\frac{\triangle\hat{a}}{\hat{a}} + \frac{\partial\sigma_B}{\partial N}\frac{N}{\sigma_B}\frac{\triangle N}{N} + \frac{\partial\sigma_B}{\partial l}\frac{l}{\sigma_B}\frac{\triangle l}{l} + \frac{\partial\sigma_B}{\partial d}\frac{d}{\sigma_B}\frac{\triangle d}{d}. \tag{3.8}$$

The expression given by

$$\frac{\partial\sigma_B}{\partial\hat{a}}\frac{\hat{a}}{\sigma_B} \tag{3.9}$$

in equation (3.8) provides a relative measure of how sensitive σ_B is to changes in the crack size. This provides a guide as to how useful this method will be in practice in recovering the crack size from a given maximum eigenvalue (the so called inverse

problem). This sensitivity is dependent on the other system parameters and the effects of these will be examined in this section. The other three components in equation (3.8),

$$\frac{\partial \sigma_B}{\partial N}\frac{N}{\sigma_B}, \qquad \frac{\partial \sigma_B}{\partial l}\frac{l}{\sigma_B} \qquad \text{and} \qquad \frac{\partial \sigma_B}{\partial d}\frac{d}{\sigma_B} \tag{3.10}$$

determine the errors that occur in σ_B as a result of errors in the system parameters; N, l and d. In this section the derivatives contained in each of these components will be calculated and numerically interpreted to analyse the sensitivity of the method.

From equation (2.100), the derivative of σ_B with respect to $\hat{a}$ is given by

$$\begin{aligned}\frac{\partial \sigma_B}{\partial \hat{a}} &= (\hat{A} + \hat{S}_1(\hat{a})) + \frac{\partial \hat{S}_1}{\partial \hat{a}}\hat{a} + 3\hat{S}_2(\hat{a})\hat{a}^2 + \frac{\partial \hat{S}_2}{\partial \hat{a}}\hat{a}^3 + \frac{\partial Q(\hat{a})}{\partial \hat{a}}\cos(p(\hat{a}) - \phi(\hat{a})) \\ &\quad - Q(\hat{a})\sin(\hat{p}(\hat{a}) - \phi(\hat{a}))\left(\frac{\partial p}{\partial \hat{a}} - \frac{\partial \phi}{\partial \hat{a}}\right).\end{aligned} \tag{3.11}$$

The derivatives of the functions $\hat{S}_j(\hat{a})$ $(j = 1, 2)$, $Q(\hat{a})$, $p(\hat{a})$ and $\phi(\hat{a})$ with respect to $\hat{a}$ are given in Appendix B, Section B.1. The expression given by equation (3.9) gives the relative error in the maximum eigenvalue σ_B for a relative change in the crack radius over the wavelength, $\hat{a}$. Figure 3.12 shows this relative error as each of the parameters is varied. Figure 3.12(a) shows that for $\hat{a} < 0.8$ the relative derivative is close to one which illustrates that changes in σ_B are sensitive to changes in $\hat{a}$. This is encouraging as it indicates that this crack sizing method is sensitive to changes in σ_B for subwavelength cracks. For $\hat{a} > 0.8$ the relative derivative is small and so the method is not very sensitive for larger values of $\hat{a}$. This result implies that the method presented in Chapter 2 should be used for sizing subwavelength cracks and for $\hat{a} > 1$ another method should be adopted; perhaps an image-based method. Figures 3.12(b), (c) and (d) show that $\frac{\partial \sigma_B}{\partial \hat{a}}\frac{\hat{a}}{\sigma_B}$ is reasonably constant, as the number of elements N (Figure 3.12(b)), the length

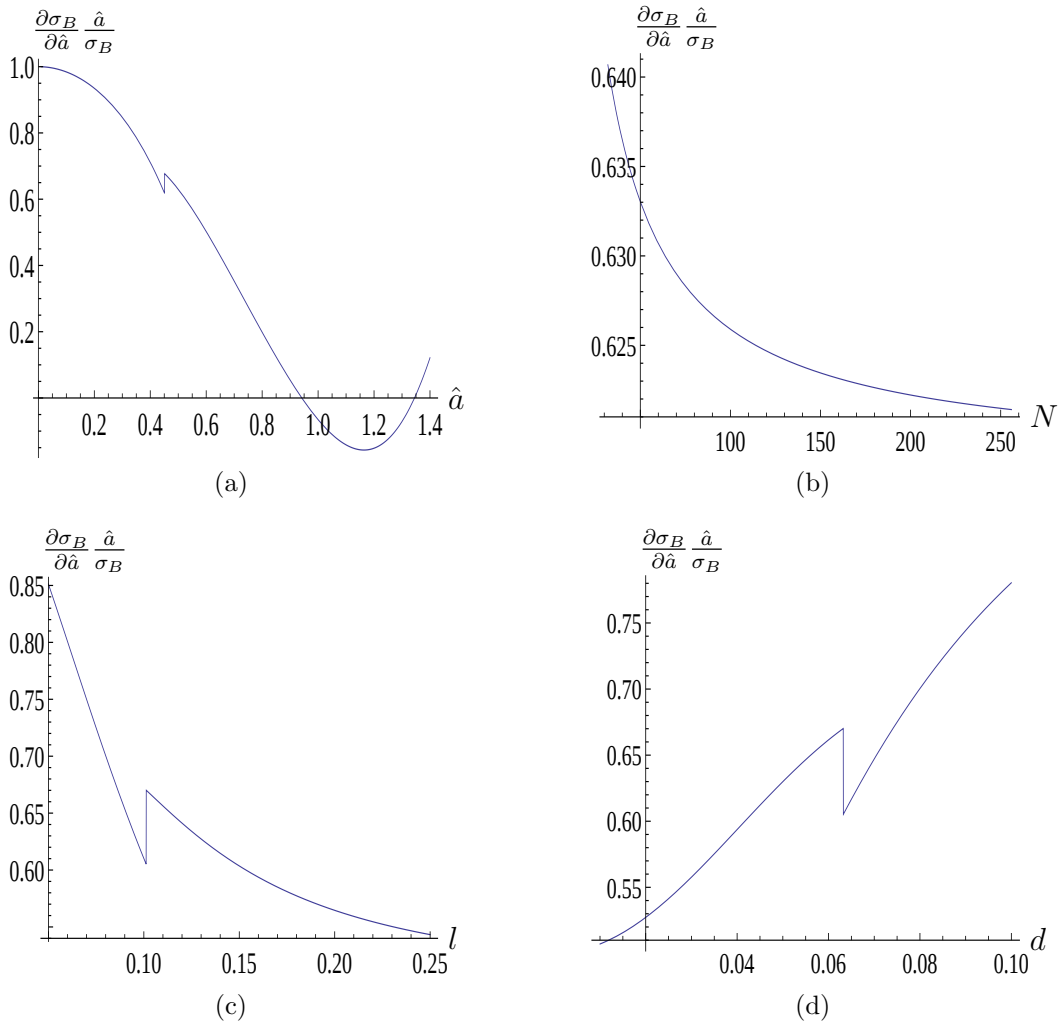

Figure 3.12: The relative derivative of the maximum eigenvalue, σ_B, with respect to $\hat{a}$, equation (3.9), as a function of (a) $\hat{a}$, (b) N, (c) l and (d) d, where all other parameters are fixed at $\hat{a} = 0.5$, N=64, l=128 mm and d=50 mm.

of the array l (Figure 3.12(c)) and the depth of the flaw d (Figure 3.12(d)) are varied. This implies that the crack sizing capability of the maximum eigenvalue method is relatively insensitive to changes in these parameters. Examining now the second of the terms in equation (3.8) the derivative of σ_B with respect to the

number of elements N is given by

$$\frac{\partial \sigma_B}{\partial N} = \left(\frac{\partial \hat{S}_1}{\partial \hat{A}} + \frac{\partial \hat{S}_1}{\partial N} \right) \hat{a} + \frac{\partial \hat{S}_2}{\partial N} \hat{a}^3 + \frac{\partial Q}{\partial N} \cos(p(\hat{a}) - \phi(\hat{a})) \\ - Q(\hat{a}) \left(\frac{\partial p}{\partial N} - \frac{\partial \phi}{\partial N} \right) \sin(p(\hat{a}) - \phi(\hat{a})). \tag{3.12}$$

Again, the derivatives of the functions $\hat{A}$, $\hat{S}_j(\hat{a})$ $(j = 1, 2)$, $Q(\hat{a})$, $p(\hat{a})$ and $\phi(\hat{a})$ with respect to N are given in Appendix B, Section B.2. Figure 3.13 plots the relative derivative

$$\frac{\partial \sigma_B}{\partial N} \frac{N}{\sigma_B} \tag{3.13}$$

as (a) $\hat{a}$, (b) N, (c) l and (d) d are varied. These plots show that for each of the parameters ($\hat{a}, N, l$ and d) the value of the expression given in equation (3.13) is pretty much constant and roughly equally to 1. In reality, the error in the number of elements in the array will be zero as this should be known with certainty within an experiment.

Turning now to the third term in equation (3.8), the derivative of σ_B with respect to the length of the array, l, is given by

$$\frac{\partial \sigma_B}{\partial l} = \left(\frac{\partial \hat{A}}{\partial l} + \frac{\partial \hat{S}_1}{\partial l} \right) \hat{a} + \frac{\partial \hat{S}_2}{\partial l} \hat{a}^3 + \frac{\partial Q}{\partial l} \cos(p(\hat{a}) - \phi(\hat{a})) \\ - Q(\hat{a}) \left(\frac{\partial p}{\partial l} - \frac{\partial \phi}{\partial l} \right) \sin(p(\hat{a}) - \phi(\hat{a})), \tag{3.14}$$

where the derivatives of the functions $\hat{A}$, $\hat{S}_j(\hat{a})$ $(j = 1, 2)$, $Q(\hat{a})$, $p(\hat{a})$ and $\phi(\hat{a})$ with respect to l are given in Appendix B Section B.3. Figure 3.14 shows the relative

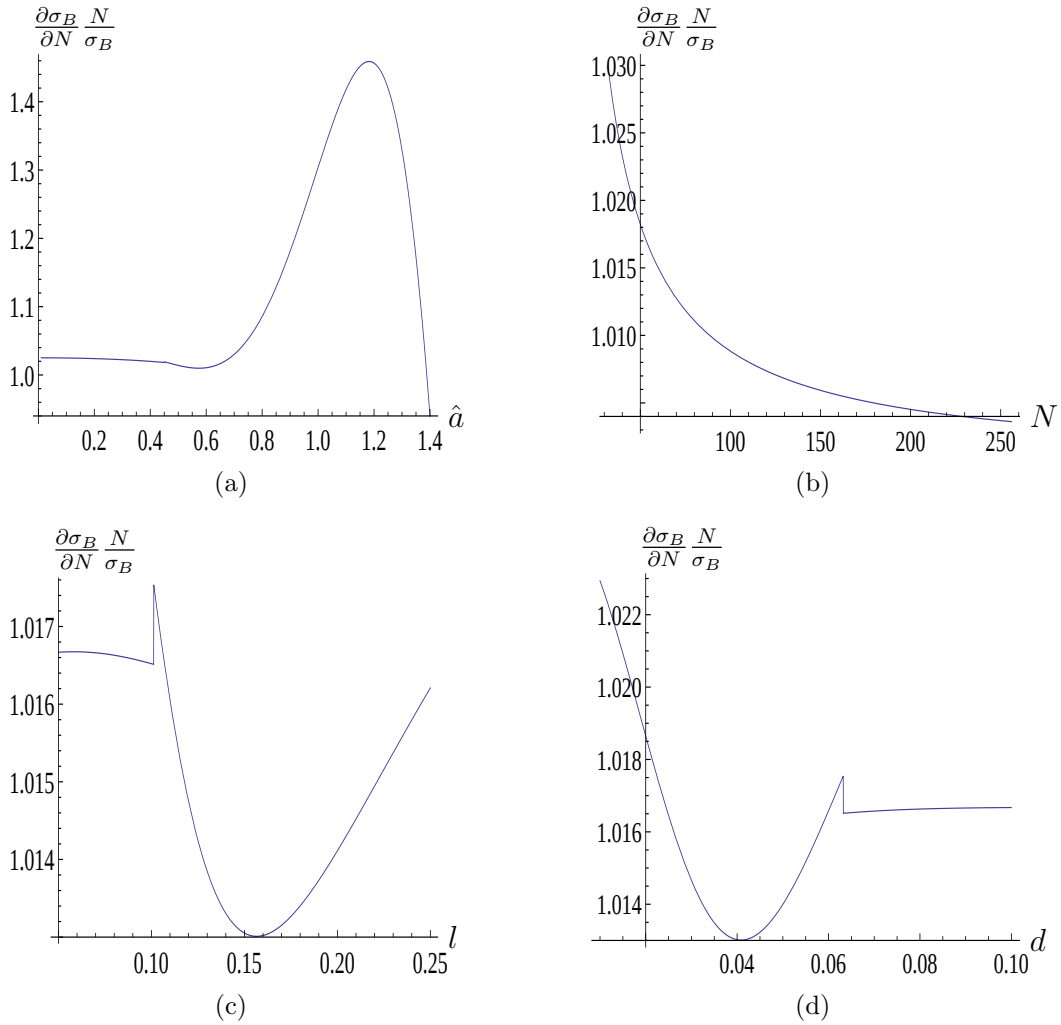

Figure 3.13: The relative derivative of the maximum eigenvalue, σ_B, with respect to N, equation (3.13)is plotted as (a) $\hat{a}$, (b) N, (c) l and (d) d are varied, with all other parameters fixed at $\hat{a} = 0.5$, N=64, l=128 mm and d=50 mm.

derivative,

$$\frac{\partial\sigma_B}{\partial l}\frac{l}{\sigma_B} \tag{3.15}$$

which gives the relative change, σ_B, caused by a relative error in the length of the array, l, as (a) $\hat{a}$, (b) N, (c) l and (d) d are varied. These plots show that the change in σ_B, due to an error in the measured length of the array l, is negligible; plots (a)-(d) show that the expression in equation (3.15) is of the order 10^{-1} as

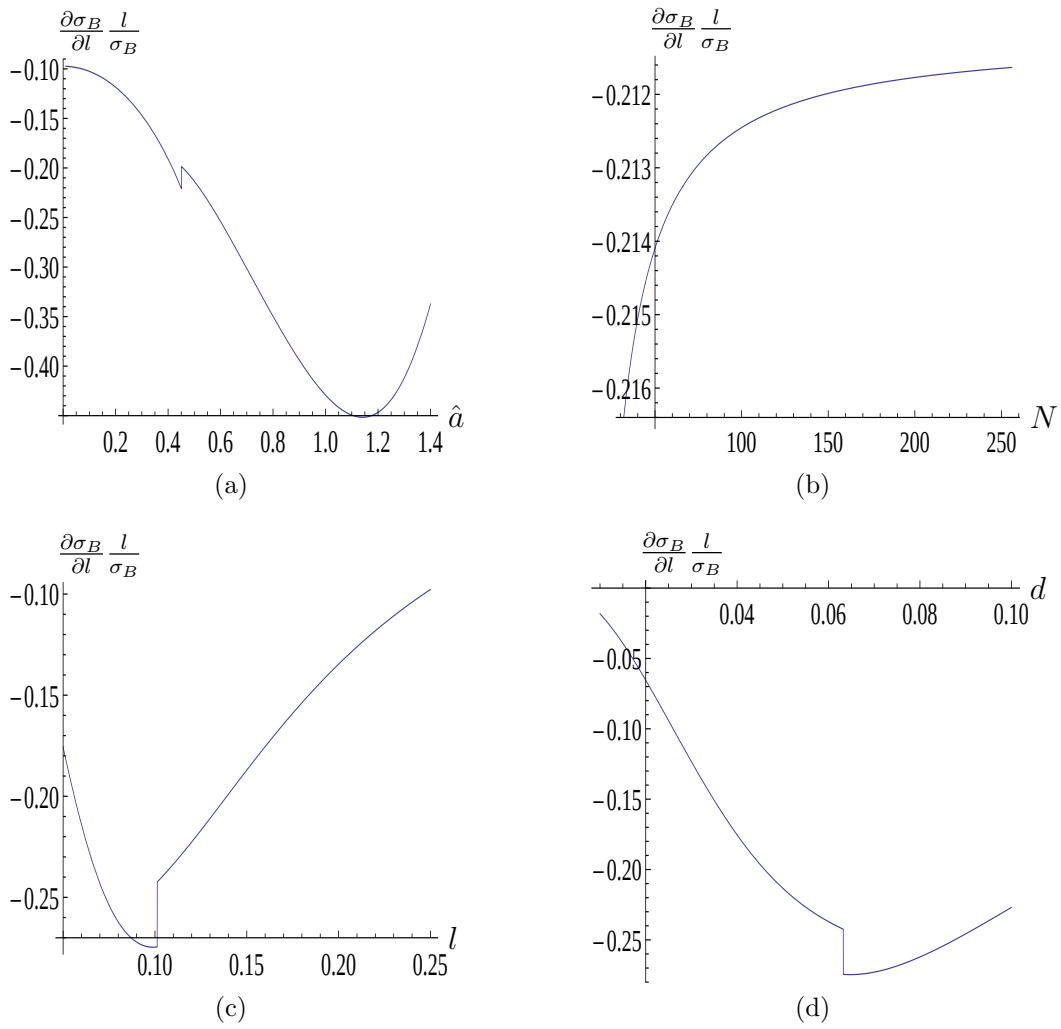

Figure 3.14: The relative derivative of the maximum eigenvalue, σ_B, with respect to l, equation (3.15), is plotted as (a) $\hat{a}$, (b) N, (c) l and (d) d are varied, with all other parameters fixed at $\hat{a} = 0.5$, N=64, l=128 mm and d=50 mm.

each of the parameters ($\hat{a}$, N, l and d) are varied. This is encouraging as it means that the inverse problem of recovering the size of the crack using this method is not sensitive to errors in the length of the array.

Finally, σ_B is differentiated with respect to the depth of the crack, d, and is

given by

$$\frac{\partial \sigma_B}{\partial d} = \left(\frac{\partial \hat{A}}{\partial d} + \frac{\partial \hat{S}_1}{\partial d} \right) \hat{a} + \frac{\partial \hat{S}_2}{\partial d} \hat{a}^3 + \frac{\partial Q}{\partial d} \cos(p(\hat{a}) - \phi(\hat{a})) - Q(\hat{a}) \left(\frac{\partial p}{\partial d} - \frac{\partial \phi}{\partial d} \right) \sin(p(\hat{a}) - \phi(\hat{a})) \tag{3.16}$$

where the $\hat{A}$, $\hat{S}_j(\hat{a})$ $(j = 1, 2)$, $Q(\hat{a})$, $p(\hat{a})$ and $\phi(\hat{a})$ with respect to d are given in Appendix B, Section B.4. The relative error in σ_B caused by a relative error in the depth of the flaw, d, is shown in Figure 3.15 where

$$\frac{\partial \sigma_B}{\partial d} \frac{\triangle d}{\sigma_B} \tag{3.17}$$

is plotted as a function of (a) $\hat{a}$, (b) N, (c) l and (d) d. Again, it is clear from these figures that there will be little error in σ_B resulting from an error in d as the expression in equation (3.17) is approximately constant and of the order 10^{-1} for each of the parameters varied in Figures 3.15 (a)-(d).

To conclude, the analysis of the derivative of σ_B with respect to the system parameters shows that small errors in the length of the array, l, the number of elements, N and the depth of the flaw, d do not create large errors in σ_B. Conversely, it has been shown that σ_B is sensitive to changes in the crack radius over the wavelength, $\hat{a}$, when $\hat{a} < 0.8$, which implies that this method should be used for sizing sub-wavelength cracks (that is, the inverse problem) and for $\hat{a} > 0.8$ another method, such as an image-based method should be used.

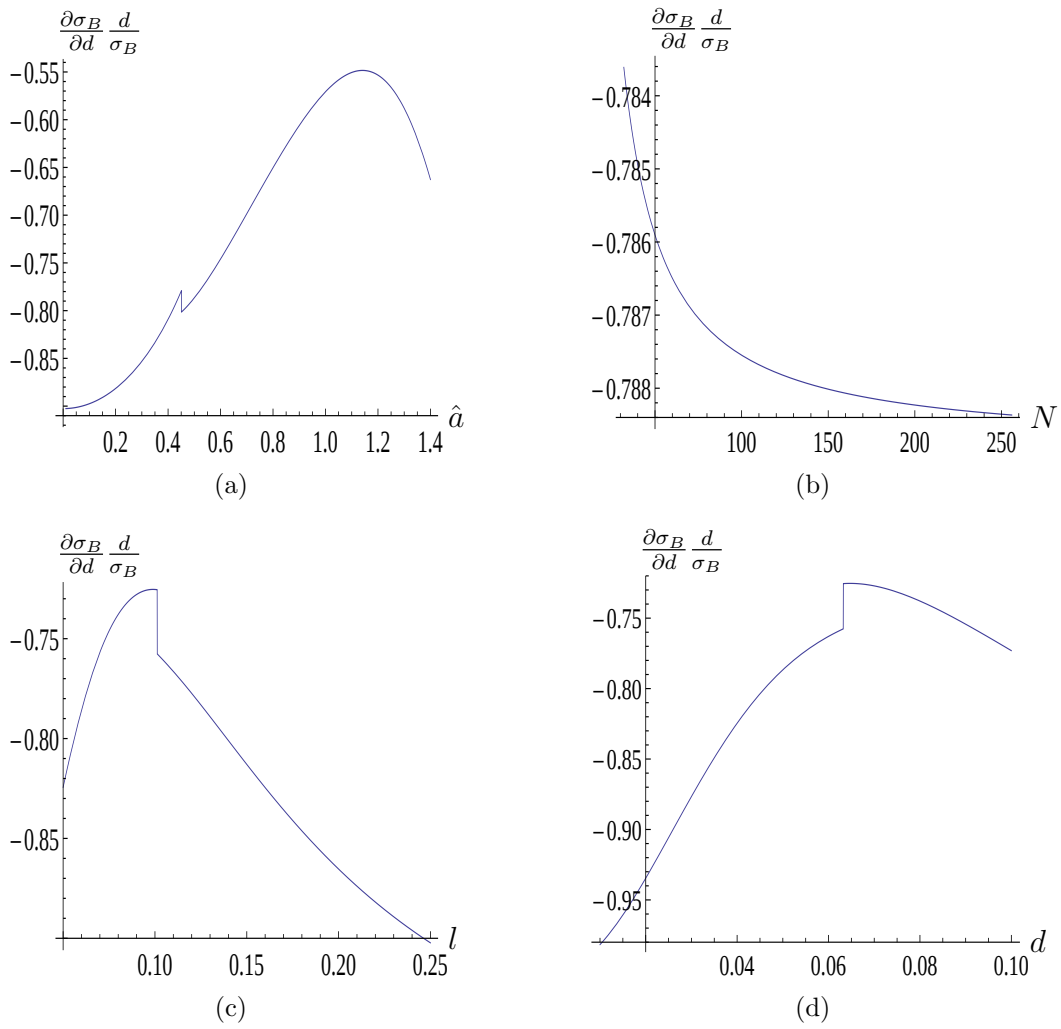

Figure 3.15: The relative derivative of the maximum eigenvalue, σ_B, with respect to d, equation (3.17) is plotted as a function of (a) $\hat{a}$, (b) N, (c) l and (d) d, with all other parameters fixed at $\hat{a} = 0.5$, N=64, l=128mm and d=50mm in each case.

3.4 Results from simulated data

In this section, the method outlined in Chapter 2, which uses the maximum eigenvalue to size a crack within a homogeneous medium, is applied to simulated data. The simulated data was generated using the finite element package PZFlex [61] and simulates a crack of length 5 mm ($a = 2.5$ mm) within a homogeneous medium (more details surrounding this simulated data is outlined in Chapter 2, Section

2.3.1). The maximum eigenvalues associated with each scattering matrix from the simulated data across a range of frequencies are compared with those calculated directly from the Kirchhoff model using equation (2.27). The scattering matrices were extracted from the FMC data and the maximum eigenvalue was numerically calculated from each across a range of frequencies. A 1.5 MHz single cycle sinusoid wave was used in the simulation and so a 50% window is taken around this central frequency to give a usable bandwidth of $0.75 - 2.25$MHz; this is the range of scattering matrices used from the simulated data and compared with those from the model via the maximum eigenvalue. The simulation includes a number of effects which are not taken into account in the Kirchhoff model used in this work; this results in amplitude differences between the scattering matrices from the simulated data and the model and therefore, the scattering matrices need to be normalised. For example, there is no attenuation from the material included in the Kirchhoff model and there is also no mode conversion of the wave considered when it encounters the crack, only a pressure wave is used in the model. The scattering matrices from the simulated data, $A_S(m, n, f)$, and from the model, $A_K(m, n, a, f)$, (where $m, n = 1, ..., N$ correspond to transmitting and receiving element indices) are normalised with respect to the l^2-norm to allow the signatures of each to be compared as crack radius, a, and frequency, f are varied. That is, for the simulated data let

$$\bar{A}_S(m, n) = \frac{A_S(m, n, f)}{\sqrt{\sum_{m=1}^{N} \sum_{n=1}^{N} A_S(m, n, f)^2}} \tag{3.18}$$

and similarly, from the Kirchhoff model (equation (2.27)) the normalised scattering matrix is

$$\bar{A}_K(m, n) = \frac{A_K(m, n, a, f)}{\sqrt{\sum_{m=1}^{N} \sum_{n=1}^{N} A_K(m, n, a, f)^2}}. \tag{3.19}$$

Let $\sigma_S(f)$ denote the numerically calculated maximum eigenvalue from the normalised scattering matrix, given by equation (3.18), at a fixed frequency, f, and let $\sigma_K(a, f)$ denote the numerically calculated maximum eigenvalue from the Kirchhoff model (equation (3.19)) at a frequency f and for a crack of radius a. Figure 3.16 shows the plot of σ_S (blue line) across the frequency range $0.75 - 2.25$ MHz and compares this with σ_K from the model for the same range of frequencies for different values of crack radii. This figure shows that $\sigma_K(a, f)$ from the normalised scattering matrix is still sensitive to changes in crack radius and that $\sigma_S(f)$ compares well with $\sigma_K(a, f)$ for crack radii between 2 mm and 2.5 mm. Next the sum of the differences over frequency between $\sigma_S(f)$ and $\sigma_K(a, f)$ is calculated as the crack radius, a is varied, and is given by

$$D(a) = ||\sigma_S(f) - \sigma_K(a, f)||_2. \tag{3.20}$$

Figure 3.17 plots $D(a)$, equation (3.20), as the crack radius, a, is varied within the model and shows a clear minimum for $a = 2.2$ mm (again, the frequency range used was 0.75-2.25 MHz). The actual crack radius in the simulation is 2.5 mm and so the percentage error in the value recovered using the maximum eigenvalue method is 12%, which is a reasonable error considering the assumptions within the model and the effects within the simulation which are not included within the model.

3.5 Conclusions

In this chapter, the sensitivity of the maximum eigenvalue approximation, σ_B, to changes in the system parameters was examined numerically. Next the derivative of σ_B with respect to each of the system parameters was determined. These

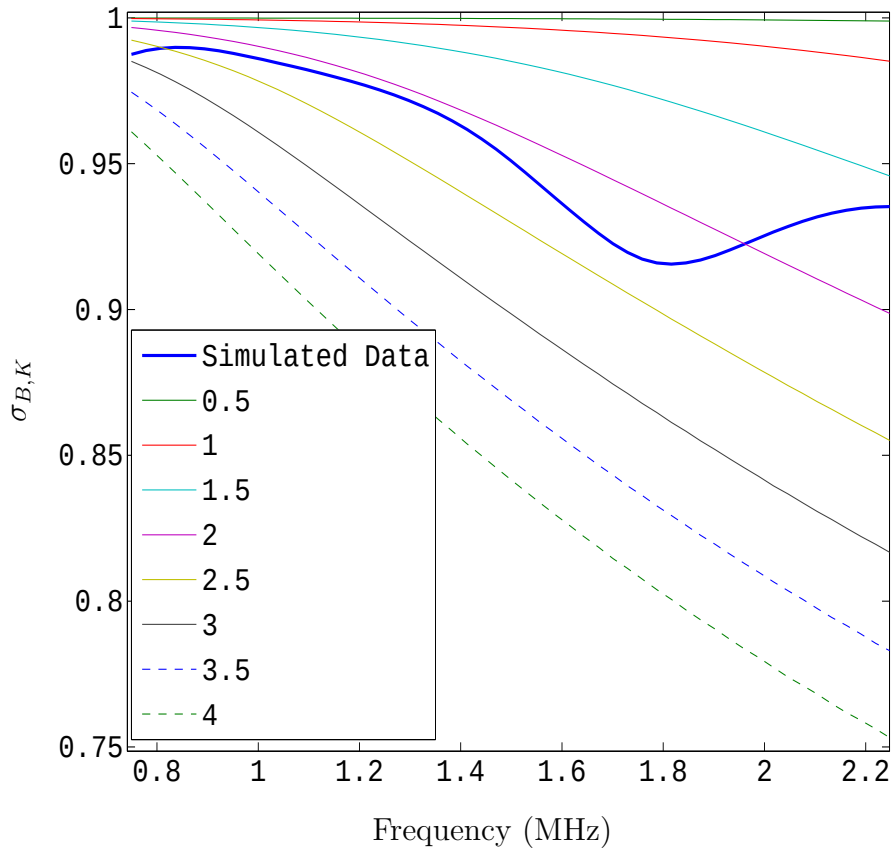

Figure 3.16: The maximum eigenvalue, $\sigma_S(f)$, from the scattering matrices extracted from the simulated data (thick blue line), as a function of frequency, in comparison with the maximum eigenvalue, $\sigma_K(a, f)$ from the scattering matrices determined using the Kirchhoff model as a function of frequency for different crack radii. The values in the legend refer to the crack radius in millimetres.

derivatives were used to determine whether σ_B is sensitive to errors in $\hat{a}, l, d$ and N. From this analysis it is concluded that σ_B is most sensitive to changes in $\hat{a}$ when $\hat{a} < 0.8$ and there is little change in σ_B for $\hat{a} > 0.8$. This implies that the method of using the maximum eigenvalue to determine the size of a crack in a homogeneous material (the inverse problem) is most effective when $\hat{a}$ is sub-wavelength. Obviously, there is a lower bound too on the values of $\hat{a}$ that the method can cope with. As $\hat{a}$ gets smaller the amplitude of the scattered wave will diminish and eventually be lost in the noise, this effect is not considered here. For

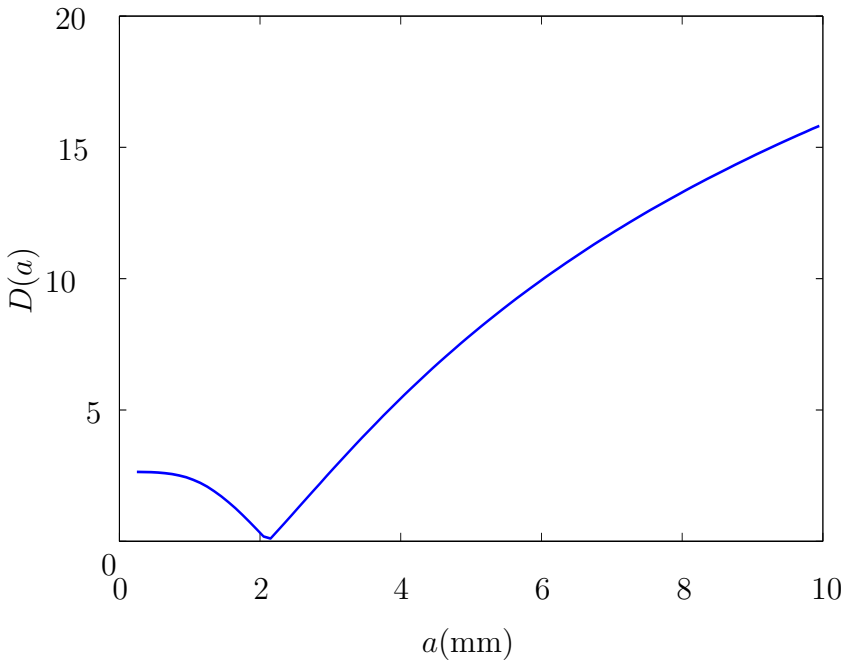

Figure 3.17: This plot shows the sum of the absolute differences, $D(a)$ (equation (3.20)), over a range of frequencies (0.75 -2.25 MHz) between the maximum eigenvalue from the scattering matrices from the simulated data, $\sigma_S(f)$, and the Kirchhoff model, $\sigma_K(a, f)$, as the crack radius, a, is varied within the model.

larger cracks another method should be adopted, perhaps an image-based method. In addition, the analysis of the derivative highlighted that errors in the measured length of the array, depth of the flaw, and number of elements has little effect on the inverse problem. Finally, the method outlined in Chapter 2 was applied to simulated data giving encouraging results. Future work may include considering the effects of including multiple cracks of varying size.

Chapter 4

A crack sizing method using the pulse echo response from the scattering matrices from the Kirchhoff model

4.1 Introduction

In this chapter another model based crack sizing method is presented which utilises the pulse echo response (that is, transmitting and receiving on the same transducer array element) within a scattering matrix from the Kirchhoff model. To begin with a single frequency method is derived which relates the first minimum of the pulse echo response to the crack length. Furthermore an analytical approximation to this first minimum is determined and the errors due to the discretisation of the array elements are explored. This work complements the work by Zhang et al. [30], where the Half-Width at Half-Maximum measurement is used numerically to size cracks

within a homogeneous medium. This single frequency method is then extended to a mutli-frequency technique. Finally, the methods are applied to finite element simulated data from a homogeneous medium and then from a heterogeneous, steel weld containing a crack. A noise reduction technique is applied to the simulated data arising from the steel weld before the crack sizing methods are applied. This involves convolution of the signals within the frequency domain and was inspired by the work of Borcea et al. within their Coherent Interferometry Methods [41].

4.2 Crack sizing using the pulse echo response from a scattering matrix

In this section, the pulse echo response from the scattering matrices will be used to determine the length of a crack inclusion. Scattering matrices (based on the Kirchhoff approximation, as derived in Chapter 2, Section 2.2) for crack inclusions of varying radii are shown in Figure 4.1(a-d), where the full aperture is used. If the aperture is limited, only a subsection of the scattering matrices in Figures 4.1 are generated, as shown in Figures 4.1(e-h) and the corresponding pulse echo plot (putting $\mathbf{e}_i = -\mathbf{e}_s$ in equation (2.8)) is demonstrated in Figures 4.1(i-l). It is clear from these images that as the length of the crack is varied, the main lobe in the pulse echo response varies. In particular, the first minimum, θ^* (as shown in Figure 4.2), varies with the crack length. In the forthcoming sections it is demonstrated that there is a one to one correspondence between the first minimum in this pulse echo response, θ^*, and the crack length. Furthermore, an analytical approximation to this first minimum is determined by considering the first zero of the Kirchhoff approximation; it is important to note that in practice this minimum will never equal zero as there will always be some reflected energy recorded by each array

element. The discretisation due to the array pitch means that this pulse-echo response is sampled at discrete points and so in all likelihood none of these points will correspond precisely to the location of this zero.

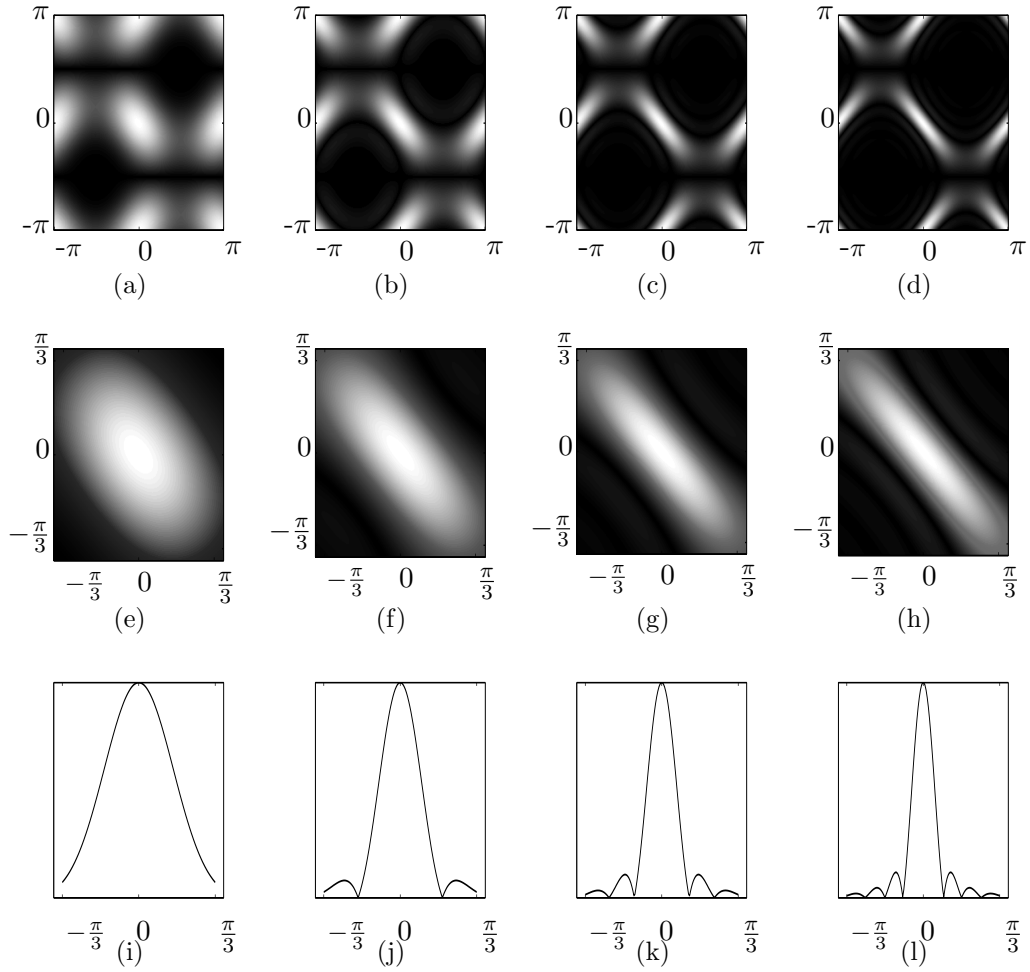

Figure 4.1: Scattering matrices generated using the Kirchhoff model, where the frequency f =2 MHz (and the corresponding wavelength is $\lambda = 0.0032$) and the crack length is (a) 2 mm (a_2 =1 mm), (b) 4 mm (a_2=2 mm), (c) 6 mm (a_2 =3 mm) and (d) 8 mm (a_2=4 mm). Figures (e-h) show the corresponding scattering matrices when the array aperture is limited and the pulse echo response extracted from these are shown in Figures(i-l). The axis on these images are the angles of incidence of the transmitting (θ_s) and receiving (θ_i) elements in the transducer.

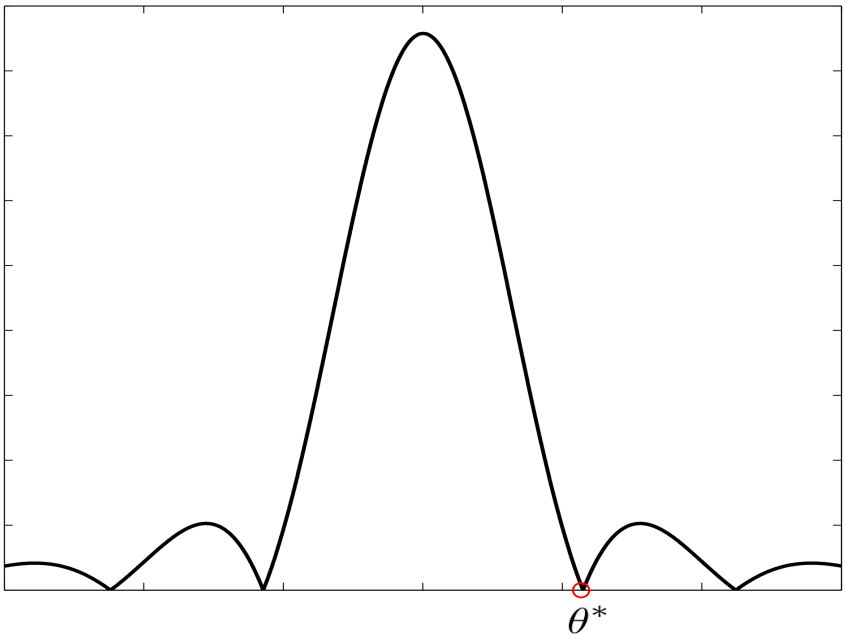

Figure 4.2: A schematic showing the location of the first zero, θ^*, from equation (4.5), in the pulse echo response from the scattering matrices, equation (4.1).

4.2.1 A single frequency crack sizing method

In this section an analytical expression is derived from the Kirchhoff model which can be used to recover the crack length from the pulse echo component of a scattering matrix. This analytical expression is an approximation to the first minimum in the pulse echo response. The Kirchhoff model is simplified for the pulse echo case where only the signals which are transmitted and received on the same transducer element are considered, that is when $\mathbf{e}_i = -\mathbf{e}_s$ is substituted into equation (2.9) to give

$$A(-\mathbf{e}_s;\mathbf{e}_s) = \frac{a_3(L((\mathbf{e}_s+\mathbf{e}_r)\cdot\mathbf{n}) + 2\mu((\mathbf{e}_s+\mathbf{e}_r)\cdot\mathbf{e}_s)(\mathbf{e}_s\cdot\mathbf{n}))}{4\rho c^2|\mathbf{e}_s\cdot\mathbf{u}_2|} J_1\Big(\frac{4\pi a_2}{\lambda}|\mathbf{e}_s\cdot\mathbf{u}_2|\Big). \tag{4.1}$$

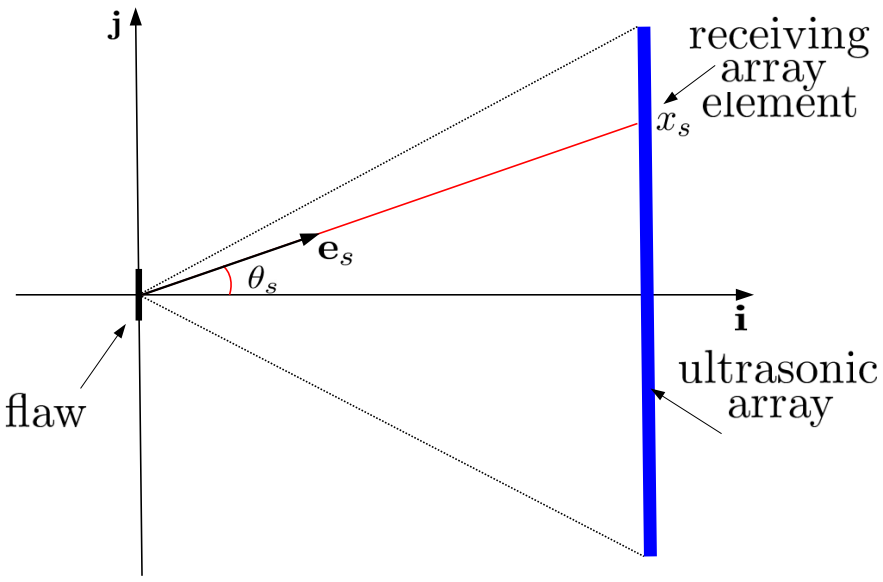

Figure 4.3: A schematic demonstrating the relationship between the array aperture angle θ_s and the receiving direction vector, $\mathbf{e}_s$ which is associated with the array element position x_s.

The angle that the vector $\mathbf{e}_s$ makes with the horizontal axis is given by θ_s as shown in Figure 4.3.

For the pulse echo case, the angles, θ_b, which the vectors, $\mathbf{e}_b$ $(b = s, r)$ make with the horizontal axis are such that $\theta_r = -\theta_s$ (this is true for a limited aperture only, since $|\theta_b| < \pi/2$ for $b = r, s$)). The various components in equation (4.1) are expressed in the following form

$$(\mathbf{e}_s{+}\mathbf{e}_r){\cdot}\mathbf{n} = 2\cos(\theta_s), \qquad (\mathbf{e}_s{+}\mathbf{e}_r){\cdot}\mathbf{e}_s = 1{+}\cos(2\theta_s), \qquad \mathbf{e}_s{\cdot}\mathbf{n} = \cos(\theta_s), \qquad \mathbf{e}_s{\cdot}\mathbf{u}_2 = \sin(\theta_s). \tag{4.2}$$

Substituting these into equation (4.1) gives the amplitude of the scattered wave in terms of the receiving angle, θ_s, as

$$A(\theta_s) = \frac{a_3|\cot\theta_s|(L + 2\mu(1 + 2\cos(2\theta_s)))}{2\rho c_1^2} J_1\Big(\frac{4\pi a_2}{\lambda}|\sin\theta_s|\Big), \tag{4.3}$$

where $s = 1, ..., N$. The first minimum of equation (4.3) varies with the crack size a_2, this minimum will be approximated here by the first zero. The pre-factor multiplying the Bessel function cannot equal zero for this problem since $-\pi/2 < \theta < \pi/2$, therefore $A(\theta) = 0$ when

$$J_1\Big(\frac{4\pi a_2}{\lambda}|\sin\theta|\Big) = 0. \tag{4.4}$$

The zeros of the Bessel function, J_n, are known and so, equation (4.4) holds when

$$a_2(\theta^*) = \frac{\lambda\beta}{4\pi\sin\theta^*}, \tag{4.5}$$

where $\beta = 3.8317$ and θ^* is the angle where the first zero of the Bessel function occurs, as demonstrated in Figure 4.2.

This provides an explicit analytical expression for the crack length a_2 in terms of the wavelength λ and the location of the first positive zero, θ^* in the pulse echo component of the scattering matrix. If we rearrange this formula to give

$$\sin\theta^* = \frac{\beta/4\pi}{a_2/\lambda} \tag{4.6}$$

then we can see that the location of this zero is inversely proportional to a_2/λ, as shown in Figure 4.4. This plot has precisely the same form as that in Figure 6(c) of Zhang et al. [30] (dashed line in Figure 4.4). They used a numerical calculation of the Half Width at Half Maximum (HWHM) to avoid any issues regarding the identification of the zeros due to noise in the experimental data. However, taking an estimate of HWHM= $\theta^*/2$ maps Figure 4.4 (solid line) onto Figure 6(c) of [30]. The use of the analytical expression in equation (4.5) results in a computationally efficient method of sizing cracks as well as providing analytical insight into the

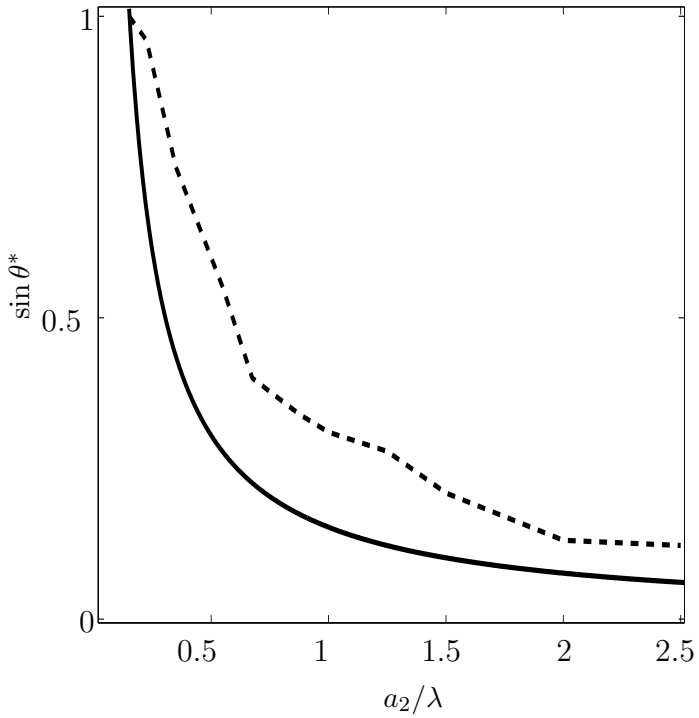

Figure 4.4: The value of the first zero ($\sin\theta^*$) as a function of crack length, $2a_2$ over the wavelength λ from equation (4.6) (solid line). To compare this with the data shown in Figure 6(c) in [30] we have approximated θ^* by 2×HWHM and plotted sin(2×HWHM) (dashed line).

approach. In addition, Figure 4.4 shows that using the formula to predict the crack size will be most sensitive when $a_2/\lambda < 1.5$ (as the gradient is largest here). This helps to predict which frequency should be used to best determine the crack size.

4.2.2 The effect of the array pitch on crack sizing

As discussed in Section 2.4, in practice a discrete, limited aperture, linear array is used and so the array in the model (equation (4.3)) is discretised where the element location is given by

$$x_s = \frac{\triangle x}{2}\left(2s - 1 - N\right), \tag{4.7}$$

where N is the number of elements in the array and the pitch, $\triangle x$, is constant and given by

$$\triangle x = \frac{l}{N-1}, \tag{4.8}$$

where l is the length of the array. The corresponding angle made by the array

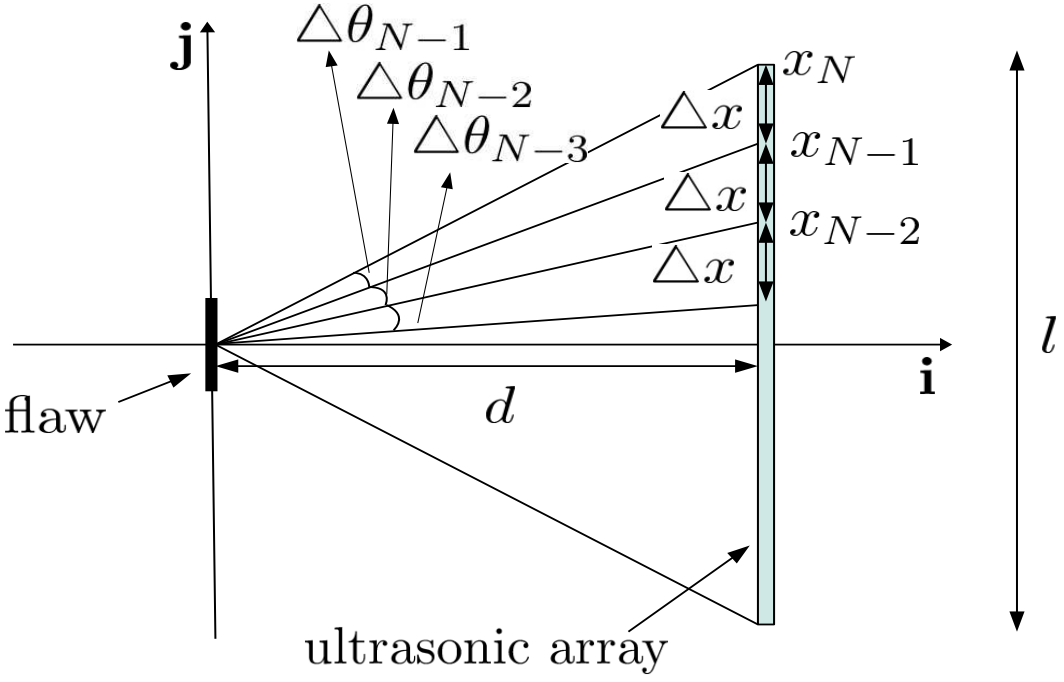

Figure 4.5: A schematic demonstrating the relationship between the array element location, x_s, equation (4.7) and the change in angle, $\triangle\theta_s$ equation (4.10), between two adjacent elements.

element s with the horizontal axis is given by

$$\theta_s = \tan^{-1}\left(\frac{x_s}{d}\right), \tag{4.9}$$

where d is the depth of the flaw, as shown in Figure 4.5. The pulse echo response can be plotted as a function of either θ_s or x_s. As a result of this discretisation, the maximum error that can occur in the approximation to the first zero, θ^*, in

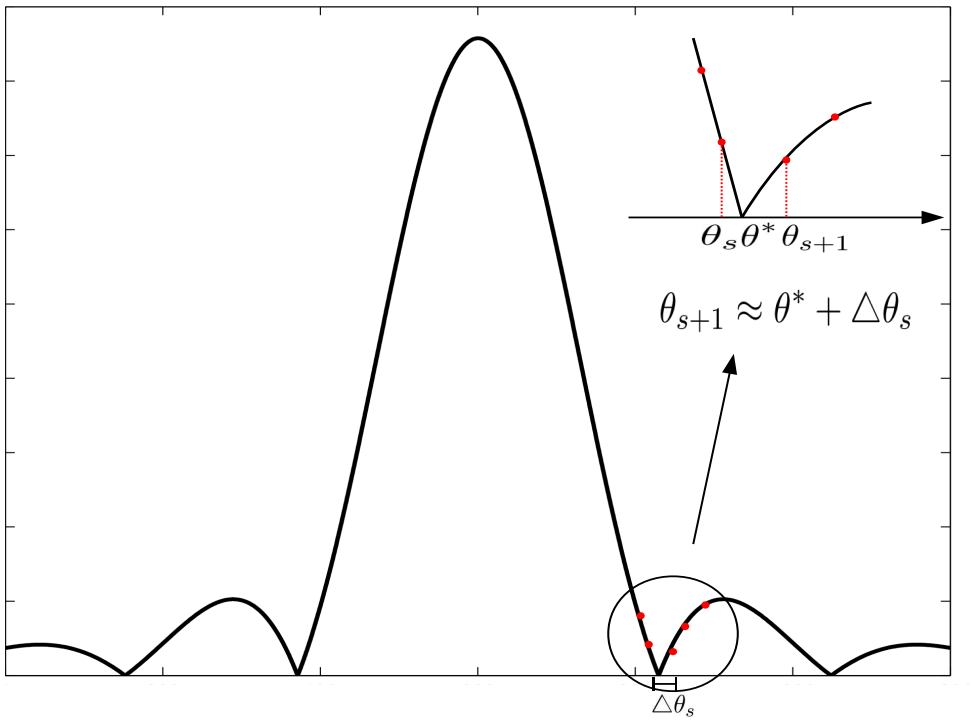

Figure 4.6: A schematic which shows the observed first minimum (θ_{s+1}) of the pulse echo plot from the discrete Kirchhoff model to be approximately the true minimum (θ^*) plus the change in angle $\triangle\theta_s$ between the adjacent array elements with the array angles θ_s and θ_{s+1}.

the pulse echo response is approximately the length of the increase in angle ($\triangle\theta_s$) between two discrete points s and $s+1$ surrounding the first zero, as demonstrated in Figure 4.6.

The angle between two adjacent array elements is a function of their position within the array since the spatial pitch, $\triangle x$, is constant; this is portrayed in Figure 4.5. However, the forthcoming analysis is simplified if the change in the angle $\triangle\theta$ is approximated by a constant. In order to approximate $\triangle\theta_s$ by a constant it is necessary to show that the difference between $\triangle\theta_s$ and $\triangle\theta_{s+b}$ for some b such that $s + b < N - 1$ (N is the total number of array elements) is small. The angle

between two adjacent elements, indexed by s and $s+1$, is given by

$$\begin{aligned}\triangle\theta_s &= \theta_{s+1} - \theta_s \\ &= \tan^{-1}\left(\frac{\triangle x(2s-N+1)}{2d}\right) - \tan^{-1}\left(\frac{\triangle x(2s-1-N)}{2d}\right)\end{aligned} \tag{4.10}$$

using equation (4.7) and so

$$\begin{aligned}\triangle\theta_s - \triangle\theta_{s+b} &= (\theta_{s+1} + \theta_{s+b}) - (\theta_s + \theta_{s+b+1}) \\ &= \left(\tan^{-1}\left(\frac{\triangle x(2s-N+1)}{2d}\right) + \tan^{-1}\left(\frac{\triangle x(2(s+b)-N+1))}{2d}\right)\right) \\ &- \left(\tan^{-1}\left(\frac{\triangle x(2s-1-N)}{2d}\right) + \tan^{-1}\left(\frac{\triangle x(2(s+b)-1-N)}{2d}\right)\right).\end{aligned} \tag{4.11}$$

Since $d \sim \mathcal{O}(10^{-2})$, $\triangle x \sim \mathcal{O}(10^{-3})$ and $2s - N \pm 1 \sim \mathcal{O}(10^2)$ (and likewise $2(s+b) - N \pm 1 \sim \mathcal{O}(10^2)$) then the arguments within the arctangent functions in equation (4.10) are of the order 10^{-1} for all s. Therefore, θ_s is small and of the order 10^{-2} and so the difference given by equation (4.11) is of the order 10^{-2}. It is assumed that the angle between each pair of adjacent array elements is equal and is taken to be the maximum in the set $\Theta = (\triangle\theta_s | s \in [1, N])$. This maximum is found by taking the derivative of equation (4.10), which is given by

$$\frac{\partial(\triangle\theta_s)}{\partial s} = \frac{4d^2}{4d^2 + (\triangle x)^2(2s+1-N)^2} - \frac{4d^2}{4d^2 + (\triangle x)^2(2s-1-N)^2}, \tag{4.12}$$

setting this equal to zero, and solving for s. This gives $s = N/2$ and so $\triangle\theta$ is approximated by

$$\triangle\theta^* = 2\tan^{-1}\left(\frac{2d}{\triangle x}\right). \tag{4.13}$$

The approximate perturbed value of a_2 given the error, $\triangle\theta^*$, in the measurement

of θ^* is therefore given by

$$a_2(\theta^* + \triangle\theta^*) = \frac{\lambda\beta}{4\pi \sin(\theta^* + \triangle\theta^*)} \tag{4.14}$$

where $\theta^* + \triangle\theta^*$ has been substituted into equation (4.5). In order to explicitly view the error between a_2 and $a_2(\theta^* + \triangle\theta^*)$ equation (4.14) is manipulated to extract a_2 (equation (4.5)) from $a_2(\theta^* + \triangle\theta^*)$, leaving an error term. The angle sum formula is applied to equation (4.14) to give

$$a_2(\theta^* + \triangle\theta^*) = \frac{\lambda\beta}{4\pi(\sin(\theta^*)\cos(\triangle\theta^*) + \cos(\theta^*)\sin(\triangle\theta^*))}. \tag{4.15}$$

Since $\triangle\theta^*$ is small the functions $\cos(\triangle\theta^*)$ and $\sin(\triangle\theta^*)$ within equation (4.15) are approximated using a Taylor series expansion to give

$$\begin{aligned} a_2(\theta^* + \triangle\theta^*) &= \frac{\lambda\beta}{4\pi(\sin(\theta^*)(1 - (\triangle\theta)^2/2 + ...) + \cos(\theta^*)(\triangle\theta - (\triangle\theta)^3/6 + ...))} \\ &= \frac{\lambda\beta}{4\pi \sin(\theta^*)(1 + \cot(\theta^*)(\triangle\theta - (\triangle\theta)^3/6 + ...) - (\triangle\theta)^2/2 + ...)}. \end{aligned} \tag{4.16}$$

and with

$$(\cot(\theta^*)(\triangle\theta - (\triangle\theta)^3/6 + ...) - (\triangle\theta)^2/2 + ...) << 1, \tag{4.17}$$

a further Taylor series expansion can be applied to equation (4.16) to give

$$\begin{aligned} a_2(\theta^* + \triangle\theta^*) &= \frac{\lambda\beta}{4\pi\sin(\theta^*)}(1 - (\cot(\theta^*)(\triangle\theta - (\triangle\theta)^3/6 + ...) - (\triangle\theta)^2/2 + ...)) \\ &= a_2(\theta^*) - \frac{\lambda\beta}{4\pi\sin(\theta^*)}(\cot(\theta^*)(\triangle\theta - (\triangle\theta)^3/6 + ...) - (\triangle\theta)^2/2 + ...) \\ &\approx a_2(\theta^*) - \frac{\lambda\beta\triangle\theta}{4\pi\sin(\theta^*)}\cot(\theta^*) \\ &= a_2(\theta^*) - \epsilon_1(\theta^*). \end{aligned} \tag{4.18}$$

where $\epsilon_1(\theta^*)$ is the approximate maximum error based on the analytic solution. The exact maximum error based on the analytical solution is simply given by

$$\epsilon_2(\theta^*) = |a_2 - a_2(\theta^* + \triangle\theta^*)|, \tag{4.19}$$

and can be used to assess the effect of the above approximations. A third error, ϵ_3, is obtained numerically by generating a pulse echo response from a scattering matrix using the Kirchhoff model (equation (4.1)), recording the location of the first minimum, θ_s^*, and then using equation (4.5) to recover the crack radius, $a_2(\theta_s^*)$, giving

$$\epsilon_3 = |a_2 - a_2(\theta_s^*)|. \tag{4.20}$$

These errors are functions of the crack radius over the wavelength a_2/λ and the pitch, $\triangle x$ (since $\triangle\theta^*$ is a function of the pitch, $\triangle x$). Figure 4.10 shows the actual maximum error, ϵ_2 (equation (4.19), red line), and the approximate maximum error, ϵ_1 (equation (4.18), green line) that can occur within the discrete model and the numerical error, ϵ_3 (equation (4.20), blue line), as a function of crack radius over wavelength, where the pitch length $\triangle x = 2$ mm is fixed. This shows that, for $a_2/\lambda < 2.5$ mm, the errors in the recovered wavelength within the model are

less than 0.5 mm, however as a_2/λ increases the error increases. As a_2/λ increases the first minimum becomes less sensitive to changes in a_2/λ because the width of the main lobe in the pulse echo response becomes very narrow, as demonstrated in Figure 4.7; this causes the increase in the error for these higher values of a_2/λ. These pulse echo response plots are not smooth due to the discretisation of the array within the Kirchhoff model, in these plots the number of elements used is 64 and the pitch is fixed at 2mm. It is clear in Figure 4.10 that for some of the higher frequencies (when a_2/λ is large) the numerical errors (blue line) are larger than the estimated maximum errors (red and green lines). This is a consequence of the discretisation of the array and is portrayed in Figure 4.8 where the red dot shows the location of the numerical minimum from the discretised model, the green dot shows the actual minimum and the distance between the red and blue dots indicates one pitch length ($\triangle\theta^*$) in the discrete model. Figure 4.8(a) shows the pulse echo plot when the frequency is equal to 6.83 MHz, here the discrete model has captured the approximate first minimum as the function is slightly non-monotonic where $0 < \theta_s < 0.2$. However, in Figure 4.8(b) the frequency is slightly increased to 6.92 MHz and now the function is monotonically decreasing until the second minimum of the Bessel function. This is due to the discretisation and as a result the error in the observed and actual location of the first minimum is greater than one pitch length. In what follows an upper bound is derived for when this phenomenon first occurs for any given pitch length. The upper bound relates the maximum pitch length which is allowed for a given value of a_2/λ (and vice versa) before these larger errors occur. In Figure 4.10 the vertical, red, dashed line shows the limit in a_2/λ for the fixed pitch, $\triangle x = 2$ mm, at $a_2/\lambda = 2.5$ which is taken from Figure 4.12 and is derived below. Figure 4.11 shows the actual maximum error, ϵ_2 (equation (4.19), red line), and the approximate maximum

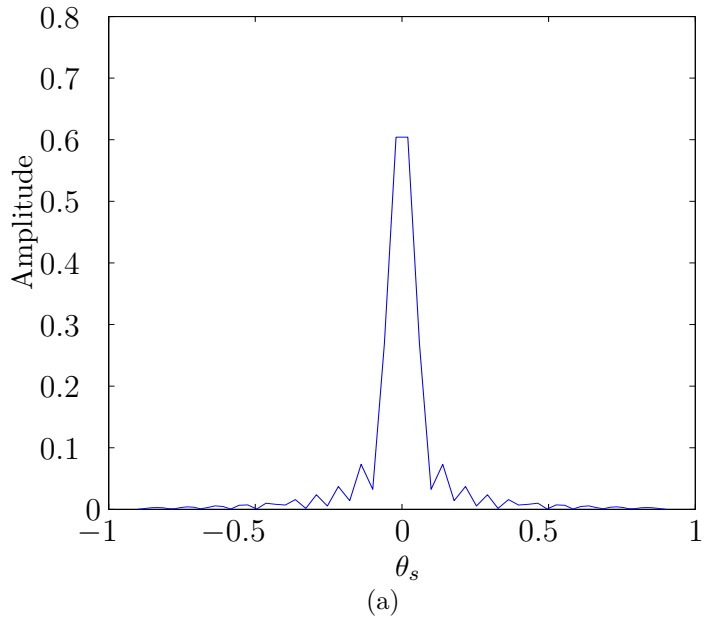

(a)

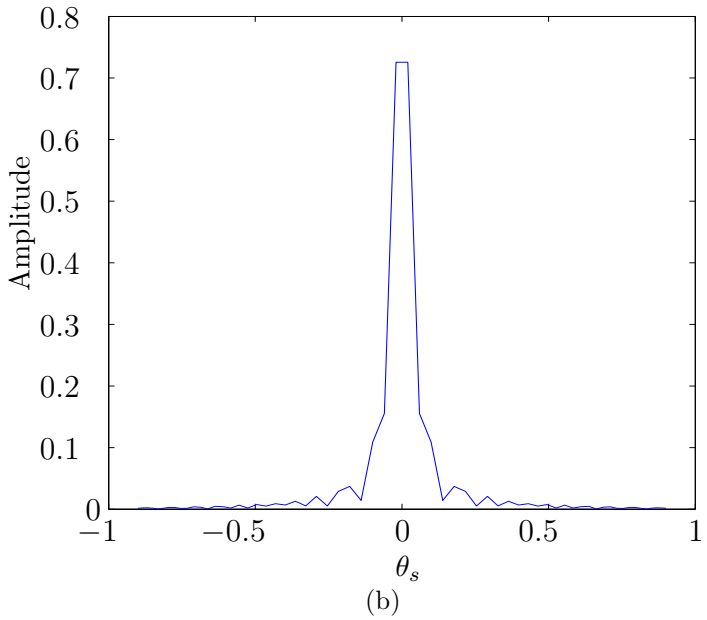

(b)

Figure 4.7: The pulse echo response for a_2/λ equal to (a) 3.3 and (b) 3.8. This shows that for large a_2/λ there is very little change in the width of the main lobe in the pulse echo response and therefore little change in the location of the first minimum. The array in the Kirchhoff model is discretised to include only 64 elements and as a result the pulse echo response shown in these figures is not smooth.

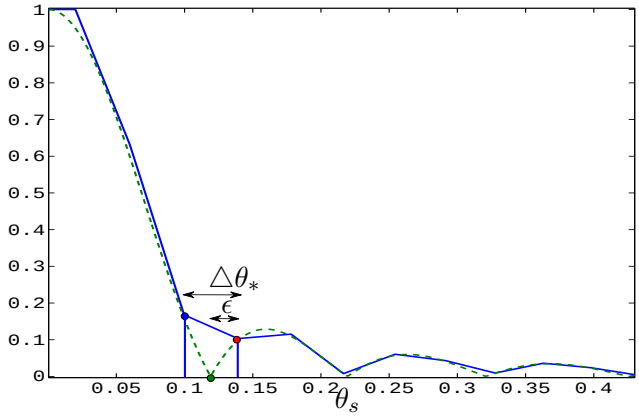

(a)

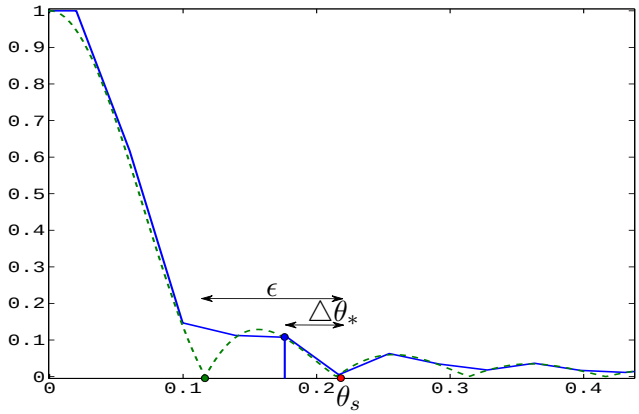

(b)

Figure 4.8: These figures explain why the numerical errors in Figure 4.10 are larger than the approximate errors in some instances. In each figure the red dot gives the location of the first numerical minimum in the discrete model (blue, solid line), the green dot shows the actual minimum in the continuous model (green, dashed line) and the distance between the blue dot and the red dot shows one pitch length (in terms of the change in the array angle, $\triangle\theta_*$). In (a) the frequency is 6.83 MHz and the pulse echo response is slightly non-monotonic between the first and second minima and so the error, ϵ, is less than a single pitch length $\triangle\theta_*$. However, in (b), the pulse echo response is monotonic until the second minima and therefore $\epsilon > \triangle\theta_*$ (that is, the error is greater than a single pitch).

error, ϵ_1 (equation (4.18), green line) that can occur within the discrete model and the numerical error, ϵ_3 (equation (4.20), blue line) as a function element pitch. Here the number of elements is fixed at $N = 64$, and so as the pitch increases the length of the array increases. This figure shows that the analytical maximum errors, ϵ_1 and ϵ_2, remain relatively small as the pitch increases. Again in Figure

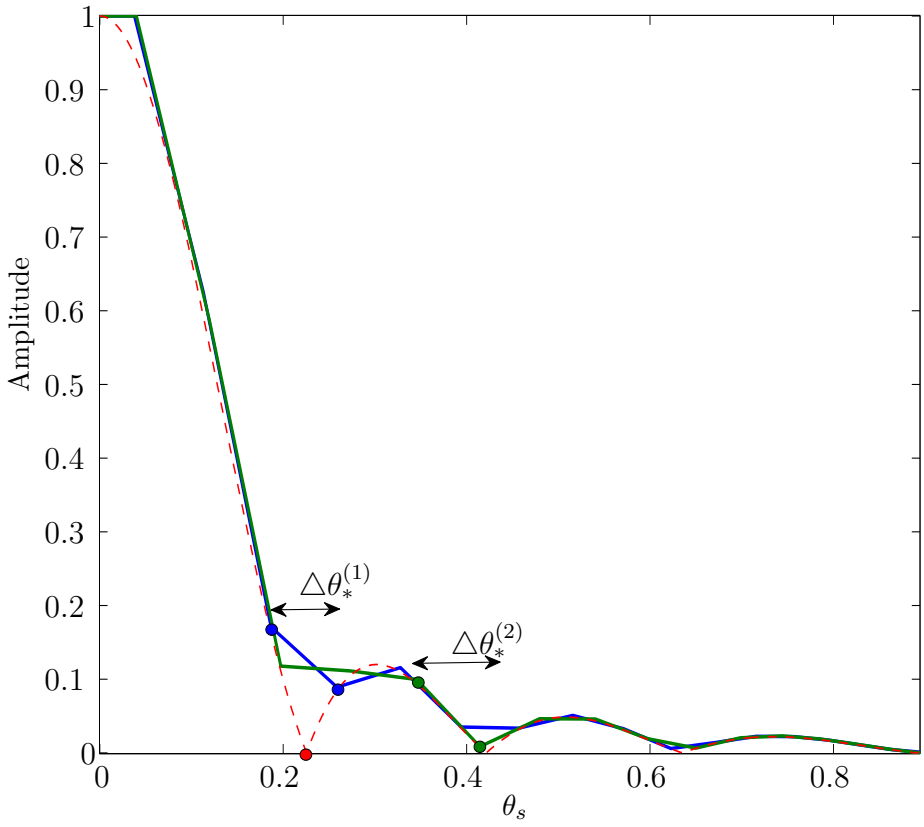

Figure 4.9: This figure demonstrates that for large pitch (green line) length the first minimum in the pulse echo response is taken to be the second minimum in the analytical model, thus resulting in an error larger than one pitch length. The red line shows the continuous pulse echo response and the actual first minimum. The blue line shows the discrete pulse echo response when $\triangle\theta_*^{(1)} = 3.8$ mm and here the error between the minimum in the continuous model (red dot) and the discrete model (second blue dot) is less than $\triangle\theta_*^{(1)}$. The green line shows the pulse echo response where $\triangle\theta_*^{(2)} = 4$ mm. Here the error between the red dot and the approximate minimum (second green dot) is greater than $\triangle\theta_*^{(2)}$.

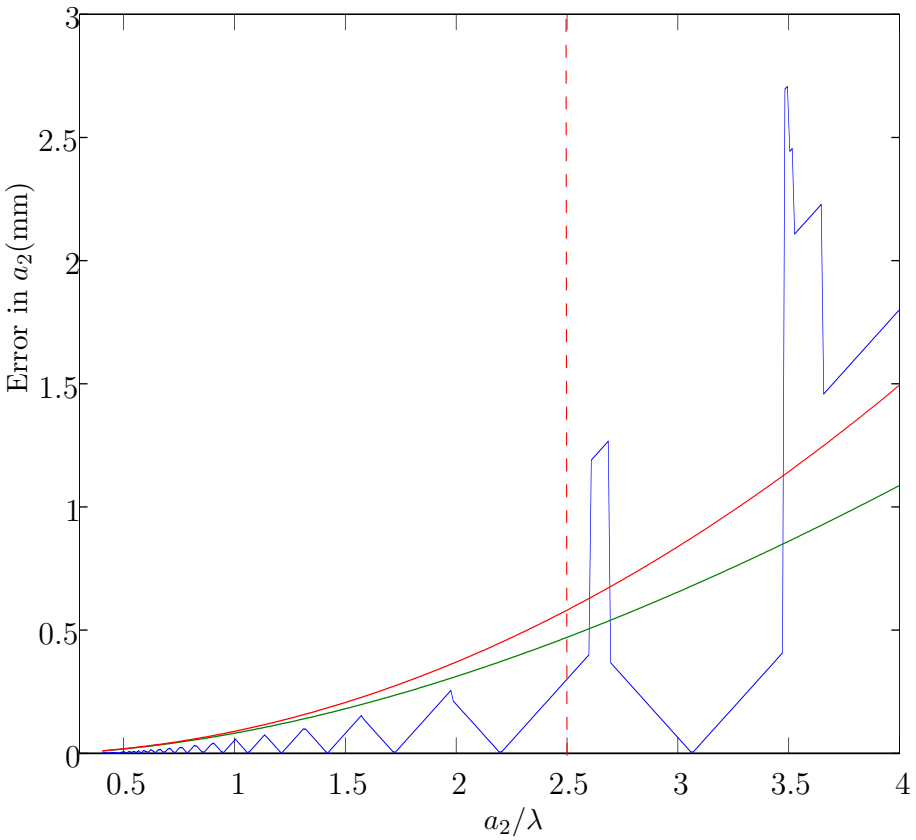

Figure 4.10: The errors due to the discretisation of the array within the Kirchhoff model as a function of crack radius over wavelength, a_2/λ. The red line shows the actual error given by equation (4.19), the green line shows the approximation to this error given by equation (4.18) and the blue line shows the numerical error given by equation (4.20). Here the pitch length is fixed at $\triangle x = 2$ mm. The vertical red dashed line indicates the limit on a_2/λ, for this fixed pitch length, for recovering the first zero of the pulse echo response. This limit is found numerically and is shown in Figure 4.15.

4.11 it is clear that as the pitch increases there are occasions where the numerical error is larger than the approximated maximum error. A similar phenomenon is occurring here as that in Figure 4.10 where a_2/λ (frequency) was varied. Figure 4.9 shows the continuous pulse echo (red dashed line) response plotted with the discrete pulse echo response when the pitch is 3.8 mm (blue line) and 4 mm (green line). When the pitch is equal to 4 mm the pulse echo response is monotonically

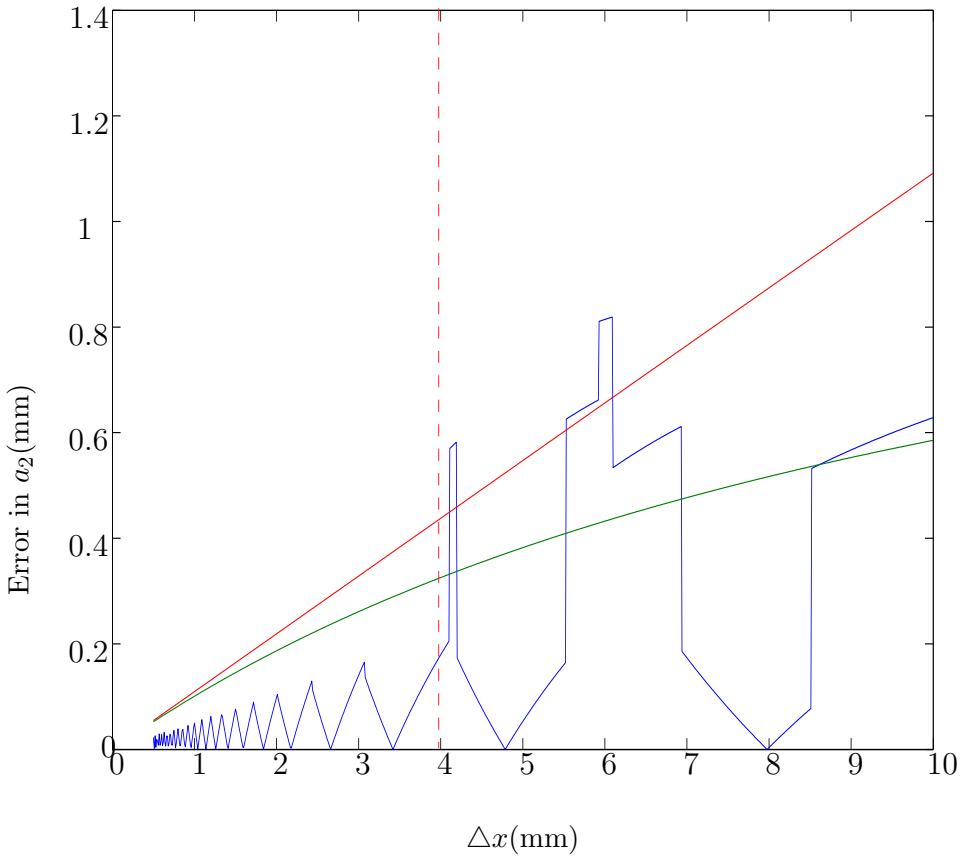

Figure 4.11: The errors due to the discretisation of the array within the Kirchhoff model as a function of the pitch, $\triangle x$ mm. The red line shows the actual error given by equation (4.19), the green line shows the approximation to this error given by equation (4.18) and the blue line shows the numerical error given by equation (4.20). In this example the crack radius over wavelength is fixed with $a_2/\lambda = 1.036$, the number of elements, N, is 64, and the depth of the crack is d. The vertical red dashed line indicates the limit on $\triangle x$, for $a_2/\lambda = 1.036$ fixed, for recovering the first zero of the pulse echo response. This limit is found numerically and is shown in Figure 4.15.

decreasing until the second minimum in the Bessel function, as a result the error in the observed first minimum is larger than one pitch length.

For each fixed crack radius over wavelength, a_2/λ, an approximate upper bound on the pitch, $\triangle x$, can be derived to ensure that the error in θ^*, due to the discretisation, cannot exceed one pitch length ($\triangle x$). This approximation is found by

considering a horizontal line through the first two lobes in the pulse echo response as demonstrated in Figure 4.12 by the dashed line at height p, where θ_1, θ_2 and θ_3 indicate the roots of $A(\theta) = p$. The limit on the pitch ($\triangle x$) for a given value of a_2/λ is taken to be $\triangle x^* = L_1$ when the value of p is such that $L_1 = L_2$. This is a

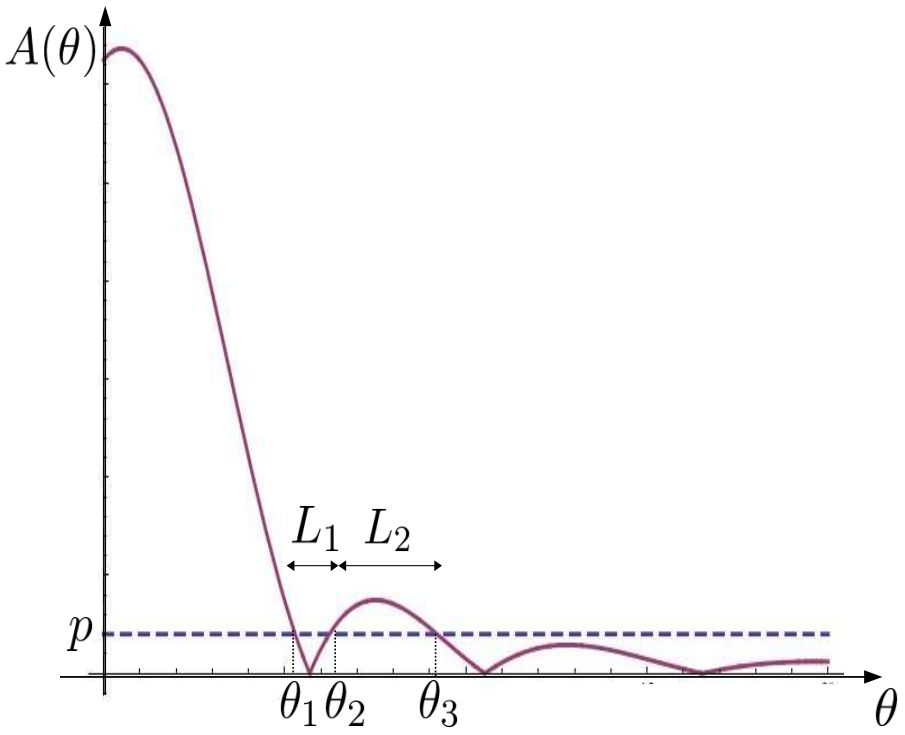

Figure 4.12: A schematic which shows a horizontal line (blue, dashed line), which cuts the vertical axis at $A(\theta) = p$, and then goes through the first two lobes in the pulse echo response $A(\theta)$ (red, solid line), given by equation (4.3). The first three roots of $A(\theta) = p$ are labelled as θ_1, θ_2 and θ_3 and the distances between each of these roots are given by L_1 and L_2.

reasonable approximation to a limit as it is not possible for the discretised pulse echo response to be monotonically decreasing until the second minimum when $\triangle x < \triangle x^*$. However, for $\triangle x > \triangle x^*$, then it is possible as demonstrated in Figure 4.13 (the blue dashed line). The limit $\triangle x^*$ is calculated by numerically finding

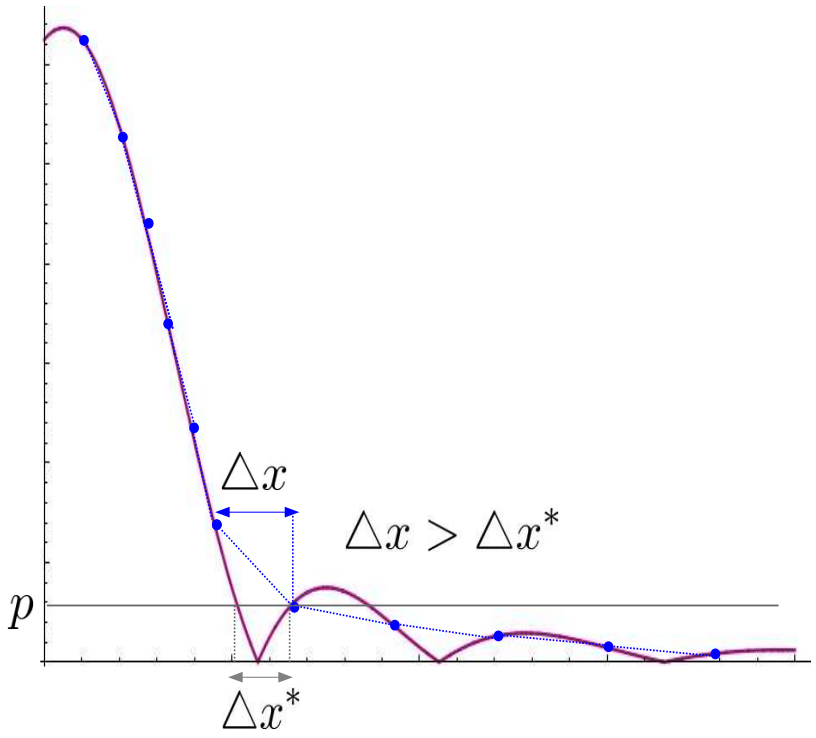

Figure 4.13: A schematic which demonstrates that for a pitch length, $\triangle x$, larger than the approximation to the upper bound on the pitch, $\triangle x^*$, it is possible for the discrete pulse echo response from the model to be monotonically decreasing beyond the first minimum. Therefore large errors in the approximation to the first minimum, θ^*, result and consequently the recovered crack radius, a_2, will be incorrect.

the three roots, θ_1, θ_2 and θ_3, of

$$A(\theta_s) = \frac{a_3|\cot\theta_s|(L + 2\mu(1 + 2\cos(2\theta_s))}{2\rho c_1^2} J_1\Big(\frac{4\pi a_2}{\lambda}|\sin\theta_s|\Big) = p \tag{4.21}$$

which are then used to calculate L_1 and L_2 via

$$L_1(a_2/\lambda, \triangle x, p) = \theta_2 - \theta_1 \qquad \text{and} \qquad L_2(a_2/\lambda, \triangle x, p) = \theta_3 - \theta_2. \tag{4.22}$$

The difference between these is given by

$$d(a_2/\lambda, \triangle x, p) = L_1(a_2/\lambda, \triangle x, p) - L_2(a_2/\lambda, \triangle x, p) \tag{4.23}$$

which are all functions of crack radius over wavelength, a_2/λ, the pitch, $\triangle x$, and the value of p. The dependencies of L_1 and L_2 on p are shown in Figure 4.14 (where $a_2/\lambda = 1$). The point of intersection of L_1 and L_2 occurs when $d = 0$ and hence the length of L_1 (and L_2) at this point is the upper bound on the pitch, $\triangle x^*$, for a given a_2/λ. There is a one-one relationship between a_2/λ and this upperbound on pitch, $\triangle x^*$, as shown in Figure 4.15.

In this section, a single frequency crack sizing method was presented. In addition, the errors, due to the discretisation of the model were approximated and an upper bound was approximated for the value of a_2/λ that can be recovered for a given pitch length. In the next section, a multi-frequency extension of this method is presented.

4.2.3 Multi-frequency crack sizing method

The previous section relied on the use of the pulse-echo response of the scattering matrix at a particular frequency. This of course discards the information contained

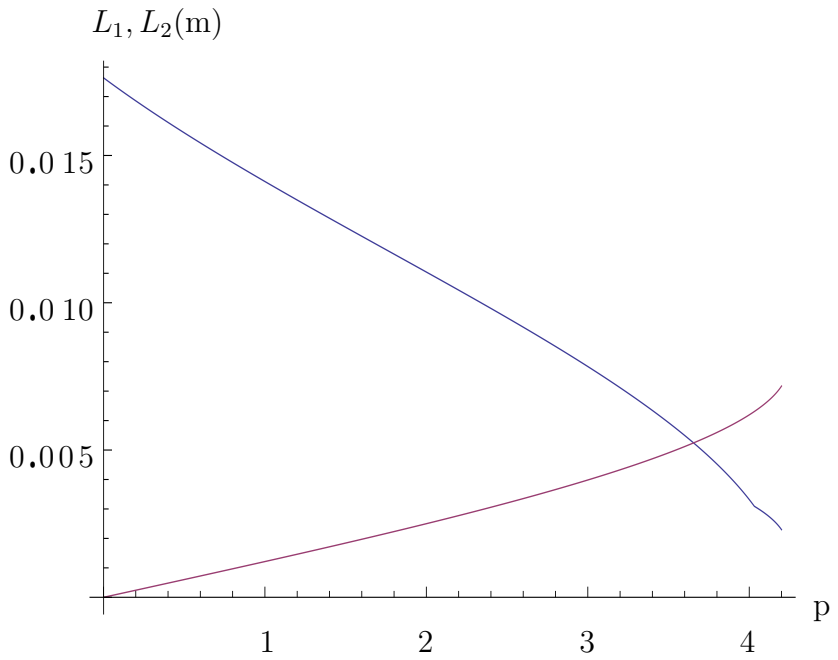

Figure 4.14: This figure plots L_1 (red line) and L_2 (blue line), equation (4.22), which are the distances between the roots θ_1, θ_2 and θ_3 where $A(\theta) = p$ as demonstrated in Figure 4.12. The crack length over radius is fixed, $a_2/\lambda = 1$, as p is varied. The y-coordinate associated with the point of intersection gives the upper bound on the pitch, $\triangle x^*$, that can be used in order to use the approximation on the error in the crack sizing method due to the array discretisation.

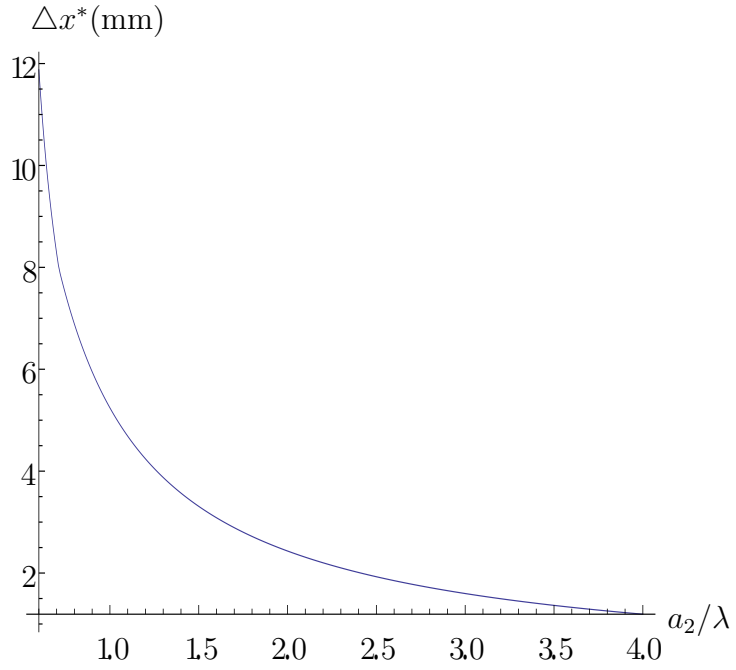

Figure 4.15: This plot shows the upper limit on the pitch $\triangle x^*$ in terms of a_2/λ, such that the approximation given by equation (4.18) is valid.

at other frequencies and so it is natural to explore the potential improvements in the methodology when the responses at a range of frequencies are brought to bear on the problem. The pulse echo response was extracted from a set of scattering matrices across a range of frequencies to create a 3D response (where the dimensions are frequency (f), array aperture angle (θ_s) and scattering amplitude ($A(\theta_s)$). An example of this 3D response is shown in Figure 4.16(a) where the amplitude of the pulse echo response is represented by a logarithmic colour scale. If a slice of this plot were taken at a single frequency the plot would be akin to those shown in Figures 4.1(i-l). The multi-frequency method is derived by approximating the first minimum (the first yellow curve in Figure 4.16(a) going from left to right) across a range of frequencies to produces a contour which relates frequency, f_m, to the first minimum within the pulse echo response, $\theta_s^{(m)}$. From

equation (4.6) these contours are given by

$$\theta_s^{(m)}(a_2) = \pm \sin^{-1}\left(\frac{\beta c}{4\pi a_2 f_m}\right) \tag{4.24}$$

where $m = 1, ..., N$. Figure 4.16(b) (blue line) displays an example of these contours where the crack radius (a_2) is 2.5 mm, the pitch ($\triangle x$) is 2 mm, the depth of the flaw is 50 mm and the number of elements is 64. A minimisation technique is then adopted to tackle the inverse problem of recovering the crack size from experimental, or simulated data. This is based on a comparison between this data and the contours produced using the Kirchhoff model. Let the contours which are extracted from the scattering matrices from simulated (or experimental) data be called $P_s^{(m)}$. Then the l^2 norm of the difference between $P_s^{(m)}$ and $\theta_s^{(m)}(a_2)$ is

$$S(a_2) = ||\theta_s^{(m)}(a_2) - P_s^{(m)}||_2. \tag{4.25}$$

This is minimised over the crack radius, a_2, to give

$$\bar{a}_2 = \min_{a_2} S(a_2) \tag{4.26}$$

where $\bar{a_2}$ is the estimated crack radius from the experimental or simulated data. As in the single frequency case, let the approximate maximum error in $\theta_s^{(m)}$ when the discrete version of the model is used (as outlined in Section 4.2.1) be $\triangle\theta$. Including this error in equation (4.24) gives

$$\theta_s(a_2) = \pm \sin^{-1}\left(\frac{\beta c}{4\pi a_2 f_s}\right) - \triangle\theta. \tag{4.27}$$

Figure 4.16(b) compares the plot including this error (green line) to the true contour (blue line) and shows that for these parameters the error is very small

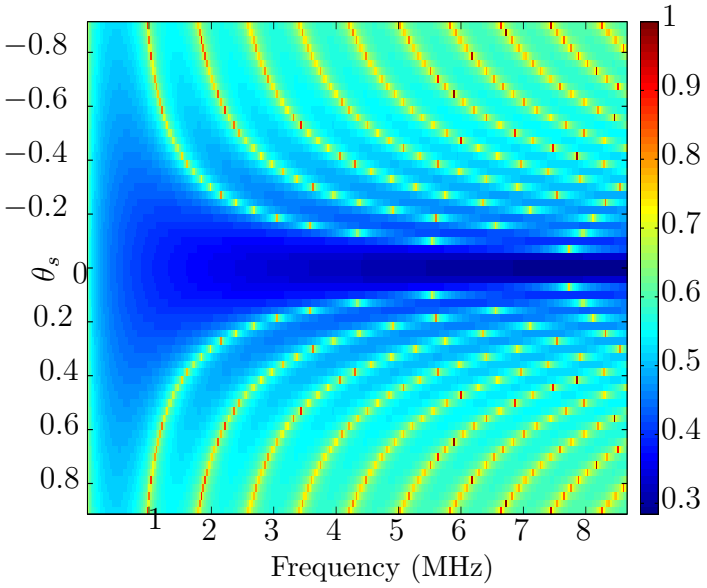

(a)

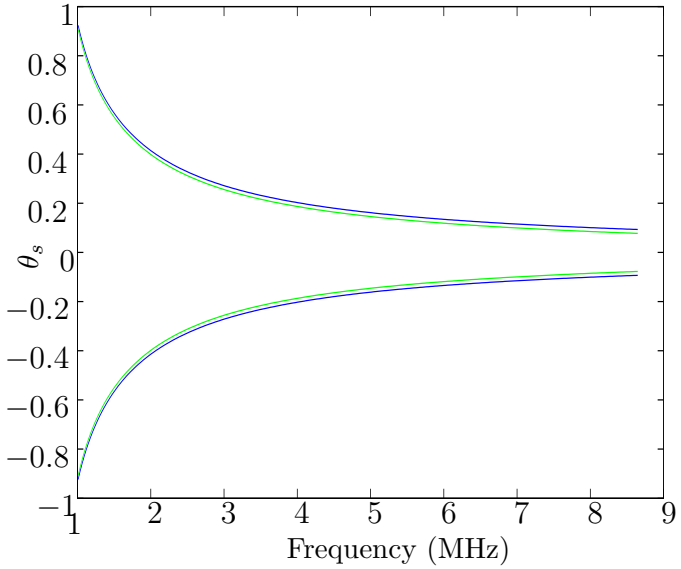

(b)

Figure 4.16: A multifrequency plot of the pulse echo response from the scattering matrices. The receiving array angle, θ_s lies along the vertical axis. The blue line in (b) is given by equation (4.24), which relates the first minimum in the pulse echo plot $\theta_s^{(m)}$ to frequency f_m. The green line shows the contour given by equation (4.27) when the maximum error (one pitch length) is included in equation (4.24). In these examples the crack radius (a_2) is 2.5 mm, the pitch ($\triangle x$) is 2 mm, the wavespeed is 6600m/s^{-1}, the depth of the flaw is 50 mm and the number of elements is 64.

between these two curves. At a single frequency the error between these two curves

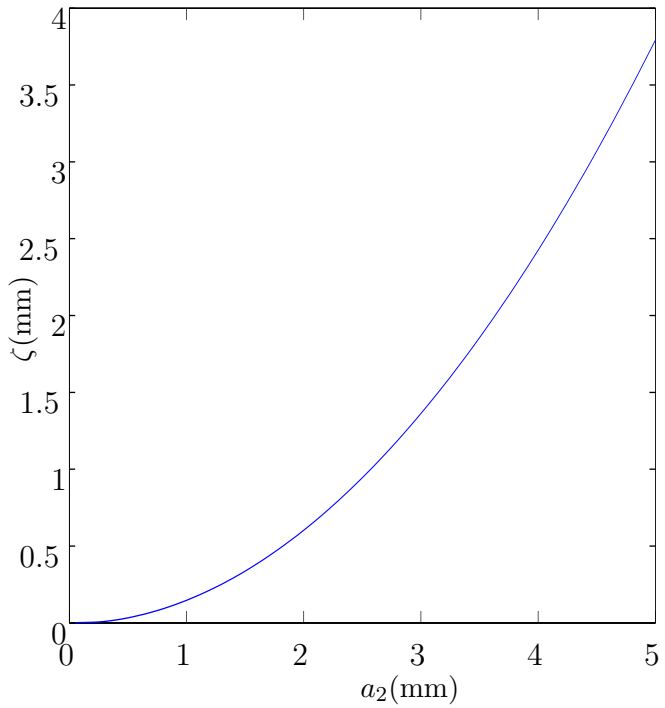

Figure 4.17: This figure shows the plot of the approximate error (given by equation (4.28)) in the recovered crack radius, a_2, due to the discretisation of the ultrasound array. Here the number of elements ($N = 64$), the pitch ($\triangle x = 2$ mm), and the depth of the flaw ($d = 50$ mm) are all fixed. For this plot the lower limit in the summation in equation (4.28), f_1, is 1 MHz and the upper limit, f_n, is 8.6 MHz.

was given in the previous section by equation (4.18). Over a range of frequencies the error can then be approximated by taking an average of these errors, that is

$$\zeta(a_2) = \frac{1}{n} \sum_{f=f_1}^{f_n} \frac{c\beta \triangle\theta \cot\theta^*}{4\pi f \sin\theta^*}, \tag{4.28}$$

where f_1 and f_n are the lower and upper bound in the frequencies sampled and θ^* is given by equation (4.6). Figure 4.17 plots this error as the radius of the crack, a_2, is varied and shows that for a_2 less than 2.5 mm the error due to discretisation is less than 1 mm.

4.2.4 Applying the single frequency crack-sizing method to data from a homogeneous medium

In this subsection, the single frequency method outlined in Section 4.2.1 is applied to the finite element simulated FMC data, described in the Chapter 2, Section 2.3.1, from a homogeneous medium which contains a 5 mm long crack inclusion; the parameters of which are given by Appendix C, Table C.1. A scattering matrix at a frequency of 2.6 MHz (which gives $a_2/\lambda = 1.02$) was extracted from the finite element simulated data and is shown in Figure 4.18(a). This is comparable with the analogous scattering matrix from the Kirchhoff model which is shown in Figure 4.18(b) and was generated using the same system parameters as the finite element simulation. Figure 4.19 shows the normalised pulse echo response from a scattering matrix associated with a frequency of 2.6 MHz ($a_2/\lambda = 1.02$); the blue curve is the response from the simulated data and the green curve is the analogous response from the Kirchhoff model. As can be seen there is a reasonable match up between the two responses. The first minimum in the pulse echo response from the simulated data are not symmetric about zero and so an average of the position of these two minima is taken for θ^* and used in equation (4.5) to give a predicted crack radius of 2.9mm. This gives an error of 0.4mm in crack radius which is not surprising considering the differing assumptions within the Kirchhoff model and the finite element simulation. For example, the crack is modelled as a slim, rectangular void within the finite element simulation. However, within the Kirchhoff the model the crack is modelled as an infinitely thin ellipsoid. In addition, there is mode conversion within the simulation whereas only a pressure wave is included within the Kirchhoff model. Also, the data from the finite element simulation is in the time domain and a discrete Fourier transform is used to take this data into the frequency domain and so there are computational errors due

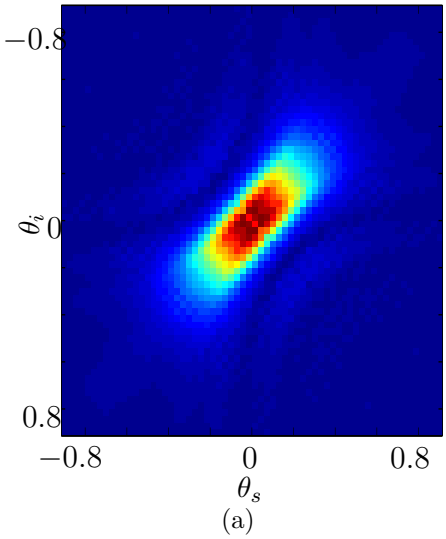

(a)

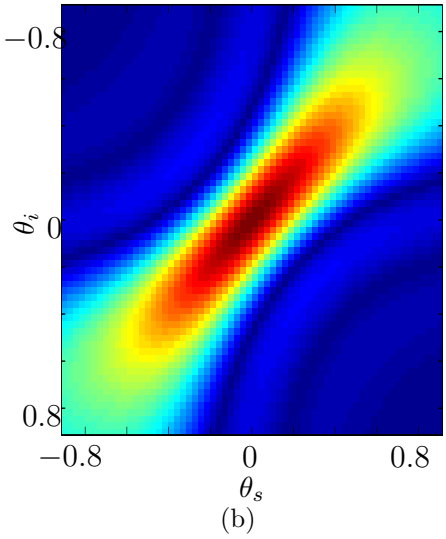

(b)

Figure 4.18: A scattering matrix extracted from the finite element simulated data (see Appendix C Table C.1) from the homogeneous medium containing a 2.5 mm radius crack is shown in (a) where the frequency is 2.6 MHz ($a_2/\lambda = 1.02$). The analogous scattering matrix from the Kirchhoff model, generated using equation (2.7), is shown in (b).

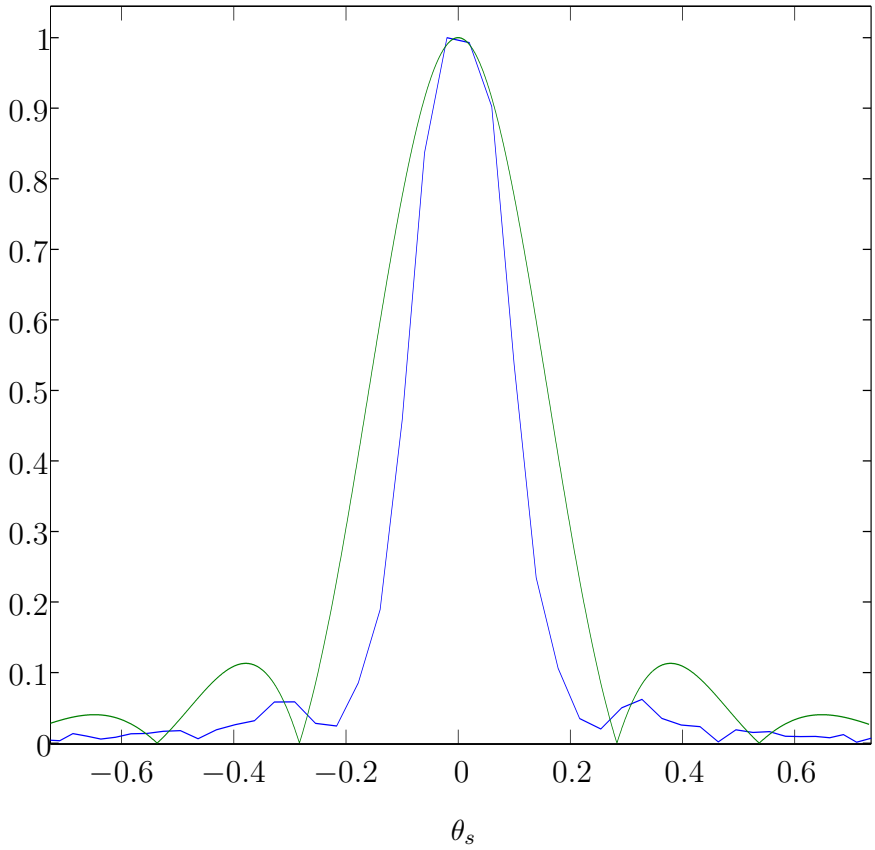

Figure 4.19: A comparison between the pulse echo response from a scattering matrix extracted from the finite element simulated data from a homogeneous medium (blue line) containing a 5 mm long crack (as described in Section 2.3.1, the system parameters are given in Appendix C Table C.1) and the analogous response generated using the Kirchhoff model (green line), equation (4.3). The signals have been normalised here with respect to the maximum scattering amplitude. The frequency used here is 2.6 MHz (and hence $a_2/\lambda = 1.02$).

to this discrete process. It is also important to note that there is a bandwidth constraint within the frequency domain on the data from the simulation as the driving function has not been deconvolved from the data. Finally, the Kirchhoff model is a high frequency approximation ($a_2/\lambda \gg 1$) and here the interest is in cracks that are commensurate with the wavelength or smaller.

4.2.4.1 Using all data points from the pulse echo repsonse to size cracks

The crack sizing method described in section 4.2.1 uses a single point of comparison between the model and the simulated data. In this section a minimisation approach is derived which is based on the difference between the pulse echo response from the model and the simulated data, where

$$S(a_2, f) = \sum_m |F(\theta_s^{(m)}, f) - A(\theta_s^{(m)}, a_2, f)|, \tag{4.29}$$

where $F(\theta_s^{(m)}, f)$ is the pulse echo response from the simulated data and $A(\theta_s^{(m)}, a_2, f)$ is that from the model given by equation (4.3). The method searches for the value of a_2 (the crack radius) which minimises $S(a_2, f)$ at a fixed frequency f. This method is applied to the pulse echo response extracted from the simulated data for a frequency of 2.6 MHz, as shown by the blue curve in Figure 4.19. When this method is adopted, the recovered crack radius is 4 mm, which gives an error of 1.5 mm. This is actually 1.1 mm larger than that obtained when the method using the first minimum in the pulse-echo response was applied to the data.

4.2.5 Applying the multi frequency crack-sizing method to data from a heterogeneous medium

The crack sizing method derived in Section 4.2.3 is applied here to the data from the simulated steel weld as described in Chapter 2 Section 2.3.1 and shown in Figure 2.4 (see Appendix C Table C.1 for the simulation parameters). An example of a typical scattering matrix at a frequency of 1.4 MHz ($a_2/\lambda = 0.56$) was extracted from this data and is shown in Figure 4.20 (a). It is clear that this scattering matrix is very noisy in comparison with that from the homogeneous medium (as shown in Figure 4.18(a)). The resulting pulse-echo response from the

scattering matrix is shown in Figure 4.20(b) and there is clearly no main lobe in this pulse echo response nor any clear first minimum. A lower ratio of crack radius over wavelength (a_2/λ) is chosen for demonstration here because the grain structure resonates at the higher frequencies. The scattered signal from the crack is distorted as a result of the heterogeneous nature of the host material and the complex path the wave energy traverses through the grain structure to and from the transducer array. In this subsection, the signals within the frequency domain scattering matrices are convolved in order to reduce the noise. This approach is inspired by the Coherent Interferometry work by Borcea et al. [41]. Once the level of noise is reduced in the scattering matrices the method outlined in Section 4.2.3 is applied.

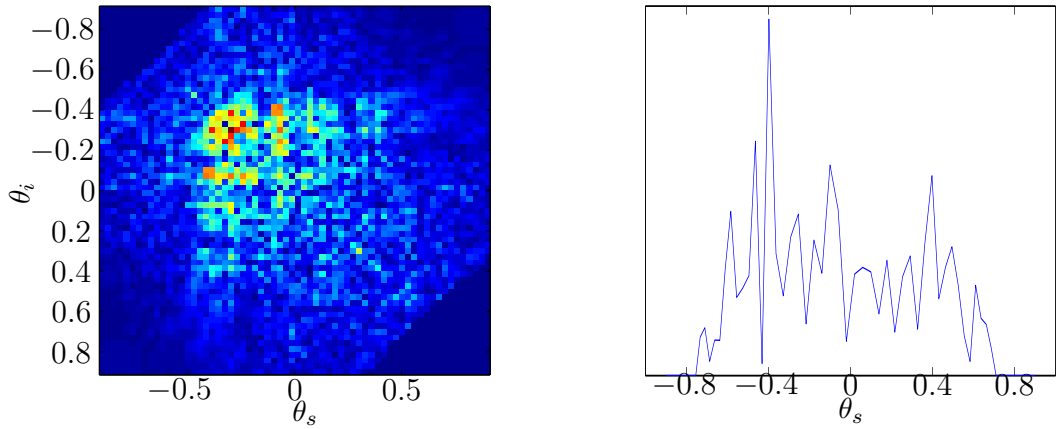

Figure 4.20: This figure demonstrates (a) a scattering matrix and (b) the associated pulse echo response extracted from the finite element simulated data of a 5mm long crack in a heterogeneous host material, where the frequency is 1.4 MHz and the other system parameters are given in Appendix C Table C.1.

4.2.5.1 Noise reduction in the scattering matrices

In a heterogeneous material, the scattered signals received by the array transducer are comprised of two types of scattering; coherent and incoherent. The coherent

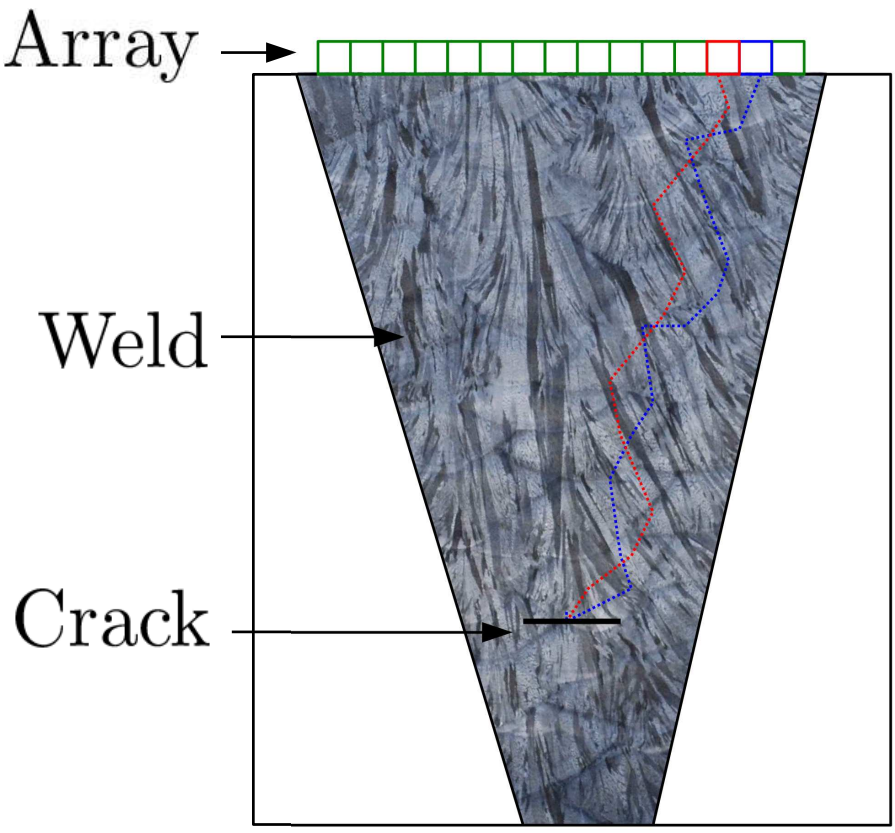

Figure 4.21: This figure demonstrates the tortuous path that the transmitted wave from two neighbouring (blue and red dashed lines) array elements could take from the ultrasonic array elements, through the weld microstructure to the flaw.

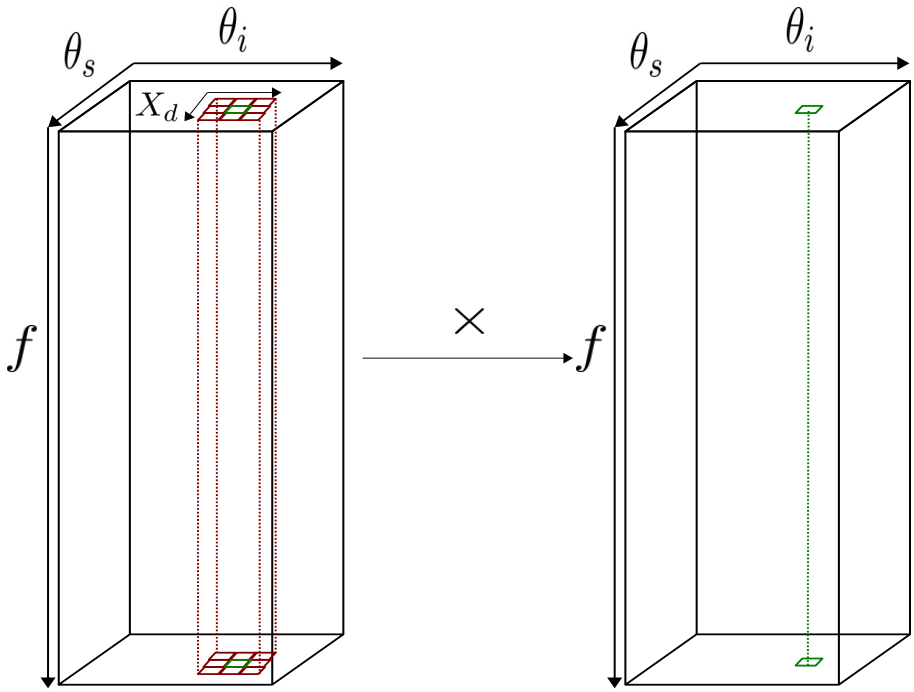

Figure 4.22: A schematic demonstrating the signals in the scattering matrices that are convolved. The signal within the green element on the left is multiplied with each of the signals within the red elements surrounding it. Once multiplied together these new amplitudes are then summed (equation (4.31)) to produce one new signal as shown by the green element in the matrix on the right.

contribution is due to the crack and the incoherent contribution is due to the heterogeneities within the host material. The coherent scattered signal will have a similar signature for each transmit-receive pair and its neighbours, this is not true for the incoherent contribution of each signal. Figure 4.21 shows a schematic which demonstrates the tortuous path that two neighbouring signals take. Convolving neighbouring signals will emphasise the coherent response and the incoherent contributions should be reduced [41]. A superscript is introduced to distinguish the transmitting array aperture angle, $\theta_i^{(m)}$, from the receiving array aperture angle, $\theta_s^{(n)}$. For a given pair of transmit ($\theta_i^{(m)}$) and receive ($\theta_s^{(n)}$) transducer array elements, the set of their neighbouring elements is denoted by

$$N(\theta_i^{(m)}, \theta_s^{(n)}) = \{\{\theta_i^{(k)}, \theta_s^{(l)}\} : k \in (m-1, m+1), l \in (n-1, n+1)\}. \tag{4.30}$$

The convolution of the elements of $F_{mn}(f_j)$ (where $F_{mn}(f_j)$ is the scattering amplitude received by array elememt n when transmitting on array element m from the simulated data) is then given by

$$G(\theta_i^{(m)}, \theta_s^{(n)}, f_j) = \sum_{\{\theta_s^{(l)}, \theta_i^{(k)}\} \in N(\theta_i^{(m)}, \theta_s^{(n)})} F(\theta_i^{(k)}, \theta_s^{(l)}, f_j) F(\theta_i^{(m)}, \theta_s^{(n)}, f_j) \tag{4.31}$$

with $j \in (1, ..., N_f)$ where N_f is the total number of frequency indices. Figure 4.22 demonstrates the convolution process within the scattering matrices. Once the signals have been convolved the pulse echo response is extracted from the scattering matrix

$$P(\theta_s^{(m)}, f_j) = G(\theta_i^{(m)}, \theta_s^{(m)}, f_j). \tag{4.32}$$

The matrix given by $P(\theta_s^{(m)}, f_j)$ can then be compared to the corresponding matrix produced using the Kirchhoff model given by equation (4.3) ($A(\theta_s^{(m)}, f_j, a_2)$) via

the contours which mark the first minimum in the pulse echo response as frequency is varied, as demonstrated in Figure 4.16(b). The contours from the model given by equation (4.24) plot the first *zero* as frequency is varied. However, this is an approximation to the first minimum, as within both the model and the simulated data there is some energy received by other array elements. Therefore, the contours from the discrete Kirchhoff model (and the simulated data) are extracted numerically by identifying the frequency (f_m) at which the amplitudes of A (and P) first fall below a prescribed decibel level (τ) for each array element scattering angle $\theta_s^{(m)}$, as demonstrated in Figure 4.23. That is,

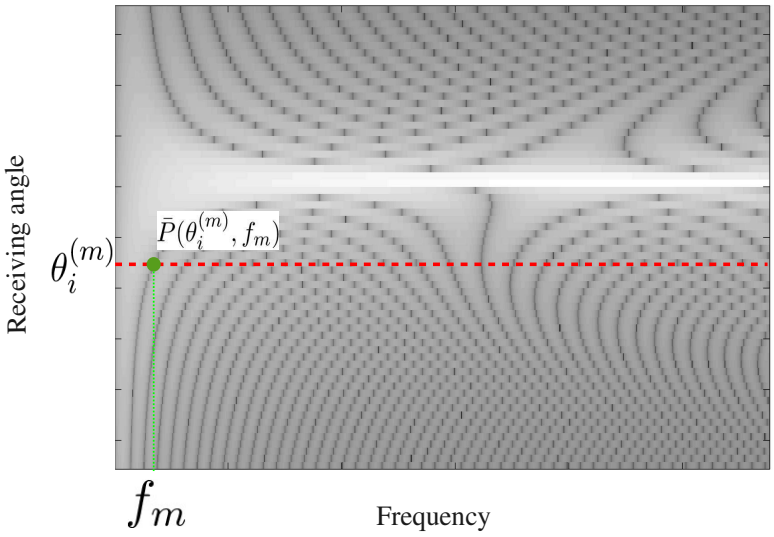

Figure 4.23: This schematic demonstrates the relationship between the receiving angle on the array, θ_i and frequency, f as given by equation (4.33). For each receiving angle, $\theta_i^{(m)}$, (shown via the red dashed line) the function $\bar{P}$ (green circle) is taken to be the frequency, f_m, (green dotted line) which first drops below the prescribed threshold τ (which is close to zero).

$$\bar{P}(\theta_s^{(m)}) = f_m \tag{4.33}$$

where

$$f_m = \inf_{f_j} P(\theta_s^{(m)}, f_j) < \tau \tag{4.34}$$

and τ is taken to be the minimum amplitude within the scattering matrix (that is -24dB). This establishes a numerical relationship between $\theta_s^{(m)}$ and f_m akin to that given by equation (4.24). A similar relationship can also be derived from the Kirchhoff model to produce $\bar{A}(\theta_s^{(m)}, f_m, a_2)$. So, by defining

$$S(a_2) = ||\bar{A}(\theta_s^{(m)}, f_m, a_2) - \bar{P}(\theta_s^{(m)}, f_m)||_2 \tag{4.35}$$

then the recovered crack radius from simulated or experimental data is given by

$$\tilde{a}_2 = \min_{a_2} S(a_2). \tag{4.36}$$

4.2.5.2 Results from sizing cracks in heterogeneous media

The noise reduction technique outlined in the previous subsection is applied to the finite element simulation of a steel weld with a 5 mm long crack inclusion. Once the noise has been reduced within the scattering matrices, using the convolution technique presented in Section 4.2.5.1, the multi-frequency crack sizing technique presented in Section 4.2.3 is applied to the response matrix to extract the crack length. Examples of a pulse echo response from this simulated data, at a frequency of 1.4 MHz ($a_2/\lambda = 0.56$), before and after the noise is reduced, are shown in Figures 4.24(a) and (b). These figures show a clear reduction in the noise across the pulse echo response and the main lobe within the response is more defined. The 3-D pulse echo response across a range of frequencies from the simulated data,

after the noise has been reduced, is shown in Figure 4.25(a) and the corresponding response generated using the Kirchhoff model (equation (4.3)) with a crack length of 5 mm is shown in Figure 4.25(b). There is a shift in the main lobe of the pulse echo response at each frequency within the finite element simulated response as shown in Figure 4.25(a). That is, the highest amplitude in each response has shifted to the left from the centre (the dark red region shown in Figure 4.25(a) represents these higher amplitudes). This is due to beam divergence as a result of the weld microstructure. This shift is accounted for in the Kirchhoff model as shown in Figure 4.25(b). The contour $\bar{P}$ is extracted from the simulated data, via equation (4.33), and is shown in Figure 4.26(b) (blue line). This can be compared with Figure 4.26(a) which shows the contours that are extracted using the raw data before neighbouring signals are convolved. Again, this shows the effect of the convolution on emphasising the effect of the crack within the frequency domain data. In addition, Figure 4.26(b) shows the contour extracted using the model, $\bar{A}$, for the correct crack length (5 mm). The optimisation process outlined in subsection 4.2.5.1 takes the corresponding contours from the Kirchhoff model and varies the crack size until the difference between the contours from the simulated data and the model are minimised. The resulting crack radius obtained using this method is 2 mm which gives a reasonable error of 0.5mm considering the assumptions within the model and the simulation. Figure 4.27 shows the error between the extracted and true crack radius as the number of nearest neighbours used within the convolution is increased. That is, the range of l and k in equation (4.30) is extended so that a greater number of neighbouring signals are multiplied together with the signal of index m and n and then summed. This means in Figure 4.22 the signal highlighted by the green element is multiplied with more nearest neighbouring signals which are depicted by the red elements. For this example,

there is a clear minimum of 0.5 mm error when just one nearest neighbour is used.

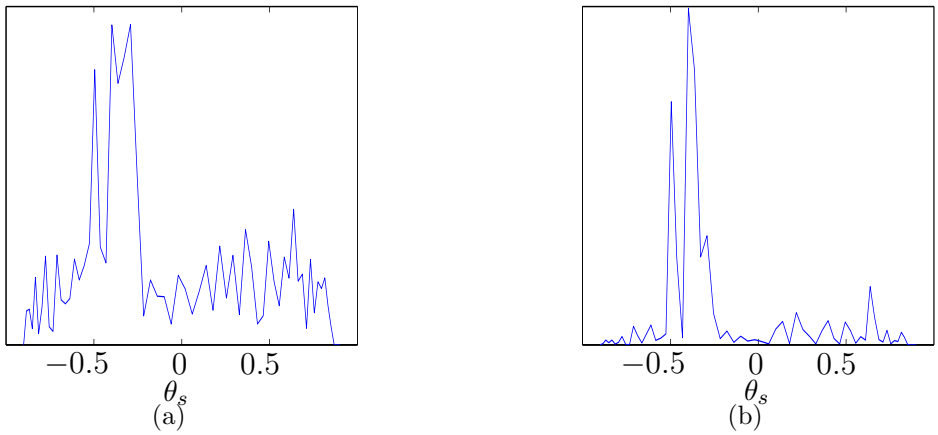

Figure 4.24: This figure shows the effect of the convolution (equation (4.31)) of the nearest neighbour signals within the scattering matrices on the pulse echo response within a scattering matrix at a single frequency. Here the frequency is 1.4 MHz. Figure (a) shows the response using the raw data and (b) shows the pulse echo response when the nearest neighbouring signals have been convolved using equation (4.31).

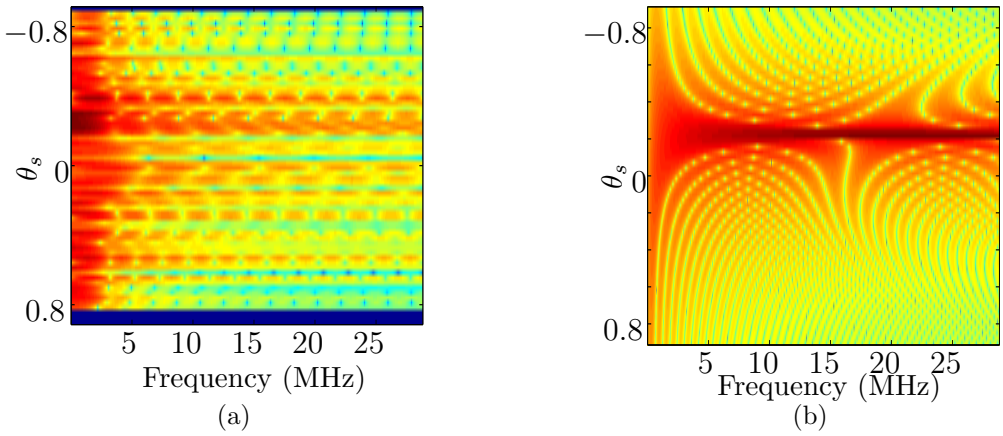

Figure 4.25: The pulse echo response from the scattering matrices as a function of frequency from (a) the PZFlex simulated data with a 2.5 mm radius crack in a heterogeneous host material after the nearest neighbour signals within the scattering matrices have been convolved (equation (4.31)) and (b) the corresponding data from the model given by equation (4.3).

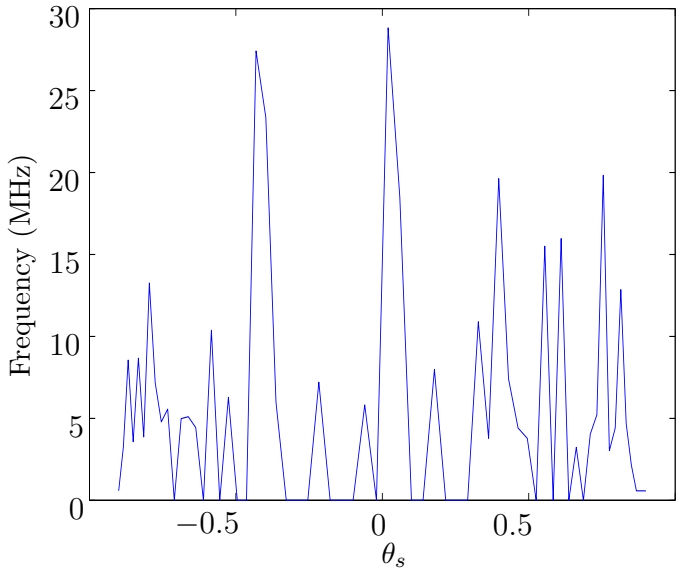

(a)

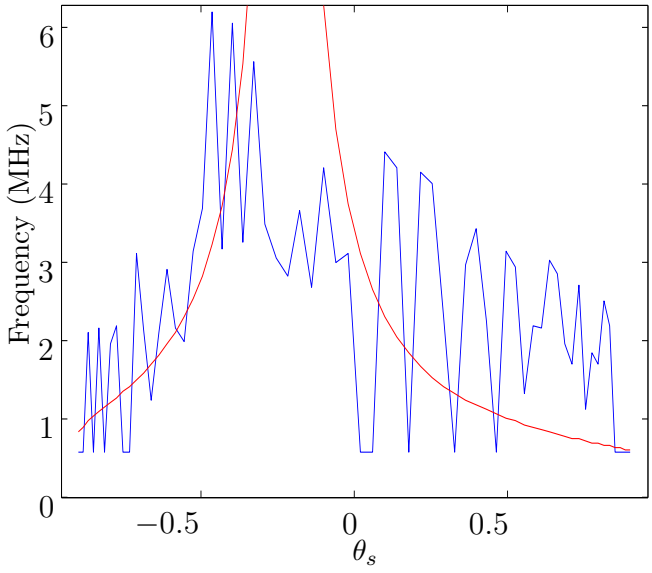

(b)

Figure 4.26: The contours extracted from the pulse echo response across a range of frequencies via equation (4.33) from the finite element simulated data of the steel weld with a 2.5 mm radius crack inclusion where (a) no convolution was applied and (b) convolution was applied to the data via equation (4.31) (blue line). In addition (b) shows the contours extracted from the Kirchhoff model (red line) where the same parameters have been used as in the simulated data. Note that due to beam divergence, as a result of the heterogeneous nature of the steel weld, there is a shift to the left in the contour extracted from the simulated data and this shift was incorporated into the model.

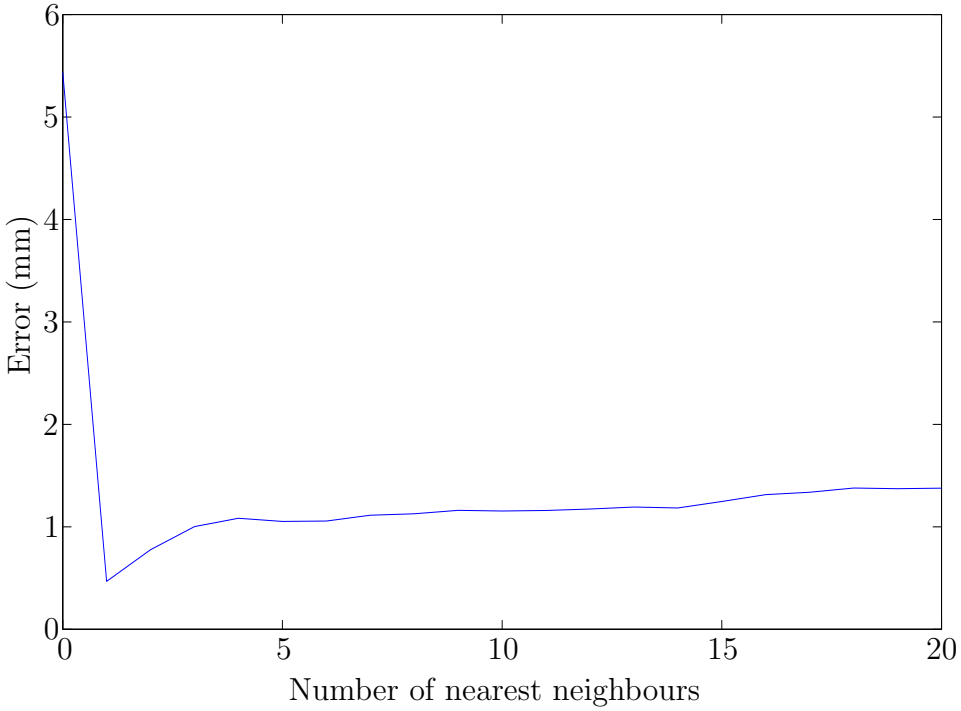

Figure 4.27: This plot shows the error in the crack radius (mm) (y-axis) extracted from the simulated data using the method described in Section 4.2.3 as the number of nearest neighbouring signals that are convolved is increased (x-axis) from 0 to 20, that is the range for N in equation (4.30) is extended so that more signals are multiplied together and summed in equation (4.31).

4.3 Conclusions

A model based, single frequency method for objectively sizing cracks, which uses the first minimum in the pulse echo response from a scattering matrix, was presented. An analytical expression, equations (4.5), was derived from the Kirchhoff model which demonstrates the one to one relationship between the crack length and this first minimum. This analytical expression provides insight into the sensitivity of the method and to the errors which are a consequence of the discretisation of the model. It was shown that the discretisation of the ultrasonic array within the model results in errors in the recovered crack length. An approximation was derived to this error and is a function of the crack radius over the wavelength and the pitch of the array. In addition, an upperbound was derived relating the maximum crack length that can be recovered for a given pitch (and vice versa). The single frequency method was applied to finite element simulated data from a homogeneous medium with a 5 mm crack inclusion. The method successfully recovered a crack length with a 0.4 mm error. An alternative method which uses all points in the pulse echo response to size the crack was also applied to the finite element simulated data. However, a larger error of 1.5 mm arose when this approach was adopted. The single-frequency method was then extended to a multi-frequency technique which uses the first minimum in the pulse echo response across a range of frequencies. The scattering matrices from the finite element simulation of a steel weld with a crack inclusion were very noisy. Before the multi-frequency method could be applied to this data it was necessary to apply a convolution technique to reduce the noise. Once the noise was reduced, the multi-frequency method was applied to the finite element simulated data of a steel weld with a 5 mm long crack inclusion. The crack length was recovered with an error of 1 mm, which is reasonable when the assumptions within the model and the simulation are considered.

Chapter 5

Detection and imaging algorithms (DORT and TFM)

5.1 Introduction

In this chapter, two imaging methods which utilise FMC ultrasonic data are presented; the first is the DORT (French acronym for the decomposition of the time reversal operator) [57] method and the second is the Total Focusing Method (TFM) [27]. To begin with, an objective detection method which does not require any *a priori* knowledge of the material heterogeneity is presented. This is then used to propose a detection criterion specific to steel welds. To illustrate this method it is applied to finite element simulated data and experimental data. Having detected a defect, the full DORT imaging method is then implemented and used to image the defect within a stainless steel weld and the results are compared to those produced using TFM. Importantly, this is the first time that the DORT method has been applied to FMC data from a steel weld.

5.2 Post Processing Algorithms

In this section, two post processing algorithms are presented which can be used to detect flaws in steel welds using the FMC data captured by the ultrasonic array. The DORT method operates in time-frequency space and is comprised of two stages. First, there is a detection stage which uses the largest singular value from the associated scattering matrices. Then there is an imaging stage which uses time reversal principles to create an image. The TFM operates in the time domain and uses the FMC data to focus the beam at each point in the inspection area to create an image.

5.2.1 The DORT Method

The DORT method [51] is an image processing method that uses time reversal techniques [66] in the time-frequency domain, along with the singular value decomposition (SVD) of the FMC data, to produce an image. Time reversal is based on the principal of last in-first out, as shown in Figure 5.1. The delay laws from the received signal are simply reversed and another ultrasonic wave is sent into the material with these laws to create improved focusing on the defect. This technique has been successfully implemented for focusing ultrasonic waves on flaws within heterogeneous materials [57]. However, it has not been applied to ultrasonic data from the inspection of a steel weld before. The DORT method can be divided into two stages; the first stage is to determine whether there is a defect in the structure or not and the second stage is the imaging of the defect and localisation within the structure. The DORT method is a time-frequency domain method which allows all the information within the data to be analysed. The first step in the DORT method takes the time domain FMC data, $\mathbf{H}$, into the time-frequency domain by

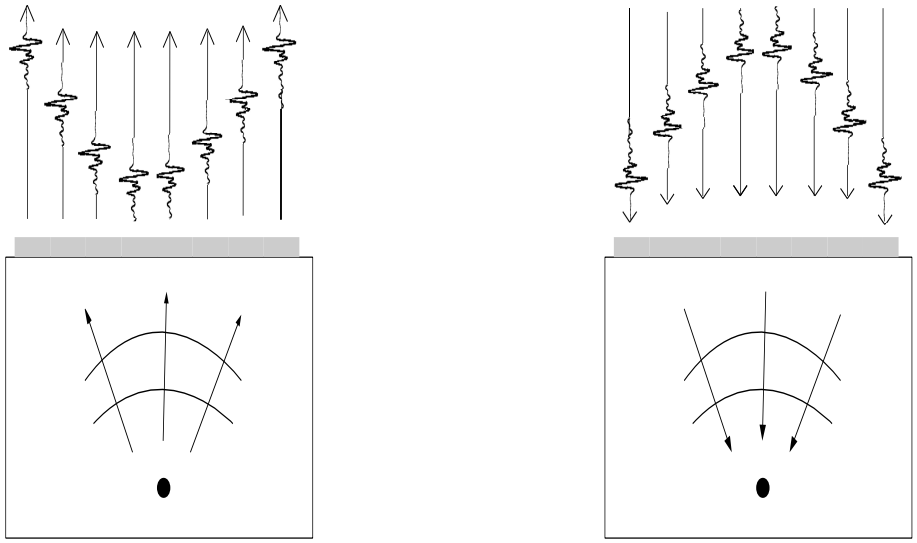

(a) (b)

Figure 5.1: A schematic of the received signal by the ultrasonic array transducer is shown in (a) and the time-reversed signal to be re-transmitted is shown in (b) which will enhance the focusing on the defect.

taking the time-windowed discrete Fourier transform (DFT) of the data to obtain the inter element response matrix, $\mathbf{K}(T_p, f_q)$, where T_p is time with $p = 1, ..., N_T$ and N_T is the total number of time samples and f_q is frequency with $q = 1, ..., N_f$ and N_f is the total number of frequency samples. For each time, T_p, and time window, $\triangle T$, a submatrix of $\mathbf{H}$ is given by

$$\hat{\mathbf{H}}(T_p, t) = \mathbf{H}(T_p - t)W(t), \tag{5.1}$$

where

$$W(t) = \left\{ \begin{array}{ll} 1 & t \in \left[\frac{-\triangle T}{2}, \frac{\triangle T}{2}\right], \\ 0 & \text{otherwise.} \end{array} \right\}$$

$$T_p = t_1 + \triangle t(p-1), \tag{5.2}$$

t_1 is the start time of the signal being sampled (in practice this will be large enough to not include reflections from the front face of the structure being inspected) and $\triangle t$ is the time between each windowed sample of the signal. The discrete Fourier transform of $\hat{\mathbf{H}}$ is calculated to produce the full set of response matrices $\mathbf{K}(T_p, f_q)$. The frequency range is given by

$$f_q = \frac{q}{\triangle T}. \tag{5.3}$$

The response matrix, $\mathbf{K}(T_p, f_q)$, is an $N \times N \times N_f \times N_T$ matrix, where N_T is the total number of time indices sampled, N_f is the number of discrete frequencies and N is the total number of elements in the ultrasonic array. The process of creating $\mathbf{K}(T_p, f_q)$ is demonstrated in Figure 5.2. Next, the SVD of each response matrix $\mathbf{K}(T_p, f_q)$ for each time, T_p, and frequency, f_q, pair is calculated. Within the DORT method, the SVD is used as a tool for flaw detection and image reconstruction. The SVD of each response matrix $\mathbf{K}(T_p, f_q)$ is given by

$$\mathbf{K} = \mathbf{U}\Lambda\mathbf{V}^T, \tag{5.4}$$

where Λ is a diagonal matrix containing real, positive singular values λ_k, $k = 1, ..., N$, the columns of $\mathbf{U}$ are the left singular vectors and the rows of $\mathbf{V}^\dagger$ are the right singular vectors. For linear scatterers, each singular value is associated with one scatterer in the material. However, Chambers and Gautesen [67] have shown that there can be up to four singular values associated with one scattering event, and this number depends upon the shape and orientation of the scatterer. Once the SVD of the data for each time-frequency pair, (T_p, f_q) is determined, the largest singular value $(\lambda_1(T_p, f_q))$ is normalized using the quadratic mean of all the

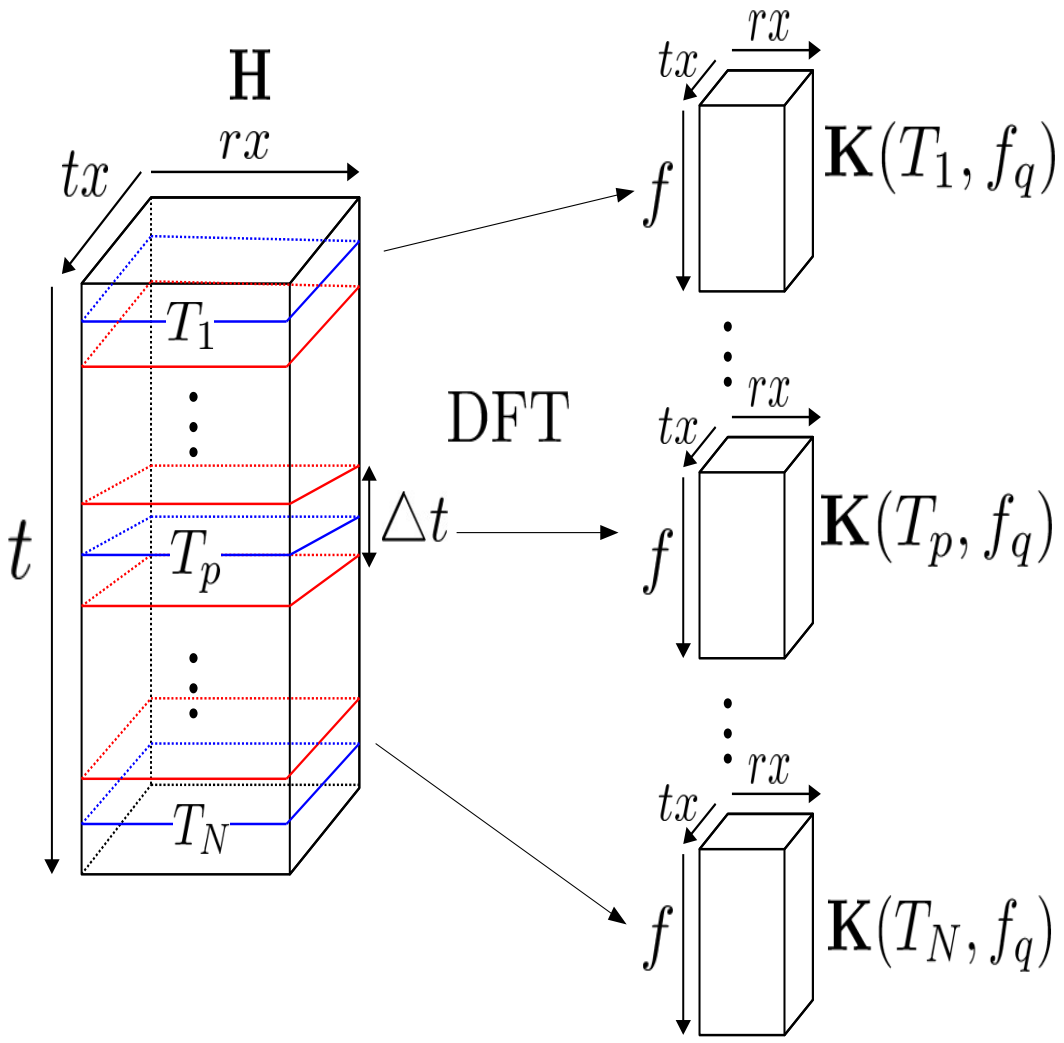

Figure 5.2: A schematic which demonstrates how the time windowed Discrete Fourier Transform (DFT) is used to create the time-frequency matrix, $\mathbf{K}(T_p, f_q)$, from the FMC data, $\mathbf{H}(t)$. For each fixed time index sampled, T_p, a time window, $\triangle t$, is taken around this fixed time to create a 3D submatrix, $\hat{H}$, of the FMC matrix, a DFT is then taken of this submatrix resulting in the matrix $\mathbf{K}(T_p, f)$. The collection of the frequency domain matrices, $\mathbf{K}(T_p, f_q)$ where $p = 1, ..., N_T$, form the 4D time-frequency matrix $\mathbf{K}$.

singular values at that time-frequency pair [59]

$$\tilde{\lambda}_1(T_p, f_q) = \frac{\lambda_1(T_p, f_q)}{\sqrt{\frac{1}{N}\sum_{p=1}^{N} \lambda_p^2(T_p, f_q)}}. \tag{5.5}$$

If there is a flaw, these normalised first singular values for some time-frequency (T_p, f_q) pairs will be above a threshold value, τ. This stage can be used as an objective flaw detection technique where no *a priori* knowledge of the material being inspected is required. In section 5.3.2 a detection threshold, τ, specific to steel welds is derived. So, if there exist

$$\tilde{\lambda}_1(T_p, f_q) > \tau \tag{5.6}$$

then it can be objectively concluded that there is a flaw within the structure. The second stage in the DORT method is the image reconstruction which does require the input of a homogenised material wavespeed, c. The image is generated using back propagation, where the propagation operator is a Green's function, and the focusing is provided by the right eigenvectors $V_1(T_p, f_q)$ associated with the singular values where $\tilde{\lambda}_1(T_p, f_q) > \tau$. The image domain is discretised by a grid, where the number of pixels in the vertical direction of this grid is dictated by the number of time samples (N_T) used to create the time-frequency matrix $\mathbf{K}$, and the number of pixels along the horizontal axis is a free parameter which will be denoted by $\hat{x}_l$ $(l = 1, ..., m)$. An example of the image domain grid is shown in Figure 5.3. The propagation operator is a Green's function given in the discretised form of a $1 \times N$ vector $\mathbf{G}_{lp}$; the elements of which are given by

$$g_{jlp}(f_q) = \frac{\mathrm{e}^{i2\pi f_q r_j/c}}{\sqrt{r_j}}, \qquad j = 1, ..., N, \tag{5.7}$$

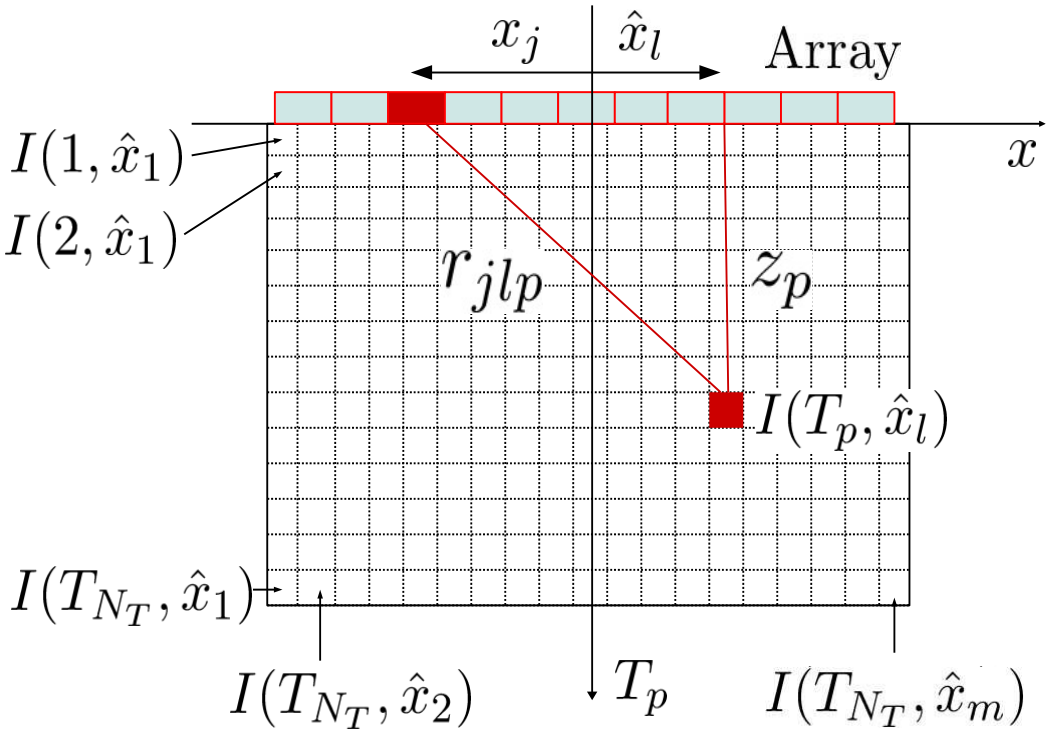

Figure 5.3: A schematic which demonstrates the geometry of the length r_i (equation (5.8)) for each spatial position in the imaging domain, $I(T_p, \hat{x}_l)$. This is used within the back propagation operator $g_{jl}(f_q)$ given by equation (5.7).

where

$$r_{jlp} = \sqrt{z_p^2 + (x_j - \hat{x}_l)^2}, \tag{5.8}$$

$z_p = cT_p/2$ is the depth in the material that is being imaged and x_j is the spatial position of array element j, as shown in Figure 5.3. Each value in the image, $I(T_p, \hat{x}_l)$, is calculated using the absolute value of the back propagated wave which is focused using the right eigenvector associated with the largest singular values that lie above the threshold τ. Hence,

$$I(T_p, \hat{x}_l) = \sum_{f_q|\tilde{\lambda}>\tau} \lambda_1(T_p, f_q) \left| \mathbf{V_p^1 G_{lp}^*} \right| \tag{5.9}$$

where $\mathbf{G}^*$ is the complex conjugate of the Green's function vector (this is the time reversed stage). In Sections 5.3 and 5.4, this method will be applied to simulated and experimental data.

5.2.2 The Total Focusing Method (TFM)

The Total Focusing Method (TFM) [27] is a time domain imaging technique which exploits FMC data and can be used for the detection of defects in NDT. The same method is used by the geophysics community within seismology to produce a map of the earth's interior which is useful for oil recovery or earthquake analysis. Within this field the approach is referred to as Kirchhoff migration [38]. Within the medical field the same approach is referred to as delay and sum beamforming [39]. The TFM algorithm first requires the image domain to be discretised into a grid of pixels, $(N_x \times N_z)$. For each pixel (x_l, z_p) (where $l = 1, ..., N_x$ and $p = 1, ..., N_z$), the signal from each transmit-receive pair is focused at that point, as demonstrated in Figure 5.4. The focusing is achieved by calculating the time of travel (T) between a given transmit-receive pair (i,s) and this pixel. This is then used to isolate

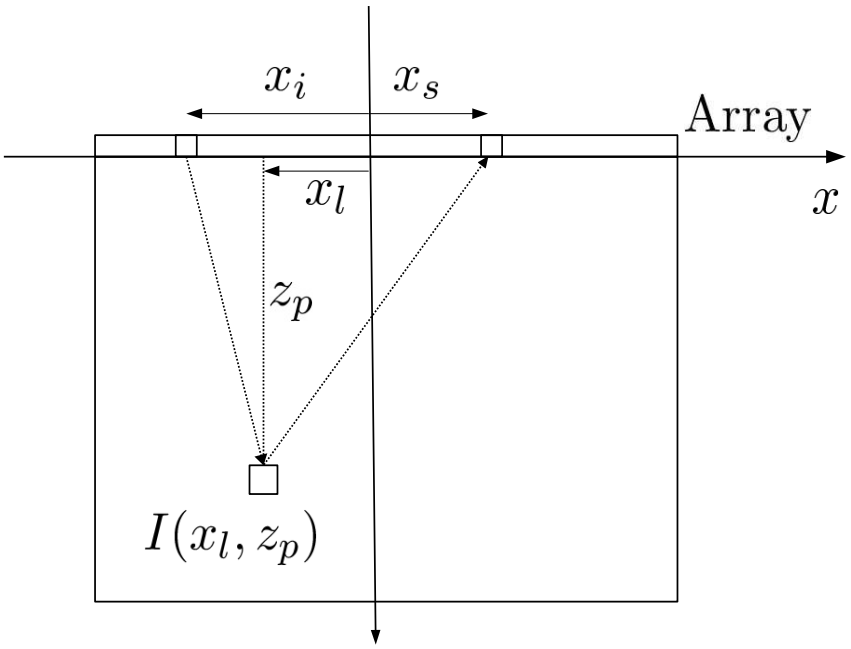

Figure 5.4: The geometry of the transmitting array element, x_i, the receiving array element, x_s, and a pixel location $I(x_l, z_p)$ used in the TFM, equation (5.10).

the corresponding amplitude of the signal $\mathbf{H}(i, s, T)$. These amplitudes are then summed over all transmit-receive pairs to create the intensity for the pixel (x_l, z_p) in the image given by

$$I(x_l, z_p) = \left| \sum_{i,s} \mathbf{H}(i, s, T) \right|, \tag{5.10}$$

where

$$T = \frac{\left(\sqrt{(x_i - x_l)^2 + z_p^2} + \sqrt{(x_s - x_l)^2 + z_p^2} \right)}{c}, \tag{5.11}$$

x_s is the x-coordinate of the receiving element and x_i is the x-coordinate of the transmitting element, z_p is the depth of the pixel and c is the wavespeed of the material. In this scheme, the array is located at $z = 0$ and here $x_i = x_s = 0$. This method is computationally very efficient for the imaging of flaws in isotropic materials. However, when the material is heterogeneous, bending and scattering of

the ultrasonic waves occurs. This means there is no longer a direct path between a transmit-receive pair and the flaw, and so the time delay calculations in equation (5.11) are no longer accurate. The imaging and detection capabilities of this method will be compared with those of the DORT method in the forthcoming sections.

5.3 Detection of flaws in steel welds

The first stage of the DORT method is adopted here which uses the set of largest singular values, $\{\tilde{\lambda_1}\}_j$, distribution from the time-frequency response matrices, $\mathbf{K}(T_p, f_q)$. If the weld contains a defect this distribution will give rise to significant values which will be larger than a specified detection threshold, τ. Within [57] Aubry and Derode presented a detection criterion based on an experimental set up which simulates the multiple scattering of waves emitted from an ultrasonic array. Their set up involved a water tank within which a set of parallel steel rods were placed to replicate a random medium. Table I in [57] presents two detection thresholds. The first is $\tau = 2.39$ which is determined using the unfiltered data ($\mathbf{K}$) from the multiple scattering regime and the second is $\tau^F = 2.69$ which is used when filtering is applied to $\mathbf{K}$ to create a response matrix which includes only single scattering responses, $\mathbf{K}^F$ (see Section IV of [57] for the details of this filtering process). Before the singular values were analysed in [57] each response matrix was truncated to remove short range correlations [59]. The singular values ($\tilde{\lambda}_i, i = 1, ..., N$), across all time-frequency (T_p, f_q) pairs, from the unfiltered matrix ($\mathbf{K}$) were compared to the quarter circle law (QCL). The QCL the distribution of singular values associated with a random matrix as derived from Random Matrix Theory (RMT) [68]. It can be seen from Figure 10(a) in [57] that the experimental

distribution of first singular values ($\tilde{\lambda}_i$, $i = 1, ..., N$) deviates from the QCL and so $\tau = 2.39$ was obtained empirically. However, when the singular value distribution, $\tilde{\lambda}_i^F$, from the filtered response matrix ($\mathbf{K}^F$) was compared to the distribution from a random Hankel matrix (see Figure 10(b) in [57]) then there was excellent agreement between the two distributions. The detection threshold in this case is $\tau^F = 2.69$ (as obtained using the numerical estimate to the distribution of singular values from a random Hankel matrix). In this thesis, it will be demonstrated that the singular value distribution from the FMC data from a steel weld does not fit with the QCL. Hence, a detection threshold specific to a steel weld is proposed and is empirically calculated using a finite element simulation. The configuration in this work differs from the multiple scattering regime in [68] as multiple scattering does not dominate the signal received. The problems which arise are mainly due to the grain structure which causes the waves to bend as they pass through the weld.

5.3.1 A comparison of the singular value distribution from a steel weld to the quarter circle law

In this subsection the distribution of singular values from the response matrix $\mathbf{K}(T_p, f_q)$ arising from a finite element steel weld is calculated. The finite element simulated data from a steel weld containing *no flaw* is used in the section, the details of which were outlined in Chapter 2, Section 2.3.1. The parameters used to generate the inter-element response matrix ($\mathbf{K}(T_p, f_q)$) are given in Appendix C, Table C.3. The singular values, $\lambda_i(T_p, f_q)$ (where $i = 1, ..., N$), are normalised using equation (5.5). These singular values are then segregated into bins to produce a probability density distribution. The bin intervals are given by

$$b_l = [(l-1)B, lB], \tag{5.12}$$

where B is the bin width and $l = 1, ..., L$ where L is the total number of bins. The total number of singular values contained within each bin is denoted as $D(b_l)$. The probability density distribution of the first singular values is estimated [59] by

$$\rho(b_l) = \frac{D(b_l)}{nB} \tag{5.13}$$

where $n = N \times N_T \times N_f$ is the total number of normalised singular values arising from the response matrix $\mathbf{K}(T_p, f_q)$. This distribution will be compared to the quarter circle law [69] which is given by

$$\rho_{QC}(\bar{\lambda}) = \frac{\sqrt{4 - \bar{\lambda}^2}}{\pi} \qquad \text{where} \qquad 0 < \bar{\lambda} < 2. \tag{5.14}$$

and gives the distribution of singular values from a square random matrix derived from RMT. The entries of the random matrix have to be independently and identically distributed for this law to be applied. Figure 5.5 shows a comparison between the QCL (green line) given by equation (5.14) and the distribution, $\rho(b_l)$, of first singular values from the response matrix $\mathbf{K}(T_p, f_q)$ (blue line) given by equation (5.13) from the finite element simulated data of a steel weld. It can be seen from this plot that the distribution from the steel weld does not fit with the QCL. No flaw is contained in these simulations and so these large singular values must stem from scattered wave emanating from some of the larger grains in the weld. These are not to be classified as flaws and so the detection criterion based on RMT and the QCL should not be used when inspecting steel welds. The next subsection investigates this in more depth and arrives at a detection criterion for steel welds which could use the distribution of first singular values from the response matrix $\mathbf{K}(T_p, f_q)$.

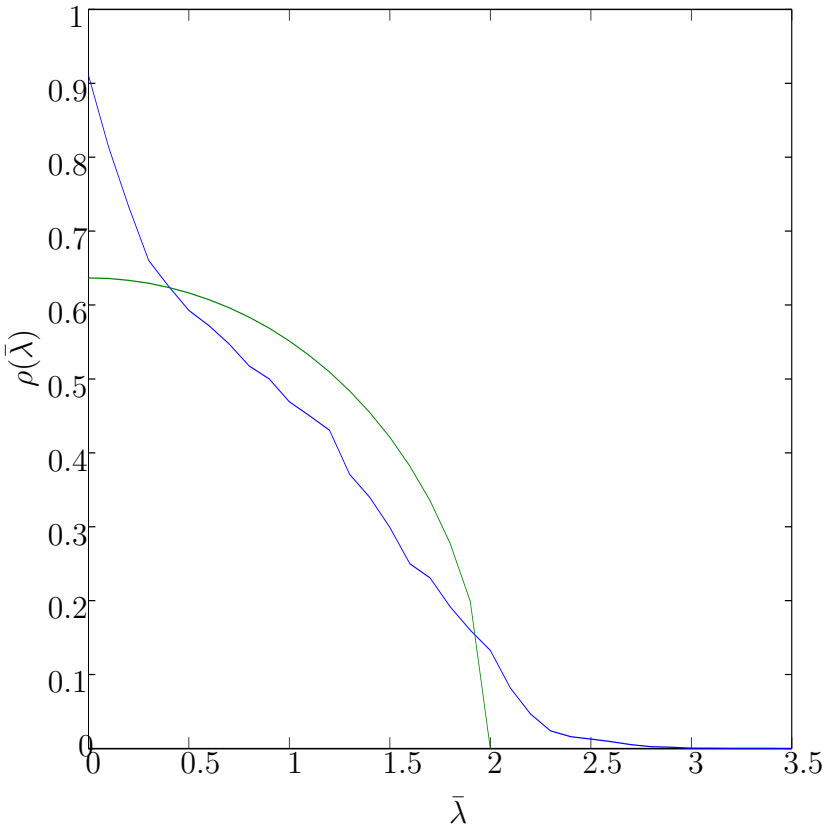

Figure 5.5: This plot shows the distribution of singular values (as given by equation (5.13), blue line), $\tilde{\lambda}_i$, as calculated from the response matrix, $\mathbf{K}(T_p, f_q)$, arising from a finite element simulatioC. This distribution is compared to that given by the Quarter Circle Law (as given by equation (5.14), green line) which is derived from Random Matrix Theory.

5.3.2 A threshold for detection of flaws in stainless steel welds using the largest singular value

The distribution of the largest singular values from the response matrix, $\mathbf{K}(T_p, f_q)$, from the finite element simulated data of a steel weld (as outlined in Chapter 2, Section 2.3.1), with and without a flaw inclusion, are analysed in this subsection. The aim is to determine a threshold specific to steel welds which can be used within the objective detection method presented in this chapter. Histograms of the normalised largest singular values for all time-frequency pairs calculated from the response matrix, $\mathbf{K}(T_p, f_q)$, from the finite element simulated data of a steel weld containing no flaw (blue bars) and with a 1.25 mm radius side drilled hole flaw (red bars) are shown in Figure 5.6. This figure shows that when there is no flaw included within the steel weld (blue bars) the highest concentration of largest singular values lie between 2 and 2.5, with the largest being 3.68. When the flaw (a 1.25 mm radius side-drilled hole) is included (red bars) there is still a large proportion of the first singular values lying between 2 and 2.5. This is to be expected as these correspond to the scattering arising from the grains within the weld structure. However, it is also clear that a significant proportion of the first singular values are greater than 3.68. These must stem from the backscatter from the flaw. It is concluded from this figure that there is a notable difference between the distribution of first singular values from the response matrix, $\mathbf{K}(T_p, f_q)$, when there is a flaw in the steel weld and from that when no flaw is present. The distribution of largest singular values can also be viewed as a heat map in the time and frequency domain as shown in Figure 5.7. The distribution where a 1.25 mm radius side drilled hole flaw was included in the finite element simulation is shown in Figure 5.7(b) and it is clear that there is a cluster of large first singular values between 0.5-1.5 MHz and $20 - 25\mu$s. By visually comparing this distribution to

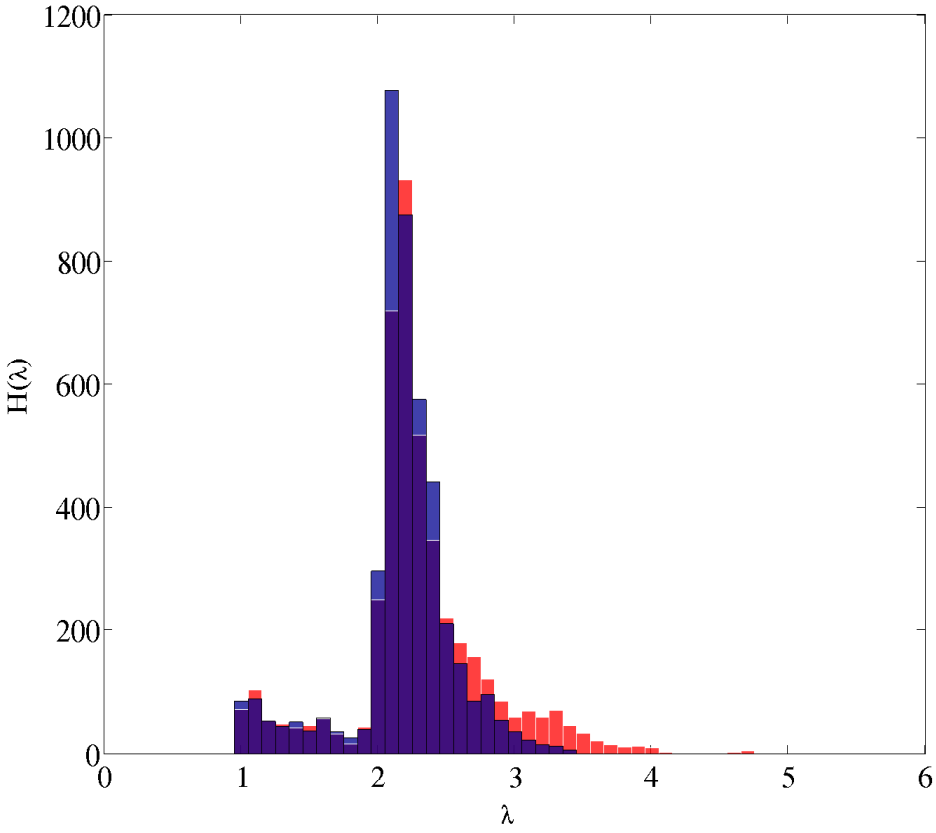

Figure 5.6: This plot shows the histogram of the largest singular values across all time-frequency pairs calculated from the response matrix, $\mathbf{K}(T_p, f_q)$, associated with the finite element simulated data (see Chapter 2 Section 2.3.1) of a steel weld (a) without a defect (blue bars) and (b) with 1.25 mm radius side drilled hole inclusion (red bars).

that shown in Figure 5.7(a), where there is no defect, it is clear that the inclusion of a defect gives rise to significantly larger singular values. In this work the detection threshold is taken to be $\tau = 3.68$, this is the maximum singular value from the distribution where no defect is included within the finite element simulation of a steel weld (as shown by the blue bars in the histogram in Figure 5.6 and by yellow on the colour bar in the heat map of the distribution in Figure 5.7).

5.3.2.1 A summary of the steps in the detection algorithm

The objective method for the detection of flaws within a stainless steel weld is summarised by the following steps:

- The time and frequency domain response matrix, $\mathbf{K}(T_p, f_q)$, is determined by taking a time windowed FFT (as outlined in Section 5.2.1) of the ultrasonic FMC data.
- The SVD of $\mathbf{K}(T_p, f_q)$ is calculated and the largest singular value, $\lambda_1(T_p, f_q)$, associated with each time frequency pair is stored.
- Each $\lambda_1(T_p, f_q)$ is then normalised (equation (5.5)) and their distribution is viewed either as a heat map (Figure 5.7) or as a histogram (Figure 5.6).
- If there exists $\tilde{\lambda}_1(T_p, f_q) > \tau$ then it is objectively concluded that there is a flaw within the steel weld.

It is worth noting that the location of the flaw is related to the times in Figure 5.7, where the super threshold singular values reside and this will be critical when the DORT method is used to create a flaw image in Section 5.4.

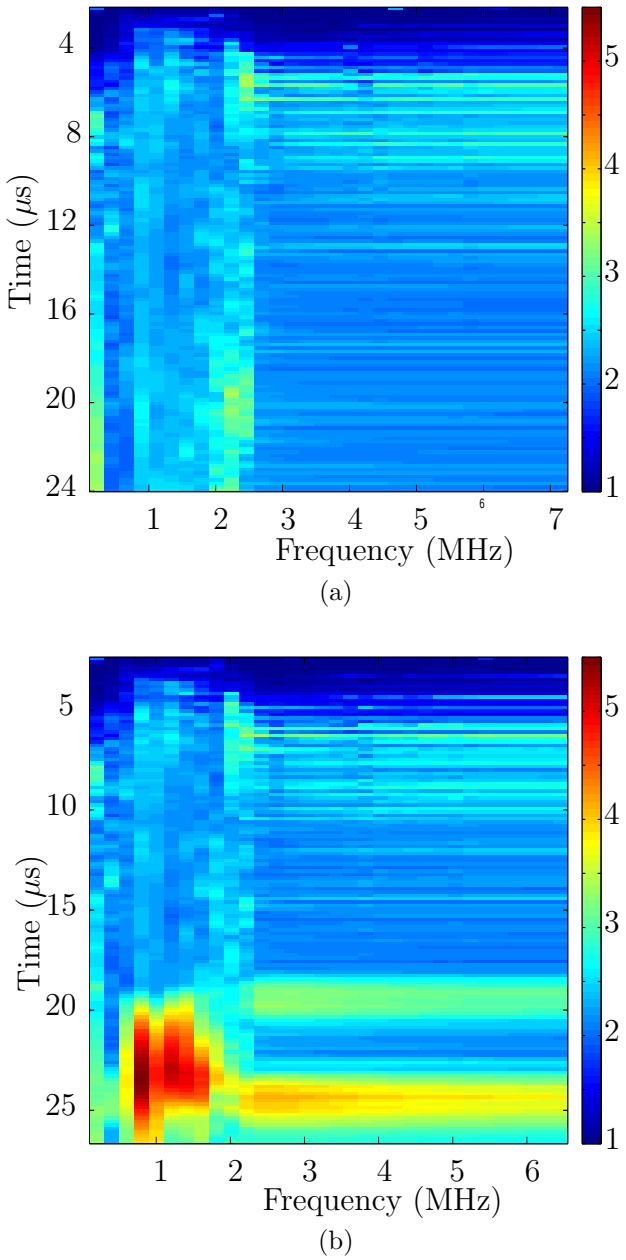

Figure 5.7: The largest singular value $\bar{\lambda}_1(T_p, f_q)$ from the response matrix ($\mathbf{K}(T_p, f_q)$), calculated from the finite element simulated data of a steel weld (see Chapter 2, Section 2.3.1 for details of the simulation), where (a) no defect is included and (b) a 1.25 mm radius side drilled hole is included within the weld geometry. For the parameters used to generate the response matrix ($\mathbf{K}(T_p, f_q)$) as in Section 5.2.1, see Appendix C Table C.3.

5.3.3 Results when the detection method is applied to finite element simulated data

The detection algorithm summarised in Section 5.3.2.1 is applied here to finite element simulated data of a steel weld (outlined in Chapter 2, Section 2.3.1). In order to analyse the effects of the microstructure within the weld, the method is applied to both a finite element simulation of a steel weld and a homogeneous medium, with each containing a horizontal crack of length 5 mm. The parameters used to generate the response matrix, $\mathbf{K}(T_p, f_q)$, from the FMC data associated with each simulation are summarised in Appendix C, Table C.3. The time step ($\triangle t$) is set at 0.5 mm (this is 151 ns in the data from the steel weld and 159 ns using the data where the host material is homogeneous) and the time window is taken to be 20% of the total time that the wave takes to reach the back wall of the test piece. Figure 5.8 shows the distribution of the largest singular values across the time and frequency domain. In each case the crack has clearly and objectively been detected as there exists a cluster of singular values larger than the threshold ($\tau = 3.68$) which was determined in Section 5.3.2. It is also clear from Figure 5.8(b) that the largest singular values resulting from the flaw are lower when the weld microstructure is included in the finite element simulation. This is due to less energy reaching the flaw (and in turn being received back by the transducer) as some of the energy in the ultrasonic waves has been scattered by the grain boundaries within the weld. Figure 5.8(a) shows two horizontal peaks that correspond to a time of 12 μs and 16 μs. These extend into the higher frequencies and are a result of the scattering from the crack tips which behave as point-like scatterers. When the weld microstructure has been included the first singular values arising from the crack tips at the higher frequencies are not as prominent as some ultrasonic energy is scattered by the grains within the weld.

In Figures 5.8(a) and (b) the time-frequency pair where the maximum singular value occurs is recorded (T^* and f^*). Figure 5.9 then shows the corresponding singular value distribution ($\tilde{\lambda_1}, ..., \tilde{\lambda_N}$) associated with the scattering matrices, $\mathbf{K}(T^*, f^*)$. Those from the finite element simulation with a crack embedded in the homogeneous medium are shown by the green line and those from the heterogeneous steel weld are shown by the blue line. A steel weld containing *no flaw* is also shown by the red line. From this figure it is clear that the first singular value is significantly larger when there is a crack inclusion within the material. In addition it is clear that the first singular value is largest when the host material is homogeneous, this is because the scattering amplitudes from the crack will be higher. This plot also shows that when the weld microstructure is included within the simulation the singular values between 2 and N are higher than those when the medium is homogeneous. As discussed above, the scattering from the grain boundaries that will give rise to these significant values.

Figure 5.10 shows the largest singular values in time-frequency space when side-drilled holes of radius (a) 0.5 mm, (b) 1.25 mm and (c) 2.5 mm are inserted into the finite element simulations which include the heterogeneous weld material. The parameters used to create the time-frequency response matrix (see section 5.2.1) are summarised in Appendix C, Table C.3. Again, it is clear from these time frequency distributions that in each case there exist singular values larger than the detection threshold, τ, and it can be concluded objectively that there exists a flaw within the structure. As expected, as the radius of the side drilled hole is increased the value of the singular values associated with the flaw also increase. This is further confirmed in Figure 5.11 where the singular value distribution $\tilde{\lambda}_n$, $n = 1, ..., N$, is calculated from the scattering matrix corresponding to the maximum first singular value, at time T^* and frequency f^*, in Figure 5.10. This

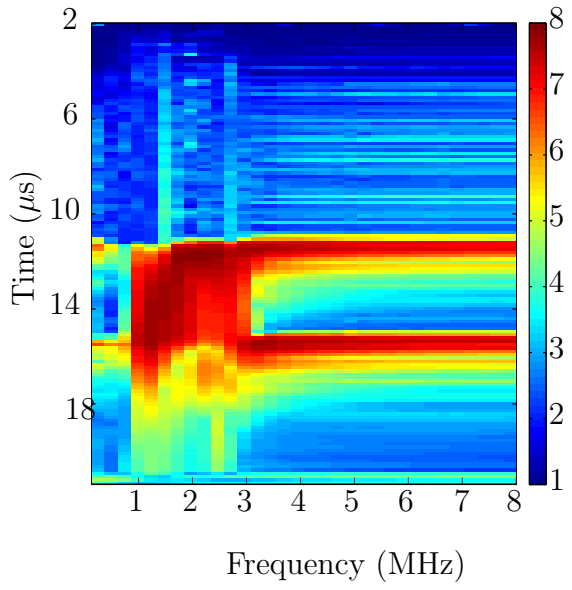

(a)

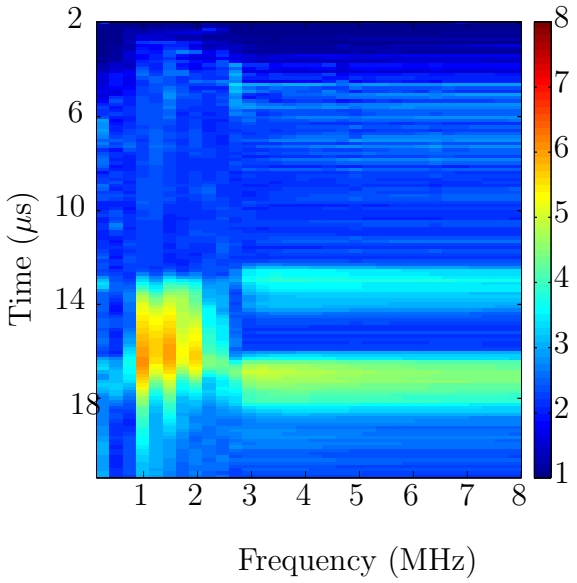

(b)

Figure 5.8: The largest singular value $\tilde{\lambda}(T_p, f_q)$ where the host material within the finite element simulation (outlined in Section 2.3.1) is (a) homogeneous and (b) a steel weld. A crack of length 5 mm is inserted into each simulation, 50 mm from the array and in the centre of the weld. The parameters used in each simulation are given in Appendix C by Table C.1. The parameters used to generate the response matrix ($\mathbf{K}(T_p, f_q)$) in each case are also summarised in Appendix C, Table C.3.

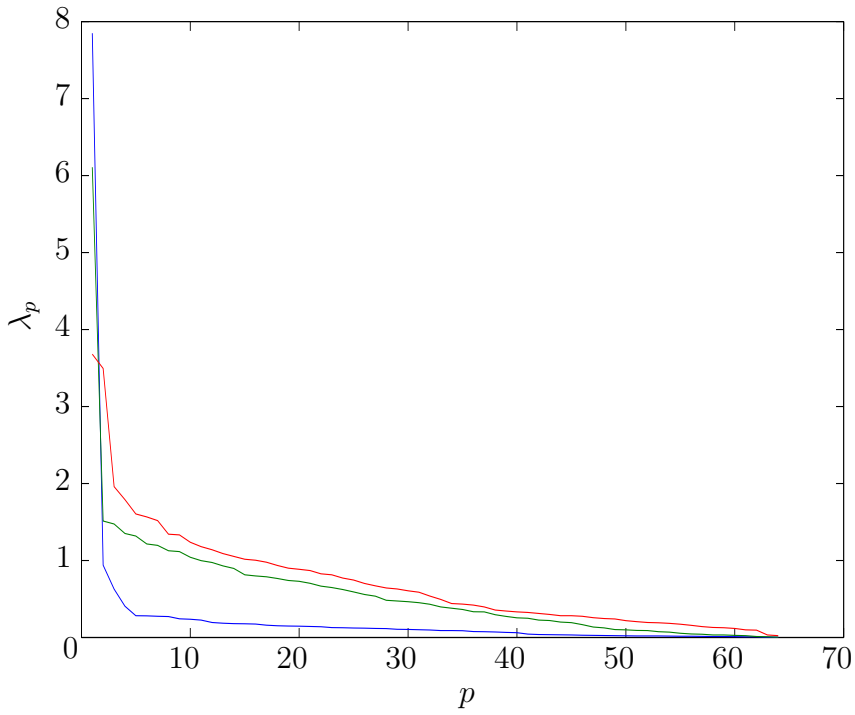

Figure 5.9: This figure shows the singular value distribution ($\tilde{\lambda}_p$ where $p = 1, ..., N$ and N is the total number of array elements) from the scattering matrix $\mathbf{K}(T^*, f^*)$, where T^* and f^* gives the time-frequency pair where the maximum first singular value occurs in the distributions shown in Figure 5.8. The finite element simulation where the material is homogeneous is shown by the green line and those from a heterogeneous steel weld is shown by the blue line. In addition the singular value distribution from a scattering matrix, $\mathbf{K}(T_p, f_q)$, from the finite element simulation of the steel weld containing no flaw is shown by the red line.

distribution is plotted as the side drilled hole radius is varied and is (a) 0.5 mm (green line), (b) 1.25 mm (blue line) and (c) 2.5 mm (red line). It can be seen that the distributions look very similar aside from the first singular value which then decreases as the radius of the side drilled hole decreases. In the next subsection this detection method is applied to experimental data.

5.3.4 Results when the detection method is applied to experimental data

In this subsection, the detection algorithm presented in Section 5.3.2.1 is applied to experimental data from a test piece which contains an inconel 82/182 weld [70]. The parent material to the right of the weld is stainless steel 316L and to the left is carbon steel 300 with an inconel 182 buttering layer between this and the weld. A schematic of the test piece is shown in Figure 5.12 which also gives the dimensions of the weld. The material properties are summarised in Appendix C, Table C.2. A 45 element ultrasonic array with a central frequency of 5 MHz was used to collect the FMC data. The probe was placed just off centre directly on the weld as shown in Figure 5.12. Again, in order to demonstrate the effect of a flaw inclusion on the largest singular value distribution, FMC data was collected from an area within the weld where it is known that there is no flaw and then from an area where there is a 12 mm long vertical crack inclusion in the centre of the weld 37 mm from the array as demonstrated in Figure 5.12. The time-frequency response matrix was calculated from the FMC data where there is no flaw ($\mathbf{K}_{NF}(T_p, f_q)$) and when there is a crack inclusion ($\mathbf{K}_{F}(T_p, f_q)$); the parameters used to calculate these response matrices are summarised in Appendix C, Table C.4. The normalised first singular value distributions, $\tilde{\lambda}_1$ (equation (5.5)), are shown in Figure 5.13, when (a) there is no defect in the inspection area and (b) there is a 12 mm long, vertical crack

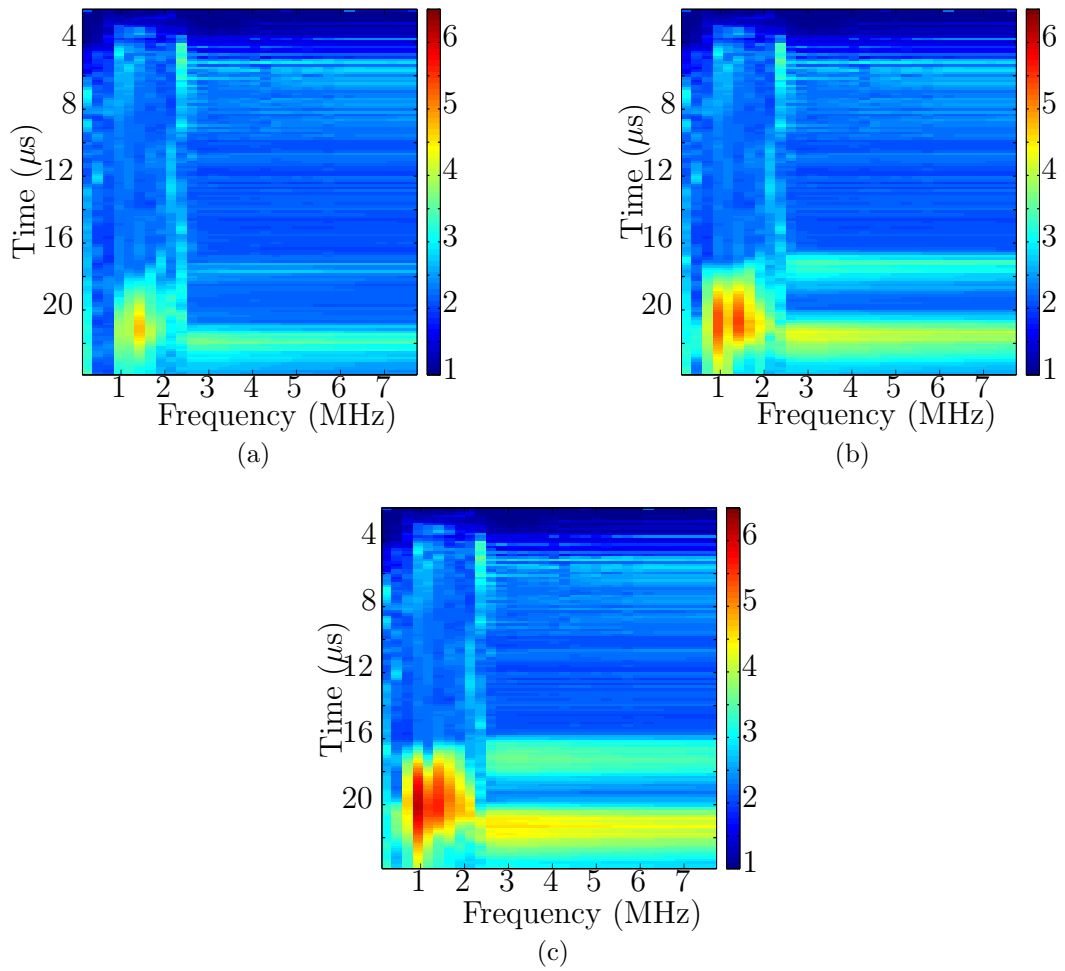

Figure 5.10: The largest singular value $\tilde{(}\lambda)(T_p, f_q)$ where the host material within the finite element simulation (outlined in Section 2.3.1) is a steel weld. A side drilled hole is inserted into the weld 50 mm from the array, in the centre of the weld and has a radius of (a) 0.5 mm, (b) 1.25 mm and (c) 2.5 mm. The largest singular value for each time-frequency pair is depicted via a colour, where the colour bar gives the associated value. The time between each windowed sample of the signal, $\triangle t$, is taken to be 20% of the total length of time of each signal. The number of time samples used is $N_t = 140$ and the number of frequencies used is 32. All other material parameters are given by Table C.1 in Appendix C.

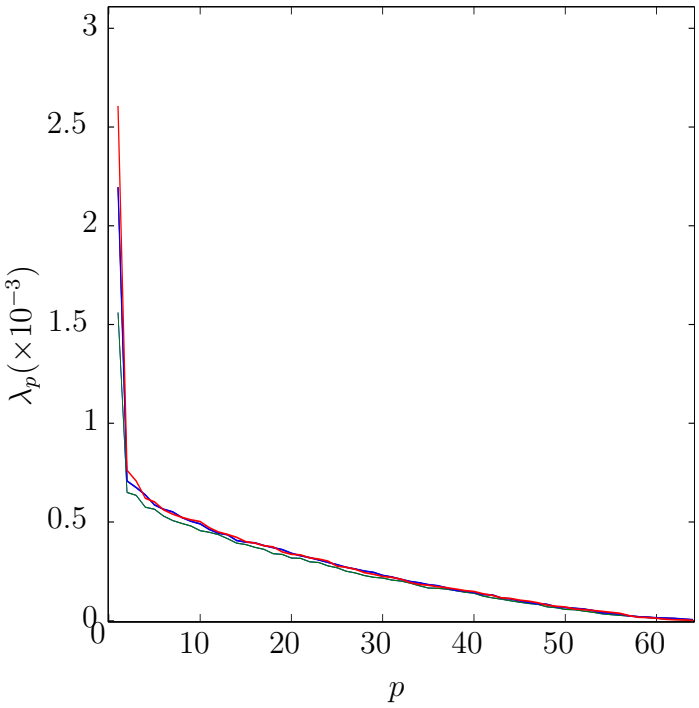

Figure 5.11: This figure shows the singular value distribution ($\tilde{\lambda}_p$ where $p = 1, ..., N$ and N is the total number of array elements) from the scattering matrix $\mathbf{K}(T^*, f^*)$, where T^* and f^* are the time-frequency pair where the maximum singular value occurs in the distributions, shown in Figure 5.10. These finite element simulations contain a heterogeneous host material (a steel weld) and the radius of the side drilled hole inclusion is (a) 0.5 mm (green line), (b) 1.25 mm (blue line) and (c) 2.5 mm (red line).

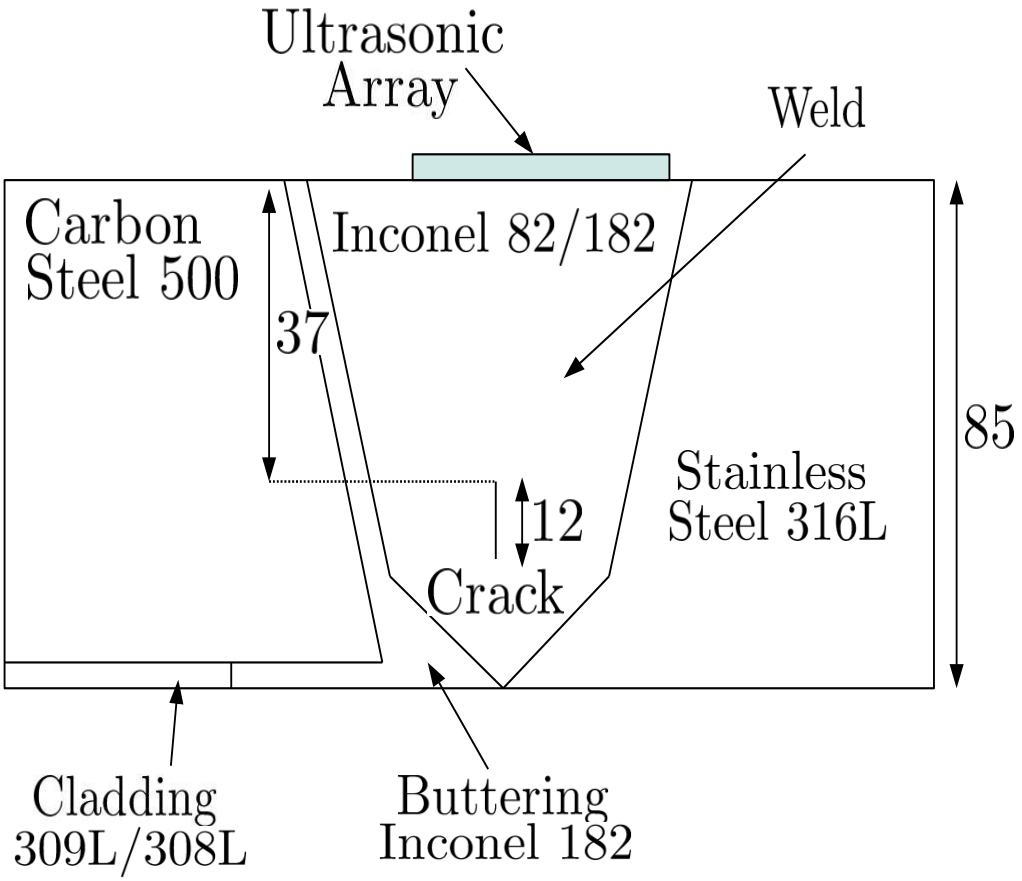

Figure 5.12: This schematic shows the test piece used to collect ultrasonic data. The block consists of a weld (the material of the weld is inconel 82/182) which joins a piece of stainless steel 316L and carbon steel 500. There is also some cladding and buttering material between the carbon steel and the weld. The test piece includes a 12 mm vertical crack 37 mm from the front face of the test piece which is 85 mm total in depth. The ultrasonic array which has 45 elements and a central frequency of 5 MHz was placed just to the right of the centre of the weld.

within the inspection area. It is clear from Figure 5.13(b) that there are singular values larger than the detection threshold, $\tau = 3.68$, at the lower frequencies. These are associated with the crack and occur at the lower frequencies as the crack is long in comparison to the wavelength of the transducer (the crack length over the wavelength of the transducer is 10.4). In the no flaw case (Figure 5.13(a)) there are some significant singular values occurring at around 22 μs which are associated with the back wall. A large time window was used in order to obtain a reasonable frequency range within the response matrix, $\mathbf{K}(T_p, f_q)$, and so, some backwall effects are included in the time samples. The histograms corresponding to these largest singular values are shown in Figure 5.14 and by comparing Figures 5.14(a) and (b) it is clear that there is a higher proportion of singular values that exceed the threshold $\tau = 3.68$ when there is a flaw present in the inspection area. Indeed, in Figure 5.14 there is an extremely large singular value around 6.5. In this section a method for the detection of flaws in steel welds was proposed and successfully applied to finite element simulated data and experimental data. In the next section the imaging stage of the DORT method is applied to this data.

5.4 Imaging flaws in steel welds using the DORT and TFM methods

In this section, the imaging stage of the DORT algorithm is applied to finite element simulated and experimental FMC data from a steel weld which contains defects. In addition, the TFM is applied to these FMC data sets to produce images for comparison. An image is created using the DORT method once the flaw has been detected using the largest singular value distribution. This highlights the time-frequency pairs where the corresponding eigenvectors can be used to back-

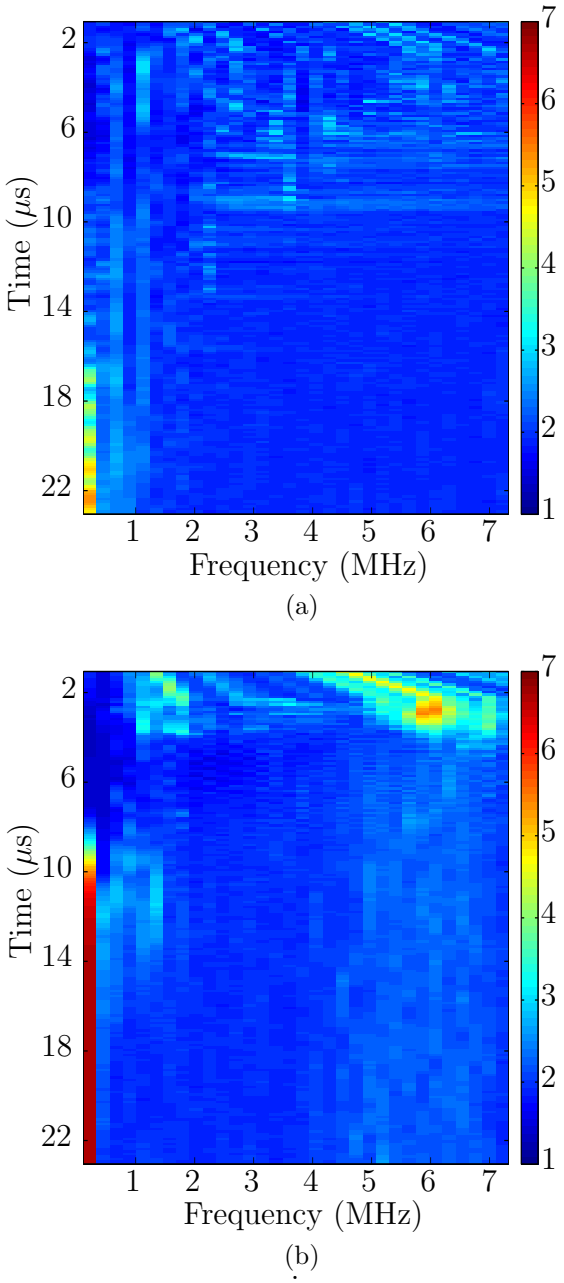

Figure 5.13: The largest singular value plots from the experimental FMC data from the steel weld (see Figure 5.12 for a schematic) where (a) there is no flaw and (b) where there is a 12 mm long vertical crack. The parameters used to generate the time-frequency response matrix in each case are given in Appendix C, Table C.4 and the material and ultrasonic array parameters used in each experiment are given in Appendix C, Table C.2.

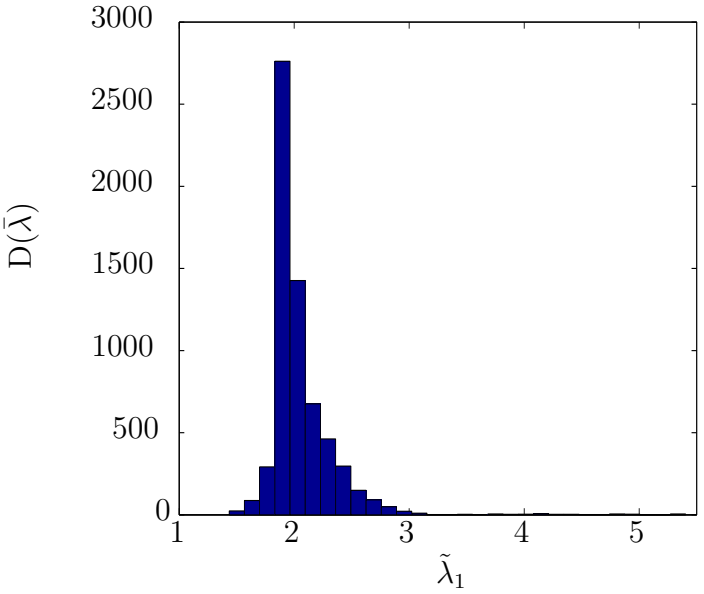

(a)

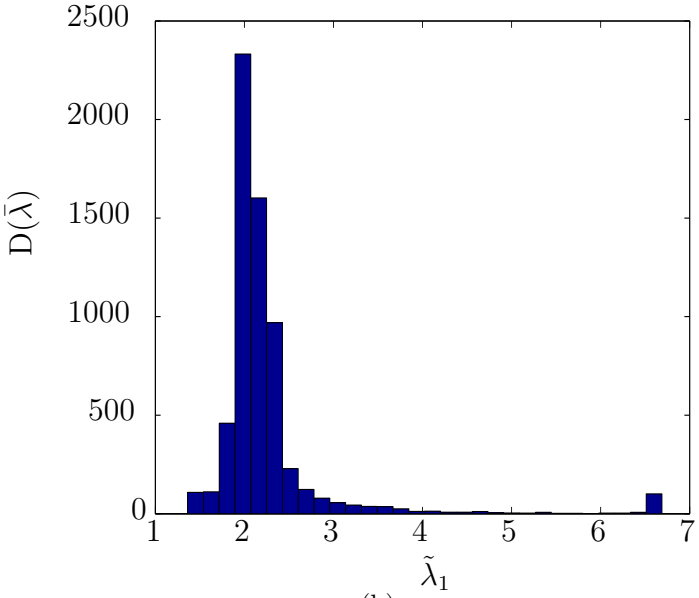

(b)

Figure 5.14: The histograms of the largest singular values across all time and frequency pairs from the experimental FMC data from a steel weld (see Figure 5.12 for a schematic) where (a) there is no flaw and (b) where there is a 12 mm long vertical crack. The parameters used to generate the time-frequency response matrix in each case are given in Appendix C, Table C.4 and the material and ultrasonic array parameters used in each experiment are given in Appendix C, Table C.2.

propagate and create an image of the defect (see equation (5.9)). It is important to note that within this work the most basic form of TFM has been used to generate the forthcoming images [27] and that there are more advanced versions of the method available [24, 25]. In the following sections all the images have been plotted on a decibel scale

$$I_{dB} = 20 \log_{10} \left(\frac{I}{I_{max}} \right), \tag{5.15}$$

where I is the image matrix produced and I_{max} is the maximum from the image matrix.

5.4.1 Image reconstruction of flaws within a steel weld using finite element simulated data

In this subsection, the DORT method (see Section 5.2.1) and the TFM method (see Section 5.2.2) are applied to the finite element simulated data from a steel weld with (a) side drilled hole inclusions of varying radii and (b) a horizontal crack (see Chapter 2, Section 2.3.1 for details of the finite element simulations). Figure 5.15 shows the image of a side drilled hole inclusion of radius 1.25 mm which was reconstructed using the DORT method. The set of singular values which lie above the detection threshold, as shown in Figure 5.10(b), were used to create this image. Figure 5.15(a) shows the full imaging domain, while Figure 5.15(b) shows an enlarged image of the flaw where the super-imposed white circular disc illustrates the approximate true size and location of the side drilled-hole. This figure shows that the DORT imaging algorithm has misplaced the flaw to the left by about 2.5 mm (this is the distance from the highest amplitude in the point spread function to the centre of the white disc). This is a result of beam divergence

of the ultrasonic wave due to the heterogeneous nature of the weld microstructure. The images from the DORT method can be compared with those generated using the TFM which are shown in Figure 5.16, where (a) shows the full imaging domain with the reflections from the back wall and front face cropped and (b) shows the area containing the flaw only. It can be seen from this figure that the TFM has detected the flaw and in (a) the reflections from the grain boundaries within the weld microstructure are also visible. In Figure 5.16(b) it can be seen that the distance between the maximum amplitude in the image and the actual location of the flaw (centre of the white disc) is out by about 2 mm in both the horizontal and vertical direction. The signal to noise ratio (SNR) for the images generated using DORT and TFM methods is calculated by taking the maximum amplitude (A_{max}) in the image and dividing by the maximum amplitude from a region in the image which does not contain any scattering from the flaw but does contain noise (A_0) , which gives

$$SNR = 20 \log_{10} \left(\frac{A_{max}}{A_0} \right). \tag{5.16}$$

The region used to represent noise has been highlighted in each of the images produced via a black or white rectangle. The maximum within the noisy region is used as this represents what could potentially be mistaken as a flaw (a false-positive outcome). The SNR in Figure 5.15 was calculated by taking A_0 to be the maximum amplitude in the region within the black rectangle in Figure 5.15(a) and this divides A_{max} to give 19.81 dB. Similarly, A_0 from Figure 5.16(a) is the maximum in the region outlined by the white rectangle, which represents the noise and divides A_{max} to give 13.14 dB. The SNR is a reasonable measure of the capabilities of the imaging techniques. However, the subjectivity in this calculation should be noted; the subjectivity arises from the choice in the noisy region from which A_0 is determined.

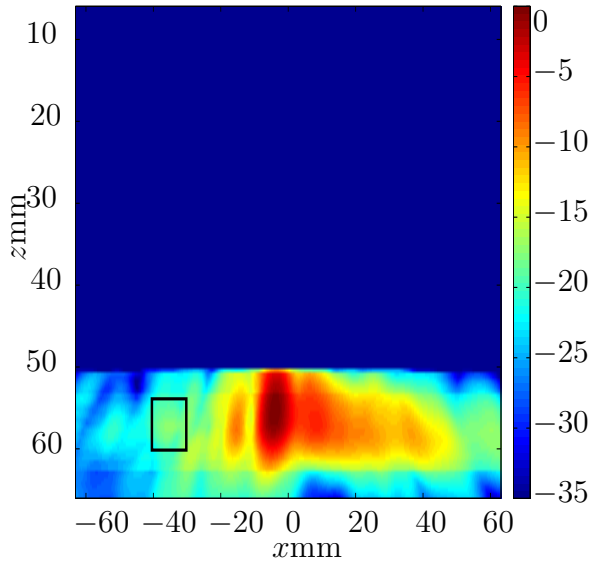

(a)

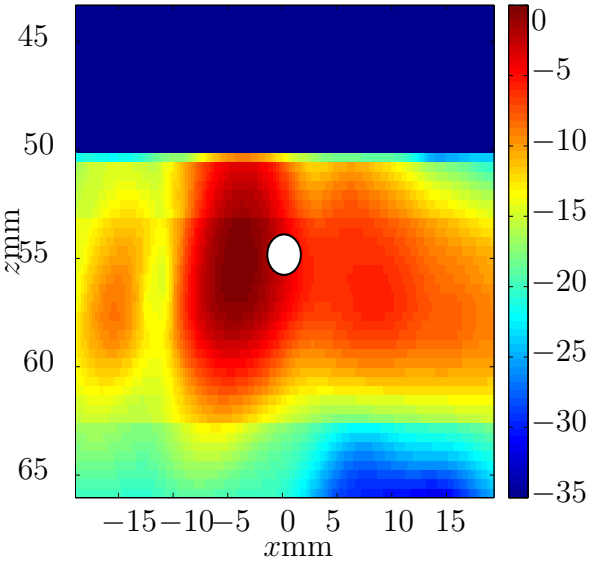

(b)

Figure 5.15: The DORT method was used to generate the image of a 1.25 mm radius side drilled hole in a steel weld from finite element simulated FMC data (see Chapter 2 Section 2.3.1 for details of the simulation). The image in (a) shows the full imaging domain and (b) the imaging domain including only the flaw where the white disc shows the approximate true location and size of the flaw. The black rectangle in (a) shows the region which represents noise and is used within the SNR calculation (given by equation (5.16)).

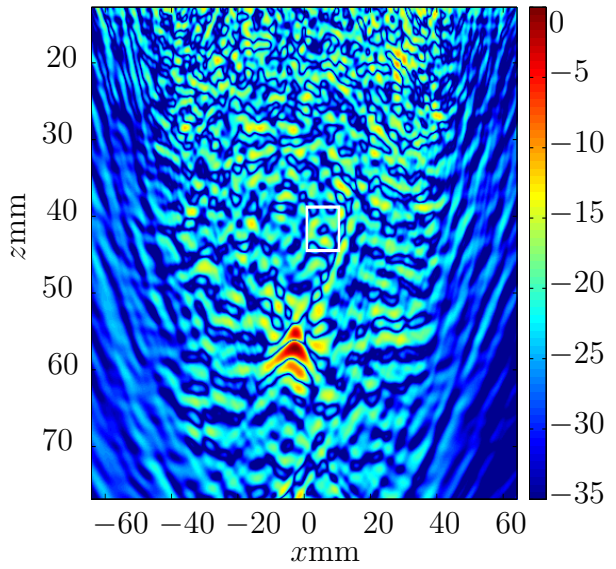

(a)

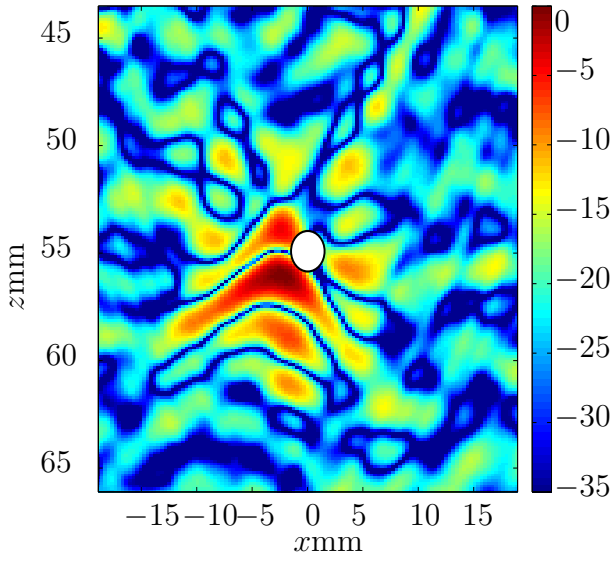

(b)

Figure 5.16: The TFM method was used to generate the image of a 1.25 mm radius side drilled hole in a steel weld from finite element simulated FMC data (see Chapter 2 Section 2.3.1 for details of the simulation). The image in (a) shows the full imaging domain and (b) the imaging domain including only the flaw where the white disc shows the approximate true location and size of the flaw. The white rectangle in (a) shows the region which represents noise and is used within the SNR calculation (given by equation (5.16))

The next data set that the imaging methods were applied to was the finite element simulated data from a steel weld with a 0.5 mm radius side drilled hole inclusion. The resulting image using the DORT algorithm is shown in Figure 5.17 where again (a) shows the full imaging domain and (b) shows the flaw domain in more detail (the white disc shows the approximate actual location of the flaw). From these images it can be seen that the DORT method has successfully imaged the side drilled hole. However, the location of the imaged side drilled hole is out by approximately 4 mm in the horizontal direction and 3 mm in the vertical direction (using the maximum amplitude of the point spread function from the image as a reference point). The image in Figure 5.17(b) appears to be comprised of horizontal bands of images. This is due to the fact that for each time (T_p) where the first singular values are larger than the detection threshold ($\tilde{\lambda}_1(T_p, f_q) > \tau$) there is a different frequency range used to reconstruct the image. The SNR of this image is 22.94 dB, where A_0 in equation (5.16) is the maximum amplitude in the region which represents the noise and is enclosed by the black box which is shown in Figure 5.17(a). It is surprising that the SNR arising from the image generated using the DORT method is higher here that when the side drilled hole of radius 1.25 mm was included. This highlights the subjectivity surrounding these imaging methods. As another area in the image shown in Figure 5.17(a) could be chosen to represent the noise in the image which would ensure that the SNR was lower than that in Figure 5.15(a). The TFM was also applied to this data set to produce the images in Figure 5.18. Figure 5.18(a) shows the full imaging domain (cropped to reduce the effects of the front face and backwall reflections) and (b) shows the imaging domain containing the flaw. Figure 5.18(a) shows that the scattering from the flaw is closer to the order of the noise as a result of the reduction in the radius of the side drilled hole. The white disc shows the location

and size of the flaw. Again, the distance between the maximum amplitude and the centre of the white disc is approximately 2mm along the vertical axis and 3 mm along the horizontal axis. The SNR in this image is calculated by dividing A_{max} by A_0, which is taken to be the maximum amplitude in the region enclosed by the black box shown in Figure 5.18(a), to give 8.03 dB. As expected the reduction in the radius of the side drilled hole has reduced the SNR of the image.

The next configuration considered is when a horizontal crack of length 5mm is included within the simulation (see Appendix C, Table C.1 for the parameters from the finite element simulation). The image reconstructed using the DORT method is shown in Figure 5.19 where the white line demonstrates the actual location and length of the flaw. The SNR in this figure is determined using equation (5.16) and is 19.05 dB where A_0 is the maximum amplitude in the region which represents the noise in the image and is depicted by the black rectangle. The image shown in this figure does not look particularly crack like and this is due to the fact that the DORT method is developed for imaging point like scatterers [51]. It has been shown that up to four eigenvalues can be associated with one scatterer depending on its size and characteristics [67]. A potential avenue for future work would entail further investigation of the singular value distribution when there is a crack like defect within the structure and developing the DORT method to include more than just the largest singular value in the image reconstruction. TThe TFM was also applied to this data to generate the images shown in Figure 5.20(a) where the white line indicates the true location and length of the crack. The SNR from the TFM image is 19.69 dB, where A_0 is the estimate to the maximum amplitude from the noise represented by the region enclosed by the white rectangle in Figure 5.20. In the next subsection the DORT and TFM algorithms will be applied to experimental data.

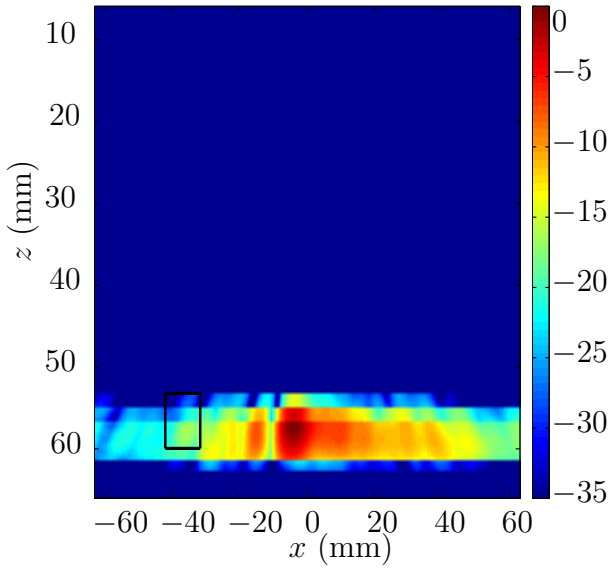

(a)

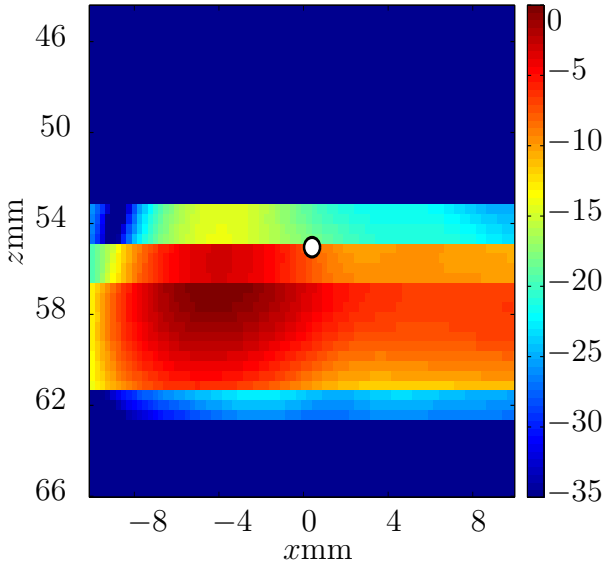

(b)

Figure 5.17: The DORT method was used to generate the image of a 0.5 mm radius side drilled hole in a steel weld from finite element simulated FMC data (see Chapter 2 Section 2.3.1 for details of the simulation). The image in (a) shows the full imaging domain and (b) the imaging domain including only the flaw where the white disc shows the approximate true location and size of the flaw. The black rectangle in (a) shows the region which represents noise and is used within the SNR calculation (given by equation (5.16)

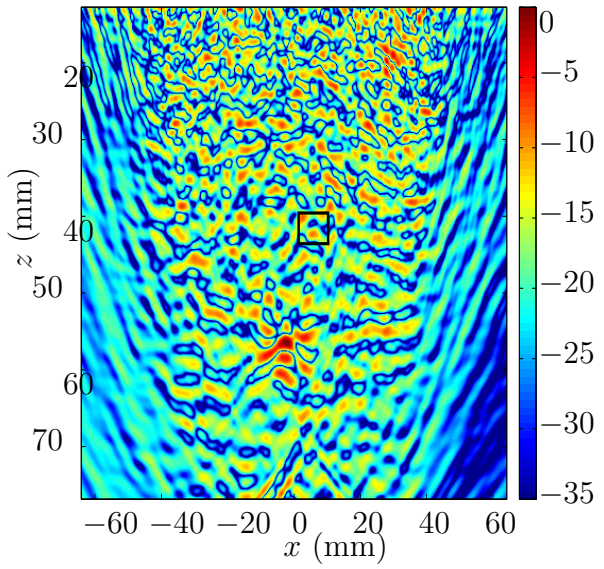

(a)

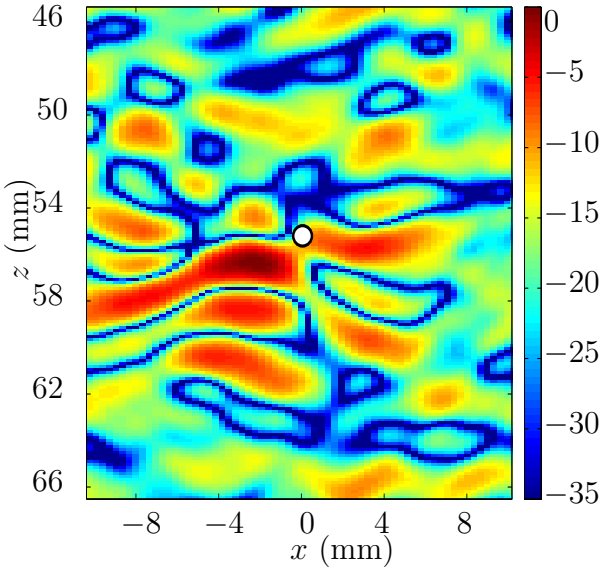

(b)

Figure 5.18: The TFM method was used to generate the image of a 0.5 mm radius side drilled hole in a steel weld from finite element simulated FMC data (see Chapter 2 Section 2.3.1 for details of the simulation). The image in (a) shows the full imaging domain and (b) an enlarged imaging domain around the flaw where the white disc shows the approximate true location and size of the flaw. The black rectangle in (a) shows the region which represents noise and is used within the SNR calculation (given by equation (5.16)

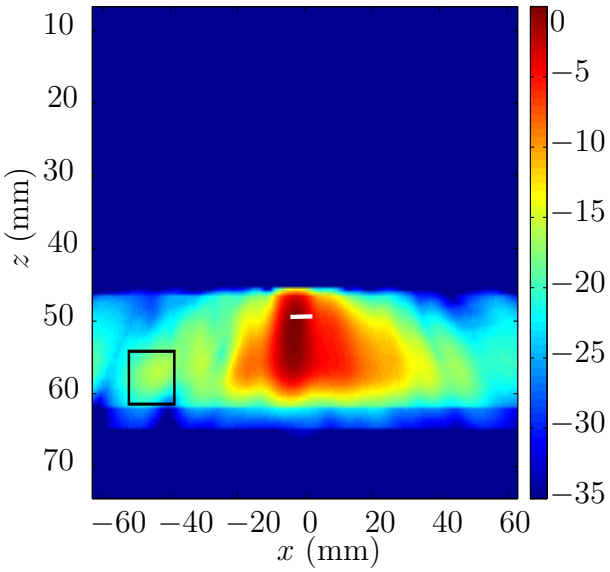

Figure 5.19: The DORT method was used to generate the image of a 2.5 mm radius horizontal crack in a steel weld from finite element simulated FMC data (see Chapter 2, Section 2.3.1 for details of the simulation). The white line indicates the approximate true location and length of the crack inclusion. The black rectangle shows the region which represents noise and is used within the SNR calculation (given by equation (5.16))

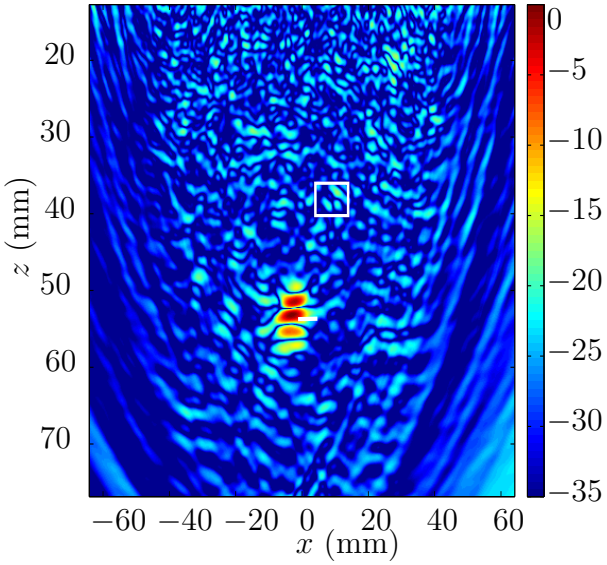

Figure 5.20: The TFM method was used to generate the image of a 2.5 mm radius horizontal crack in a steel weld from finite element simulated FMC data (see Chapter 2, Section 2.3.1 for details of the simulation). The white line shows the approximate location and size of the crack and the white rectangle shows the region which represents noise and is used within the SNR calculation (given by equation (5.16)).

5.4.2 Image reconstruction of a flaw within a steel weld using experimental data

In this subsection the DORT and TFM imaging algorithms are applied to the experimental FMC data outlined in Section 5.3.4 which is from an Inconel weld with a 12 mm vertical crack inclusion approximately 37 mm from the array (the parameters from this experiment are given in Appendix C, Table C.2). The DORT method was applied to this FMC data set to produce the image in Figure 5.21(a) where it can be seen that there is some interference at a depth of about 5 mm. This is a result of the reflection from the front face of the test piece. It can be seen from Figure 5.13(b) that there is a cluster of larger singular values between 2-4μs and 6 -7 MHz which are associated with this front face reflection. The white vertical line indicates the position of the flaw. The interference from the front face is removed by increasing the starting time, t_1, for the sampling when creating the time-frequency matrix, $\mathbf{K}(T_p, f_q)$, to ensure that reflections from this front face are not included. The image with the front face reflections removed is shown in Figure 5.13(b) where the vertical, white line shows the actual location and length of the crack inclusion. This figure shows a very large reflection at about 37 mm which is the depth where the flaw is located within the weld. However, the image does not appear very crack-like. This reflection is from the tip of the crack inclusion and the DORT reconstruction is undoubtedly picking up on the spherical wave that is scattered from that point. The SNR is calculated by taking the maximum amplitude in the image (this occurs at the reflection from the crack tip) and dividing by the maximum within the black rectangle shown in Figure 5.21(b), which encloses a region that represents the noise in the image, to give 13.49 dB. As expected, this is much lower than that calculated from the images produced from the finite simulated data. The TFM algorithm was applied to

this data and the resulting image is shown in Figure 5.22, the vertical white line shows the length and location of the crack. At about 85 mm the backwall is only just visible and it almost impossible to detect the crack within this image. The SNR is calculated by taking the maximum amplitude at the location of the crack and dividing by the maximum within the noise (the region enclosed by the black rectangle in Figure 5.22) to give 1.21 dB. Again, the SNR here is far lower than that when the methods are applied to the finite element simulated data. There is a lot more noise in the experimental data and this is due to a variety of factors. For instance in the experimental set up contact between the test piece and the transducer is imperfect, there is loss due to the transmission/reception sensitivities of the array, there is electrical noise and there will be some thermal losses too. In this case the image generated using the DORT method provides a higher SNR than that generated using TFM.

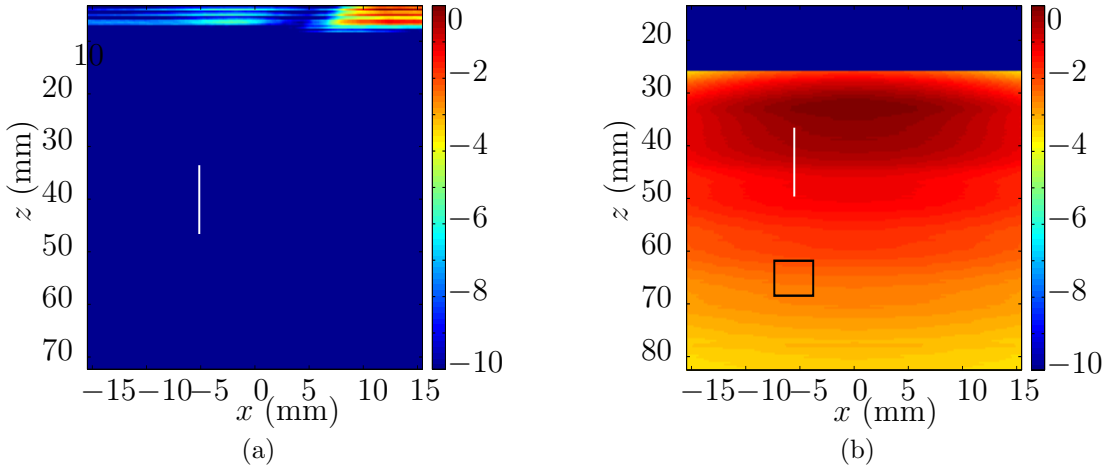

Figure 5.21: The DORT method was applied to experimental FMC data (see Figure 5.12 for a schematic of the experimental configuration) from a steel weld with a 12 mm long vertical crack inclusion 37 mm from the front face of the test piece. Figure(a) includes the response from the reflections from the front face of the test piece and (b) shows the image reconstuction of the domain containing the flaw where the white line indicates the approximate true location and length of the crack.

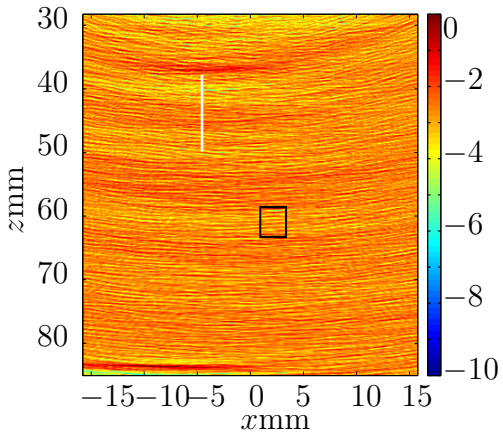

Figure 5.22: The TFM method was applied to experimental FMC data (see Figure 5.12 for a schematic of the experimental configuration) from a steel weld with a 12 mm long vertical crack inclusion 37 mm from the front face of the test piece.The black line indicates the approximate true location and length of the crack. The back wall of the test piece can be identified at 85 mm.

5.5 Conclusions

In this chapter the DORT and TFM detection and imaging algorithms were presented. A detection algorithm, based on the first stage of the DORT method, was outlined within which a detection criterion specific to steel welds was proposed. This detection algorithm was then applied successfully to finite element simulated data of a steel weld containing a side drilled hole (of radius 0.5 mm and 1.25 mm) and a horizontal crack (of length 5 mm). In addition, the method was applied to experimental FMC data from a steel weld with a 12 mm, vertical crack inclusion and compared to the results from FMC data where no flaw was present in the weld. The detection method objectively detected the flaw within the weld using the experimental FMC data. The DORT imaging method and the TFM method were then applied to these data sets. Both methods produced images which display the side drilled holes within the finite element simulated data. The final finite element simulated FMC data set from the steel weld contained a 5 mm long crack

and again both methods successfully detected the flaw. The image of the crack produced using the DORT method is not very crack like and this is due to the fact that the DORT method is designed for imaging point like reflectors. An avenue for future work would be to explore the potential improvements for imaging cracks and volumetric flaws using the DORT method by using all the singular values that exceed the threshold; even though they might not be the largest at a given time frequency pair. The methods were also applied to experimental data from a steel weld containing a 12 mm long vertical crack. The image produced using the DORT method shows a large reflection from the crack tip but it is almost impossible to identify the flaw within the image generated using TFM. The images can be compared via the SNR calculation. Whilst there is subjectivity surrounding this metric as the choice of noisy region affects the SNR, it transpired that the DORT method outperformed the TFM method.

Chapter 6

Conclusions

A mathematical model based approach has enabled some objective methods to be developed for sizing flaws within heterogeneous media. This eliminates the need for subjective thresholds that are often used within image processing techniques. Model based techniques for characterising defects within an elastic solid are derived using the Kirchhoff model which is a high frequency approximation to the scattering from a crack within a homogeneous medium from an elastic wave.

In Chapter 2, the scattering matrices from the model were used to derive an objective method for sizing cracks within an elastic solid. These scattering matrices were approximated by Toeplitz matrices in order to make analytical progress. Further approximations were then made to derive a formula which relates the maximum eigenvalue from a scattering matrix to the length of a crack within a homogeneous medium. It was shown that there is a one to one relation between the maximum eigenvalue and the crack length and so this method can be used to extract the crack length from ultrasonic data (the inverse problem). The advantage of deriving an analytical expression is that it can be interrogated to assess the effects of the system parameters on the method.

In Chapter 3, the sensitivity of the maximum eigenvalue approximation to changes in the system parameters was examined. First, the effects of varying the system parameters, such as the depth of the flaw in the model, the length of the array and the number of elements in the array, were numerically analysed. As expected, as the length of the array and the number of elements were increased simultaneously (this means a fixed pitch length) the sensitivity of the maximum eigenvalue to the crack radius increased. Similarly, as the depth of the flaw was decreased the crack sizing capabilities of the method increased. This analysis is practically useful when considering experimental design. Next the derivative of the maximum eigenvalue with respect to each of the system parameters was determined. These derivatives were used to analytically examine the sensitivity of the maximum eigenvalue to changes in the crack length, the depth of the flaw, the number of elements in the array and the length of the array. From this analysis it was concluded that the method is most sensitive to changes in the crack radius over the wavelength when the ratio is less than 1 and becomes less sensitive as this ratio is increased. This implies that the method of using the maximum eigenvalue to determine the size of a crack in a homogeneous material (the inverse problem) is most effective when the crack is sub-wavelength. For larger cracks another method should be adopted, perhaps an image-based method. In addition, the analysis of the derivative highlighted that errors in the measured length of the array, depth of the flaw, and number of elements has little effect on the inverse problem. Finally, the method outlined in Chapter 2 was applied to finite element simulated data from a homogeneous medium with a crack inclusion of 5 mm. The recovered crack length using this method was 4.4 mm. Future work may include applying this method to scattering matrices from a heterogeneous medium; although techniques for significantly reducing the noise within the scattering matrices may need to be

developed before the method can be successfully used.

The Kirchhoff model was used again in Chapter 4 to develop a frequency domain method for objectively sizing cracks, which uses the first minimum in the pulse echo response from a scattering matrix. An analytical expression was derived from the Kirchhoff model which demonstrates the one to one relationship between the crack radius and this first minimum. This analytical expression provides insight into the sensitivity of the method and to the errors which are a consequence of the discretisation of the model. It was shown that the discretisation of the ultrasonic array within the model results in errors in the recovered crack length. An approximation was derived to this error which was a function of the crack radius over the wavelength and the pitch of the array. In addition an upperbound was derived which relates the maximum crack length which can be recovered for a given pitch (and vice versa). The single frequency method was applied to finite element simulated data from a homogeneous medium with a crack inclusionof length 5 mm. The method successfully recovered a reasonable crack length with a 0.4 mm error. An alternative method which uses all points in the pulse echo response to size the crack was also applied to the finite element simulated data. However, a larger error of 1.5 mm was incurred when this approach was adopted. This single-frequency method was then extended to a multi-frequency technique which uses the first minimum in the pulse echo response across a range of frequencies. Before this method was applied to finite simulated data from a steel weld with a crack inclusion, it was necessary to apply a convolution technique to the data to reduce the noise within the scattering matrices. Once the noise was reduced, the multi-frequency method was applied to the finite element simulated data of a steel weld with a 5 mm long crack inclusion. The crack length was recovered with an error of 1 mm, which is reasonable when the assumptions within the model and

the simulation are considered.

In Chapter 5, the DORT and TFM methods for the detection and imaging of defects were explored (these are not based on the Kirchhoff model). The DORT method is an empirical time-frequency method based on time reversal principles and the TFM is an empirical time domain technique which uses delay and sum calculations to generate an image. The DORT method had not been applied before to ultrasonic data from a steel weld containing defects. The first stage of the DORT method was used to create an objective flaw detection method within which a detection criterion specific to steel welds was proposed. The detection algorithm uses the largest singular value from the SVD of the time-frequency domain data and if there exist largest singular values above the specified detection threshold then it can be objectively concluded that there is a flaw in the weld. This detection algorithm was applied successfully to finite element simulated data of a steel weld with side drilled hole (of radius 0.5 mm and 1.25 mm) and horizontal crack (of length 5 mm) inclusions. In addition the method was applied to experimental FMC data from a steel weld with a 12 mm, vertical crack inclusion and compared to the results from FMC data where no flaw was present in the weld. The detection method objectively detected the flaw within the weld using the experimental FMC data. The full DORT imaging method and the TFM method were then applied to these data sets. Both methods produced images which detect the side drilled holes within the finite element simulated data. The final finite element simulated FMC data set from the steel weld contained a 5 mm long crack and again both methods successfully detected the flaw. The image of the crack produced using the DORT method does not appear very crack like and this is due to the fact that the DORT method is designed for imaging point like reflectors. An avenue for future work would be to explore the potential improvements for imaging cracks

and volumetric flaws using the DORT method by using all the singular values that exceed the threshold; even though they might not be the largest at a given time frequency pair. The methods were also applied to experimental data from a steel weld containing a 12 mm long vertical crack. The image produced using the DORT method shows a large reflection from the crack tip but it is almost impossible to identify the flaw within the image generated using TFM. The images can be compared via the SNR calculation. There is subjectivity surrounding this metric as the choice of noisy region affects the SNR, however in each instance the DORT method produced images with a lower SNR than those produced using the TFM method.

Further future work may include the investigation of the effects of including curved cracks, and multiple cracks, within a structure. The Kirchhoff model would need to be adapted in order to include a non-linear crack. In addition, it would be interesting and beneficial to explore the potential inclusion of heterogeneities within the Kirchhoff model. In particular, to include heterogeneities akin to those within steel welds. If this was achieved, the methods outlined in this thesis could be used with this model and would perhaps produce more accurate results.

This thesis has made the first few steps in using a mathematical modelling based approach to make the detection, imaging and sizing of flaws in steel welds more objective. It is hoped that this will provide the impetus for such an approach to be taken up by engineers in the field where this objectivity in appraising a safety critical structure may have certain advantages.

Appendix A

Kirchhoff model and analysis of scattering matrices

In Chapter 2, Section 2.5.2 the coefficients $b_l^{(i)}$, $(l = 1, ..., 6,\ i = 1, 2)$ and $d_l^{(i)}$ $(l = 1, ..., 8,\ i = 1, ..., 10)$ from equations (2.87) and (2.90) are included in the approximation to the maximum eigenvalue from a scattering matrix and are defined in this appendix.

A.1 List of the coefficients $b_l^{(i)}$ and $d_l^{(i)}$.

The terms $b_l^{(i)}$ in equation (2.90), where $i = 1, 2$ and $l = 1, ..., 6$ are independent of $\hat{a}$ and again are functions of the number of the system parameters. Defining

$$b_1^{(1)} = -\frac{\sqrt{4-(\triangle y)^2}\pi}{6c^2(N-2)^2\rho}\left(\mu\left((\triangle y)^2(N+2)^2-4\right)-2L\right)\left((N-1)N\pi\sin\left(\frac{(N-4)\pi}{6(N-2)}\right)\right.$$
$$\left.+\,3(N-2)^2\cos\left(\frac{(N-4)\pi}{6(N-2)}\right)\right), \tag{A.1}$$

$$b_2^{(1)} = \frac{2\sqrt{4-(\triangle y)^2}\pi}{9c^2(N-2)^2\rho}\Bigg(2(N-1)\pi\sin\left(\frac{(N-4)\pi}{6(N-2)}\right)\left(\mu\left((\triangle y)^2\left(2N^2+5N+2\right)-2\right)-L\right)$$
$$+9(\triangle y)^2\mu(N-2)^2(N+2)\cos\left(\frac{(N-4)\pi}{6(N-2)}\right)\Bigg), \tag{A.2}$$

$$b_3^{(1)} = -\frac{2(\triangle y)^2\sqrt{4-(\triangle y)^2}\mu\pi}{9c^2(N-2)^2\rho}\Bigg(\left(7N^2+N-8\right)\pi\sin\left(\frac{(N-4)\pi}{6(N-2)}\right)$$
$$+9(N-2)^2\cos\left(\frac{(N-4)\pi}{6(N-2)}\right)\Bigg), \tag{A.3}$$

$$b_4^{(1)} = \frac{8(\triangle y)^2\sqrt{4-(\triangle y)^2}\mu(N-1)\pi^2\sin\left(\frac{(N-4)\pi}{6(N-2)}\right)}{9c^2(N-2)^2\rho}, \tag{A.4}$$

$$b_5^{(1)} = 0, \tag{A.5}$$

$$b_6^{(1)} = 0, \tag{A.6}$$

$$b_1^{(2)} = \frac{(\triangle y)^2\sqrt{4-(\triangle y)^2}(N+2)^2\pi^3}{48c^2(N-2)^2\rho}\left(\mu\left((\triangle y)^2(N+2)^2-4\right)-2L\right)$$
$$\times\left((N-1)N\pi\sin\left(\frac{(N-4)\pi}{6(N-2)}\right)+3(N-2)^2\cos\left(\frac{(N-4)\pi}{6(N-2)}\right)\right), \tag{A.7}$$

$$b_2^{(2)} = -\frac{\pi^3(\triangle y)^2\sqrt{4-(\triangle y)^2}(N+2)}{36c^2(N-2)^2\rho}\Bigg(\pi(N-1)\sin\left(\frac{\pi(N-4)}{6(N-2)}\right)\Bigg(\mu\Bigg(8\left((\triangle y)^2-1\right)$$
$$+7(\triangle y)^2N^3+30(\triangle y)^2N^2+4\left(9(\triangle y)^2-4\right)N\Bigg)-4L(2N+1)\Bigg)$$
$$+18(N-2)^2\sin\left(\frac{\pi(N-1)}{3(N-2)}\right)\left(\mu\left((\triangle y)^2(N+2)^2-2\right)-L\right)\Bigg), \tag{A.8}$$

$$b_3^{(2)} = \frac{(\triangle y)^2\sqrt{4-(\triangle y)^2}\pi^3}{18c^2(N-2)^2\rho}\Bigg((N-1)\pi\sin\left(\frac{(N-4)\pi}{6(N-2)}\right)\Bigg(\mu\Bigg(32(\triangle y)^2+13(\triangle y)^2N^3$$
$$+60(\triangle y)^2N^2+14\left(6(\triangle y)^2-1\right)N-16\Bigg)-L(7N+8)\Bigg)$$
$$+9(N-2)^2\cos\left(\frac{(N-4)\pi}{6(N-2)}\right)\left(\mu\left(3(\triangle y)^2(N+2)^2-2\right)-L\right)\Bigg), \tag{A.9}$$

$$b_4^{(2)} = -\frac{2(\triangle y)^2\sqrt{4-(\triangle y)^2}\pi^3}{9c^2(N-2)^2\rho}\Bigg((N-1)\pi\sin\left(\frac{(N-4)\pi}{6(N-2)}\right)$$
$$\times\left(2\mu\left(3(\triangle y)^2\left(N^2+3N+2\right)-1\right)-L\right)$$
$$+9(\triangle y)^2\mu(N-2)^2(N+2)\cos\left(\frac{(N-4)\pi}{6(N-2)}\right)\Bigg), \tag{A.10}$$

$$b_5^{(2)} = \frac{(\triangle y)^4\sqrt{4-(\triangle y)^2}\mu\pi^3}{9c^2(N-2)^2\rho}\Bigg(\left(11N^2+5N-16\right)\pi\sin\left(\frac{(N-4)\pi}{6(N-2)}\right)+9(N-2)^2\cos\left(\frac{(N-4)\pi}{6(N-2)}\right) \tag{A.11}$$

and

$$b_6^{(2)} = -\frac{4(\triangle y)^4\sqrt{4-(\triangle y)^2}\mu(N-1)\pi^4\sin\left(\frac{(N-4)\pi}{6(N-2)}\right)}{9c^2(N-2)^2\rho}. \tag{A.12}$$

The terms $d_l^{(i)}$ in equation (2.90) where $i = 1, .., 10$ and $l = 1, .., 6$ are independent of $\hat{a}$ and again are functions of the number of the system parameters. Defining

$$H_1^{(1)} = \frac{1}{36(N-2)^2\sqrt{\pi}}, \qquad H_2^{(2)} = \frac{1}{6(N-2)^2}, \tag{A.13}$$

and

$$\hat{B} = (-1+N)N\pi \sin\left(\frac{(N-4)\pi}{6(N-2)}\right) + 3(N-2)^2 \sin\left(\frac{(N-1)\pi}{3(-2+N)}\right) \tag{A.14}$$

then substituting these into $d_l^{(1)}$ gives

$$d_1^{(1)} = 5H_1^{(1)}\hat{B}T^2(T^2-24), \tag{A.15}$$

$$d_1^{(2)} = 4H_1^{(1)}\hat{B}\pi(\triangle y)T\left(2N\left(7T^2-78\right)+3\left(T^2-4\right)\right), \tag{A.16}$$

$$d_1^{(3)} = H_1^{(1)}\hat{B}6\pi^2(\triangle y)^2(3N+1)\left(N\left(13T^2-44\right)+T^2+12\right), \tag{A.17}$$

$$d_1^{(4)} = H_1^{(1)}\hat{B}4\pi^3(\triangle y)^3(3N+1)\left(36N^2+9N-1\right)T, \tag{A.18}$$

$$d_1^{(5)} = H_1^{(1)}\hat{B}(\triangle y)^4(11N-3)(3\pi N+\pi)^3, \tag{A.19}$$

$$d_1^{(6)} = H_1^{(2)}\hat{B}\frac{5T\left(T^2-8\right)}{\sqrt{\pi}}, \tag{A.20}$$

$$d_1^{(7)} = H_1^{(2)} \hat{B} \sqrt{\pi} (\triangle y) \left(N \left(41T^2 - 88 \right) + 7T^2 + 24 \right), \tag{A.21}$$

$$d_1^{(8)} = H_1^{(2)} \hat{B} \pi^{3/2} (\triangle y)^2 \left(111N^2 + 34N - 1 \right) T, \tag{A.22}$$

$$d_1^{(9)} = H_1^{(2)} \hat{B} \pi^{5/2} (\triangle y)(3N+1)^2 (11N - 3), \tag{A.23}$$

and

$$d_1^{(10)} = 0, \tag{A.24}$$

where T is given by equation (2.105) Next, defining

$$H_2^{(1)} = -\frac{\sqrt{\pi}}{27(N-2)^2} \qquad \text{and} \qquad H_2^{(2)} = \frac{2\sqrt{\pi}}{9(-2+N)^2)} \tag{A.25}$$

and substituting into $d_2^{(i)}$ gives

$$d_2^{(1)} = H_2^{(1)} 5(N-1)T^2 \left(T^2 - 24 \right) \sin \left(\frac{\pi(N-4)}{6(N-2)} \right), \tag{A.26}$$

$$\begin{aligned} d_2^{(2)} = H_2^{(1)} 2(\triangle y) T (81(N-2)^2 T^2 + \pi(N-1)(55N+6)T^2 - 864(N-2)^2 \\ - 24\pi(N-1) - 600\pi(N-1)N) \sin \left(\frac{\pi(N-1)}{3(N-2)} \right), \end{aligned} \tag{A.27}$$

$$d_2^{(3)} = H_2^{(1)} 6\pi(\triangle y)^2 (3N^3(75T^2 + 2\pi(19T^2 - 62) - 240) + N^2(-855T^2 + \pi(364 - 83T^2) + 2880) - 10N(\pi(3T^2 - 2) - 72(T^2 - 4)) + 180T^2 - \pi(T^2 + 12)) \sin\left(\frac{\pi(N-1)}{3(N-2)}\right), \tag{A.28}$$

$$d_2^{(4)} = H_2^{(1)} 2\pi^2(\triangle y)^3 T \Bigg(27(69N^2 + 26N + 1)(N-2)^2 \sin\left(\frac{\pi(N-1)}{3(N-2)}\right) + \pi(837N^4 - 477N^3 - 339N^2 - 23N + 2) \sin\left(\frac{\pi(N-4)}{6(N-2)}\right)\Bigg), \tag{A.29}$$

$$d_2^{(5)} = H_2^{(1)} \pi^3(\triangle y)^4 \Bigg(54(7N-1)(-3N^2 + 5N + 2)^2 \sin\left(\frac{\pi(N-1)}{3(N-2)}\right) + \pi(159N^3 - 175N^2 + 13N + 3)(3N+1)^2 \sin\left(\frac{\pi(N-4)}{6(N-2)}\right)\Bigg), \tag{A.30}$$

$$d_2^{(6)} = H_2^{(2)} \pi^3(\triangle y)^4 \Bigg(54(7N-1)\left(-3N^2 + 5N + 2\right)^2 \sin\left(\frac{\pi(N-1)}{3(N-2)}\right) + \pi\left(159N^3 - 175N^2 + 13N + 3\right)(3N+1)^2 \sin\left(\frac{\pi(N-4)}{6(N-2)}\right)\Bigg), \tag{A.31}$$

$$d_2^{(7)} = H_2^{(2)} 5(N-1)T\left(T^2 - 8\right) \sin\left(\frac{\pi(N-4)}{6(N-2)}\right), \tag{A.32}$$

$$d_2^{(8)} = H_2^{(2)}\pi(\triangle y)^2 T\Bigg(\pi(N-1)\left(321N^2+64N-1\right)\sin\left(\frac{\pi(N-4)}{6(N-2)}\right) + 90(7N+1)(N-2)^2\sin\left(\frac{\pi(N-1)}{3(N-2)}\right)\Bigg), \tag{A.33}$$

$$d_2^{(9)} = H_2^{(2)}\pi^2(\triangle y)^3\Bigg(9\left(93N^2+22N-3\right)(N-2)^2\sin\left(\frac{\pi(N-1)}{3(N-2)}\right) + \pi(378N^4-273N^3-121N^2+13N+3)\sin\left(\frac{\pi(N-4)}{6(N-2)}\right)\Bigg), \tag{A.34}$$

and

$$d_2^{(10)} = 0. \tag{A.35}$$

Also, define

$$H_3 = \frac{8\pi^{3/2}\Delta y}{9(N-2)^2} \tag{A.36}$$

which is substituted into $d_3^{(i)}$ to give

$$d_3^{(1)} = d_3^{(6)} = d_3^{(10)} = 0, \tag{A.37}$$

$$d_3^{(2)} = H_3(N-1)T\left(3T^2-32\right)\sin\left(\frac{\pi(N-4)}{6(N-2)}\right), \tag{A.38}$$

$$d_3^{(3)} = H_3 36(\triangle y)(N-2)^2\left(T^2-3\right)\sin\left(\frac{\pi(7-4N)}{3(N-2)}\right) - \pi\triangle y(N-1)\left((37N+5)T^2-116N\right)\cos\left(\frac{\pi(5-2N)}{3(N-2)}\right), \tag{A.39}$$

$$d_3^{(4)} = H_3\pi(\triangle y)^2 T\Bigg(18(11N+2)(N-2)^2\sin\left(\frac{\pi(N-1)}{3(N-2)}\right) + \pi(N-1)(N(135N+38)+1)\sin\left(\frac{\pi(N-4)}{6(N-2)}\right)\Bigg), \tag{A.40}$$

$$d_3^{(5)} = H_3\pi^2(\triangle y)^3(3N+1)\Bigg(90N(N-2)^2\sin\left(\frac{\pi(N-1)}{3(N-2)}\right) + \pi(N-1)(N(51N+4)-1)\sin\left(\frac{\pi(N-4)}{6(N-2)}\right)\Bigg), \tag{A.41}$$

$$d_3^{(7)} = (N-1)\left(13T^2-24\right)\sin\left(\frac{\pi(N-4)}{6(N-2)}\right), \tag{A.42}$$

$$d_3^{(8)} = (\triangle y)T\left(99(N-2)^2\sin\left(\frac{\pi(N-1)}{3(N-2)}\right) + \pi(N-1)(103N+10)\sin\left(\frac{\pi(N-4)}{6(N-2)}\right)\right), \tag{A.43}$$

and

$$d_3^{(9)} = \pi(\triangle y)^2\Bigg(9(29N+3)(N-2)^2\sin\left(\frac{\pi(N-1)}{3(N-2)}\right) + \pi(N-1)(N(180N+31)-3)\sin\left(\frac{\pi(N-4)}{6(N-2)}\right)\Bigg). \tag{A.44}$$

Let

$$H_4 = \frac{32\pi^{5/2}(\triangle y)^2}{9(N-2)^2}, \tag{A.45}$$

which gives $d_4^{(i)}$ in the following form:

$$d_4^{(1)} = H_4 d_4^{(2)} = d_4^{(6)} = d_4^{(7)} = d_4^{(10)} = 0, \tag{A.46}$$

$$d_4^{(3)} = H_4 4(N-1)\left(T^2-3\right)\sin\left(\frac{\pi(N-4)}{6(N-2)}\right), \tag{A.47}$$

$$d_4^{(4)} = H_4(\triangle y)T\Bigg(21(N-2)^2\sin\left(\frac{\pi(N-1)}{3(N-2)}\right) + \pi(N-1)(29N+4) \times \sin\left(\frac{\pi(N-4)}{6(N-2)}\right)\Bigg), \tag{A.48}$$

$$d_4^{(5)} = H_4\pi(\triangle y)^2\Big(3(19N+3)(N-2)^2\sin\left(\frac{\pi(N-1)}{3(N-2)}\right) + \pi(N-1)N(49N+13)\sin\left(\frac{\pi(N-4)}{6(N-2)}\right)\Big), \tag{A.49}$$

$$d_4^{(8)} = H_4 11(N-1)\sin\left(\frac{\pi(N-4)}{6(N-2)}\right), \tag{A.50}$$

and

$$d_4^{(9)} = H_4 27\triangle y(N-2)^2\sin\left(\frac{\pi(N-1)}{3(N-2)}\right) + \pi\triangle y(N-1)(38N+3)\sin\left(\frac{\pi(N-4)}{6(N-2)}\right). \tag{A.51}$$

Finally, let

$$H_5 = \frac{64\pi^{7/2}(\triangle y)^3}{3(N-2)^2} \tag{A.52}$$

which gives

$$d_5^{(1)} = d_5^{(2)} = d_5^{(3)} = d_5^{(6)} = d_5^{(7)} = d_5^{(8)} = d_5^{(10)} = 0, \tag{A.53}$$

$$d_5^{(4)} = H_5 \frac{14}{9}(N-1)T \sin\left(\frac{\pi(N-4)}{6(N-2)}\right), \tag{A.54}$$

$$d_5^{(5)} = 3\triangle y(N-2)^2 \sin\left(\frac{\pi(N-1)}{3(N-2)}\right) + \frac{1}{9}\pi\triangle y(N-1)(47N+6)\sin\left(\frac{\pi(N-4)}{6(N-2)}\right), \tag{A.55}$$

$$d_5^{(9)} = 2(N-1)\sin\left(\frac{\pi(N-1)}{3(N-2)}\right), \tag{A.56}$$

$$d_6^{(1)} = d_6^{(2)} = d_6^{(3)} = d_6^{(4)} = d_6^{(6)} = d_6^{(7)} = d_6^{(8)} = d_6^{(9)} = d_6^{(10)} = 0 \tag{A.57}$$

and

$$d_6^{(5)} = -\frac{256\pi^{9/2}(\triangle y)^4(N-1)\sin\left(\frac{\pi(N-4)}{6(N-2)}\right)}{9(N-2)^2}. \tag{A.58}$$

Appendix B

Derivatives from Chapter 3

In Chapter 3, the derivative of the approximation to the maximum eigenvalue from a scattering matrix (equation (2.100)) is determined. Within the expression given by equation (2.100) the functions $\hat{A}$, $\hat{S}_j(\hat{a})$ $(j = 1, 2)$, $Q(\hat{a})$, $p(\hat{a})$ and $\phi(\hat{a})$ need to be differentiated with respect to the crack length over wavelength $\hat{a}$, the array length l, the number of elements in the array N and the depth of the flaw d. These derivatives are determined within this appendix.

B.1 Derivative with respect to the crack size over the wavelength

The derivatives with respect to the crack size over the wavelength of the functions stated above are given in this section. First, from equation (3.11) the derivative of $\hat{S}_j(\hat{a})$ for $(j = 1, 2)$ is given by

$$\frac{\partial \hat{S}_j}{\partial \hat{a}} = \sum_{r=1}^{6} b_r^{(j)} \frac{\partial S_r^{(1)}}{\partial \hat{a}}, \tag{B.1}$$

using equation (2.85), and

$$\frac{\partial S_r^{(1)}}{\partial \hat{a}} = \frac{\partial t^*}{\partial \hat{a}} \left((t^*+1)^{r-1} + \sum_{k=1}^{h} B_k \binom{r-1}{k} (t^*+1)^{r-k-1} \right) \tag{B.2}$$

is determined using equation (2.85) with

$$\frac{\partial t^*}{\partial \hat{a}} = \frac{T}{2\pi \hat{a}^2 (\triangle y)} \tag{B.3}$$

which is calculated using equation (2.103). In equation (3.11), the partial derivative of $Q(\hat{a})$, given by equation (2.99), is of the form

$$\frac{\partial Q}{d\hat{a}} = \left(\hat{S}_3 + \hat{S}_4 \right)^{-1/2} \left(\hat{S}_3 \frac{\partial \hat{S}_3}{\partial \hat{a}} + \hat{S}_4 \frac{\partial \hat{S}_4}{\partial \hat{a}} \right), \tag{B.4}$$

where

$$\frac{\partial \hat{S}_3}{\partial \hat{a}} = \frac{\partial B}{\partial \hat{a}} \sum_{j=0}^{4} D_k \hat{a}^j + B \sum_{j=0}^{4} j D_j \hat{a}^{j-1} + B \sum_{j=0}^{4} \frac{\partial D_j}{\partial \hat{a}} \hat{a}^j \tag{B.5}$$

and

$$\frac{\partial \hat{S}_4}{\partial \hat{a}} = \frac{\partial B}{\partial \hat{a}} \sum_{j=5}^{9} D_j \hat{a}^{j-5} + B \sum_{j=5}^{9} (j-5) D_j \hat{a}^{j-6} + B \sum_{j=5}^{9} \frac{\partial D_j}{\partial \hat{a}} \hat{a}^{j-5} \tag{B.6}$$

are determined using equations (2.94) and (2.95). The derivative of the prefactor B (equation (2.91)) is

$$\frac{\partial B}{\partial \hat{a}} = -\frac{5}{2} \frac{1}{(\pi \hat{a} (\triangle y)(2N - 2t^* - 3))^{7/2}} \left(\pi (\triangle y)(2N - 2t^* - 3) - \frac{T}{\hat{a}} \right) \tag{B.7}$$

and

$$\frac{\partial D_j}{\partial \hat{a}} = \sum_{r=1}^{8} \frac{\partial S_r^{(2)}}{\partial \hat{a}} d_r^{(j)} \tag{B.8}$$

from equation (2.96), with

$$\frac{\partial S_r^{(2)}}{\partial \hat{a}} = -\frac{\partial t^*}{\partial \hat{a}} \left((t^*+1)^{r-1} + \sum_{k=1}^{h} B_k \binom{r-1}{k} (t^*+1)^{r-k-1} \right) \tag{B.9}$$

which is obtained using equation (2.86). In equation (3.11), the derivative of $p(\hat{a})$ (equation (2.92)) is

$$\frac{\partial p}{\partial \hat{a}} = \pi(\triangle y) t^* + \hat{a}\pi(\triangle y) \frac{\partial t^*}{\partial \hat{a}} = \pi(\triangle y) t^* + \frac{T}{2\hat{a}}. \tag{B.10}$$

Finally, from equation (3.11) we have that

$$\frac{\partial \phi}{\partial \hat{a}} = \left(\frac{\partial \hat{S}_4}{\partial \hat{a}} \hat{S}_3 - \frac{\partial \hat{S}_3}{\partial \hat{a}} \hat{S}_4 \right) \Big/ (\hat{S}_3^2 + \hat{S}_4^2). \tag{B.11}$$

B.2 Derivative with respect to the number of elements in the array

The derivatives of the functions $\hat{A}$, $\hat{S}_j(\hat{a})$ $(j = 1, 2)$, $Q(\hat{a})$, $p(\hat{a})$ and $\phi(\hat{a})$ with respect to the number of elements in the array are given here. Where, from equation (2.82),

$$\frac{\partial \hat{A}}{\partial N} = \frac{2\pi(\triangle y)}{\rho c^2} \frac{\partial(\triangle y)}{\partial N} \left(\frac{1}{4} \left(1 - \frac{(\triangle y)^2}{4} \right)^{-1/2} \left(L + 2\mu \left(1 - \frac{(\triangle y)^2}{4} \right) \right) - \mu \sqrt{1 - \frac{(\triangle y)^2}{4}} \right) \tag{B.12}$$

and where

$$\frac{\partial(\triangle y)}{\partial N} = -\frac{(\triangle y)}{N-1} \tag{B.13}$$

from equation (2.20). The derivative of $\hat{S}_j$ $(j = 1, 2)$ with respect to N is given by

$$\frac{\partial \hat{S}_j}{\partial N} = \sum_{r=1}^{8} \frac{\partial b_r^{(j)}}{\partial N} S_r^{(1)} + b_r^{(j)} \frac{\partial S_r^{(1)}}{\partial N} \tag{B.14}$$

from equation (2.89), where the derivative of $S_j^{(1)}$, from equation (2.85), is

$$\begin{aligned} \frac{\partial S_r^{(1)}}{\partial N} = \frac{\partial t^*}{\partial N} &\left((t^*+1)^{r-1} + \sum_{k=1}^{r} B_k \binom{r-1}{k} (t^*+1)^{r-k-1} \right) \\ &- \frac{1}{2} \left(\left(\frac{N}{2} + 2 \right)^{r-1} + \sum_{k=1}^{r} B_k \binom{r-1}{k} \left(\frac{N}{2} + 2 \right)^{r-k-1} \right) \end{aligned} \tag{B.15}$$

and from equation (2.103)

$$\frac{\partial t^*}{\partial N} = \frac{1}{2} + \frac{T}{2\pi \hat{a} (\triangle y)^2} \frac{\partial(\triangle y)}{\partial N} = \frac{1}{2} - \frac{T}{2\pi \hat{a} (\triangle y)(N-1)}. \tag{B.16}$$

The derivatives of the coefficients $b_r^{(j)}$ were calculated using Mathematica. The derivative of Q (equation (2.99)) is defined as

$$\frac{\partial Q}{\partial N} = \left(\hat{S}_3 \frac{\partial \hat{S}_3}{\partial N} + \hat{S}_4 \frac{\partial \hat{S}_4}{\partial N} \right) (\hat{S}_3^2 + \hat{S}_4^2)^{-1/2}, \tag{B.17}$$

where

$$\frac{\partial \hat{S}_3}{\partial N} = \frac{\partial B}{\partial N} \sum_{k=0}^{4} D_k \hat{a}^k + B \sum_{k=0}^{4} \frac{\partial D_k}{\partial N} \hat{a}^k \tag{B.18}$$

and

$$\frac{\partial \hat{S}_4}{\partial N} = \frac{\partial B}{\partial N} \sum_{k=5}^{9} D_k \hat{a}^{k-5} + B \sum_{k=5}^{9} \frac{\partial D_k}{\partial N} \hat{a}^{k-5} \tag{B.19}$$

from equations (2.94) and (2.95), with

$$\frac{\partial D_k}{\partial N} = \sum_{r=1}^{8} \frac{\partial d_r^{(k)}}{\partial N} S_r^{(2)} + d_r^{(k)} \frac{\partial S_r^{(2)}}{\partial N} \tag{B.20}$$

from equation (2.96), and

$$\begin{aligned} \frac{\partial S_r^{(2)}}{\partial N} &= (N+1)^{r-1} + \sum_{k=1}^{r} B_k \binom{r-1}{k} (N+1)^{r-k-1}) \\ &\quad - \frac{\partial t^*}{\partial N} \left((t^*+1)^{r-1} + \sum_{k=1}^{h-1} B_k \binom{r-1}{k} (t^*+1)^{h-k-1} \right) \end{aligned} \tag{B.21}$$

using equation (2.86). Again, the derivatives of the coefficients $d_r^{(k)}$ were calculated using Mathematica. Also,

$$\frac{\partial B}{\partial N} = -\frac{5}{2} \frac{\pi \hat{a}}{(\pi \hat{a} (\triangle y)(2N - 2t^* - 3))^{7/2}} \left((2N - 2t^* - 3) \frac{\partial (\triangle y)}{\partial N} - 2\pi \hat{a} (\triangle y) \frac{\partial t^*}{\partial N} + 2(\triangle y) \right). \tag{B.22}$$

The derivative of p (equation(2.92)) with respect to N is given by

$$\frac{\partial p}{\partial N} = \hat{a}\pi \left(t^* \frac{\partial (\triangle y)}{\partial N} + (\triangle y) \frac{\partial t^*}{\partial N} \right) \tag{B.23}$$

and finally,

$$\frac{\partial \phi}{\partial N} = \frac{1}{\hat{S}_3^2 + \hat{S}_4^2} \left(\hat{S}_3 \frac{\partial \hat{S}_4}{\partial N} - \hat{S}_4 \frac{\partial \hat{S}_3}{\partial N} \right). \tag{B.24}$$

B.3 Derivative with respect to the length of the array

The derivatives of the functions $\hat{A}$, $\hat{S}_j(\hat{a})$ $(j = 1, 2)$, $Q(\hat{a})$, $p(\hat{a})$ and $\phi(\hat{a})$ with respect to the length of the array, l are given here. Where, from equation (2.82),

$$\frac{\partial \hat{A}}{\partial l} = \frac{2\pi}{\rho c^2}\frac{\partial(\triangle y)}{\partial l}\left(\mu(\triangle y)\sqrt{1-(\triangle y)^2/4} - \frac{(\triangle y)}{4}\left(1-\frac{(\triangle y)^2}{4}\right)^{-1/2}\left(L + 2\mu\left(1-\frac{(\triangle y)^2}{4}\right)\right)\right) \tag{B.25}$$

with

$$\frac{\partial(\triangle y)}{\partial l} = \frac{1}{(N-1)\sqrt{4d^2+l^2}}(1 - l^2(4d^2+l^2)^{-3/2}), \tag{B.26}$$

from equation (2.20). The derivative of $\hat{S}_j$, for $j = 1, 2$, is defined as

$$\frac{\partial \hat{S}_j}{\partial l} = \sum_{r=1}^{8}\frac{\partial b_r^{(j)}}{\partial l}S_r^{(1)} + b_r^{(j)}\frac{\partial S_r^{(1)}}{\partial l} \tag{B.27}$$

from equation (2.89) with

$$\frac{\partial S_r^{(1)}}{\partial l} = \frac{\partial t^*}{\partial l}\left((t^*+1)^{r-1} + \sum_{k=1}^{r} B_k \binom{r-1}{k}(t^*+1)^{r-k-1}\right) \tag{B.28}$$

where

$$\frac{\partial t^*}{\partial l} = \frac{T}{2\pi\hat{a}(\triangle y)^2}\frac{\partial(\triangle y)}{\partial l} \tag{B.29}$$

from equation (2.103). The derivatives of the coefficients $b_r^{(j)}$ were calculated using Mathematica. The partial derivative of Q (equation (2.99)) with respect to l is defined as

$$\frac{\partial Q}{\partial l} = \left(\hat{S}_3\frac{\partial \hat{S}_3}{\partial l} + \hat{S}_4\frac{\partial \hat{S}_4}{\partial l}\right)(\hat{S}_3^2 + \hat{S}_4^2)^{-1/2} \tag{B.30}$$

where

$$\frac{\partial \hat{S}_3}{\partial l} = \frac{\partial B}{\partial l} \sum_{k=0}^{4} D_k \hat{a}^k + B \sum_{k=0}^{4} \frac{\partial D_k}{\partial l} \hat{a}^k, \tag{B.31}$$

and

$$\frac{\partial \hat{S}_4}{\partial l} = \frac{\partial B}{\partial l} \sum_{k=5}^{9} D_k \hat{a}^{k-5} + B \sum_{k=5}^{9} \frac{\partial D_k}{\partial l} \hat{a}^{k-5}, \tag{B.32}$$

from equations (2.94) and (2.95) with

$$\frac{\partial D_k}{\partial l} = \sum_{r=1}^{8} \frac{\partial d_r^{(k)}}{\partial l} S_r^{(2)} + d_r^{(k)} \frac{\partial S_r^{(2)}}{\partial l} \tag{B.33}$$

and

$$\frac{\partial S_h^{(2)}}{\partial l} = -\frac{\partial t^*}{\partial l} \left((t^*+1)^{r-1} + \sum_{k=1}^{r} B_k \binom{r-1}{k} (t^*+1)^{r-k-1} \right). \tag{B.34}$$

Again, the derivatives of the coefficients $d_r^{(k)}$ were calculated using Mathematica. The next derivative is

$$\frac{\partial B}{\partial l} = -\frac{5}{2} \frac{\pi \hat{a}}{(\pi \hat{a} (\triangle y)(2N - 2t^* - 3))^{7/2}} \left((2N - 2t^* - 3) \frac{\partial (\triangle y)}{\partial l} - 2\pi \hat{a} (\triangle y) \frac{\partial t^*}{\partial l} \right) \tag{B.35}$$

from equation (2.91). The partial derivative of p with respect to l is

$$\frac{\partial p}{\partial l} = \frac{\hat{a}\pi}{2} \left((\triangle y) \frac{\partial t^*}{\partial l} + t^* \frac{\partial (\triangle y)}{\partial l} \right) \tag{B.36}$$

and finally

$$\frac{\partial \phi}{\partial l} = \frac{1}{\hat{S}_3^2 + \hat{S}_4^2} \left(\hat{S}_3 \frac{\partial \hat{S}_4}{\partial l} - \hat{S}_4 \frac{\partial \hat{S}_3}{\partial l} \right). \tag{B.37}$$

B.4 Derivative with respect to the depth of the flaw

The derivatives of the functions $\hat{A}$, $\hat{S}_j(\hat{a})$ $(j = 1, 2)$, $Q(\hat{a})$, $p(\hat{a})$ and $\phi(\hat{a})$ with respect to the depth of the flaw, d are given here. Where, from equation (2.82),

$$\frac{\partial \hat{A}}{\partial d} = \frac{2\pi}{\rho c^2}\frac{\partial(\triangle y)}{\partial d}\left(\mu(\triangle y)\sqrt{1-(\triangle y)^2/4} - \frac{(\triangle y)}{4}\left(1-\frac{(\triangle y)^2}{4}\right)^{-1/2}\left(L + 2\mu\left(1-\frac{(\triangle y)^2}{4}\right)\right)\right) \tag{B.38}$$

with

$$\frac{\partial(\triangle y)}{\partial d} = -\frac{4ld}{(N-1)(4d^2+l^2)^{3/2}}, \tag{B.39}$$

from equation (2.20). For $j = 1, 2$,

$$\frac{\partial \hat{S}_j}{\partial d} = \sum_{r=1}^{8}\frac{\partial b_r^{(j)}}{\partial d}S_r^{(1)} + b_r^{(j)}\frac{\partial S_r^{(1)}}{\partial d} \tag{B.40}$$

from equation (2.89), with

$$\frac{\partial S_r^{(1)}}{\partial d} = \frac{\partial t^*}{\partial d}\left((t^*+1)^{r-1} + \sum_{k=1}^{r} B_k \binom{r-1}{k}(t^*+1)^{r-k-1}\right) \tag{B.41}$$

where

$$\frac{\partial t^*}{\partial d} = \frac{T}{2\pi\hat{a}(\triangle y)^2}\frac{\partial(\triangle y)}{\partial d}. \tag{B.42}$$

The partial derivative of Q (equation (2.99)) with respect to d is defined as

$$\frac{\partial Q}{\partial d} = \left(\hat{S}_3\frac{\partial \hat{S}_3}{\partial d} + \hat{S}_4\frac{\partial \hat{S}_4}{\partial d}\right)(\hat{S}_3^2 + \hat{S}_4^4)^{-1/2} \tag{B.43}$$

where

$$\frac{\partial \hat{S}_3}{\partial d} = \frac{\partial B}{\partial d}\sum_{k=0}^{4} D_k \hat{a}^k + B\sum_{k=0}^{4}\frac{\partial D_k}{\partial d}\hat{a}^k \tag{B.44}$$

and

$$\frac{\partial \hat{S}_4}{\partial d} = \frac{\partial B}{\partial d}\sum_{k=5}^{9} D_k \hat{a}^{k-5} + B\sum_{k=5}^{9}\frac{\partial D_k}{\partial d}\hat{a}^{k-5} \tag{B.45}$$

from equations (2.94) and (2.95), with

$$\frac{\partial D_k}{\partial d} = \sum_{r=1}^{8}\frac{\partial d_r^{(k)}}{\partial d}S_r^{(2)} + d_r^{(k)}\frac{\partial S_r^{(2)}}{\partial d} \tag{B.46}$$

and

$$\begin{aligned}\frac{\partial S_r^{(2)}}{\partial d} &= \frac{\partial S_r^{(2)}}{\partial(\triangle y)}\frac{\partial(\triangle y)}{\partial d} \\ &= -\frac{\partial t^*}{\partial(\triangle y)}\frac{\partial(\triangle y)}{\partial d}\left((t^*+1)^{r-1} + \sum_{k=1}^{r} B_k\binom{r-1}{k}(t^*+1)^{r-k-1}\right).\end{aligned} \tag{B.47}$$

The derivative with respect to d of the function B given by equation (2.91) is

$$\frac{\partial B}{\partial d} = -\frac{5}{2}\frac{\pi\hat{a}}{(\pi\hat{a}(\triangle y)(2N-2t^*-3))^{7/2}}\left((2N-2t^*-3)\frac{\partial(\triangle y)}{\partial d} - 2\pi\hat{a}(\triangle y)\frac{\partial t^*}{\partial d}\right). \tag{B.48}$$

The partial derivative of p with repsect to d is

$$\frac{\partial p}{\partial d} = \frac{\hat{a}\pi}{2}\left((\triangle y)\frac{\partial t^*}{\partial d} + t^*\frac{\partial(\triangle y)}{\partial d}\right) \tag{B.49}$$

and finally

$$\frac{\partial \phi}{\partial d} = \frac{1}{\hat{S}_3^2 + \hat{S}_4^2}\left(\hat{S}_3\frac{\partial \hat{S}_4}{\partial d} - \hat{S}_4\frac{\partial \hat{S}_3}{\partial d}\right). \tag{B.50}$$

Appendix C

Data

Ultrasonic Transducer Array Parameters	Flaw type	Value	Units
Number of elements		64	-
Pitch		2	mm
Element width		1.5	mm
Transducer centre frequency		1.5	MHz
Array Length		128	mm
Average velocity (heterogeneous)		6300	ms^{-1}
Average velocity (homogeneous)		6600	ms^{-1}
Density of host material		8280	kg/m^3
Flaw (a)	Side drilled holes, radius	0.5-2.5	mm
Flaw (b)	Horizontal crack, length	5	mm
Depth of flaw		50	mm
Depth of sample		78.6	mm
Time sampling		173	ns

Table C.1: Parameters used in the finite element simulations of a homogeneous medium and a steel weld (heterogeneous medium). The parameters in each remained the same, however the inclusion of the weld grain structure in the simulation resulted in a slower average velocity. In the simulations the type of defect within the medium can be chosen as (a) side drilled hole defects, and (b) crack-like defects.

Ultrasonic Transducer Array Parameters	Value	Units
Number of elements	45	-
Pitch	2	mm
Element width	1.5	mm
Centre frequency (data with flaw)	5	MHz
Centre frequency (data with no flaw)	2	MHz
Array Length	90	mm
Average velocity	5760	ms^{-1}
Density of host material	8280	kg/m^3
Flaw	vertical crack, 12 long	mm
Depth of flaw	37	mm
Depth of sample	85	mm
Time sampling	1	ns

Table C.2: The parameters associated with experimental data from a test piece which contains an inconel 82/182 weld [70]. The parent material to the right of the weld is stainless steel 316L and to the left is carbon steel 300 with an inconel 182 buttering layer between this and the weld. Two data sets were collected, one where a flaw was (12mm long) known to be in the inspection area and another where there was no defect within the inspection area.

Parameters to create inter-element response	Value
Distance to back wall	76.8 mm
Time window ($\triangle T$)	15.7 mm
Number of time samples (N_T)	140
Number of frequencies (N_f)	32
Time step ($\triangle t$)	0.5 mm

Table C.3: Parameters used to generate the inter-element response matrix, $\mathbf{K}(T_p, f_q)$, from the ultrasonic data arising from the finite element simulation of a steel weld containing no flaw, side drilled hole inclusions of varying radii and a 2.5 mm, horizontal crack (see Table C.1 for simulation parameters). These parameters also apply to the response matrix, $\mathbf{K}(T_p, f_q)$, arising from the finite element simulation of a homogeneous medium with a crack inclusion.

Parameters to create inter-element response	Value
Distance to back wall	85mm
Time window ($\triangle T$)	17mm
Number of time samples (N_T)	200
Number of frequencies (N_f)	32
Time step ($\triangle t$)	0.34mm

Table C.4: Parameters used to generate the inter-element response matrix, $\mathbf{K}(T_p, f_q)$, from the experimental,ultrasonic data arising from the inconel steel weld. The parameters associated with this test piece and the experimental configuration are summarised in Table C.2.

Bibliography

[1] C. Hellier. *Handbook of Nondestructive Evaluation*. McGraw Hill Professional, New York, USA, 2012.

[2] R.D. Adams and P. Cawley. A review of defect types and non destructive testing techniques for composites and bonded joints. *NDT &E Int.*, 21(4):208–222, 1988.

[3] L. Cheng and G.Y. Tian. Pulsed electromagnetic *NDE* for defect detection and characterisation in composites. *IEEE Int. Instrumentation and Measurement Technology Conference*, pages 1902–1907, 2012.

[4] A. Ettemeyer. Laser shearography for inspection of pipelines. *Nuclear Engineering and Design*, 160:237–240, 1996.

[5] J.L. Rose. *Ultrasonic Waves in Solid Media*. Cambridge University Press, Cambridge, UK, 1999.

[6] L. Schmerr and S. Song. *Ultrasonic Nondestructive Evaluation Systems*. Springer, New York, USA, 2010.

[7] J. F. C. Windmill, J.C. Jackson, E. J. Tuck, and D. Robert. Keeping up with bats: Dynamic auditory tuning in a moth. *Current Biology*, 16(24):2418–2423.

[8] A.S. Feng, P.M. Narins, C.H. Xu, W.Y. Lin, Z.L. Yu, Q. Qiu, Z.M. Xu, and J.X. Shen. Ultrasonic communication in frogs. *Nature*, 400:333–336, 2006.

[9] P. Hoskins, K. Martin, and A. Thrush. *Diagnostic Ultrasound: Physics and Equipment*. Cambridge University Press, Cambridge, UK, 2010.

[10] S. Stein and M. Wysession. *An Introduction to Seismology, and Earthquakes and Earth Structures*. Blackwell Publishing, Hoboken, New Jersey, 2003.

[11] J. P. Charlesworth and J. A. G. Temple. *Engineering Applications of Ultrasonic Time of Flight Diffraction*. Research Studies Press Ltd, Baldock, Hertfordshire, England, 2001.

[12] X. Zhao, T. Qian, G. Mei, C. Kwan, R. Zane, C. Walsh, T. Paing, and Z. Popovic. Active health monitoring of an aircraft wing with an embedded piezoelectric sensor/actuator network: Wireless approaches. *Smart Mater. Struct.*, 16(4):1219–1225, 2007.

[13] P. W. Loveday. Guided wave inspection and monitoring of railway track. *Journal of Non-Destructive Engineering*, 31:303–309, 2012.

[14] P. Anugonda, J.S. Wiehn, and J.A. Turner. Diffusion of ultrasound in concrete. *Ultrasonics*, 39(6):429–435, 2001.

[15] B.W. Drinkwater and P.D. Wilcox. Ultrasonic arrays for non-destructive evaluation: A review. *NDT & E Int*, 39(7):525–541, 2006.

[16] G.D. Conolly, M.J.S. Lowe, S.I. Rokhlin, and J.A.G. Temple. Imaging of defects within austenitic steel welds using an ultrasonic array. *AIP Conference Proceedings, Illinois, Chicago*, 1096, 22-25 July 2009.

[17] A. Safari and E.K. Akdogan. *Piezoelectric and Acoustic Materials for Transducer Applications*. Springer, 233 Spring Street, New York, USA, 2008.

[18] A. Tarantola. *Inverse Problem Theory and Methods for Model Parameter Estimation*. SIAM, Philedelphia, USA, 2005.

[19] A. Kirsch. *An Introduction to the Mathematical Theory of Inverse Problems*. Springer, New York, US, 2011.

[20] J. Zhang, B.W. Drinkwater, and P.D. Wilcox. Longitudinal wave scattering from rough crack-like defects. *IEEE Ultrasonics, and Ferroelectrics and Frequency Control*, 58(10):2171–2179, 2011.

[21] H. Ammari, J. Garnier, H. Kang, W.K. Park, and K. Solna. Imaging schemes for cracks and inclusions. *SIAM Journal on Applied Mathematics*, 71(1):68–91, 2011.

[22] M. Bertero and M. Piana. *Inverse Problems in Biomedical Imaging: Modeling and Methods of Solution*. 2006.

[23] Lester W.Schmerr. *Fundamentals of Ultrasonic Nondestructive Evaluation: A Modelling Approach.* Plenum Press, New York, 1998.

[24] P.D. Wilcox, C. Holmes, and B.W. Drinkwater. Advanced reflector characterization with ultrasonic phased arrays in *NDE* applications. *IEEE Ultrasonics, and Ferroelectrics and Frequency Control*, 38(8):701–711, 2005.

[25] J. Zhang, B.W. Drinkwater, P.D. Wilcox, and A.J Hunter. Defect detection using ultrasonic arrays: The multi-mode total focusing method. *NDT & E Int*, 43(2):123–133, 2010.

[26] A.J Hunter, B.W. Drinkwater, and P.D. Wilcox. The wavenumber algorithm for full matrix imaging using an ultrasonic array. *IEEE Trans. Ultrason. Ferroelectr. Freq. Control*, 55(11):2450–2462, 2008.

[27] C. Holmes, B.W. Drinkwater, and P.D. Wilcox. Post processing of the full matrix of ultrasonic transmit receive array data for non destructive evaluation. *NDT & E Int*, 38(8):701–711, 2005.

[28] A. Velichko and P.D. Wilcox. An analytical comparison of ultrasonic array imaging algorithms. *The Journal of the Acoustical Society America*, 127(4):2378–2384, 2010.

[29] J. Zhang, B.W. Drinkwater, and P.D. Wilcox. Comparison of ultrasonic array imaging algorithms for nondestructive evaluation. *IEEE Ultrasonics, and Ferroelectrics and Frequency Control*, 60(8):1732–1745, 2013.

[30] J. Zhang, B.W. Drinkwater, and P.D. Wilcox. The use of ultrasonic arrays to characterize crack-like defects. *J Nondestructive Eval*, 29(4):222–232, 2010.

[31] A. Velichko and P. Wilcox. Reversible back-propagation imaging algorithm for postprocessing of ultrasonic array data. *IEEE Ultrasonics, and Ferroelectrics and Frequency Control*, 56(11):2492–2264, 2009.

[32] J. Zhang, B.W. Drinkwater, and P.D. Wilcox. Defect characterization using an ultrasonic array to measure the scattering coefficient matrix. *IEEE Ultrasonics, and Ferroelectrics and Frequency Control*, 55(10):2254–2264, 2008.

[33] C. Fan, M. Caleap, M. Pan, and B. W. Drinkwater. A comparison between ultrasonic array beamforming and super resolution imaging algorithms for non-destructive evaluation. *Ultrasonics*, 54:1842–1850, 2014.

[34] C. Li, D. Pain, P.D, Wilcox, B.W, and Drinkwater. Imaging composite material using ultrasonic arrays. *NDT & E Int.*, 53:8–17, 2013.

[35] J. Zhang, B.W. Drinkwater, and P.D. Wilcox. Effect of roughness on imaging and sizing rough crack-like defects using ultrasonic arrays. *IEEE Ultrasonics, and Ferroelectrics and Frequency Control*, 59(5):939–948, 2012.

[36] J. Zhang, B.W. Drinkwater, and P.D. Wilcox. Effects of array transducer inconsistencies on total focusing method imaging performance. *NDT & E Int.*, 44:361–368, 2011.

[37] A. J. Hunter, B. W. Drinkwater, and P.D. Wilcox. Least-squares estimation of imaging parameters for an ultrasonic array using known geometric image features. *IEEE Ultrasonics, and Ferroelectrics and Frequency Control*, 58(2):414–426, 2011.

[38] L. Borcea, G. Papanicolaou, and C. Tsogka. Interferometric array imaging in clutter. *Inverse problems*, 21:1419–1460, 2005.

[39] J.F. Synnevag, A. Austeng, and S. Holm. Adaptive beamforming applied to medical ultrasound imaging. *IEEE Ultrasonics, and Ferroelectrics and Frequency Control*, 54(8):1606–1613, 2007.

[40] J. Davies, F. Simonetti, M. Lowe, and P. Cawley. Review of synthetically focused guided wave imaging techniques with application to defect sizing. *AIP Conference Proceedings, Maine, USA*, 820(1):142–149, 31 July- 5 August 2006.

[41] L. Borcea, G. Papanicolaou, and C. Tsogka. Coherent interferometric imaging in clutter. *Geophysics*, 71(4):165–175, 2006.

[42] L. Borcea, G. Papanicolaou, and C. Tsogka. Adaptive time-frequency detection and filtering for imaging in heavy clutter. *SIAM Journal on Imaging Sciences*, 54(8):1541–1550, 2007.

[43] R.Alonso, L. Borcea, G. Papanicolaou, and C. Tsogka. Detection and imaging in strongly backscattering randomly layered media. *Inverse Problems*, 27(2):1541–1550, 2011.

[44] L. Borcea, G. Papanicolaou, and C. Tsogka. Coherent interferometry in finely layered random media. *Multiscale modeling and simulation*, 5(1):62–83, 2006.

[45] L. Borcea, G. Papanicolaou, and C. Tsogka. Theory and applications of time reversal and interferometric imaging. *Inverse Problems*, 19:139–164, 2003.

[46] M. Fink, , C. Prada, F.Wu, and D.Cassereau. Self focusing in inhomogeneous media with time reversal acoustic mirrors. *IEEE Ultrasonics Symposium, and Montreal, and Canada*, 2:681–686, 3-6 July 1989.

[47] C. Prada, F. Wu, and M. Fink. The iterative time reversal process: A solution to self focusing in the pulse echo mode. *The Journal of the Acoustical Society America*, 90(2):1119–1129, 1991.

[48] C. Prada, J.L. Thomas, and M. Fink. The iterative time reversal process: Analysis of the convergence. *The Journal of the Acoustical Society America*, 97(1):62–71, 1994.

[49] S. M. Popoff, A. Aubry, G. Lerosey, M. Fink, A. C. Boccara, and S. Gigan. Exploiting the time-reversal operator for adaptive optics, and selective focusing and scattering pattern analysis. *Physical Review Letters*, 107:263901, 2011.

[50] M. Tanter, J. L. Thomas, and M.Fink. Time reversal and the inverse filter. *The Journal of the Acoustical Society America*, 108:223–234, 2000.

[51] C. Prada, S. Manneville, D. Spoliansky, and M. Fink. Decomposition of the time reversal operator: Detection and selective focusing on two scatterers. *The Journal of the Acoustical Society America*, 99(4):2067–2076, 1996.

[52] S. Komilikis, C. Prada, and M.Fink. Characterisation of extended objects with the *DORT* method. *IEEE Ultrasonics Symposium*, 2:1401–1404, 1996.

[53] E. Cochard, C. Prada, J. F Aubry, and M. Fink. Ultrasonic focusing through the ribs using the *DORT* method. *Am. Assoc. Phys. Med.*, 36(8):3495–3503, 2009.

[54] D.H. Chambers and J. G Berryman. Analysis of the time reversal operator for a small spherical scatterer in an electromagnetic field. *IEEE Trans. on Antennas and Propagation*, 52:1729–1738, 2004.

[55] D.H. Chambers and J. G Berryman. Target characterisation using decomposition of the time-reversal operator: Electromagnetic scattering from small ellipsoids. *Inverse Problems*, 22:2145–2163, 2006.

[56] J. Davies, F. Simonetti, M. Lowe, and P. Cawley. Highly resolved detection and selective focusing in a waveguide using the *DORT* method. *The Journal of the Acoustical Society America*, 105(5):2634–2642, 1999.

[57] A. Aubry and A.Derode. Detection and imaging in a random medium: A matrix method to overcome multiple scattering and aberration. *J. Appl. Phys.*, 106(4):044903, 2009.

[58] A. Aubry and A. Derode. Multiple scattering of ultrasound in weakly inhomogeneous media: Application to human soft tissues. *The Journal of the Acoustical Society America*, 129(225):225–233, 2011.

[59] A. Aubry and A. Derode. Singular value distribution of the propagation matrix in a random scattering media. *Waves in Random and Complex Media*, 20(3):333–363, 2010.

[60] G. Harvey, A.Tweedie, C. Carpentier, and P. Reynolds. Finite element analysis of ultrasonic phased array inspections on anisotropic welds. *AIP Conf. Proc., and San Diego, and California*, 1335:827–834, 18-23 July 2010.

[61] PZFlex Weidlinger Associates Inc. 399 West El Camino Real Mountain View CA 94040-2607.

[62] A. J. Schwartz, M. Kumar, B.L. Adams, and D.P. Field. *Electron Backscatter Diffraction in Materials Science*. Springer, New York, USA, 2009.

[63] S. Chatillon, L. de Roumilly, J. Porre, C. Poidevin, and P. Calmon. Simulation and data reconstruction for ndt phased array techniques. *Ultrasonics*, 44:951–955, 2006.

[64] D. Hertz. Simple bounds on the extreme eigenvalues of toeplitz matrices. *IEEE Trans. Inform. Theory.*, 38(1):175–176, 1992.

[65] M. Abramowitz and I.A. Stegun. *Handbook of Mathematical Functions with Formulas, and Graphs and Mathematical Tables*. Dover Publications, New York, USA, 1972.

[66] J.G Minonzio, C. Prada, A.Aubry, and M. Fink. Multiple scattering between two elastic cylinders and invariants of the time reversal operator: Theory and

experiment. *The Journal of the Acoustical Society America*, 106(2):875–883, 2006.

[67] D.H. Chambers and A.K. Gautesen. Time reversal for a single spherical scatterer. *The Journal of the Acoustical Society America*, 119(7):2616–2624, 2001.

[68] A. Aubry and D. Derode. Random matrix theory applid to acoustic backscattering and imaging in complex media. *Phys. Rev. Lett.*, 102:084301, 2009.

[69] V.A. Marčenko and L.A. Pastur. Distribution of eigenvalues for some sets of random matrices. *Math. USSR-Sbornik*, 1(4):457–483, 1967.

[70] C. Nageswaran, C. Carpentier, and Y.Y. Tse. Microstructural quantification, and modelling and array ultrasonics to improve the inspection of austenitic welds. *Insight*, 51(12):660–666, 2009.